Ultracold RbSr

Optical and magnetic spectroscopy, Feshbach resonances and molecular structure

Barbé, V.P.J.

Publication date
2021

Document Version
Final published version

License
Other

Ultracold RbSr: Optical and magnetic spectroscopy, Feshbach resonances and molecular structure

Vincent Barbé

Van der Waals-Zeeman Institute, Institute of Physics

University of Amsterdam

A thesis submitted for the degree of

Doctor of Philosophy

September 2020

Ultracold RbSr: Optical and magnetic spectroscopy, Feshbach resonances and molecular structure

ACADEMISCH PROEFSCHRIFT

ter verkrijging van de graad van doctor
aan de Universiteit van Amsterdam
op gezag van de Rector Magnificus
prof. dr. ir. K.I.J. Maex
ten overstaan van een door het College voor Promoties ingestelde commissie,
in het openbaar te verdedigen in de Agnietenkapel
op woensdag 24 februari 2021, te 10.00 uur

door Vincent Philippe Jean Barbé
geboren te La Roche-Sur-Yon

Promotiecommissie

Promotor:	prof. dr. F.E. Schreck	Universiteit van Amsterdam
Copromotor:	dr. B.B. Pasquiou	Universiteit van Amsterdam
Overige leden:	prof. dr. S. Ospelkaus-Schwarzer	Leibniz Universität Hannover
	prof. dr. ir. G.C. Groenenboom	Radboud Universiteit Nijmegen
	prof. dr. J.T.M. Walraven	Universiteit van Amsterdam
	prof. dr. ir. H.B. van Linden van den Heuvell	Universiteit van Amsterdam
	dr. R. Gerritsma	Universiteit van Amsterdam

Faculteit der Natuurwetenschappen, Wiskunde en Informatica

The research reported in this thesis was carried out at the Van der Waals-Zeeman Institute, Institute of Physics, University of Amsterdam. The research for/publication of this doctoral thesis received financial assistance from the Netherlands Organisation for Scientific Research (NWO) through the Programme grant No. 680.92.18.05, Quantum Simulation 2.0 and the Vici grant No. 680-47-619, and from the European Research Council (ERC) under the European Union's Seventh Framework Programme (FP7/2007-2013) (Grant agreement No. 615117 QuantStro).

À mon père et ma mère.

Summary

Atoms and molecules are the constituents of the material world. The binding of atoms into diatomic and polyatomic molecules is the basis of all chemistry, and renders possible the emergence of stars and galaxies, atmospheres and oceans, DNA and proteins.

The last decades have witnessed the rapid development of experimental methods for the study of atoms and molecules at the microscopic level. Manipulating individual particles and individual quantum states has become possible, a physicist's dream once thought to be delusional. The development of laser light sources in the second half of the 20^{st} century, followed by their application to the cooling and trapping of particles, has permitted the creation of highly quantum-degenerate gases of atoms in the form of Bose-Einstein condensates and Fermi seas, and the extensive study of their properties. Molecules, on the other hand, have proven more stubborn. Harder to cool down, harder to control at high densities, they come with a body of complexity that makes them both extremely appealing and very difficult objects of study. To this date, only a handful of experimental groups in the world have obtained gases of diatomic molecules, the simplest form of all molecules, in the quantum-degenerate regime.

This thesis reports on the experimental investigation of the RbSr molecule, which is a strongly polar, open-shell molecule. Such molecules are the subject of intense and ongoing experimental interest around the world, but have never been brought to the quantum-degenerate regime thus far. Hopefully, the methods and results presented in this thesis will lead to a change of this situation in the future.

Two major results led to peer-reviewed publications in the context of this PhD thesis. The first is the experimental observation of magnetic Feshbach resonances between alkali and closed-shell atoms, never achieved before. This result opens the door to the magnetic association of atom pairs into molecules of a new kind, among them RbSr, that have never been produced in the laboratory due to a lack of known magnetic resonances. The second major result is the understanding of the potential energy curve of ground-state RbSr, an achievement of high importance for our future research. Based on this potential energy curve, we could predict the collisional properties of Rb-Sr mixtures of any isotopic combination, the binding energies of all molecular states in the electronic ground state and the position of

yet-unobserved Feshbach resonances. In addition, an extensive part of my PhD was dedicated to the exploration of electronically-excited potential energy curves of RbSr. The results of this work are subject to an ongoing theoretical analysis, which will be published in the future. The last years of my PhD have been dedicated to the implementation of experimental methods for the production and loading of cold Rb-Sr gases in an optical lattice, and to the implementation and characterization of a magnetic field stabilization system for RbSr magnetoassociation. This work is subject to ongoing development and improvement in the laboratory and I will discuss it succinctly in the outlook of this thesis.

This manuscript serves two purposes. First, it will give the general and specialized reader a state-of-the-art account of the properties, applications and methods of formation of ultracold RbSr molecules. Second, it will present the theoretical and experimental concepts that underlie my PhD work in the RbSr laboratory. I have tried to synthetize in a clear and exhaustive manner the knowledge I have accumulated throughout the years, so that those who will come after me can rely upon it. The rotational and vibrational structure of RbSr is discussed in depth, along with the spectroscopy methods that I have used to explore it. The physics of Feshbach resonances in ultracold atom experiments is covered extensively, with particular attention given to bi-alkali resonances and resonances between alkali and closed-shell atoms, such as those I have observed in RbSr. From this knowledge I hope that new results and new ideas will emerge, for science is a long and unpredictable road.

Samenvatting

Atomen en moleculen zijn de bestanddelen van de materiële wereld. De verbinding van atomen in twee-atomige en meeratomige moleculen is de basis van alle chemie, en maakt het ontstaan mogelijk van sterren en sterrenstelsels, atmosferen en oceanen, DNA en proteïnen.

De laatste decennia zijn we getuige geweest van een snelle ontwikkeling van experimentele methodes om atomen en moleculen op microscopisch niveau te bestuderen. Het is mogelijk geworden om individuele deeltjes en kwantumtoestanden te manipuleren – voor natuurkundigen een droom die ooit een waanvoorstelling leek. De ontwikkeling van laserlichtbronnen in de tweede helft van de twintigste eeuw, gevolgd door hun toepassing bij het koelen en insluiten van deeltjes, heeft het mogelijk gemaakt kwantum-ontaarde gassen uit atomen te verkrijgen in de vorm van Bose-Einsteincondensaten en Fermi-zeeën, en hun eigenschappen uitgebreid te bestuderen. Moleculen hebben daarentegen bewezen koppiger te zijn. Aangezien ze moeilijker zijn af te koelen en bij hoge dichtheden lastiger te beheersen, gaan ze gepaard met een complexiteit die ze tegelijkertijd extreem aantrekkelijk en erg lastig maakt om te bestuderen. Tot op de dag van vandaag hebben slechts een handjevol experimentele groepen in de wereld gassen verkregen uit twee-atomige moleculen, het eenvoudigste type moleculen in het kwantum-ontaarde regime.

Dit proefschrift doet verslag van het experimenteel onderzoek aan het RbSr-molecuul, een sterk polair open-shell molecuul. Zulke moleculen zijn over de hele wereld het onderwerp van intense en voortdurende experimentele interesse, maar zijn tot dusver nooit naar het kwantum-ontaarde regime gebracht. Hopelijk brengen de methoden en resultaten die in dit manuscript worden gepresenteerd in de toekomst verandering in deze situatie.

Twee belangrijke resultaten leidden in de context van dit proefschrift tot peer-reviewed publicaties. Het eerste was de experimentele waarneming van magnetische Feshbach-resonanties tussen alkali-atomen en aardalkali-atomen, wat nooit eerder was gelukt. Dit resultaat opent de deur voor de magnetische associatie van paren van atomen tot moleculen van een nieuw type, waaronder RbSr, die nooit in het laboratorium zijn geproduceerd vanwege een gebrek aan bekende magnetische resonanties. Het tweede belangrijke resultaat is het begrijpen van de potentiaalcurve van RbSr in de grondtoestand, een prestatie van groot belang voor ons toekomstige onderzoek. Op basis van deze potentiaalcurve konden we de botsingseigenschappen voorspellen van Rb-Sr-mengsels van elke isotopische combinatie, evenals

de bindingsenergieën van alle moleculaire toestanden in de elektronische grondtoestand en de positie van nog niet waargenomen Feshbach-reso-nanties. Daarnaast was een groot deel van mijn promotieonderzoek gewijd aan de verkenning van elektronisch geëxciteerde potentiaalcurves van RbSr. De resultaten hiervan zijn het onderwerp van een nog lopende theoretische analyse die in de toekomst zal worden gepubliceerd. De laatste jaren van mijn promotieonderzoek heb ik gewijd aan de implementatie van experimentele methoden voor de productie en het laden van koude Rb-Sr-gassen in een optisch rooster, en aan de implementatie en karakterisatie van een stabilisatiesysteem voor magnetische velden voor RbSr-magneto-associatie. Dit werk wordt nog verder ontwikkeld en verbeterd in het laboratorium en zal in het kort door mij worden besproken in de discussie van dit proefschrift.

Deze tekst dient twee doeleinden. Ten eerste geeft het de algemene en gespecialiseerde lezer een state-of-the-art verslag van de eigenschappen, toepassingen en methoden van de vorming van ultrakoude RbSr-moleculen. Ten tweede presenteert het de theoretische en experimentele concepten die ten grondslag liggen aan mijn promotieonderzoek in het RbSr-laboratorium. Ik heb geprobeerd de kennis die ik door de jaren heen heb vergaard op een heldere en grondige manier te synthetiseren, zodat zij die na mij komen erop kunnen vertrouwen. De rotationele en vibrationele structuur van RbSr wordt uitgebreid besproken, samen met de spectroscopiemethoden die ik heb gebruikt om het te onderzoeken. De fysica van Feshbach-resonanties in ultrakoude-atoomexperimenten wordt uitgebreid behandeld, met bijzondere aandacht voor bi-alkali-resonanties en resonanties tussen alkali- en aardalkali-atomen, zoals die ik heb waargenomen in RbSr. Ik hoop dat er op basis van deze kennis nieuwe resultaten en nieuwe ideeën zullen ontstaan, want de wetenschap is een lange en onvoorspelbare weg.

Translated from the English version by Felix van de Vorst (felixvandevorst@gmail.com).

Contents

Chapter 1

Ultracold molecules and RbSr: an introduction

1.1 Of ultracold atoms and molecules

Ultracold atoms and ions are an extremely fast-evolving and fruitful field of research since more than 40 years now. The expansion of the field has been accompanied by the awarding of three Nobel prizes in physics in 1997, 2001 and 2012. The former was awarded for the development of methods to cool and trap atoms with laser light, the second for the achievement of Bose–Einstein condensation in dilute gases of alkali atoms, and for early fundamental studies of the properties of the condensates, and the latest for the development of experimental methods that enable measuring and manipulation of individual quantum systems. These experimental techniques are based on *laser cooling* methods and have led to the creation of ensemble of atoms and ions in the μK and nK regimes, orders of magnitude colder than the lowest gas temperatures obtained with the best cryogenic He-based buffer gas cooling methods (limited by the boiling temperature of He to a few K at best). In this extreme temperature regime in which ultracold atom or ion experiments operate, the phase space density (PSD) of the gas is very high and effects of quantum degeneracy are unveiled.

The PSD is given by $\text{PSD} = n \times {\lambda_{\text{th}}}^3$, where n is the density n of the gas (typically expressed in particles.cm^{-3}) and $\lambda_{\text{th}} = h/\sqrt{2\pi m k_B T}$ is the thermal de Broglie wavelength of the atomic matter wave for an ensemble of atoms of mass m at the temperature T, with h and k_B the Planck and Boltzmann constants respectively. The typical densities and temperatures obtained in our experiments are indicated below.

Temperature (T):	10^{-6} to 10^{-9} K	(liquid He: 4 K)	
Density (n):	10^{11} to 10^{15} cm^{-3}	(ambiant air: $\sim 10^{19}$ cm^{-3})	(1.1)
PSD:	0.01 to $\gg 1$		

The thermal wavelength is very large in ultracold experiments and leads to the abovementioned unusually large PSDs. Atomic densities, on the other hand, are typically very small compared to "normal life" gases. These low densities are a natural consequence of the design of laser cooling experiments, and are required to maintain the existence of a cold gas of neutral atoms. Indeed, at very low densities the collisions between atoms are largely dominated by two-body elastic collisions[1], whereas at higher densities the gas would rapidly suffer from three-body recombinations that produce molecules and heat the gas considerably. This extreme regime, where the thermal wavelength λ_{th} is comparable or greater than the interparticle spacing can really be considered the hallmark of ultracold atom experiments.

Ultracold molecules are to ultracold atoms what the grey wolf is to the Labrador. The laser techniques that permit to cool very hot ensembles of atoms down to ultracold temperatures can not be applied straightforwardly to molecules, owing to the absence of *cycling transitions* in such systems. Neutral atoms display several such electronic transitions, which are almost fully closed with respect to the cycle of absorption – spontaneous emission of photons during Doppler cooling: after electronic excitation through absorption of a resonant laser photon, the atom decays from the excited state towards its initial state due to a spontaneous emission event. This allows the scattering of 10^4 – 10^5 or more cooling photons from the same laser source and brings us straight into the ultracold regime. For instance, the fully-cycling $^1S_0$ – $^3P_1$ electronic transition of Sr at $\lambda = 689$ nm allows us to cool gases directly from ∼mK temperatures (obtained in our initial Sr magneto-optical trap (MOT)) down to about 0.5 μK — which is sufficiently cold to achieve quantum degeneracy in dense clouds [1][2]. Such cycling transitions are simply absent in molecules, due to their complex

[1] An elastic collision is defined as a collision during which the momentum of the two partners is changed/redistributed, while the total kinetic energy of the pair is conserved. This is the type of collisions one observes on a snooker table. Inelastic collisions, on the other hand, lead to changes of the internal degrees of freedom of the collisional partner. Inelastic processes include two-body spin-changing collisions (very strong in non-polarized Cs for instance, but very weak in ^{87}Rb as we discuss briefly in Section 5.2 of Chapter 5), and three-body recombination losses that occur when two atoms form a molecule, with the molecular binding energy being transferred to the molecule and to a third collisional partner in the form of kinetic energy.

[2] The Doppler temperature, which is the lowest temperature that one can obtain using Doppler cooling with a certain electronic transition is given by $k_B \times T_D = \hbar\gamma/2$, where γ is the linewidth of the transition, with $\gamma/2\pi = 7.50$ kHz for the $^1S_0$ – $^3P_1$ transition of Sr at $\lambda = 689$ nm. The Doppler temperature of this transition is thus $T_D = 180$ nK, and is extremely low due to the semi-forbidden character of the transition that implies a very small linewidth. The final temperature of this cooling stage is actually limited by the recoil temperature $T_r = \hbar^2k^2/k_Bm$, which is $T_r = 481$ nK for ^{84}Sr and corresponds to the kinetic energy $\hbar^2k^2/2m$ transferred to the atom of mass m upon absorption of a photon of wavelength $k = 2\pi/\lambda$. As a comparison, the $^1S_0$ – $^1P_1$ transition of Sr at $\lambda = 461$ nm

internal structure. In addition to electronic and hyperfine degrees of freedom, also present in atoms, they display vibrational and rotational degrees of freedom which complicate laser cooling tremendously[3]. Upon excitation towards an electronically excited molecular state, a molecule typically decays to several different states with rotational and vibrational quantum numbers differing from that of the initial state (most often the non-excited initial state would be the molecular state of lowest rotational and vibrational quantum numbers, aka the rovibrational ground state[4], and the excited molecule would decay to vibrationally and/or rotationally excited states). These states are not addressed by the laser cooling beam, because their energy differs from that of the initial molecular state by typically much more than the linewidth of the cooling transition: the molecule is thus lost from the optical cycle. The scattering of 10^4 – 10^5 resonant photons without significant losses may be considered a huge success (comparable to the amount of scattered photons needed to slow an atom or small molecule from room temperature velocities, i.e. several 100 m/s, to standstill), and typical cycles currently implemented involve 10^2 – 10^3 photons. An excellent up-to-date discussion on the prospects and difficulties of laser cooling of molecules can be found in Ref. [2]. These difficulties have not stopped people from developing methods for the laser cooling of molecules though. These methods are referred to as "direct laser cooling" in the literature and typically require a cryogenic buffer gas cooling stage to cool the initial molecular gas down to a few K before laser cooling, a wise choice of molecular species to limit the decay to non-desired molecular states, and several additional lasers (for a total of around 7 to 15 lasers typically) to repump the molecules that fell into an off-resonant state back into the optical cooling cycle. Another successful method is the production of a molecular beam with a skimmer, followed by expansion cooling in vacuum It produces a mK-cold beam of molecules in its own frame of motion, with a very large velocity in the laboratory frame that is then reduced using either Stark [3] or Zeeman deceleration [4]. While these direct cooling methods are very fast-evolving and break records every year, they are to this date limited by

that we use for Zeeman slowing and for the initial Sr MOT has $\gamma/2\pi = 30.5\,\mathrm{MHz}$, corresponding to a Doppler temperature of $T_D = 732\,\mu\mathrm{K}$. Note that this transition is not fully cycling. After a few 10^4 scattering events, the atom excited to the $^1P_1$ state decays to another electronically excited state (a $^1D_2$ state) instead of coming back to the ground state. In such cases a repumping laser is required to bring back the atoms in the cooling cycle.

[3]The internal structure of diatomic molecules, and in particular that of RbSr in its electronic ground state, is discussed extensively in Chapter 2. In this chapter, electronic degrees of freedom are denoted by the quantum numbers n (n stands for all quantum numbers necessary to the description of the electronic state, and is not to be confused with the atomic density n discussed in this introduction chapter) and the vibrational and rotational degrees of freedom of ground-state RbSr are denoted as v and N respectively.

[4]The term "rovibrational" is a contraction of "rotational" and "vibrational", and the rovibrational ground state for RbSr consists of the molecular state with no rotation ($N = 0$) and of lowest vibrational excitation. The term "rovibronic", contraction of "rotational", "vibrational" and "electronic" is also used in the literature and indicates additionally the electronic state of motion. In this section the electronic manifold considered is the RbSr $^2\Sigma^+$ electronic ground state term, therefore the "rovibrational ground state" implicitly indicates the rovibronic ground state of RbSr.

the small densities of molecules achieved, typically in the range 10^7 – $10^8\,\mathrm{cm}^{-3}$, with temperatures in the range of $1 - 1000\ \mu$K for state-of-the-art direct cooling experiments. The best phase space densities obtained to this date using direct molecule cooling methods are of order 10^{-8} – 10^{-7} [5] [6], still orders of magnitude away from the quantum-degenerate regime PSD ~ 1 of ultracold atom experiments.

Another road has been taken on the route towards ultracold molecular samples: the assembly of molecules from ultracold atom samples. This approach led to the creation of a few quantum-degenerate samples of molecules. Among them, a Bose-Einstein Condensate (BEC) of weakly-bound Li_2 molecules [7], and a Fermi sea of polar KRb molecules in the rovibrational ground state (aka ground-state molecules) [8]. This approach also led to the production of several ultracold samples of polar molecules [9–16]. However, to this date no ultracold sample of strongly polar, open-shell molecules has been obtained. This thesis reports on an experimental effort oriented towards this new frontier.

1.2 Why RbSr?

1.2.1 A molecule strongly polar...

The large sensitivity of polar molecules, such as RbSr, to external DC and AC electric fields make them very appealing in view of several applications, as explained in Section 1.3. A polar molecule exhibits a *permanent dipole moment* in its own molecular frame (depicted in Figure 2.1 for a diatomic molecule), owing to the imbalance of electronegativity between the atoms constituting the molecule. Heteronuclear diatomic molecules such as RbSr provide the most simple polar molecular system: the closed-shell Sr atom is more electronegative than the alkali atom Rb, and "pulls" the valence electron of Rb towards its own nucleus, creating a gradient of charge along the internuclear axis. While a complete multipole expansion is in general necessary to account for the full complexity of this charge distribution, the first-order *dipole moment* term is largely sufficient to describe the sensitivity of the molecule to external electric fields. This permanent dipole moment is strongest in the vibrational ground state (i.e. the molecular state of largest binding energy) of the molecule, as seen from Figures 1.1 and 1.5 and can be measured either through beam deflection experiments [17] or through more precise quantum optics, single-quantum state resolved experiments [9]. The non-SI Debye unit, defined as $1\,\mathrm{D} = 3.33564 \times 10^{-30}\ \mathrm{C.m}^{-1}$, is the unit of choice for molecular electric dipole moments, and a molecule with a dipole moment $d > 1\,\mathrm{D}$ is typically considered strongly polar because it is suitable for dipole-dipole interaction engineering in an optical lattice (see Subsections 1.3.1 and 1.3.2)[5]. The RbSr molecule plays in that league with a dipole moment in the rovibrational ground-state of $\boldsymbol{d = 1.54\,D}$[6].

The electric dipole moment quantifies the strength of the interaction of the molecule with external DC and AC electric fields, as well as the strength of its electric dipole-dipole interactions with adjacent molecules. In absence of external fields, however, the molecule doesn't exhibit any dipole moment in the laboratory frame because the rotational eigenstates $|N, m_N\rangle$ that describe the angular distribution of the nuclei in field-free space are parity eigenstates[7]. In layman's terms, the Sr can be found with equal probability "up" or "down" compared to Rb with respect to any axis, which results in no net dipole moment in the laboratory frame. It is therefore necessary to apply external electric fields to *mix parity eigenstates* and produce an experimentally observable dipole moment. The first approach to polarizing the molecules is to use a DC electric field $\vec{\mathrm{E}}_{\mathrm{DC}}$. The interaction of this field with the dipole moment $\vec{\mathrm{d}}$ of the molecule (also denoted as DC Stark effect) is

[5] Throughout this chapter dipole moments are denoted as $\vec{\mathrm{d}}$ and d indicates the corresponding magnitude $|\vec{\mathrm{d}}|$.

[6] This value is approximated by the value of the RbSr dipole moment at the equilibrium position of the PEC, where most of the internuclear probability $|\chi_{v,N=0}(R)|^2$ of the rovibrational ground state wavefunction is located.

[7] See Equation 2.39 for an explicit expression of the RbSr rotational eigenstates $|N, m_N\rangle$ in the electronic ground state $^2\Sigma^+$. Their parity is given by $(-1)^N$.

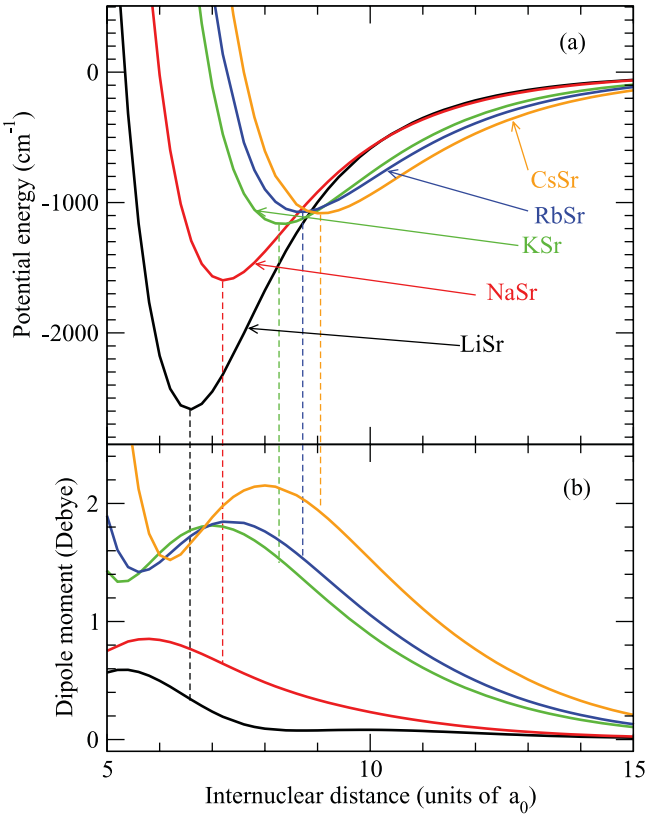

FIGURE 1.1: (a) Potential energy curves (PECs) and (b) permanent dipole moments (PDMs) for the $X\,^2\Sigma^+$ ground state of the alkali-Sr diatomic molecules. Vertical lines guide the eye to locate the value of the PDM at the equilibrium distance. The Bohr radius is $a_0 = 0.529177210$ Å. From Ref. [18].

$$H_{\mathrm{DC}} = -\vec{\mathrm{d}} \cdot \vec{\mathrm{E}}_{\mathrm{DC}} \,, \tag{1.2}$$

and the electric field $\vec{\mathrm{E}}_{\mathrm{DC}}$ can in practice be produced by a set of fixed-voltage electrodes, creating a voltage gradient across the molecular cloud and forcing the molecules to align to the field direction. The smaller the distance between the + and - electrodes the better (less voltage is required to achieve large fields, which allows to create fields with less noise or higher fields), and accordingly for fields of amplitude $\mathrm{E}_{\mathrm{DC}} > 1$ kV.cm^{-1} it is typically best to implement in-vacuum electrodes for ultracold experiments. Compared to electrodes placed around the vacuum chamber, in-vacuum electrodes also reduce drastically the accumulation

of charges on the glass cell containing the atoms, which is limiting the reliability of the E-field magnitude from one experimental run to the other. The DC field admixes a given state $|N, m_N\rangle$ with other rotational states of rotational numbers $N \pm 1$ [19]. The resulting dressed eigenstate, denoted as $|\widetilde{N}, \widetilde{m}_N\rangle = |N, m_N\rangle + \sum_i c_i |N', m_{N'}\rangle$ is not a parity eigenstate anymore and exhibits a dipole moment in the laboratory frame: at large fields this dipole moment saturates to a value close to the dipole moment of the molecule itself for the rotational ground state $|\widetilde{0}, \widetilde{0}\rangle$. Additionally the Stark effect H_{DC} induces a shift of the energy of $|\widetilde{N}, \widetilde{m}_N\rangle$ that gets larger for larger fields $\mathrm{E_{DC}}$, as shown in Figure 1.3 for RbSr, and can be employed to deflect the molecules [17] or to slow them down as in a Stark decelerator [3]. An important parameter for this DC field approach is the characteristic field at which the dipole moment in the laboratory frame saturates, and at which it can be said that the molecule is almost fully polarized: it is given by $E = B/d$, where B is the rotational constant of the vibrational state of interest, and in the vibrational ground state of RbSr in which $B = h \times 539.6\,\mathrm{MHz}$ [20][8] it is **E = 0.7 kV.cm^{-1}**.

The second approach to polarizing molecules consists in using AC electric fields. The interaction between the dipole moment of the molecule and the field of pulsation ω (also denoted as AC Stark effect) is

$$H_{\mathrm{AC}} = -\vec{\mathrm{d}} \cdot \vec{\mathrm{E}}_{\mathrm{AC}}(t) = -\vec{\mathrm{d}} \cdot \vec{\mathrm{E}}_{\mathrm{AC}}\, e^{-i\omega t} + \mathrm{c.c.}\,, \tag{1.3}$$

and also couples rotational states of different parity. Optical frequencies derived from laser beams in the range $\omega/2\pi = 10 - 10000$ THz can couple molecular states belonging to electronic states of different parities (see Chapter 2, Figure 4.1 for the ground and excited electronic states of RbSr), but are not suitable to coherent schemes owing to the typically short lifetime of the excited state. THz radiation in the $\omega/2\pi = 0.1 - 10$ THz range is promising in terms of manipulation of the dipole moment of molecules, as was recently demonstrated by one of our collaborators in the context of RbSr [21], but suffers from a technological gap that limits the (currently) achievable intensities to low values of order W.cm^{-2}. Microwave and radiofrequency (RF) radiation, in the ranges $\omega/2\pi = 1 - 100\,\mathrm{GHz}$ and $\omega/2\pi =$ 10 kHz – 100 GHz respectively, are on the contrary available for cheap prices at very large intensities: they reveal the full splendor of molecules by coupling rotational states $|N, m_N\rangle$ within the same electronic manifold, a situation inexistent in atomic or ionic systems. These rotational states have lifetimes larger than any experimentally relevant timescale and make such schemes very competitive for coherent physics including quantum gates, simulations

[8] This value has not been updated after our work on the ground state PEC of RbSr, but the characteristic field value should be almost unchanged.

of spin systems and precision measurements involving the engineering of correlated quantum ensembles. The simplest of such RF dipolar schemes is a $\pi/2$ pulse creating an equal superposition of the $|N, m_N\rangle = |0,0\rangle$ state and of one of the three $|N, m_N\rangle = |1,0\rangle$, $|1,-1\rangle$ or $|1,+1\rangle$ states of a given vibrational manifold [22], which produces a *transition dipole moment* of about $d/\sqrt{3}$ in the laboratory frame (where d is the dipole moment of the molecule in its own frame, in a given vibrational state). This scheme has been implemented using the $|0,0\rangle$ and $|1,-1\rangle$ of the vibrational ground state of KRb [23]. However, the palette of complex dipolar patterns that can be engineered by the superposition of several microwave and RF fields of different intensities, polarization, frequencies is essentially infinite, and is particularly rich in RbSr as we show in the next sections.

1.2.2 ... and open-shell ...

On top of exhibiting an electric dipole in its own frame, the RbSr molecule exhibits an unpaired valence electron, which distinguishes it from the other ultracold polar molecules that have been produced so far. The Rb atom is an alkali, open-shell atom with one unpaired valence electron in its 5s shell and accordingly has a total spin $S = 1/2$. The Sr atom, on the other hand, is an alkaline-earth, closed-shell atom with two 5*s* valence electrons. Its total spin wavefunction is thus antisymmetric, owing to Pauli's exclusion principle, and it has $S = 0$. The resulting diatomic RbSr molecule is open-shell, with $S = 1/2$ and a ground state $^2\Sigma^+$ doublet electronic term (the superscript 2 indicates the multiplicity of the total spin $2S + 1$, see Chapter 2). The unpaired RbSr electron confers RbSr with a strong magnetic sensitivity, which is largely absent in closed-shell molecules. A complete state-of-the-art discussion of the magnetic hyperfine structure of RbSr is given in Ref. [24].

To this date, the only polar molecules that have been assembled from ultracold atoms are bi-alkali molecules. The electronic ground state of such molecules is a singlet $^1\Sigma^+$ of total spin $S = 0$, with no unpaired electron. They are thus closed-shell molecules, which exhibit a very small magnetic sensitivity. Note that NaLi molecules have been produced in the rovibrational ground state of the triplet $^3\Sigma^+$ term, where the total spin is $S = 1$ and the two valence electrons are unpaired [15]. However, the equilibrium distance of the triplet potential energy curve (PEC) of a bi-alkali pair is much larger than that of the singlet PEC, as shown in Chapter 2, Figure 5.5. Accordingly, the ground-state triplet molecule looses much of its polar character compared to its ground-state singlet version[9]: it is only d = 0.2 D for triplet NaLi.

[9]The term ground-state molecule usually refers to the rovibrational ground state (i.e. the ground state of rotational and vibrational motion) in the literature. It doesn't necessarily denotes the rovibronic ground state, which is the rovibrational ground state of the singlet PEC in bi-alkali systems.

The reason for the success of bi-alkali experiments is the availability in such systems of large magnetic Feshbach resonances that allow very fast and efficient magnetoassociation of a pair of atoms into a weakly-bound molecule. Such large resonances don't exist in dimers of an alkali and a closed-shell atom such as RbSr, but narrow resonances have been predicted in the past [25, 26] — a complete presentation of Feshbach resonances in RbSr and bi-alkali systems is given in Chapter 5. This PhD thesis reports on the first experimental observation of Feshbach resonances between alkali and closed-shell atoms, which has opened the door to future magnetoassociation in these systems and has been followed by the detection of resonances in LiYb [27].

1.2.3 ... with several stable isotopic combinations

The number of available atomic isotopes of the species of interest is a very important criterion to assess before the construction of an ultracold atom experiment, and it is even more important in the case of molecule assembly projects such as our RbSr experiment. The reasons are two-fold. First, the quantum statistical properties are very different for bosonic and fermionic species (they follow respectively Bose-Einstein and Fermi-Dirac statistics, which has a huge impact on collisional and exchange properties). Second, the collisional properties of a new system are unknown prior to experimental investigation. In particular, in the ultracold regime the s-wave scattering length a_s largely governs the collisional properties of pairs of distinguishable particles. It is defined by the PEC of the atom pair[10] and by its mass, and it changes from isotopologue to isotopologue (in our case the isotopologues are ^{87}Rb^{88}Sr, ^{87}Rb^{87}Sr, ^{85}Rb^{87}Sr, ...) due to the change in atom pair mass with changing number of neutrons. Theoreticians can compute the PEC of an atom pair only up to a finite accuracy, and it is never sufficient to infer the s-wave scattering length of the dimer prior to experimental investigation. Therefore, having several stable isotopes of each species at disposal multiplies the probability of finding an isotopologue with suitable collisional properties. There are two naturally-occurring stable (i.e. non-radioactive) isotopes of Rb[11]: ^{85}Rb and ^{87}Rb. There are four of Sr: ^{88}Sr, ^{87}Sr, ^{86}Sr and ^{84}Sr. Both Rb isotopes are bosonic, and all stable Sr isotopes are bosonic at the exception of fermionic ^{87}Sr. This leaves us with 8 isotopologue combinations, of which 6 correspond to bosonic diatomic RbSr molecules (^{87}Rb^{88}Sr, ^{87}Rb^{86}Sr, ^{87}Rb^{84}Sr, ^{85}Rb^{88}Sr, ^{85}Rb^{86}Sr and ^{85}Rb^{84}Sr) and 2 to fermionic molecules (^{87}Rb^{87}Sr and ^{85}Rb^{87}Sr). That is quite a large playground. Furthermore, it is possible to produce quantum-degenerate

[10] The PEC of the atom pair is an electromagnetic property that is independent of mass. All RbSr isotopologues are thus defined by the same ground-state PEC.

[11] Strictly speaking, ^{87}Rb is radioactive and decays to ^{87}Sr, However its half-life 4.92×10^{10} years. We should be able to perform a few experiments within this time span

gases of both Rb and Sr (Bose-Einstein condensates for bosons, Fermi seas for the fermion ^{87}Sr), and we do so on a daily basis in the RbSr laboratory.

Forming a given isotopologue of RbSr requires favorable intra-species and inter-species s-wave scattering lengths. These scattering lengths determine to a large extent the scattering properties of the mixture. A positive scattering length is highly preferable to avoid collapse of the clouds at high densities, and a medium scattering length around $a_s \sim 30 - 300\,a_0$ is suitable to ensure fast thermalization of the gas through elastic collisions[12]. We use this thermalization process heavily in the RbSr experiment, because we can produce very pure BECs and Fermi seas of Sr efficiently. During the formation of the quantum gas, Sr is cooled down using evaporative cooling and the Rb atoms are sympathetically cooled through elastic collisions with the cold Sr atoms. To make this *cross-thermalization* process efficient and reach quantum degeneracy with both species in the same trap, it is thus preferable to have a Rb-Sr inter-species scattering length of about $a_s \sim 30 - 300\,a_0$. One of the major results of the present PhD thesis is a much improved understanding of the ground-state PEC of RbSr, which is discussed extensively in Chapter 2 and led to the publication presented in Chapter 3. This improved understanding allowed us to derive the s-wave scattering length of each isotopologue of RbSr. We indicate in Table 1.1 the values of these scattering lengths. The intra-species scattering lengths of Rb and Sr are also essential to the formation of RbSr molecules, because they define in which mixture it is easy to obtain large samples of quantum degenerate atoms. The scattering length of the bosonic ^{84}Sr isotope ($a_s = 124\ a_0$) is positive and lies in the range $a_s \sim 30 - 300\,a_0$. It is thus possible to perform efficient evaporative cooling with ^{84}Sr and to produce BECs of up to 10^7 ^{84}Sr atoms in our experiment. Similarly, the scattering length of the fermionic ^{87}Sr isotope isotope ($a_s = 97\ a_0$ for the collision of two ^{87}Sr atoms in different m_I states) allows the formation of Fermi seas at $T/T_F = 0.10(1)$ with 3×10^4 atoms in each one of the $m_I = -9/2, -7/2, ..., +9/2$ nuclear spin states of ^{87}Sr[13].

[12] If the scattering length is too small, the elastic two-body collisional cross-section and thermalization is very slow. If it is too large, three-body losses create heating and loss of atoms during the thermalization process.

[13] T_F is the Fermi temperature and $T/T_F \ll 1$ indicates a deeply quantum-degenerate gas.

TABLE 1.1: Rb-Sr inter-species s -wave scattering lengths in units of the Bohr radius a_0 ($a_0 = 0.529177210$ Å). The determination of these scattering lengths is a key achievement of this thesis — see also our publication presented in Chapter 3.

	^{84}Sr	^{86}Sr	^{87}Sr	^{88}Sr
^{85}Rb	689(20)	90.6(2)	44.3(3)	−35.8(1.0)
^{87}Rb	92.7(2)	−43.0(1.1)	1421(98)	170.3(6)

However ^{88}Sr has a negative scattering length ($a_s \sim -1\ a_0$) and ^{86}Sr has a very large scattering length ($a_s \sim 830\ a_0$), which prevents the production of Sr BECs with a large number of atoms in these systems (though it is still possible to produce them) [28, 29]. As for Rb, the intra-species scattering length of ^{87}Rb is close to 100 a_0 in both $F = 1$ and $F = 2$ hyperfine manifolds, and the scattering length of ^{85}Rb in its ground-state hyperfine manifold $F = 2$ can be tuned using a Rb-Rb magnetic Feshbach resonance [30]. Therefore both Rb isotopes are suitable for quantum gas preparation. Dismissing the isotopic combinations involving ^{88}Sr or ^{86}Sr for which only small Sr BECs can be achieved, we see from Table 1.1 that two Rb-Sr mixtures fulfill the inter-species scattering length condition $a_s \sim 30 - 300\ a_0$ that ensures efficient cross-thermalization: the ^{87}Rb-^{84}Sr and ^{85}Rb-^{87}Sr mixtures. The former corresponds to a bosonic molecule and the second to a fermionic molecule: very different types of physics can be addressed with these two molecules, owing to their different statistics, and we are currently investigating the formation of bosonic ^{87}Rb^{84}Sr.

1.3 Envisioned applications of RbSr molecules

In this section we describe succinctly the applications of ultracold RbSr molecules, based on several publications to which the reader is reported for full implementation details. These applications take advantage of the large electric dipole moment of RbSr and of its open-shell character.

1.3.1 Quantum simulation: engineering spin models with dipole-dipole and spin-rotation interactions

One of the major challenges of theoretical physics in the 21st century is to fully understand strongly correlated systems of interacting particles. In particular, condensed matter materials of fundamental and technological interest such as high-temperature superconductors involve the interaction of many electrons evolving in a ionic crystalline structure. The exponential growth of the size of the Hilbert space (growing for instance as 2^N for a system of N electronic spins or *qubits*) with the number of electrons prevents numerical methods based on classical computers to address the full extent of their properties. Such a full understanding would be extremely helpful to guide the design of new materials.

One way forward is *quantum simulation*, also referred to as *analog quantum computation*. Quantum simulators consist of synthetic quantum systems produced in the laboratory, such as ultracold atoms or molecules trapped in an optical lattice or ions captured in Paul or Penning traps. The Hamiltonian describing the motion and the interaction of these particles is engineered in such a way that it can be mapped onto the Hamiltonian describing a phenomenon of interest, for instance the Hamiltonian describing the motion of electrons in the ionic crystal of a promising material. A quantum simulator is a well-controlled system, that allows one to explore it differently and hopefully in much more detail than its solid-state analogue. The full extent of the properties of the material of interest is not simulated, as it is a formidable task and is actually not required to shed light on new interesting phenomena. Instead, it is the model used to capture the properties of the material which is simulated. Such models include the Hubbard model, the *t-J* model used in the context of high-temperature superconductivity in doped antiferromagnets, and many lattice spin systems that theoreticians study heavily, such as the Ising and Heisenberg models. These models also find interesting applications beyond condensed matter physics, for instance in high-energy physics, and there is thus considerable interest in addressing them with quantum simulators.

Ultracold polar molecules are a very promising platform for quantum simulation, in particular in the context of the simulation of spin lattices models. It is indeed possible to simulate the behaviour of electrons in a solid by arranging arrays or molecules in an optical lattice[14], i.e. a periodic potential created by laser beams. The strongly anisotropic dipole-dipole interaction $\hat{H}_{\mathrm{DDI}}$ between polar molecules mimics the interactions between the electrons in the crystal and is given by

$$\hat{H}_{\mathrm{DDI}} = \frac{1}{4\pi\varepsilon_0}\left[\frac{\vec{\mathrm{d}}_i \cdot \vec{\mathrm{d}}_j - 3\left(\vec{r}_{ij}\cdot\vec{\mathrm{d}}_i\right)\left(\vec{r}_{ij}\cdot\vec{\mathrm{d}}_j\right)}{\left|\vec{r}_i - \vec{r}_j\right|^3}\right], \tag{1.4}$$

where $\vec{\mathrm{d}}_i$ and $\vec{\mathrm{d}}_j$ are the laboratory-frame dipole moments of each molecule at the lattice sites i and j respectively, $\vec{r}_i$ and $\vec{r}_j$ are the position vectors for each lattice site and $\vec{r}_{ij} = \vec{r}_i - \vec{r}_j / \left|\vec{r}_i - \vec{r}_j\right|$ is the unit vector joining the molecules [31]. The dipole moment of each molecule in the laboratory frame is induced by applying either DC or AC polarizing electric fields as described in the previous section. Note that typical spacings between optical lattice sites are of the order of 500 nm (while in a real crystal they are on the order of 1 Å or 10^{-10} m), so that for dipole moments of 1 D in the laboratory frame the DDI between two adjacent molecules is of order $\sim h\times$ kHz. This approach opens the experimental possibility of creating and exploring lattice spin systems that capture the properties of interesting materials and that are the subject of intense theoretical efforts, such as the abovementioned Ising models and Heisenberg models. It was shown that polar, open-shell molecules such as RbSr are of particular interest for quantum simulation applications, because the coupling of their rotational momentum N with the electronic spin S of the unpaired valence electron can be used to engineer very rich and versatile lattice spin Hamiltonians. A toolbox with which many such Hamiltonians can be engineered has been theoretically established in Ref. [32]. Two example spin lattices are illustrated in Figure 1.2 and are described by the Hamiltonians $H^{(\mathrm{I})}_{\mathrm{spin}}$ and $H^{(\mathrm{II})}_{\mathrm{spin}}$ presented below.

$$\begin{aligned} H^{(\mathrm{I})}_{\mathrm{spin}} &= \sum_{i=1}^{\ell-1}\sum_{j=1}^{\ell-1} J\left(\sigma^z_{i,j}\sigma^z_{i,j+1} + \cos\zeta\,\sigma^x_{i,j}\sigma^x_{i+1,j}\right) \\ H^{(\mathrm{II})}_{\mathrm{spin}} &= J_\perp \sum_{x-\mathrm{links}} \sigma^x_j\sigma^x_k + J_\perp \sum_{y-\mathrm{links}} \sigma^y_j\sigma^y_k + J_z \sum_{z-\mathrm{links}} \sigma^z_j\sigma^z_k \end{aligned} \tag{1.5}$$

Here σ_i and σ_j are the Pauli matrices referring to spin i and j respectively, and the coefficients $J_\perp$ and J_z determine the coupling strengths. We have given these Hamiltonians as reference

[14] Optical lattices are discussed extensively in Chapter 5 in the context of magnetoassociation of atom pairs into molecules.

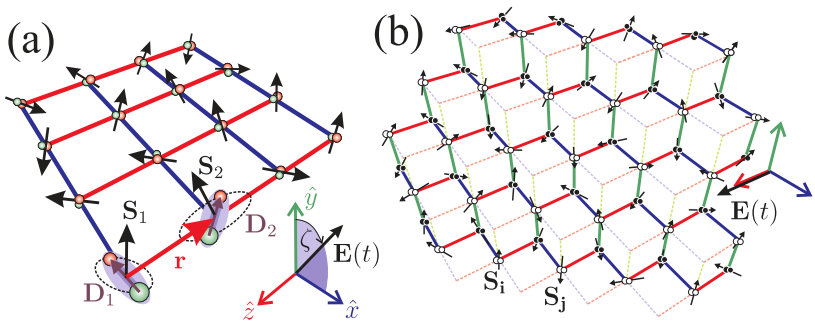

FIGURE 1.2: Example anisotropic spin models that can be simulated with polar molecules trapped in optical lattices. (a) Square lattice in 2D with nearest neighbor orientation dependent Ising interactions along $\hat{x}$ and $\hat{z}$. Effective interactions between the spins $\vec{S}_1$ and $\vec{S}_2$ of the molecules in their rovibrational ground states are generated with a microwave field $\vec{\mathrm{E}}_{\mathrm{AC}}(t)$ (see Equation 1.3) inducing dipole-dipole interactions between the molecules with dipole moments $\vec{D}_1$ and $\vec{D}_2$, respectively. (b) Two staggered triangular lattices with nearest neighbors oriented along orthogonal triads. The interactions depend on the orientation of the links with respect to the electric field (dashed lines are included for perspective). From Ref. [32].

and report the reader to the paper for further details.

Scalability is a decisive advantage of quantum simulation platforms based on ultracold molecules. It is indeed possible to fill an optical lattice with up to 10^5-10^6 molecules, whereas state-of-the-art competing platforms such as Rydberg atoms and ions are currently restricted to a few hundred particles in the very best cases. One of the major challenges encountered in ongoing experiments is to reach a filling close to unity (i.e. exactly one molecule per site with no holes in between). This is to this date one of the limiting factors for the observation of some highly-interesting dipolar physics with molecules in lattices. We designed our experiment in such a way that it should be capable of supporting about 10^5 RbSr molecules in a 1064 nm optical lattice.

1.3.2 Quantum computation: molecules as qudits

Another promising application of polar molecules is *digital quantum computation*. In this approach, the internal levels of a particle are used as bits, similar to the classical bits of a transistor in a classical computer taking the values 0 or 1, but with the extra possibility of having superposition states $|\phi\rangle = \alpha|0\rangle + \beta|1\rangle$. This approach is in principle more general than quantum simulation, and holds the promise of solving several sets of physics and

mathematics problems that classical computing cannot address. Polar molecules are a natural and competitive platform for quantum computation. Indeed, their rich and anharmonic rotational structure $|N, m_N\rangle$ can be used to encode qubits and can be manipulated with microwave and RF fields. The molecule can be used as a *qudit* (many-level system) instead of a *qubit* (two-level system, typically two electronic or motional states in atom or ion quantum computers). The dipole-dipole interaction between each molecule, Equation 1.4, is used to implement quantum logical gates between the qudits, and the experimentalist tracks the coherent evolution of the molecular ensemble, eventually reading out the state of the qudits - in full analogy with the readout of the output of a classical logic gate. In this context, one of the most important challenges is that of the coherence time of the quantum states: it must vastly exceed the gate timescale set by the dipole-dipole interaction. For polar molecules in optical lattices, the dipole-dipole interaction energy is typically in the $\sim h\times$kHz range (see previous subsection) and thus coherence times of order ms or more are required. We refer the reader to Ref. [33] for an excellent discussion of quantum computation with polar molecules.

1.3.3 Precision measurements: towards new physics?

One of the fields of research where cold atoms had the largest impact in the last 30 years is that of precision measurements. As of 2019 it is possible to measure the second (unit of time of the International System of Units) with an uncertainty of about 10^{-18} [34], which corresponds to a precision better than one second over the age of the entire universe and finds many applications, from GPS technology to fundamental physics. Cold atoms also provide the best gravitometers, which can reach unprecedented precision in the mapping of the geological landscape of the earth and are foreseen to be used for gravitational wave detection in frequency bands where Michelson-type interferometers such as LIGO, Virgo and LISA are not sensitive [35, 36].

Molecules have a richer internal structure than atoms, owing to their vibrational and rotational degrees of freedom, and can provide extremely accurate information about the interactions between their constituents. They promise for instance excellent sensitivity to the electron-to-proton mass ratio or to yet unknown long-range forces beyond standard electromagnetism [37]. One of the most advanced precision measurements currently being performed in experiments with polar molecules is that of the electron electric dipole moment or eEDM. According to the Standard Model of particle physics, the electron is a point charge particle and consequently its electric dipole moment d_e is (almost) null. The Standard Model predicts an upper bound of $d_e < 10^{-39}\, e$.cm, with e the elementary unit of

charge and 1 e.cm = 4.80321 $\times$ 10^{10} D. However, many extensions to the Standard Model predict larger values for the eEDM. thus any non-zero measurement above 10^{-39} e.cm would be indicative of new physics, that could shed light on the existence of dark matter and/or on the matter-antimatter asymmetry problem. It is in principle possible to measure a hypothetical eEDM by measuring the Stark shift $H_{\text{eEDM}} = -\vec{d}_e \cdot \vec{E}_{\text{DC}}$ of a of free electron, but the magnitude of this shift is limited by the electric field magnitude itself. Polar, open-shell molecules can be instead used for eEDM detection, and present a considerable advantage in this respect: the effective internal field of the polar molecule, interacting with the eEDM of its unpaired electron can be up to a million times larger than any static laboratory field. The current best experimental upper value of the eEDM is $d_e < 1.1 \times 10^{-29}$ e.cm and has been obtained by the ACME collaboration with the molecule ThO, of which the $^3\Delta_1$ electronic state of molecule provides an effective internal field of $E_{\text{eff}} \simeq 84\,\text{GV.cm}^{-1}$ at an applied electric field of moderate magnitude E = 0.14 kV.cm^{-1}. This result is presented in Ref. [38].

The eEDM measurements discussed above currently rely on molecular beams, and are therefore limited by the interaction time of the molecules with the external field. To overcome this limitation, the next generation eEDM experiments are foreseen to consist of large samples of ultracold molecules trapped in an optical lattice, where much longer interaction times and better statistical sensitivity could provide a $\times$1000 increase in the accuracy of the eEDM measurement. The ThO molecule cannot be easily cooled and trapped, but D. DeMille (Yale University, USA) and Timo Fleig (Paul Sabatier University, France) recently proposed to use the molecule RaAg [39]. This molecule is similar to RbSr, since it consists of one alkaline-earth atom (Ra) and one strongly electronegative alkali-like atom (Ag) and has the same electronic ground state term, $^2\Sigma$. The effective internal field of RaAg is very large, $E_{\text{eff}} = 65\,\text{GV.cm}^{-1}$ for an applied field E = 0.26 kV.cm^{-1} at which the molecule is fully polarized. It is therefore a competitive molecule for further improvements of the sensitivity to eEDM detection. The experimental tools that we develop in the RbSr experiment, in particular magnetoassociation and optical association in an optical lattice will hopefully prove useful in view of the assembly of such molecules, and provide a framework for the exploration of other exotic molecules of similar fundamental interest.

1.3.4 Quantum chemistry: chemistry in the zero-energy, single partial wave regime

The production of molecules in the ultracold regime opens the door to the observation of chemistry at the single quantum state level, where the evolution from reactants to products can in principle be detected in a time- and quantum-state resolved manner. This type of

chemistry, where the contribution of single partial waves[15] and internal degrees of freedom can be tracked (as opposed to room temperature chemistry, which averages over numerous partial waves and hyperfine states) is referred to as cold chemistry [40]. This type of research is actively pursued by our collaborators in Nijmegen [41], using Zeeman-decelerated crossed molecular beams. In the KRb experiment at JILA, the reactants, intermediates, and products of the reaction $^{40}K^{87}Rb + {}^{40}K^{87}Rb \rightarrow K_2Rb_2^* \rightarrow K_2 + Rb_2$ in the s-wave and p-wave collisional regimes were directly observed [42]. Similar work can be undertaken with the energetically favorable reaction RbSr + RbSr $\rightarrow Rb_2 + Sr_2$, and more generally one may want to explore collision rates, intermediates and products of the collision of RbSr molecules with Sr or Rb atoms, or Sr_2 or Rb_2 molecules as a function of temperature, rotational momenta, spin polarization, ... The possibilities are infinite and open a vast and beautiful field of research in a truly unique regime.

1.3.5 Suppressing inelastic and reactive collisions: towards evaporative cooling of cold molecules

One of the biggest ongoing challenges in the field of cold molecules is that of evaporative cooling, which is routinely used in ultracold atom experiments to cool down neutral atoms to nK temperatures and reach quantum degeneracy. The idea is to decrease the depth of the potential that confines the atoms (which means diminishing the laser intensity in the case of an optical dipole trap — or increasing the intensity of an anti-trapping laser beam — , or the magnetic field gradient in the case of a magnetic trap), so that the atoms with the largest energy escape from the trap. After a few *elastic* collisions[16], typically three or four, the total energy is redistributed among the atoms and the gas reaches equilibrium at a lower temperature than it started with. That's the "cup of coffee" cooling effect. However with ultracold molecules, the large number of additional degrees of freedom (rotational, vibrational) leads to a typically much larger three-body recombination cross-section than that of atoms: two molecules form a complex and the binding energy of the complex is transferred to a third molecule in the form of kinetic energy. Additionally, some molecules are *reactive*. That is the case of RbSr for which the chemical reaction RbSr + RbSr $\rightarrow Rb_2 + Sr_2$ is energetically favorable, as discussed in Subsection 1.3.4, and leads to two-body losses. Both inelastic and reactive losses, together denoted as *quenching* processes, are detrimental and as rule of thumb a ratio $\beta_{el}/\beta_{qu} > 100$ between elastic and quenching collisions rates has to be obtained to permit evaporation.

[15] The $s, p, d, ...$ partial waves indicate the $N = 0, 1, 2, ...$ rotational degrees of freedom of the pair of colliding particles. See Chapter 2 for a complete introduction to these concepts, in the context of RbSr.

[16] See Section 1.1 for a definition of two- and three-body losses.

Molecules typically display very unfavorable ratios between elastic and quenching collisions, but it has been predicted that it is possible to suppress quenching collisions in polar species by polarizing the molecules with DC electric fields and by preparing the molecular sample not in the rovibrational ground state, of rotational contribution $|N, m_N\rangle = |0, 0\rangle$, but in a rotationally excited state such as the first excited state $|1, 0\rangle$ (The projection m_N is taken along the quantization axis defined by the direction of the DC electric field) [20]. Two molecules separated by a large distance R exert onto each other forces that are second-order in the dipole-dipole interaction[17], resulting in a van der Waals interaction of the form $-C_6/R^6$. The C_6 coefficient characterizing these forces[18] is always attractive for the rovibrational ground state $|\widetilde{0}, \widetilde{0}\rangle + |\widetilde{0}, \widetilde{0}\rangle$ of the molecule pair[19], but it can be negative for the rotationally excited $|\widetilde{1}, \widetilde{0}\rangle + |\widetilde{1}, \widetilde{0}\rangle$ pair state. This condition is achieved when the Stark-shifted energy of the $|\widetilde{1}, \widetilde{0}\rangle + |\widetilde{1}, \widetilde{0}\rangle$ pair state is set just above the energy of the closest pair of opposite parity $|\widetilde{0}, \widetilde{2}\rangle + |\widetilde{0}, \widetilde{0}\rangle$. The molecules then exhibit *repulsive van der Waals interactions*, preventing them from reaching chemical range (i.e. short intermolecular distances R) where they might react or bind together. This situation is pictured in Figure 1.3, and the rate coefficients of the detrimental inelastic and reactive losses are shown on Figure 1.4 as a function of the applied electric field. The field at which the $|\widetilde{1}, \widetilde{0}\rangle + |\widetilde{1}, \widetilde{0}\rangle$ pair state crosses the $|\widetilde{0}, \widetilde{2}\rangle + |\widetilde{0}, \widetilde{0}\rangle$ state, and at which these quenching collisions get suppressed in RbSr + RbSr collisions, is **E = 2.27 kV.cm^{-1}**. This field is easily achievable with standard electrodes, and it should therefore be possible to shield ultracold RbSr molecules against quenching collisions and to observe thermalization and evaporation dynamics. This will hopefully lead to an elastically colliding gas of strongly polar RbSr molecules, deep in the quantum regime[20]. At the time of this writing, such two-body elastic dynamics have been observed in KRb, with a setup involving an optical lattice to suppress further collisional losses [43]. Furthermore, large modulation of the chemical reaction rate could be observed in the same system, using electric fields [44]. These new results pave a very hopeful road for RbSr and for the future of ultracold gases of polar molecules.

[17] In the sense of second-order perturbation theory. The dipole-dipole interaction is given in Equation 1.4.

[18] Not to be confused with the C_6 van der Waals coefficient of the atom pair constituting the molecules.

[19] We remind the reader that the notation $|\widetilde{N}, \widetilde{m}_N\rangle$ indicates the non-polarized state $|N, m_N\rangle$ admixed with states of different parities $(-1)^N$ in presence of the polarizing DC electric field.

[20] As opposed to a lattice gas where collisions are suppressed because molecules don't tunnel between lattice sites — the production of such a gas is our primary goal.

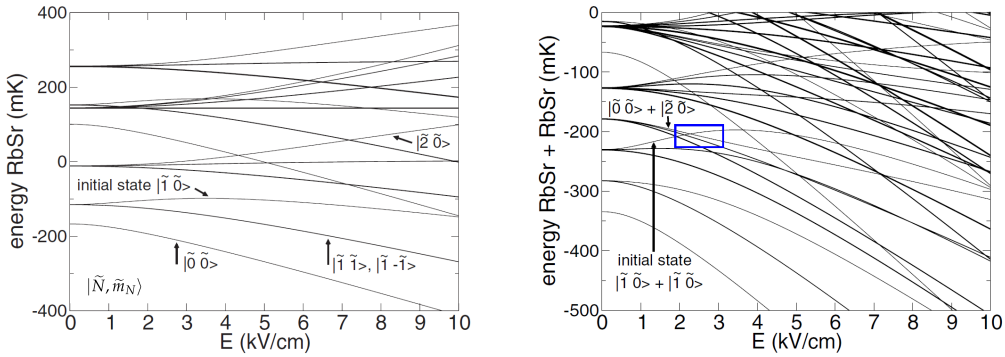

FIGURE 1.3: **Left panel:** Energy spectrum of a single RbSr molecule in a DC electric field. The dressed states are noted $|\widetilde{N}, \widetilde{m}_N\rangle$. **Right panel:** Energy of the combined RbSr + RbSr molecular states.The initial colliding state is indicated with an arrow as well as the "crossing" state, at the crossing field E = 2.27 kV.cm^{-1} indicated inside the blue box. Above the crossing point, quenching rates get suppressed and may allow evaporation. From Ref. [20].

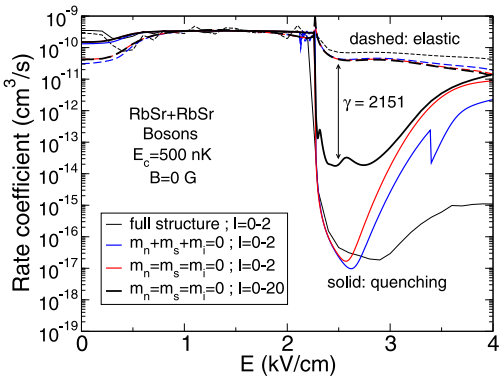

FIGURE 1.4: Elastic (red), inelastic (green), reactive (black), and quenching (blue) rate coefficients as a function of the electric field for a fixed collision energy of $E_c = 500\,\mathrm{nK}$, for bosonic ^{87}Rb^{84}Sr + ^{87}Rb^{84}Sr collisions initially in the state indicated in Figure. 1.3. From Ref. [20].

1.4 Methods for the assembly of diatomic molecules at high PSD

The goal of our experiment is to produce RbSr molecules, at high PSD, in the rotational, vibrational and electronic ground state of RbSr where the dipole moment of the molecule is the largest — see Subsection 1.2.1. Starting from a pair of atoms at almost zero relative motional energy, we need to create a molecular bond associated with a binding energy close to $D_e = 1152^{+9}_{-16}$ cm^{-1}= $h \times 34.6$ THz, or about 14 kJ.mol^{-1}, with D_e the depth of the ground-state PEC of RbSr. This process is depicted in Figure 1.5 and in the following subsections we discuss the different experimental options one can use to assemble such molecules.

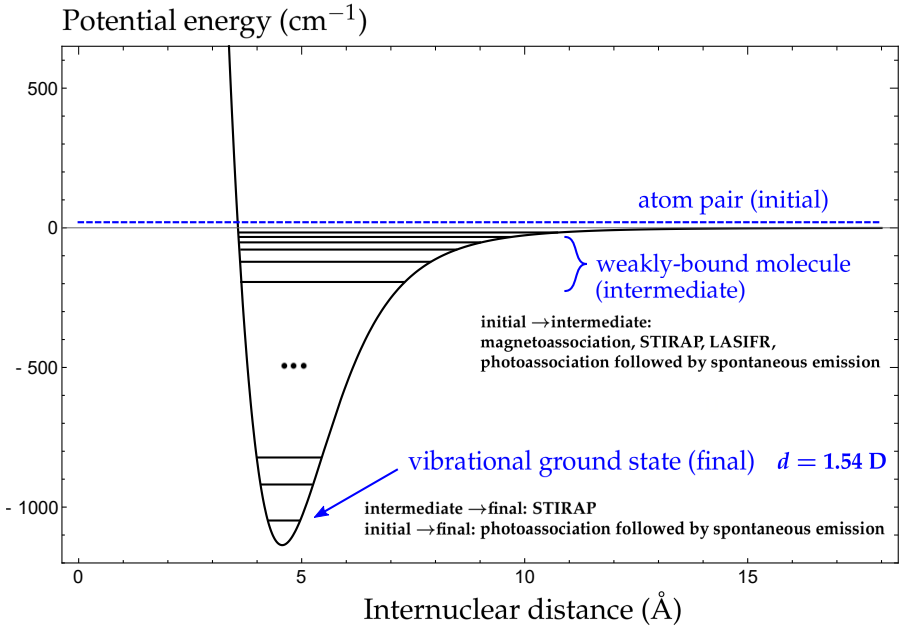

FIGURE 1.5: Methods for the formation of RbSr molecules in the electronic and (ro)vibrational ground state. The depicted PEC (see Chapter 2 for an introduction to this concept) is the $^2\Sigma^+$ ground-state PEC, and the horizontal black lines indicate the energy of each vibrational state. The rotational structure is not depicted, and the vibrational progression is not to scale for ease of reading. Note that one method permits to create molecules in only one step, but it produces a vibrationally-hot sample of molecules — see Subsection 1.4.3.

1.4.1 Magnetoassociation: the current standard in bi-alkali experiments

Magnetoassociation is the process through which one exploits a magnetic Feshbach resonance between two atoms to adiabatically transfer the atom pair into a molecular bound state. The typical binding energies that one can achieve with such a method range from $h\times$ kHz to a few tens of $h\times$ GHz. These binding energies are limited by the static magnetic fields achievable in the laboratory (in principle a few Tesla (T) using superconducting coils, but only up to a few 0.1 T using room temperature copper coils as common in ultracold atom experiments) and by the rather small natural magnetic moment of atom pairs, with typical values on the order of 1 MHz/G and reaching about 10 MHz/G for the most magnetic atoms ($1\ G\ =\ 10^{-4}$ T. The Gauss (G) is the non-SI unit of choice for magnetic field magnitudes in cold atom experiments). In this approach it is therefore necessary to implement a second-step in the assembly process, to transfer the weakly-bound molecular state (sometimes referred to as Feshbach state in the literature) to the vibrational ground state of much larger binding energy. This second step is performed using STIRAP (see next subsection).

Magnetoassociation is the consecrated method for the assembly of bi-alkali molecules (Li_2, Cs_2, KRb, RbCs, NaRb, NaK, ...) owing to the availability of large Feshbach resonances in such systems. In alkali+closed-shell atom systems such as RbSr, CsYb, LiYb, ... Feshbach resonances exist, but are very narrow and it is much more challenging to use them for magnetoassociation. An important asset of this method is that it doesn't require the coupling of the system to electronically excited states, which prevents any decoherence issue associated with the finite lifetime of such states. Magnetoassociation and Feshbach resonances are discussed extensively in Chapter 5 in the context of bi-alkali and RbSr, and we refer the reader to it for further details. That is the method we are currently investigating for the formation of $^{87}Rb^{84}Sr$.

1.4.2 STIRAP: a coherent association scheme based on two laser fields

STIRAP stands for stimulated Raman adiabatic passage and consists in producing a coherent superposition between the initial state (molecule or atom pair) and the target state (molecule) using two laser fields in a similar way as for a two-photon spectroscopy experiment — see Figure 2.3. The first laser couples the initial state $|\mathrm{i}\rangle$ to an electronically excited molecular state $|\mathrm{e}\rangle$, and the second laser couples this excited state to the target state $|\mathrm{f}\rangle$. The coherent superposition state is of the form $|\mathrm{dark}\rangle\ =\ \cos\theta\,|\mathrm{i}\rangle - \sin\theta\,|\mathrm{f}\rangle$ and is called "dark" because $|\mathrm{e}\rangle$, which has a finite lifetime, doesn't contribute to the superposition. The mixing angle θ depends on the relative intensities between laser 1 and laser 2 and can be dynamically adjusted to transfer adiabatically all the probability density from $|\mathrm{i}\rangle$ to $|\mathrm{f}\rangle$. In a STIRAP scheme the difference in energy between $|\mathrm{i}\rangle$ and $|\mathrm{f}\rangle$ is given by the difference in frequency

$h \times (\nu_{\text{laser}\,2} - \nu_{\text{laser}\,1})$ between the two lasers and can be arbitrarily large[21], provided that a sufficiently stable phase relationship between the two lasers can be assured, in order to preserve the coherence of the dark state over the course of the STIRAP transfer. We refer the reader to Ref. [45] for a complete introduction to STIRAP, and to Ref. [46] for a recent review of its experimental applications.

STIRAP is the method of choice for transferring weakly-bound molecules (produced using magnetoassociation, see Subsection 1.4.1) to the rovibrational ground state in bi-alkali experiments. Additionally, it was shown in our group that STIRAP can be used to efficiently associate atom pairs of Sr, held on the sites of an optical lattice, into Sr_2 molecules [47, 48]. In this case $|\text{i}\rangle$ is the ground state of relative and center-of-mass motion of an atom pair in a lattice well (see Chapter 5 for a discussion of optical lattices) and $|\text{f}\rangle$ is the $\nu = -2$ vibrational state of binding energy $E_b = h \times 644.7372(2)\,\text{MHz}$[22]. This method could also be used to produce weakly-bound RbSr molecules. However, the adiabaticity criterion for fast and near-unit efficient STIRAP requires $\alpha \gg \pi^2$ [48], where $\alpha = \tilde{\gamma} \times T_{\text{pulse}} = (\Omega_{\text{FB}}^2/\gamma_e) \times T_{\text{pulse}}$ with γ_e the natural linewidth of $|\text{e}\rangle$, Ω_{FB} the Rabi frequency characterizing the coupling of $|\text{i}\rangle$ and $|\text{e}\rangle$ induced by the "free-bound" laser 1 (in general $\tilde{\gamma} = \Omega_m^2/\gamma_e$ and $\Omega_m = \min(\Omega_{\text{FB}}, \Omega_{\text{BB}})$ is the maximally achievable Rabi Frequency of the limiting arm of the STIRAP — the "bound-bound" Ω_{BB} Rabi frequency is much larger than Ω_{FB} at similar laser intensities in the STIRAP schemes we envisioned) and T_{pulse} the STIRAP laser's pulse time, which sets the timescale of the molecule formation sequence. In Sr_2 the molecular excited state was chosen to be weakly bound by $E_b = h \times 228.38(1)\,\text{MHz}$ with respect to the excited $^1S_0 + {}^3P_1$ dissociation asymptote of Sr_2 (which corresponds to an optical excitation at $\lambda = 689\,\text{nm}$ from the $^1S_0 + {}^1S_0$ ground state asymptote). The $^3P_1$ excited state of Sr has a natural linewidth $\gamma = 2\pi \times 7.5\,\text{kHz}$ and the molecular state itself exhibits a natural linewidth of $\gamma_e = 2\pi \times 44(13)\,\text{kHz}$, which is of the same order of magnitude. Thanks to this very narrow linewidth it is possible to form Sr_2 molecules in less than 400 μs. However the situation is much less favorable in Rb-Sr. We had the unpleasant surprise to observe that RbSr molecular states bound close to the Rb $(^2S_{1/2}) + \text{Sr}\ (^3P_1)$ dissociation asymptote (which corresponds to one ground-state Rb atom and one Sr atom optically excited at $\lambda = 689\,\text{nm}$) exhibit linewidths typically two

[21] Note that when STIRAP couples an ultracold atom pair close to the zero-collisional energy threshold (initial state) to a molecular state supported by a PEC associated with the same threshold (final state), the difference in energy between the two states is almost exactly the binding energy of the molecular state — up to the collisional energy of the pair, as is clear from Figure 2.3.

[22] Note that in that case the initial state is a discrete unit-normalized state, analogous to a molecular state — see Chapter 5 for a full discussion on discrete trap states. It is detrimental to STIRAP to work instead with a thermal distribution of atom pair states, because the addition of Rabi frequencies of each state of the distribution leads to decoherence of the dark state. Accordingly, it is also possible to produce molecules from a BEC of atoms using STIRAP [49], since a BEC is a coherent ensemble of atoms occupying the same quantum state of motion.

or three orders of magnitude larger[23]: $\gamma_e/2\pi \sim$ MHz as shown in Chapter 2, Tables B.1 and B.2. We didn't measure the Rabi frequencies of the corresponding photoassociation lines, but compared their rescaled stimulated transition rates $\Gamma/\gamma_e \propto {\Omega_{FB}}^2/\gamma_e$ with those of Sr_2. We found that they are comparable or much weaker in the case of ^{87}Rb-^{84}Sr [51]. Therefore we concluded that STIRAP molecule association should prove much more challenging in RbSr than in Sr_2. Indeed, while it is possible to increase α by increasing T_{pulse} arbitrarily, one then faces decoherence effects linked for instance to laser phase noise or lattice intensity noise that are irrelevant on μs timescales but could destroy the dark state coherence on ms timescales. The ^{87}Rb-^{87}Sr combination exhibits values of Γ/γ_e comparable to Sr_2, however the ^{87}Rb-^{87}Sr s-wave scattering length is very large (see Table 1.1), which might make it extremely hard or even impossible to populate an optical lattice with a large number of ^{87}Rb and ^{87}Sr atom pairs. The ^{87}Rb-^{84}Sr combination is much more promising because in that case we can produce quantum degenerate gases and load them in an optical lattice. However Γ/γ_e is then orders of magnitude smaller than in Sr_2.

STIRAP was our plan A for the formation of weakly-bound RbSr molecules. Two generations of PhD students have attempted to form ^{87}Rb^{84}Sr molecules in an optical lattice using this method [51, 52], which proved unsuccessful. This failure could be explained by either of the following three hypothesis:

1. Decoherence of the dark state, induced by a large γ_e and thus a too small $\alpha = \tilde{\gamma} \times T_{pulse}$ compared to uncontrolled sources of decoherence.

2. Double Mott insulator improperly prepared: most lattice sites are not filled with Rb-Sr atom pairs.

3. Lattice light ($\lambda = 1064$ nm) optically exciting RbSr molecules to electronically excited RbSr* states.

Confronted with the failure of the previous STIRAP attempts and the unfavorably small α values that we estimated for ^{87}Rb-^{84}Sr, we chose to abandon STIRAP using an excited state close to the $^1S_0 + {}^3P_1$ asymptote for the time being. The hypothesis 1 and 3 have been favored in the past to explain the failure of STIRAP in the RbSr team, and none of them has been ruled out completely at the time of this writing. In particular, hypothesis 3 would also impair our current magnetoassociation attempts if it proved true. It is the opinion of the author of this thesis that hypothesis 2 is a likely hypothesis, and we have been working

[23] We didn't expect such broad linewidths, owing to the narrow linewidth of the Sr $^1S_0$ – $^3P_1$ atomic transition. These large widths might be caused by the mixing of the excited potentials correlating to $^3P_1$ with the ones correlating to the Rb asymptotes — the D_1 and D_2 lines of Rb have respectively $\gamma_e/2\pi = 5.746(8)$ MHz and $\gamma_e/2\pi = 6.065(9)$ MHz [50] —, or to predissociation of the atom pair into the $^3P_0$ continuum of scattering states above the Rb ($^2S_{1/2}$) + Sr ($^3P_0$) aymptote.

in the last two years on the improvement and characterization of the double Mott insulator production, but definitive evidence for the absolute quality of the sample is still lacking — producing molecules would of course provide such evidence. STIRAP should be attempted again using the same molecular scheme as before, if it is proven experimentally that either hypothesis 2 or 3 is correct and might have impaired molecule production in the past.

Meanwhile it has been proposed that STIRAP could prove successful using an intermediate electronically excited state correlating to the Rb $(^2P_{1/2})$ + Sr $(^1S_0)$ and/or Rb $(^2P_{3/2})$ + Sr $(^1S_0)$ dissociation asymptotes instead of the Rb $(^2S_{1/2})$ + Sr $(^3P_1)$ asymptote [53]. They correspond to an optical excitation at $\lambda = 780\,\text{nm}$ and $\lambda = 795\,\text{nm}$ from the Rb $(^2S_{1/2})$ + Sr $(^1S_0)$ ground state asymptote respectively (D_2 and D_1 lines of atomic Rb), and we recently built a laser system for RbSr photoassociation spectroscopy close to the D_1 asymptote. It might be wise in the future to attempt STIRAP using some of the detected excited molecular states, especially if magnetoassociation proves unsuccessful.

1.4.3 Photoassociation followed by spontaneous emission: an incoherent association scheme

Another method for the association of molecules in the electronic ground state is the photoassociation of electronically excited RbSr* molecules (as done with a photoassociation laser beam as in a photoassociation spectroscopy experiment — see Section 4.2), followed by a spontaneous emission event. Upon emission of the photon, the excited molecule relaxes to one or several RbSr vibrational level(s) in the electronic ground state. While in general such processes populate several vibrational states with weighted relaxation probabilities, it is possible to choose the excited molecular state wisely so that it relaxes with almost unit probability to a given vibrational level. This method is used to produce Sr_2 molecules in the experiments led by Tanya Zelevinsky at Columbia University [54], and was theoretically investigated by Devolder et al. in a 2018 publication [53]. Rather than a thousand words, we quote the conclusions of Devolder et al.:

"We have modeled the photoassociation of (^{87}Rb,^{84}Sr) atom pairs close to two atomic transitions: the allowed 5s $^2S_{1/2} \rightarrow$ 5p $^2P_{1/2,\,3/2}$ Rb transition, and the 5s^2 $^1S_0 \rightarrow$ 5s5p $^3P_{0,1,2}$ intercombination transition in strontium. As expected the photoassociation spectra show opposite behaviours. In the former case, the photoassociation rates are very high close to the asymptote. In the latter case, the photoassociation rates are very low close to the asymptotes. The distributions of ground-state vibrational levels after spontaneous emission are also different. Mainly one vibrational level is populated in the former case, but this level is highly excited. In the latter case, the lowest rovibrational level of the ground state could

be populated, but many other vibrational levels as well. Therefore a further step of internal cooling is necessary to achieve a significant creation of ultracold RbSr molecules in their lowest rovibrational level."

Our newly-built laser system for photoassociation spectroscopy close to the $(^2P_{1/2}) + \mathrm{Sr}\,(^1S_0)$ dissociation asymptote ($\lambda = 795\,\mathrm{nm}$) might therefore allow us to produce vibrationally-cold weakly-bound RbSr molecules using this method. One will need to care about the final rotational and hyperfine distributions though: the excited molecules will probably relax to several m_F states unless a wise choice of polarization (both for the laser light and the initial atomic sample m_F distribution) is made.

1.4.4 A newly-proposed method: association using a Laser-Assisted Self-Induced Feshbach Resonance (LASIFR)

A new method for the formation of polar molecules has been proposed recently by Devolder et al. [21]. It is a Feshbach resonance scheme, that couples an atom pair state and a target molecular state within the same electronic manifold — in our case the $^2\Sigma^+$ electronic ground state of RbSr. This method is conceptually fully analogous to magnetoassociation using magnetic Feshbach resonances, except that the resonance condition between the two states is achieved via the dressing with a resonant photon instead of an externally applied DC magnetic field. While magnetic Feshbach resonances in RbSr arise from the dependence of the hyperfine coupling constants $\Delta\zeta_{\mathrm{Rb}}(R)$ and $\Delta\zeta_{\mathrm{Sr}}(R)$ on the internuclear distance R between Rb and Sr — see Chapter 5 —, LASIFR resonances arise from the R-dependence of the permanent dipole moment $\mathrm{d}(R)$ of the polar molecule[24], which results in an R-dependent interaction of the molecular dipole moment with the AC electric field $H_{\mathrm{AC}}(R) = -\vec{\mathrm{d}}(R)\cdot\vec{\mathrm{E}}_{\mathrm{AC}}(t)$ that couples free atom pair states with essentially no dipole moment to vibrational molecular states with a dipole moment in the molecular frame. In the context of RbSr the dressing photon of the AC field is actually a THz photon, and the largest Feshbach energy width in $^{87}\mathrm{Rb}^{84}\mathrm{Sr}$ is obtained for a vibrational state of binding energy $E_b \simeq hc \times 6.2\ \mathrm{cm}^{-1}$, i.e. at a frequency of 0.2 THz. Easily available commercial sources at such frequencies suffer from a technological gap that limits their output power to about 10 – 100 mW, and the smallest diffraction spot one can obtain from a 0.2 THz source is of order $\lambda \sim$ mm. The corresponding intensities are thus of order 1-10 $\mathrm{W.cm}^{-2}$, which according to Devolder et al. corresponds to resonance widths of about $\Gamma_{12} \simeq h \times 2\pi \times 10^{-3} - 10^{-4}\,\mathrm{kHz}$[25]. These widths are

[24] Note that the dipole moment d discussed in Subsection 1.2.1 is the vibrationally-average dipole moment $\mathrm{d} = \langle\chi^{\mathrm{vib}}_{v,N=0}|\mathrm{d}(R)|\chi^{\mathrm{vib}}_{v,N=0}\rangle$ in the rovibrational ground state of radial wavefunction $\chi^{\mathrm{vib}}_{v,N=0}(R)$.

[25] See Chapter 5, Equation 5.7 for a definition of the Breit-Wigner energy width Γ_{12} of a Feshbach resonance.

extremely small and probably not useful for Feshbach association. For comparison the magnetic Feshbach resonance we are currently trying to exploit in ^{87}Rb^{84}Sr displays a width of $h \times 0.58\,\mathrm{kHz}$ and is already very challenging[26]. However, the rapid evolution of multi-Watt quantum cascade lasers at THz frequencies might provide tunable, spectrally pure and high-output power sources in the near future. Furthermore the optimal frequency for Feshbach association depends on the molecule considered, and some molecules might display interesting transitions at more achievable frequencies. Maybe the future of polar molecules will be THz?

[26] Note that the Breit-Wigner energy width of a magnetic Feshbach resonance cannot be tuned with the magnetic field. The width of an optical Feshbach resonance or a LASIFR resonance, on the other hand, depends linearly on the electric field intensity.

Chapter 2

The ground-state potential energy curve of RbSr: theory and experiments

In this chapter I will introduce the reader to the concept of potential energy curves (PECs) of two neutral atoms colliding at ultracold temperatures, and describe the experimental methods that our group developed and used to probe the ground-state PEC of RbSr. Excellent introductions to the physics of ultracold atom pairs and molecules can be found in the PhD thesis produced in the group of Olivier Dulieu at Laboratoire Aimé Cotton [55, 56], as well as in reference molecular spectroscopy textbooks [57–59].

The result of our work, combined with the work of our colleagues in Warszawa, led to the publication presented in Chapter 3.

2.1 Two neutral atoms colliding at ultracold temperatures: theoretical description

2.1.1 The molecular Hamiltonian for a diatomic system

The molecular Hamiltonian describing a system of two neutral atoms interacting with one another in field-free space is

$$\hat{H} = -\frac{\hbar^2}{2m}\sum_{i=1}^{N}\vec{\nabla}_i^2 - \frac{\hbar^2}{2}\sum_{\alpha=A}^{B}\frac{1}{M_\alpha}\vec{\nabla}_\alpha^2 + V\left(\{\vec{\rho}_i\},\vec{R}_A,\vec{R}_B\right) , \tag{2.1}$$

where N is the total number of electrons, M_A, M_B and eZ_A, eZ_B are respectively the mass and the total charge of the two nuclei, and m is the mass of the electron [55, 56]. The inertial

frame of reference is the laboratory frame, in which $\vec{R}_A$, $\vec{R}_B$ are the position of each one of the nuclei with respect to the origin, and $\{\vec{\rho}_i\}$ represents the position of each electron i. The internuclear distance is R and the corresponding vector $\vec{R} = \vec{R}_A - \vec{R}_B$ indicates the orientation of the molecular axis in the laboratory frame. The nabla operators $\vec{\nabla}$ and the corresponding Laplace operators $\vec{\nabla} \cdot \vec{\nabla} = \vec{\nabla}^2$ act on the three spatial degrees of freedom of the particle indicated in subscript, i.e. $\vec{\nabla}_i$ and $\vec{\nabla}_\alpha$ for electrons and nuclei respectively[1].

The term $V\left(\{\vec{\rho}_i\}, \vec{R}_A, \vec{R}_B\right)$ encompasses all interaction terms between the particles. Limiting ourselves to the Coulomb interactions it reads

$$V\left(\{\vec{\rho}_i\}, \vec{R}_A, \vec{R}_B\right) = \frac{e^2}{4\pi\epsilon_0}\left(\frac{Z_A Z_B}{R} - \sum_{i=1}^{N}\frac{Z_A}{\rho_{A,i}} - \sum_{i=1}^{N}\frac{Z_B}{\rho_{B,i}} + \sum_{i>j}\sum_{j=1}^{N}\frac{1}{\rho_{i,j}}\right), \tag{2.2}$$

where $R = \left\|\vec{R}_A - \vec{R}_B\right\|$ is the internuclear distance, $\rho_{A,i}$ and $\rho_{B,i}$ the distance of the electron i to the nucleus A and B respectively, and $\rho_{i,j}$ the distance between the electrons i and j[2].

2.1.2 The center of mass motion

The motion of the center of mass of the molecule or atom pair can be separated from its relative motion, by choosing the origin (O) of the frame of reference to be at the center of mass of the two nuclei[3]. The position of each electron then reads $\vec{\rho}_i = \vec{\rho}_i^{\,(O_{\text{lab}})} - \vec{R}_C$, where $\vec{\rho}_i^{\,(O_{\text{lab}})}$ are the electronic positions referred to an arbitrary origin (O_{lab}) fixed in the laboratory frame and $\vec{R}_C = \frac{M_A}{M_A+M_B}\vec{R}_A + \frac{M_B}{M_A+M_B}\vec{R}_B$ is the position of the center of mass of the nuclei. The

[1] Setting $\vec{\rho}_i = \vec{e}_X X_i + \vec{e}_Y Y_i + \vec{e}_z Z_i$, where $\vec{e}_X$, $\vec{e}_Y$ and $\vec{e}_Z$ are the position unit vectors in the laboratory frame, the electronic nabla operator denoting momentum is $\vec{\nabla}_i = \vec{e}_X\frac{\partial}{\partial X_i} + \vec{e}_Y\frac{\partial}{\partial Y_i} + \vec{e}_Z\frac{\partial}{\partial Z_i}$ and the Laplace operator denoting kinetic energy is $\vec{\nabla}^2 = \frac{\partial^2}{\partial X_i^2} + \frac{\partial^2}{\partial Y_i^2} + \frac{\partial^2}{\partial Z_i^2}$. Similar expressions are readily obtained for the nuclear operators, the cross terms $\vec{\nabla}_i \cdot \vec{\nabla}_j$ and the operators acting on the nuclear center of mass $\vec{R_C}$ and on the internuclear distance $\vec{R}$ — see Equations 2.5, 2.7 and 2.6 where these terms appear. These Cartesian-coordinate expressions are presented here for clarity, but spherical coordinates are typically more useful, as should be clear from the rest of this chapter.

[2] We dismiss here any interaction term involving electronic and nuclear spins. The RbSr molecule is an open-shell molecule with electronic spin $s = 1/2$ in its electronic ground state, and both Sr and Rb have a nuclear spin i_{Rb} and i_{Sr} (with the exception of bosonic Sr for which $i_{\text{Sr}} = 0$). The spin-dependent terms include the hyperfine structure $|f, m_f\rangle$ (written alternatively $|F, m_F\rangle$, with s and i written alternatively S and I), induced by the coupling of the electronic and nuclear spins; it is discussed extensively in Chapter 5, along with its relation to the motional degrees of freedom of Equation 2.1 in the context of RbSr Feshbach resonances in the electronic ground state. These terms also include the motional couplings to the electronic spin s, which are very important for electronically excited states of RbSr where spin-orbit coupling is strong, but lead to extremely small corrections in the RbSr electronic ground state; we discuss both cases in Section 4.1.

[3] The origin of the frame of reference can be chosen alternatively to be the center of mass of the molecule, the center of mass of the two nuclei or the position of one nucleus [57]. These choices lead to sets of equations different from Equations 2.3, 2.4, 2.5, 2.7 and 2.6. In particular, they imply different expressions for the cross kinetic terms that lead to non-adiabatic corrections of the molecular spectrum (here, the mass polarization term). The convention adopted in Ref. [55] is to set the origin at the geometrical center of the two nuclei. We follow here the convention used in Refs. [57] and [56], where it is set at the center of mass of the two nuclei. These two choices are almost equivalent in RbSr, because Rb and Sr have approximately the same mass.

total mass of the diatomic system is $M = M_A + M_B + N \times m$ and the reduced nuclear mass is $\mu = \frac{M_A M_B}{M_A + M_B}$. In this coordinate system, the molecular Hamiltonian given in Equation 2.1 can be written

$$\hat{H} = \hat{T}_e + \hat{T}_{\text{mass pol.}} + \hat{T}_C + \hat{T}_N + V(\{\vec{\rho}_i\}, \vec{R}) \tag{2.3}$$

$$\hat{T}_e = -\frac{\hbar^2}{2m} \sum_{i=1}^{N} \vec{\nabla}_i^2 \tag{2.4}$$

$$\hat{T}_{\text{mass pol.}} = -\frac{\hbar^2}{2(M_A + M_B)} \sum_{i,j=1}^{N} \vec{\nabla}_i \cdot \vec{\nabla}_j \tag{2.5}$$

$$\hat{T}_N = -\frac{\hbar^2}{2\mu} \vec{\nabla}_R^2 \tag{2.6}$$

$$\hat{T}_C = -\frac{\hbar^2}{2M} \vec{\nabla}_C^2 \,. \tag{2.7}$$

The terms $\hat{T}_e$, $\hat{T}_N$ and $\hat{T}_C$ are the kinetic energy operators associated respectively with the motion of the electrons, the motion of the two nuclei with respect to one another, and the center of mass motion. The term $\hat{T}_{\text{mass pol.}}$ is a correction term, referred to as the mass polarization term, that expresses kinetic correlations between the motion of the electrons and of the nuclei. The motion of the center of mass of the two nuclei is obtained through diagonalization of $\hat{T}_C$, which is a single-particle problem. In free-space, the corresponding eigenfunctions are plane waves denoted by the quantum number K, which labels the corresponding momentum $\vec{P} = \hbar\vec{K}$ of the molecule or atom pair. In an optical lattice, the correct quantum numbers are instead the band index n_{band} and the quasi-momentum q.

The center of mass motion is extremely well controlled in ultracold atom experiments. The laser cooling and evaporation techniques that we use allow us to bring a gas of hot Rb and Sr atoms at around $T_{\text{Rb}} = 200$ °C and $T_{\text{Sr}} = 530$ °C to the quantum regime of μK temperatures or colder. Once this regime is reached, the Rb and Sr atoms are extremely slow and can be trapped onto the sites of an optical lattice — see Chapter 5, Subsection 5.1.2 —, in which the center-of-mass motion of Rb-Sr pairs is essentially frozen. In the rest of this chapter, we will dismiss the center of mass motion and focus on the internal degrees of freedom of the diatomic system.

2.1.3 The molecular frame

The molecule or atom pair can rotate in the reference frame of the laboratory. To track this rotational motion, it is natural to introduce spherical coordinates (R, θ, ϕ), where the zenith

is the Z axis of the XYZ space-fixed coordinate system of the laboratory[4]. Furthermore, the motion of the electrons is advantageously described in the frame of the molecule itself, referring the positions of the electrons to those of the nuclei: the spatial distribution of the electrons in such a frame is independent of (θ, ϕ), because the Coulomb interaction between the electrons and the nuclei is independent of the orientation of the molecular axis in space.

The molecule-fixed frame xyz, which is non-inertial due to the rotation of the nuclei, is constructed by rotating the laboratory-fixed frame XYZ using the rotations associated with the three Euler angles $(\alpha, \beta, \gamma) = (\phi, \theta, \chi)$, as shown in Figure 2.1. For a diatomic molecule, the third Euler angle χ is an arbitrary constant[5]. The z axis of the molecular frame is taken to be the internuclear axis for the diatomic molecule, and the origin is kept at the position of the center of mass of the two nuclei.

The electronic motion in the molecular frame

In the molecular frame, z is aligned with the internuclear axis and the vectorial position of each electron i is denoted as $\{\vec{r}_i\} = \{x_i, y_i, z_i\}$. The total orbital angular momentum of the electrons in the molecule-fixed system of coordinates xyz takes the same form as it does in the space-fixed system of coordinates XYZ[6]. It reads $\vec{L} = -i\hbar \sum \vec{r}_i \times \vec{\nabla}_i$, summing over all electrons i and its components are

$$\begin{aligned} L_x &= -i\hbar \sum_{i=1}^{N} \left(y_i \frac{\partial}{\partial z_i} - z_i \frac{\partial}{\partial y_i} \right) \\ L_y &= -i\hbar \sum_{i=1}^{N} \left(z_i \frac{\partial}{\partial x_i} - x_i \frac{\partial}{\partial z_i} \right) \\ L_z &= -i\hbar \sum_{i=1}^{N} \left(x_i \frac{\partial}{\partial y_i} - y_i \frac{\partial}{\partial x_i} \right) . \end{aligned} \tag{2.8}$$

[4] In absence of external fields breaking the isotropy of space, the choice of Z is arbitrary. In the context of ultracold atom experiments, typically externally applied electric or magnetic fields will define preferential directions in the laboratory frame. For instance, the direction of polarization of a laser field in a photoassociation experiment.

[5] For molecules involving more than two atoms, one has to use all three (ϕ, θ, χ) Euler angles to transform the laboratory-fixed coordinate system into the molecule-fixed system. Since there is no nucleus lying off-axis in a diatomic molecule, χ is in this case undefinable and the corresponding Euler rotation is therefore redundant. The spherical angles (θ, ϕ) are therefore sufficient to define the orientation of the axis. We do not dismiss χ, in order for the reader to be able to relate easily the derived equations to the ones in the reference books [57, 59], and because the corresponding formalism is simpler and more general than the one obtained using only spherical angular coordinates (θ, ϕ).

[6] We remind the reader that the origin (O) of the XYZ system of coordinates is set at the position of the center of mass of the two nuclei. Therefore, it is not strictly speaking space-fixed. However, it does not rotate along with the molecular axis. This is the meaning we attach to the term space-fixed in this chapter.

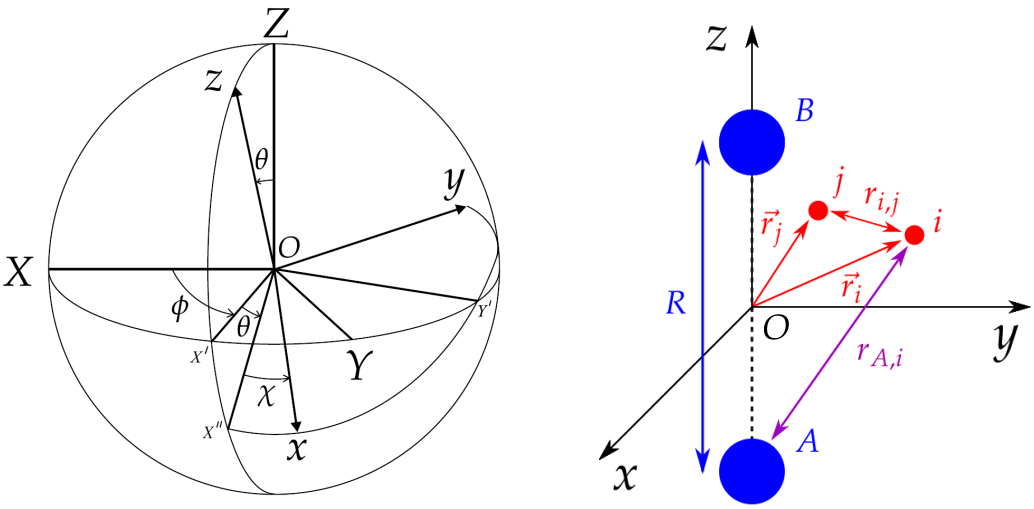

FIGURE 2.1: **Left picture:** passage from the laboratory-fixed frame XYZ to the non-inertial frame xyz of the rotating molecule. The molecular frame xyz is obtained through three successive Euler rotations: 1) Rotation about the initial Z axis through an angle ϕ $(0 \leq \phi \leq 2\pi)$. 2) Subsequent rotation about the resultant Y' axis through an angle θ $(0 \leq \theta \leq \pi)$. 3) Rotation about the resultant Z'' axis through an angle χ $(0 \leq \chi \leq 2\pi)$. Adapted from Ref. [57]. **Right picture:** Molecular frame and molecule-fixed system of coordinates. The internuclear axis connecting the nuclei A and B defines the z axis of the xyz molecular frame, of which the rotation in the laboratory frame XYZ is parametrized by the Euler angles (ϕ, θ, χ).

Accordingly, the gradient operator $\vec{\nabla}_i$ and the electronic kinetic energy operator $\hat{T}_e$ also take the same form in xyz as they do in XYZ. Fortunately, we experimentalists need not worry about the treatment of these $3N$ electronic degrees of freedom. They reduce to simple vectorial and algebraic relations, among which the projection L_z along the internuclear axis and its eigenvalues Λ play a crucial role for the diatomic molecule — see Subsection 2.1.5.

The nuclear motion in the molecular frame

The changes of distance between the nuclei in the molecular frame are referred to as vibrational motion. This motion is parametrized by the internuclear distance R along the molecular axis, which is the same in the space-fixed and molecule-fixed systems of coordinates.

The rotational motion of the nuclei, on the other hand, has a very different expression in these two systems of coordinates. It is advantageously represented by a rotational angular momentum vector operator in the molecular frame[7]. However, the angular momentum (i.e., the rotational motion) of the molecular axis is null in this frame because the frame and the axis rotate together. One way around this is to note that in the frame xyz of the molecule, the space-fixed frame XYZ appears to rotate due to the rotation of the nuclei. The corresponding angular momentum $\vec{l}$ of a point which is stationary in XYZ, measured in xyz has a well-known expression [59] and is related to the rotational angular momentum operator $\vec{\ell}$ of the molecular axis in xyz through $\vec{\ell} = -\vec{l}$, because the angular velocity of the space-fixed frame measured with respect to the molecular axis is the inverse of the angular velocity of the molecular axis measured with respect to the space-fixed frame[8]. The molecule-fixed components of the rotational angular momentum $\vec{\ell}$ are thus

$$\begin{aligned}
\ell_x &= -l_x = i\hbar \left[\cot\theta \cos\chi \left.\frac{\partial}{\partial\chi}\right)_s + \sin\chi \left.\frac{\partial}{\partial\theta}\right)_s - \operatorname{cosec}\theta \cos\chi \left.\frac{\partial}{\partial\phi}\right)_s \right] \\
\ell_y &= -l_y = i\hbar \left[-\cot\theta \sin\chi \left.\frac{\partial}{\partial\chi}\right)_s + \cos\chi \left.\frac{\partial}{\partial\theta}\right)_s + \operatorname{cosec}\theta \sin\chi \left.\frac{\partial}{\partial\phi}\right)_s \right] \\
\ell_z &= -l_z = i\hbar \left.\frac{\partial}{\partial\chi}\right)_s ,
\end{aligned} \tag{2.9}$$

and the fact that χ is an arbitrary constant imposes the condition

[7] The powerful techniques of angular momentum algebra can be used in such a representation. It makes the search for eigenvectors and eigenvalues easy, and allows one to evaluate the relations between the nuclear rotation and other vectors in the molecular frame, such as the electronic orbital angular momentum $\vec{L}$ or in some situations the total electronic spin $\vec{S}$.

[8] We adopt here the notation of Refs. [56, 59]. The rotational angular momentum $\vec{\ell}$ of the nuclei is instead denoted as $\vec{O}$ in Ref. [55] and as $\vec{N}$ in Ref. [57].

$$\ell_z = 0\,. \tag{2.10}$$

Note that $\vec{\ell}$ rotates the nuclei only, not the electrons, leaving the electronic positions $\{\vec{\rho}_i\}$ in space-fixed coordinates unchanged. This is indicated by the subscript s for space-fixed — we go back to this point in Subsection 2.1.4. The magnitude $\vec{\ell}^2 = (\vec{e}_x\ell_x + \vec{e}_y\ell_y + \vec{e}_z\ell_z)^2$ of $\vec{\ell}$ reads

$$\vec{\ell}^2 = -\hbar^2\left\{\mathrm{cosec}\,\theta\frac{\partial}{\partial\theta}\left(\sin\theta\frac{\partial}{\partial\theta}\right) + \mathrm{cosec}\,\theta^2\left[\frac{\partial^2}{\partial\phi^2} + \frac{\partial^2}{\partial\chi^2} - 2\cos\theta\frac{\partial^2}{\partial\phi\partial\chi}\right]\right\}_s\,. \tag{2.11}$$

The eigenfunctions $|\ell\ m_\ell\ k\rangle$ of $\vec{\ell}^2$ are normalized Wigner D-matrices[9]

$$|\ell\ m_\ell\ k\rangle \equiv (-1)^{m_\ell - k}\sqrt{\ell + 1/2}\,D^{\ell}_{m_\ell,\,k}(\phi,\theta,\chi)\,, \tag{2.12}$$

with the phase convention

$$D^{\ell}_{m_\ell,\,k}(\phi,\theta,\chi) = e^{im_\ell\Phi}D^{\ell}_{m_\ell,\,k}(0,\theta,0)\,e^{ik\chi}\,. \tag{2.13}$$

The three quantum numbers ℓ, m_ℓ and k are respectively the magnitude of the nuclear rotation, the projection of the nuclear rotational angular momentum along the Z axis of the space-fixed frame[10] and its projection along the z axis of the molecule-fixed frame. The corresponding eigenvalue equations are

[9] The normalization factor $\sqrt{\ell + 1/2}$ ensure the normalization condition $\langle\ell\ m_\ell\ k|\ell\ m_\ell\ k\rangle = 1$, integrating over all angular space. Another common phase convention is $D^{\ell}_{m_\ell,\,k}(\phi,\theta,\chi) = e^{-im_\ell\Phi}D^{\ell}_{m_\ell,\,k}(0,\theta,0)\,e^{-ik\chi}$. In that case, the complex conjugate $D^{\ell *}_{m_\ell,\,k}(\phi,\theta,\chi)$ of the function $D^{\ell}_{m_\ell,\,k}(\phi,\theta,\chi)$ has to be used instead of $D^{\ell}_{m_\ell,\,k}(\phi,\theta,\chi)$ for the eigenfunctions of $\vec{\ell}^2$. Setting $k = 0$, one retrieves the well-known spherical harmonics $|\ell\ m_\ell\ k = 0\rangle \equiv |\ell\ m_\ell\rangle$, which are the rotational motion eigenvectors of a free particle in 3D. The quantum numbers ℓ, m_ℓ are positive integers, with $m_\ell = -\ell, -\ell+1, ..., +\ell$.

[10] The molecule-fixed components (ℓ_x, ℓ_y, ℓ_z) of $\vec{\ell}$ and its space-fixed components (ℓ_X, ℓ_Y, ℓ_Z) are related by a simple unitary rotation involving the Euler angles. For our purpose of interpreting the shape of the eigenfunctions of $\vec{\ell}^2$, only the expression $\ell_Z = -i\hbar\frac{\partial}{\partial\phi}$ is required.

$$\begin{aligned}
\vec{\ell}^2\,|\ell\ m_\ell\ k\rangle &= \ell(\ell+1)\,|\ell\ m_\ell\ k\rangle \\
\ell_Z\,|\ell\ m_\ell\ k\rangle &= -i\hbar\frac{\partial}{\partial\phi}\Big)_s\,|\ell\ m_\ell\ k\rangle = m_\ell\,|\ell\ m_\ell\ k\rangle \\
\ell_z\,|\ell\ m_\ell\ k\rangle &= -i\hbar\frac{\partial}{\partial\chi}\Big)_s\,|\ell\ m_\ell\ k\rangle = k\ |\ell\ m_\ell\ k\rangle \quad \text{with}\ \ k=0\,.
\end{aligned} \tag{2.14}$$

The condition $k = 0$ is imposed by Equation 2.10, and indicates that the rotational momentum of the molecular axis is by definition zero about the axis itself. We stress again that the rotational motion of the molecule is null in the molecular frame xyz. The components of $\vec{\ell}$, Equation 2.9, are thus not strictly speaking measured along the axis xyz of the molecule-fixed frame. They are instead measured along the axis of a space-fixed frame, which is instantaneously coincident with the molecular frame. They encompass the information about the rotational motion of the nuclei in a useful vectorial form in the molecular frame xyz.

2.1.4 The separation of the diatomic Hamiltonian in the molecular frame

In this section we show how to decouple the rotation of the molecular frame from the inner motion of the electrons. The general reader might want to skip this section and head directly to the final result, Equation 2.26, and to the next sections of this chapter, where the results of the diagonalization of the diatomic Hamiltonian are presented and put into the context of our experimental work.

In the molecular frame, the expression of the Coulomb interaction between the electrons and the nuclei is

$$\begin{aligned}
V\left(\{\vec{r}_i\},\vec{R}\right) &= V\left(\{\vec{r}_i\},R\right) \\
&= \frac{e^2}{4\pi\epsilon_0}\left(\frac{Z_A Z_B}{R} - \sum_{i=1}^{N}\frac{Z_A}{r_{A,i}} - \sum_{i=1}^{N}\frac{Z_B}{r_{B,i}} + \sum_{i>j}\sum_{j=1}^{N}\frac{1}{r_{i,j}}\right)\,.
\end{aligned} \tag{2.15}$$

This expression is independent of the molecular axis orientation, which is the main simplification compared to Equation 2.1 and justifies using this frame. The distances $r_{A,i}$ and $r_{B,i}$ are indeed independent of the angles (θ,ϕ), which is not the case of the space-fixed distances $\rho_{A,i}$ and $\rho_{B,i}$ involved in Equation 2.2. The total electronic Hamiltonian in the molecular frame reads[11]

[11] Note that the Coulomb interaction between the nuclei is included into the electronic Hamiltonian. This convention is used in order to interpret the eigenvalues of the electronic system as the potential energy curves (PECs)

$$\hat{H}_e = \hat{T}_e + V\left(\{\vec{r}_i\}, R\right) \ . \tag{2.16}$$

The nuclear kinetic energy operator $\hat{T}_N$, in contrast to $\hat{T}_e$, has different expressions in the molecular frame and in space-fixed coordinates. The reason is that the motion of the nuclei imposes a motion of the frame itself, which leads to its coupling with the electronic motion. The operator $\hat{T}_N$ can be expressed in the space-fixed frame of the laboratory using the three Euler angles that define the molecular frame orientation, which leads to

$$\hat{T}_N = -\frac{\hbar^2}{2\mu}\vec{\nabla}_R^2 = -\frac{\hbar^2}{2\mu R^2}\frac{\partial}{\partial R}\left(R^2\frac{\partial}{\partial R}\right) + \frac{\vec{\ell}^2}{2\mu R^2} \ , \tag{2.17}$$

where $\vec{\ell}$ is the nuclear rotational angular momentum, expressed in the molecular frame xyz, and $\vec{\ell}^2 = (\vec{e}_x\ell_x + \vec{e}_y\ell_y + \vec{e}_z\ell_z)^2$ is its magnitude — see Equations 2.9 and 2.11 respectively. The angular term in Equation 2.17 changes only the nuclear orientation, leaving the space-fixed electronic coordinates $\{\vec{\rho}_i\}$ unchanged (this is indicated by the subscript s in Equation 2.11).

The internuclear distance R and the corresponding partial derivatives $\frac{\partial}{\partial R}$ and $\frac{\partial^2}{\partial R^2}$ are not affected by the passage to electronic molecule-fixed coordinates. The rotational operator $\vec{\ell}$, on the other hand, must be written differently in these two coordinate systems. Indeed, the effect of the operator $\vec{\ell}$ is to rotate the nuclei only. This operation leaves the laboratory space-fixed electronic coordinates $\{\vec{\rho}_i\}$ unchanged, but modifies the electronic coordinates $\{\vec{r}_i\}$ in the molecule-fixed system due to the change of the positions of the electrons with respect to the nuclei. The partial operators that change the orientation of the nuclei, while preserving the position of the electrons $\{\vec{r}_i\}$ in the molecular frame, are

$$\begin{aligned}
\frac{\partial}{\partial\theta}\Big)_m &= \frac{\partial}{\partial\theta}\Big)_s + i\sin\chi L_x + i\cos\chi L_y \\
\frac{\partial}{\partial\phi}\Big)_m &= \frac{\partial}{\partial\phi}\Big)_s - i\sin\theta\cos\chi L_x + i\sin\theta\sin\chi L_y + i\cos\theta L_z \\
\frac{\partial}{\partial\chi}\Big)_m &= \frac{\partial}{\partial\chi}\Big)_s + iL_z \ ,
\end{aligned} \tag{2.18}$$

where the subscripts s and m indicate that either the space-fixed electronic coordinates $\{\vec{\rho}_i\}$ or the molecule-fixed coordinates $\{\vec{r}_i\}$ are left unchanged by the rotation of the nuclei. The electronic molecule-fixed components L_x, L_y and L_z of the total electronic orbital angular momentum that appear in Equation 2.18 account for the rotation that is necessary to impose

along which the nuclei are moving — see Equation 2.40. The convention is different in Ref. [57], where the nuclear repulsion is treated separately.

on the electrons in the molecular frame to "follow" the rotation of the nuclei. The molecule-fixed components of the nuclear rotation angular momentum vector, Equation 2.9, are thus

$$\begin{aligned}
\ell_x &= -i\hbar \left[\cot\theta \cos\chi \frac{\partial}{\partial\chi}\Big)_m + \sin\chi \frac{\partial}{\partial\theta}\Big)_m - \operatorname{cosec}\theta \cos\chi \frac{\partial}{\partial\phi}\Big)_m \right] - L_x \\
\ell_y &= -i\hbar \left[-\cot\theta \sin\chi \frac{\partial}{\partial\chi}\Big)_m + \cos\chi \frac{\partial}{\partial\theta}\Big)_m + \operatorname{cosec}\theta \sin\chi \frac{\partial}{\partial\phi}\Big)_m \right] - L_y \\
\ell_z &= -i\hbar \frac{\partial}{\partial\chi}\Big)_m - L_z \,,
\end{aligned} \tag{2.19}$$

It is therefore natural to introduce $\vec{N} = \vec{\ell} + \vec{L}$, the total angular momentum exclusive of spin. The components of $\vec{N}$ are

$$\begin{aligned}
N_x &= -i\hbar \left[\cot\theta \cos\chi \frac{\partial}{\partial\chi}\Big)_m + \sin\chi \frac{\partial}{\partial\theta}\Big)_m - \operatorname{cosec}\theta \cos\chi \frac{\partial}{\partial\phi}\Big)_m \right] \\
N_y &= -i\hbar \left[-\cot\theta \sin\chi \frac{\partial}{\partial\chi}\Big)_m + \cos\chi \frac{\partial}{\partial\theta}\Big)_m + \operatorname{cosec}\theta \sin\chi \frac{\partial}{\partial\phi}\Big)_m \right] \\
N_z &= -i\hbar \frac{\partial}{\partial\chi}\Big)_m \,,
\end{aligned} \tag{2.20}$$

and Equation 2.10 imposes the condition

$$N_z = L_z \,. \tag{2.21}$$

$\vec{N}$ has the same structure in the molecular frame as the nuclear rotation operator — see Equation 2.9. However, $\vec{N}$ rotates the whole molecule, not only the nuclei. The electrons follow the rotation of the molecular axis instantaneously and thus their molecule-fixed coordinates $\{\vec{r}_i\}$ remain unchanged under the action of $\vec{N}$. The magnitude of $\vec{N}^2$ is

$$\vec{N}^2 = -\hbar^2 \left\{ \operatorname{cosec}\theta \frac{\partial}{\partial\theta} \left(\sin\theta \frac{\partial}{\partial\theta} \right) + \operatorname{cosec}\theta^2 \left[\frac{\partial^2}{\partial\phi^2} + \frac{\partial^2}{\partial\chi^2} - 2\cos\theta \frac{\partial^2}{\partial\phi\partial\chi} \right] \right\}_m \,, \tag{2.22}$$

and its eigenfunctions have the same form as given in Equation 2.12, i.e.

$$|N\ m_N\ k\rangle \equiv (-1)^{m_N - k} \sqrt{N + 1/2}\, D^N_{m_N,\,k}(\phi,\theta,\chi) \,. \tag{2.23}$$

The three quantum numbers N, m_N and k are respectively the magnitude of the total angular momentum exclusive of spin, the projection N_Z of this total angular momentum along the

Z axis of the space-fixed frame and its projection N_z along the z axis of the molecule-fixed frame. The corresponding eigenvalue equations are

$$\begin{aligned}
&\vec{N}^2 \,|N\, m_N\, k\rangle = N(N+1)\,|N\, m_N\, k\rangle \quad \text{with } N \geq |k| \\
&N_Z \,|N\, m_N\, k\rangle = -i\hbar \frac{\partial}{\partial \phi}\Big)_m |N\, m_N\, k\rangle = m_N\,|N\, m_N\, k\rangle \quad \text{with } m_N = -N, -N+1, ..., +N \\
&N_z \,|N\, m_N\, k\rangle = -i\hbar \frac{\partial}{\partial \chi}\Big)_m |N\, m_N\, k\rangle = k\;|N\, m_N\, k\rangle \quad \text{with } k = \Lambda\,,
\end{aligned} \tag{2.24}$$

where the condition $k = \Lambda$, with Λ the projection of the total electronic angular momentum $\vec{L}$ along the internuclear axis, is imposed by Equation 2.21. Therefore, a well-defined value of L_z is associated with each eigenstate of $\vec{N}^2$, with the restriction $N \geq |\Lambda|$ where N and Λ are positive integers. In the molecule-fixed frame xyz, the nuclear kinetic energy operator $\hat{T}_N$ reads

$$\hat{T}_N = \underbrace{-\frac{\hbar^2}{2\mu R^2}\frac{\partial}{\partial R}R^2\frac{\partial}{\partial R}}_{\hat{H}_{\text{vibration}}} + \underbrace{\frac{\vec{N}^2}{2\mu R^2}}_{\hat{H}_{\text{rotation}}} + \underbrace{\frac{\vec{L}^2 - 2\vec{N}\cdot\vec{L}}{2\mu R^2}}_{\hat{H}_{\text{Coriolis}}}, \tag{2.25}$$

using $\vec{N} = \vec{\ell} + \vec{L}$ and Equations 2.8, 2.17 and 2.20[12]. Therefore the complete molecular Hamiltonian[13], expressed in the molecule-fixed coordinate system $\{R, \phi, \theta, \chi, \{\vec{r}_i\}\}$, is

$$\hat{H} = \hat{H}_{\text{vibration}} + \hat{H}_{\text{rotation}} + \hat{H}_{\text{Coriolis}} + \hat{T}_{\text{mass pol.}} + \hat{H}_e\,. \tag{2.26}$$

The Coriolis terms appear due to the passage from the laboratory frame of reference to the non-inertial, rotating molecular frame. They induce correlations between nuclear and electronic motion and we have dismissed them in our work — see Subsection 2.1.6.

2.1.5 The electronic Hamiltonian and the potential energy curve(s)

The physical intuition that underlies most quantum chemistry calculations is that nuclear and electronic motions have well separated energy scales (optical for the electronic motion, RF to microwave for the nuclear motion). The reason is that nuclei are much heavier than

[12]Note that the momentum vector operators $\vec{N}$ and $\vec{L}$ commute (the operator $\vec{N}$ acts on the angular degrees of freedom (ϕ, θ, ϕ) while $\vec{L}$ acts on the electronic degrees of freedom $\{\vec{r}_i\}$), therefore $-\vec{N}\cdot\vec{L} - \vec{L}\cdot\vec{N} = -2\vec{N}\cdot\vec{L}$.

[13]We remind the reader that we have dismissed the center-of-mass motion from the molecular Hamiltonian, Equation 2.3, to focus on the relative motion of the diatomic system.

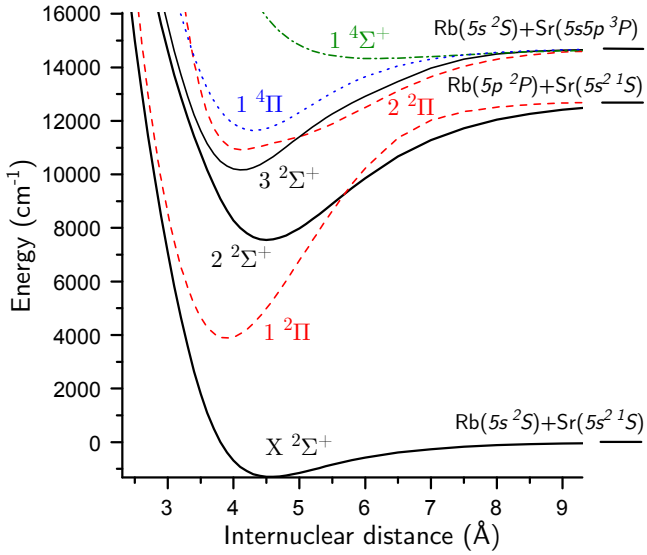

FIGURE 2.2: The RbSr PECs, taking into account kinetic and electrostatic terms and dismissing spin-dependent interactions, which are extremely weak in the electronic ground state. These PECs are calculated using the MRCI method for all states correlating to the experimentally relevant asymptotes. Plotted using the tabulated values of Ref. [60].

electrons, and thus typically much slower. Therefore, the electronic distribution around the nuclei adapts mostly *adiabatically* to changes of internuclear distances, which implies that the electronic motion is uncorrelated with the vibrational and rotational motion of the nuclei[14]. Accordingly, the appropriate electronic eigenbasis is obtained by diagonalizing the electronic Hamiltonian $\hat{H}_e$, Equation 2.16, which contains static R-dependent Coulomb interactions but no nuclear kinetic term[15]. The corresponding eigenvalue equations are

$$\hat{H}_e \psi_n^{\mathrm{el}}(\vec{r}, R) = U_n(R) \psi_n^{\mathrm{el}}(\vec{r}, R) \quad \text{with} \quad \{|n\rangle\}_n = \{|^{2S+1}|\Lambda|^{\pm}\rangle\}_{S,\Lambda} \,, \tag{2.27}$$

where we use the notation $\vec{r} \equiv \{\vec{r}_i\}$ for the electronic positions. The index n denotes symbolically the electronic eigenstate, and the set $\{|n\rangle\}_n$ constitutes a complete basis of the electronic Hilbert space. The corresponding eigenfunctions and eigenvalues are ψ_n^{el} and $U_n(R)$, and the curves of the eigenvalues $U_n(R)$ against the internuclear distance R constitute the potential energy curves (PECs) of the corresponding electronic states.

[14] Any deviation to this behaviour will lead to non-adiabatic corrections to the Born-Oppenheimer approximation — see Subsection 2.1.6, Equation 2.33.

[15] From the technical point of view, this amounts to setting a fixed distance R between the nuclei, calculating the eigenvalues of $\hat{H}_e$, and move on to the next value of R. For this reason, the electronic Hamiltonian given in Equation 2.16 is also referred to as the clamped nucleus Hamiltonian in the literature.

A given PEC correlates asymptotically, i.e. at $R \to +\infty$, with the energy of a pair of free atoms with zero relative kinetic energy (translational as well as rotational)[16]. The labels n are the molecular term symbols that indicate the symmetries of the molecular Hamiltonian[17]. There is only one PEC that correlates asymptotically with a pair of free Rb and Sr atoms in their respective electronic ground state $^2S_{1/2}$ and $^1S_0$. This is the ground-state PEC of RbSr, associated with the molecular term $^2\Sigma^+$, and we refer to it as $V_{^2\Sigma^+}(R) = V_g(R)$.

Obtaining the single-electron orbital basis that is most appropriate to solve the electronic problem and diagonalizing the electronic many-body Hamiltonian $\hat{H}_e$ are non-trivial theoretical problems, affairs of quantum chemistry experts. In order to match the $h\times$MHz resolution that we can achieve on the measurement of molecular binding energies in ultracold atom experiments, these calculated curves must be refined by fitting to experimental data.

2.1.6 Molecular states and binding energies: the nuclear motion along the ground-state PEC

Once the electronic eigenfunctions are known, an arbitrary wavefunction of the total system (electrons+nuclei) can be written down. Following the *Born-Oppenheimer separation*, it is expanded as a series of terms, each of which is the product of a nuclear wavefunction and an electronic wavefunction. It reads

$$\Psi^{\text{tot}}(\vec{r},\vec{R}) = \sum_m a_m\, \phi_m^{\text{el}}(\vec{r},R)\psi_m^{\text{nuc}}(R,\phi,\theta)\,, \tag{2.28}$$

and the wavefunctions can be written in Dirac notation $|\Psi^{\text{tot}}\rangle \equiv \Psi^{\text{tot}}(\vec{r},\vec{R})$, $|m\rangle \equiv \phi_m^{\text{el}}(\vec{r},R)$ and $|R,\phi,\theta\rangle_m \equiv \psi_m^{\text{nuc}}(R,\phi,\theta)$, leading to

$$|\Psi^{\text{tot}}\rangle = \sum_m a_m\, |m\rangle\, |R,\phi,\theta\rangle_m\ . \tag{2.29}$$

[16]Neutral atoms are designated by their LS atomic term symbol $^{2S+1}L_J$, where S is the electronic spin, L the orbital electronic angular momentum and J the total electronic angular momentum associated with $\vec{J} = \vec{L} + \vec{S}$ (with $s,p,d... = 0,1,2...$ for L and J). All three are good quantum numbers for $L = 0$, due to the absence of spin-orbit coupling. LS terms with equal J and $L \neq 0$ can be coupled through spin-orbit coupling, in which case only J is a good quantum number (neglecting hyperfine structure). For instance, the small coupling of the optically excited term $^3P_1$ of Sr to a $^1P_1$ term gives $^3P_1$ a finite lifetime, while in absence of spin-orbit coupling the selection rule $\Delta S = 0$ would forbid the spontaneous emission of the photon required for the transition $^3P_1 \to {}^1S_0$.

[17]Molecules are designated by their molecular term symbol $^{2S+1}|\Lambda|^{\pm}$, where S is the electronic spin, Λ is the expectation value of the projection L_z of the orbital electronic angular momentum onto the internuclear axis (with $\Sigma,\Pi,\Delta... = 0,1,2,...$), and $\pm$ indicates the sign change of the electronic wavefunction upon reflection through an arbitrary plane containing the molecular axis. In presence of spin-orbit coupling, the terms $^{2S+1}|\Lambda|^{\pm}$ get mixed with each other and $|\Lambda|$ is thus not a good quantum number: it is replaced by Ω, the projection of $\vec{J} = \vec{L} + \vec{S}$ onto the internuclear axis. Note that, unlike for neutral atoms, L (or J in presence of spin-orbit coupling) is not a good quantum number for a diatomic molecule because the molecular Hamiltonian is not spherically symmetric; instead, the projection Λ (or Ω) is indicative of the cylindrical symmetry around the internuclear axis.

The nuclear wavefunctions ψ_m^{nuc} involve only the nuclear coordinates (ϕ, θ) defining the molecule orientation, and the electronic wavefunctions ϕ_m^{el} involve the electronic coordinates and depend parametrically on the internuclear distance R. The probability amplitudes a_m characterize the contributions of each term in the expansion of the total wavefunction. The time-independent Schrödinger equation is obtained using Equations 2.26 and 2.25, and reads

$$\left(\hat{T}_N + \hat{T}_{\text{mass pol.}} + \hat{H}_e - E\right) \sum_m a_m \left|m\right\rangle \left|R, \phi, \theta\right\rangle_m = 0 \,. \tag{2.30}$$

The eigenvalue E is the internal energy of the diatomic system, i.e. its binding energy in the case of a molecular state. Multiplying by $\langle n|$ on the left, one obtains[18]

$$\sum_m a_m \Big[\left(\left\langle n\right| \hat{T}_N \left|m\right\rangle + \left\langle n\right| \hat{T}_{\text{mass pol.}} \left|m\right\rangle\right) + U_n(R) - E \Big] \left|R, \phi, \theta\right\rangle_m = 0 \,. \tag{2.31}$$

The *Born-Oppenheimer* or *adiabatic approximation* consists in neglecting the off-diagonal matrix elements that couple different electronic states n and m within the electronic eigenbasis $\{|n\rangle\}_n$. It amounts to restricting the total wavefunction to only one term of the expansion given in Equation 2.29, i.e.

$$\Big[\left\langle n\right| \hat{T}_N \left|n\right\rangle + \left\langle n\right| \hat{T}_{\text{mass pol.}} \left|n\right\rangle + U_n(R) - E \Big] \left|R, \phi, \theta\right\rangle_n \simeq 0 \tag{2.32}$$

$$\left|\Psi^{\text{tot}}\right\rangle \simeq \left|n\right\rangle \left|R, \phi, \theta\right\rangle_n \,. \tag{2.33}$$

The diagonal matrix elements are referred to as adiabatic contributions to the energy of the system, as opposed to the non-adiabatic off-diagonal contributions that are discarded in the adiabatic approximation. The rotational Hamiltonian $\hat{H}_{\text{rotation}}$ is fully diagonal in $\{|n\rangle\}_n$, because the total rotational operator $\vec{N}^2$ doesn't act on the electronic degrees of freedom $\vec{r}$ and on the internuclear distance R. The electronic wavefunctions $\phi_n^{\text{el}}(\vec{r}, R)$ are thus unaffected by the rotation of the whole molecule and $[\hat{H}_e, \vec{N}^2] = 0$. On the other hand, the terms $\hat{H}_{\text{vibration}}$,

[18] The Dirac notation $\langle m| \hat{T}_N |n\rangle$ indicates integration over electronic coordinates, i.e. $\langle m| \hat{T}_N |n\rangle = \int \phi_m^{\text{el}*}(\vec{r}, R) \hat{T}_N \phi_n^{\text{el}}(\vec{r}, R) \mathrm{d}\vec{r}$.

$\hat{H}_{\text{Coriolis}}$ and $\hat{T}_{\text{mass pol.}}$ display both diagonal and off-diagonal matrix elements[19]. Following the notation of Ref. [57], the contribution of $\hat{H}_{\text{rotation}}$ and the adiabatic contribution of $\hat{H}_{\text{vibration}}$ are

$$\langle n|\,\hat{H}_{\text{rotation}}\,|n\rangle\,|R,\phi,\theta\rangle_n = \langle n|\,\frac{\vec{N}^2}{2\mu R^2}\,|n\rangle\,|R,\phi,\theta\rangle = \frac{\vec{N}^2}{2\mu R^2}\,|R,\phi,\theta\rangle_n \tag{2.34}$$

$$\langle n|\,\hat{H}_{\text{vibration}}\,|n\rangle\,|R,\phi,\theta\rangle_n = \left[-\frac{\hbar^2}{2\mu R^2}\frac{\partial}{\partial R}R^2\frac{\partial}{\partial R} + Q_{n,n}\right]|R,\phi,\theta\rangle_n \tag{2.35}$$

$$Q_{n,n} = -\frac{\hbar^2}{2\mu}\,\langle n|\,\frac{\partial^2}{\partial R^2}\,|n\rangle\ . \tag{2.36}$$

The adiabatic correction $Q_{n,n}$ is typically small compared to the other diagonal contributions, and we have dismissed it in our work on the ground-state PEC of RbSr. The same goes for $\langle n|\,\hat{H}_{Coriolis}\,|n\rangle$ and $\langle n|\,\hat{T}_{\text{mass pol.}}\,|n\rangle$. It is important to understand that however small, these matrix elements — as well as the non-adiabatic contributions — lead to corrections of the molecular binding energies. However within our experimental precision, we could not resolve them in the RbSr electronic ground state[20]. Under these approximations, Equations 2.32 reads

$$\left[\frac{\hbar^2}{2\mu R^2}\frac{\partial}{\partial R}R^2\frac{\partial}{\partial R} + \frac{\vec{N}^2}{2\mu R^2} + U_n(R) - E\right]|R,\phi,\theta\rangle_n = 0\,. \tag{2.37}$$

[19] It is interesting to look at the structure of the Coriolis couplings $\vec{L}^2 - 2\vec{N}.\vec{L}$ for the RbSr $^2\Sigma^+$ term, in the electronic eigenbasis $\{|n\rangle\}_n = \{|^{2S+1}|\Lambda|\rangle\}_{S,\Lambda}$. We consider a molecular state $|S\Lambda\rangle\,|N\ m_N\ \Lambda\rangle$ with the electronic wavefunction $|^{2S+1}|\Lambda|\rangle = |S\Lambda\rangle$ and the rotational wavefunction $|N\ m_N\ \Lambda\rangle$, as written in Equation 2.41. The term $\vec{L}^2 = L_z^2 + (1/2)\,[L_+L_- + L_-L_+]$, where $L_\pm = L_x \pm iL_y$, acts on the electronic part with $L_z\,|S\Lambda\rangle = \Lambda\,|S\Lambda\rangle$ and $L_\pm\,|S\Lambda\rangle \propto |S\ \Lambda \pm 1\rangle$. Therefore the L_z^2 term is null for $^2\Sigma^+(\Lambda{=}0)$, and the $L_+L_- + L_-L_+$ term is fully diagonal in $\{^{2S+1}|\Lambda|\}_{S,\Lambda}$: $(L_+L_- + L_-L_+)\,|S\Lambda\rangle \propto |S\Lambda\rangle$. This term is in general non-zero and is referred to as $P_{n,n}$ in Ref. [57]. The term $\vec{N}.\vec{L} = N_zL_z + (1/2)\,[N_+L_- + N_-L_+]$, where $N_\pm = N_x \pm iN_y$, acts on the rotational part with $N_z\,|N,m_N,\Lambda\rangle = \Lambda\,|N,m_N,\Lambda\rangle$ and $N_\pm\,|N,m_N,\Lambda\rangle = \sqrt{N(N+1)-\Lambda(\Lambda\mp1)}\,|N,m_N,\Lambda\mp1\rangle$, as seen from Equations 2.23 and 2.22. Therefore the N_zL_z term is null for $^2\Sigma^+(\Lambda = 0)$, but the $N_\pm L_\mp$ terms produce $N_\pm L_\mp\,|S\Lambda\rangle\,|N\ m_N\ \Lambda\rangle \propto |S\ \Lambda\mp1\rangle\,|N\ m_N\ \ \Lambda\mp1\rangle$ which for $^2\Sigma^+$ is non-zero for $N > 0$ and branches to states with $|\Lambda| = 1$. Thus, the Coriolis coupling $\vec{N}.\vec{L}$ admixes $^2\Sigma^+$ states with $N > 0$ with the electronically excited $^2\Pi$ states. These non-adiabatic corrections to the binding energies of the rotating molecular states are very small for the ground state $^2\Sigma^+$, because the corresponding matrix elements are much smaller than the large energy difference between the $^2\Sigma^+$ and $^2\Pi$ electronic states — see Figure 2.2.

[20] In particular, the adiabatic corrections that lead to a common offset in the binding energies of weakly-bound molecular states are "swallowed" in the fitted C_6 and C_8 coefficients that we discuss in Subsection 2.1.7. An important exception arises when two PECs cross. In that case the non-adiabatic matrix elements can be of the same order of magnitude as the difference in electronic energies $U_n(R) - U_m(R)$. This leads to an avoided crossing between the two PECs, and to important corrections to the binding energies of molecular states that display a large interradial probability density $|\chi_v^{\text{vib}}(R)|^2$ (defined as the probability density of finding the two nuclei at the distance R from one another) close to the crossing point. The electronic ground state of RbSr consists of only one PEC, therefore such crossings don't occur and the abovementioned corrections can be treated perturbatively.

Since the radial partial operators do not act on the angular degrees of freedom (θ, ϕ), the left-hand term commutes with $\vec{N}^2$ and thus the eigenbasis of $\vec{N}^2$ is also an eigenbasis for this term. One can thus separates the nuclear wavefunction $|R, \phi, \theta\rangle_n \equiv \psi_n^{\text{nuc}}(R, \phi, \theta)$ into a product of a radial and an angular wavefunction, according to[21,22]

$$\psi_n^{\text{nuc}}(R, \phi, \theta) = \frac{\chi_{v,N}^{\text{vib}}(R)}{R} \times \text{Y}_N^{\text{rot}}(\theta, \phi) \,. \tag{2.38}$$

The eigenfunctions $|N, m_N, \Lambda\rangle \equiv \text{Y}_N^{\text{rot}}(\theta, \phi)$ of the total angular momentum exclusive of spin, Equation 2.22, have eigenvalues of the form $\hbar^2 N(N+1)$, where N is a positive integer. The electronic ground state of RbSr is a Σ term, as discussed in Subsection 2.1.5, therefore $\Lambda = 0$ and we denote the corresponding rotational eigenstates as $|N, m_N, \Lambda = 0\rangle = |N, m_N\rangle$ throughout this thesis. They are the well-known spherical harmonics

$$\text{Y}_N^{\text{rot}}(\theta, \phi) = (-1)^{m_N} \sqrt{\frac{2N+1}{4\pi} \frac{(N-m_N)!}{(N+m_N)!}} P_N^{m_N} \cos(\theta) e^{i m_N \phi} \quad \text{for } \Lambda = 0 \,, \tag{2.39}$$

where $P_N^{m_N}$ is an associated Legendre function. For a given value of the rotational quantum number N, Equation 2.37 reduces to the radial equation of motion

$$\left[-\frac{\hbar^2}{2\mu} \frac{\text{d}^2}{\text{d}R^2} + \frac{\hbar^2 N(N+1)}{2\mu R^2} + U_n(R) - E \right] \chi_{v,N}^{\text{vib}}(R) = 0 \,. \tag{2.40}$$

The complete wavefunction for the stationary state of the diatomic system is therefore

$$\Psi^{\text{tot}}(\vec{r}, \vec{R}) = \phi_n^{\text{el}}(\vec{r}, R) \text{Y}_N^{\text{rot}}(\theta, \phi) \frac{\chi_{v,N}^{\text{vib}}(R)}{R} \,, \tag{2.41}$$

where electronic, rotational and vibrational motions are explicitly separated. The very essence of the adiabatic approximation appears clearly in Equation 2.40: the energy of the electronic cloud $U_n(R)$ acts as an effective external potential through which the nuclei are moving, hence the name potential energy curve. Furthermore, the rotation of the molecule (nuclei

[21] This is in complete analogy with the problem of the hydrogen atom, where the radial and rotational motions of the electron around the proton are separated as a product of wavefunctions $|nlm\rangle \equiv \Psi_{nlm}(r, \theta, \phi) = R_{nl}(r) \text{Y}_l^{m_l}(\theta, \phi)$. The quantum numbers n, l and m_l are in that case the principal, orbital and magnetic quantum numbers respectively.

[22] With the identification $|N, m_N, \Lambda\rangle \equiv \text{Y}_N^{\text{rot}}(\theta, \phi)$ we dismiss the third Euler angle χ by setting $\chi = 0$. We remind the reader that for a diatomic molecule this angle is arbitrary and so is the unphysical phase factor $\exp^{ik\chi}$ in Equation 2.23. The solutions to the diatomic problem, Equation 2.29, are equivalent to those obtained without the artificial use of χ provided the rotational Hilbert space is restricted to the kets $|N\, m_N\, k\rangle$ for which $k = \Lambda$. This guarantees that the actions of N_z and L_z on a state $|\Lambda\, S\rangle\, |N\, m_N\, k\rangle$ have the same effect, owing to Equation 2.21, even though one acts in the electronic Hilbert space and the other in the rotational Hilbert space. For a discussion on this matter, see "Hougen's isomorphic Hamiltonian" in Ref. [57].

and electrons) acts as a centrifugal barrier that keeps the two nuclei farther apart, as shown in Figure 2.5. The shape of the wavefunctions $\chi^{\text{vib}}_{\nu,N}$ therefore depends on N. We explicitly indicate with the notation $U_g(R) = V_g(R)$, where g denotes the RbSr electronic ground state, that the electronic energy acts as an effective potential. The radial equation of motion is thus

$$\left[-\frac{\hbar^2}{2\mu}\frac{\mathrm{d}^2}{\mathrm{d}R^2} + \frac{\hbar^2 N(N+1)}{2\mu R^2} + V_g(R) - E\right]\chi^{\text{vib}}_{\nu,N}(R) = 0\,, \tag{2.42}$$

and the molecular Hamiltonian, Equation 2.26, reduces to

$$\hat{H} = \frac{1}{2\mu}\left[-\hbar^2\frac{\mathrm{d}^2}{\mathrm{d}R^2} + \frac{\hat{N}^2}{R^2}\right] + \hat{V}_g(R)\,. \tag{2.43}$$

The eigenstates of positive energy E correspond to atom pair scattering states[23], for which the vibrational part $\chi^{\text{vib}}_{\nu,N}(R)$ is replaced by a scattering wavefunction $\chi^{scat}_{k,N}(R)$ denoted by the quantum number k that quantifies the relative kinetic energy $E = \frac{\hbar^2 k^2}{2\mu}$ of the pair along the internuclear axis. The (non)-rotating pairs with rotational quantum number $N = 0, 1, 2, 3, ...$ are referred to as s-, p-, d-, f-wave, ... scattering states respectively[24]. Examples of the associated scattering wavefunctions $\chi^{scat}_{k,N}(R)$ at $E = k_B \times 1.0\ \mu$K and $N = 0$ are plotted in Chapter 3, Figure 3.5. On the other hand, the eigenstates of negative energy refer to molecular bound states, associated with the vibrational quantum number ν and the rotational quantum number N[25,26]. Hence, once the PEC in the electronic ground state is known, one can predict the binding energies $E_b = -E$ of the molecular bound states by solving Equation 2.42. Conversely, we experimentalists can do a spectroscopic search for molecular bound states, assign the appropriate quantum numbers to them and derive the ground-state PEC from a fitting procedure based on Equation 2.42. The part of the RbSr ground-state PEC that we addressed with our ultracold atom experiments is its dispersive "long-range" attractive part, which is discussed in Subsection 2.1.7.

[23] An exception to this arises when a molecular state is bound in the centrifugal barrier of the potential, i.e. a molecular state exists with positive energy for $N > 0$. This phenomenon is referred to as a shape resonance.

[24] In the case of scattering states, the quantum number ℓ or l is often used in place of N in the literature.

[25] Scattering and molecular states are subject to different normalizations in absence of external confinement. This is discussed extensively in Section 5.1.

[26] Molecules associated with the rotational quantum number $N = 0, 1, 2, 3...$ are sometimes referred to as s-wave, p-wave, d-wave, f-wave... molecules in the literature. For a given vibrational quantum number ν, the binding energies of the associated rotational states follow the progression $E_b(\nu, N) = E_b(\nu, 0) - N(N+1)\langle 1/R^2\rangle_{\text{vib}}$. The integral $B_\nu = \langle 1/R^2\rangle_{\text{vib}} = \int_0^\infty |\chi^{\text{vib}}_{\nu,N=0}(R)|^2 R^{-2} dR$, where $\chi^{\text{vib}}_{\nu,N=0}$ is the vibrational wavefunction obtained for $N = 0$ in Equation 2.42, can be identified as the rotational constant of the corresponding vibrational state.

2.1.7 The long-range part of the ground-state PEC: our experimental playground

The electrostatic potential between two neutral atoms A and B, Equation 2.2, can be written in the compact form

$$V^{\mathrm{el}} = \sum_{k\in A}\sum_{l\in B}\frac{q_k q_l}{4\pi\epsilon_0\|\vec{r}_{kl}\|}\,, \tag{2.44}$$

where k, q_k and l, q_l label all the individual particles and their charges contained in the atom A and B respectively, and $\vec{r}_{kl}$ is the distance between two such charges [40, 55]. When the two atoms are far away from each other, one can treat the electrostatic interactions as a perturbation of the two single-atom electronic Hamiltonians. In this long-range scenario $\|\vec{r}_{kl}\|$ is the sum of the internuclear distance R and a corrective term, negligible compared to R. Hence, it is possible to use a Taylor expansion of the electrostatic potential around R^{-1}. Introducing the tensor operators Q_j^m, given by

$$\begin{aligned} Q_j^m(A) &= \sqrt{\frac{4\pi}{2j+1}}\sum_{k\in A} q_k r_{Ak}^j \mathrm{Y}_j^m\left(\theta_{\vec{r}_{Ak}},\phi_{\vec{r}_{Ak}}\right)\\ Q_j^m(B) &= \sqrt{\frac{4\pi}{2j+1}}\sum_{l\in B} q_l r_{Bl}^j \mathrm{Y}_j^m\left(\theta_{\vec{r}_{Bl}},\phi_{\vec{r}_{Bl}}\right)\,, \end{aligned} \tag{2.45}$$

where r_{Ak} and r_{Bl} are the distances between the electron k and l to their nucleus A and B respectively, $\vec{r}_{Ak}$ and $\vec{r}_{Bl}$ are the associated vectors, $(\theta_{\vec{r}_{Ak}},\phi_{\vec{r}_{Ak}})$ and $(\theta_{\vec{r}_{Bl}},\phi_{\vec{r}_{Bl}})$ are the respective polar angles of $\vec{r}_{Ak}$ and $\vec{r}_{Bl}$ and Y_j^m are spherical harmonics. The electrostatic potential can be written using a multipole expansion, which leads to

$$V^{\mathrm{el}} = \sum_{l_A,l_B=0}^{\infty}\frac{V_{l_A l_B}(A,B)}{R^{l_A+l_B+1}}\,, \tag{2.46}$$

where $V_{l_A l_B}(A,B)$ is defined as

$$V_{l_A l_B}(A,B) = \frac{1}{4\pi\epsilon_0}\sum_{m=-\min(l_A,l_B)}^{\min(l_A,l_B)}\frac{(-1)^{l_B}\,(l_A+l_B)!}{\sqrt{(l_A+m)!\,(l_A-m)!\,(l_B+m)!\,(l_B-m)!}}Q_{l_A}^m(A)Q_{l_B}^{-m}(B)\,. \tag{2.47}$$

The quantization axis for each m is chosen along the internuclear axis. One recognizes in the terms of this expansion interactions of the type charge-charge, charge-dipole, dipole-dipole and charge quadrupole, ..., scaling with R^{-1}, R^{-2}, R^{-3}, ... respectively. The first-order

term of the perturbation $\Delta E^{(1)}$ cancels out for neutral atoms in an S state ($L = 0$), since such atoms do not display any nuclear or electronic moments. The leading term of the perturbative treatment is thus the second-order correction term $\Delta E^{(2)}$, which is proportional to $R^{-(l_A+l_B+1)^2}$ with $l_A, l_B \geq 1$ in absence of charge. Hence the second-order correction to the electronic energy can be written

$$\Delta E^{(2)} = -\frac{C_6}{R^6} - \frac{C_8}{R^8} - \frac{C_{10}}{R^{10}} - \dots , \tag{2.48}$$

where the leading C_6 term is the van der Waals interaction, and the C_n coefficients are referred to as *dispersion* coefficients. The C_6 coefficient defines the characteristic radius of the PEC, which is $R_e = (\mu C_6/\hbar^2)^{1/4} \sim 70$ Å for RbSr[27,28]. The molecular Hamiltonian in the electronic ground state, Equation 2.43, takes the asymptotic form

$$\hat{H} \xrightarrow[R\to\infty]{} \frac{1}{2\mu}\left[-\hbar^2\frac{\mathrm{d}^2}{\mathrm{d}R^2} + \frac{\hat{N}^2}{R^2}\right] - \frac{C_6}{R^6} - \frac{C_8}{R^8} - \frac{C_{10}}{R^{10}} - \dots . \tag{2.49}$$

The long-range expansion series, Equation 2.48, does not converge. However, it is usually sufficient to consider only the first terms of the series. This is clear from our fit of the long-range part of the RbSr ground-state PEC presented in Chapter 3, for which restricting ourselves to a Lennard-Jones potential model including only C_6 and C_8 coefficients was sufficient to fit our data within experimental error bars. This perturbative approximation is justified for large internuclear distances, where the electronic clouds of the two atoms do not overlap significantly. A typical distance at which the clouds start to overlap is given by the LeRoy radius $R_L = 2(r_A + r_B) = 2(\sqrt{\langle nl|\, r^2\, |nl\rangle_A} + \sqrt{\langle n'l'|\, r^2\, |n'l'\rangle_B})$ [61][29], where r_A and r_B are the atomic radii of the atoms A and B in their respective electronic orbitals $|nl\rangle$ and $|n'l'\rangle$. For a pair of ground-state Rb and Sr atoms, $R_L = 2(r_{\mathrm{Rb}} + r_{\mathrm{Sr}}) = 2(2.65$ Å$+2.19$ Å$) = 9.68$ Å [62], therefore the approximation $R \gg R_L$ is justified for binding energies much lower than $C_6/{R_L}^6 = h \times 650$ GHz, where h is Planck's constant[30]. All binding energies

[27] The symbol Å represents the ångström unit of length. 1 Å = 10^{-10} m.

[28] Note that for pairs of identical atoms interacting through an excited PEC (i.e. a PEC for which the dissociation limit corresponds to one atom in the electronic ground state and one atom in an electronically excited state, or two excited atoms in different electronic states), the long-range expansion includes a $-C_3/R^3$ term. This term has much shorter range than the van der Waals $-C_6/R^6$ term and therefore defines the range of the potential. Such a situation arises for instance in Sr_2 close to the Sr ($^1S_0$) + Sr ($^3P_1$) dissociation asymptote.

[29] The symbols n and l stand for the principal and orbital quantum numbers respectively.

[30] This estimation is made using $1\,\mathrm{cm}^{-1} = h \times 30$ GHz and the value of the fitted C_6 coefficient for RbSr in its electronic ground state ($1.784(15) \times 10^7$ Å^6 cm^{-1} — see Chapter 3). Note that for a given molecular state of binding energy -E and of vibrational wavefunction $\chi^{\mathrm{vib}}_{v,N}(R)$, the actual average internuclear distance is $\langle R\rangle = \int_0^\infty |\chi^{\mathrm{vib}}_{v,N}(R)|^2 R dR$. Here it is estimated using the classical outer-turning point of the ground-state PEC at the energy E, which is defined as the largest internuclear distance at which $V_g(R) = E$. That is the distance around which most of the interradial probability density $|\chi^{\mathrm{vib}}_{v,N}(R)|^2$ lies for weakly-bound molecular states.

we measured in the electronic ground state of RbSr lie below $h \times 10$ GHz, therefore this dispersive approach is valid for our dataset.

2.2 Two-colour and magnetic Feshbach spectroscopy: probing the ground-state PEC of RbSr

Our experimental exploration of the dispersive, long-range part of the ground-state PEC of RbSr using two-colour and magnetic Feshbach spectroscopy is described thoroughly in the two publications presented in Chapter 3 and Chapter 6. In the following subsections, the interested reader will find additional information about the assignment of quantum numbers to the detected molecular states.

This assignment is a non-trivial task. The initial scattering state is defined by its rotational quantum number N[31], while the detected molecular state are defined by their vibrational and rotational quantum numbers v and N — see Subsection 2.1.6. To these are added the hyperfine contribution $|f, m_f\rangle$ of both states[32]. The difference in energy between the $f = 1$ and $f = 2$ hyperfine manifolds of ^{87}Rb is $h \times 6.835$ Ghz in absence of a magnetic field [50], which is bigger than the typical difference in binding energies of near-threshold RbSr molecular states with same F but different v and/or N. It is therefore necessary to determine correctly F for both the initial scattering state and the detected molecular state in order to assign correctly v and N to the latter one. The $|i, m_i\rangle$ nuclear spin contribution of Sr, on the other hand, is only present in ^{87}Sr ($i = 9/2$) and is irrelevant in this respect. Indeed, the gyromagnetic ratio of ^{87}Sr is very small (see Equation 5.46) and, at our magnetic fields of a few G for two-colour spectroscopy and a few hundred G for Feshbach spectroscopy, it does not lead to Zeeman splittings comparable to the Zeeman splittings of the m_f states of Rb or to the RbSr rotational and vibrational splittings.

2.2.1 Two-colour spectroscopy

We report in the publication presented in Chapter 3 the detection of many RbSr molecular states via two-colour spectroscopy, also known as Autler-Townes spectroscopy [63]. Two-colour spectroscopy is a versatile molecular spectroscopy technique, that we used to measure the binding energy of RbSr molecule in the electronic ground state. In a two-colour scheme, an excitation laser, referred to as free-bound laser (L_{FB}), photoassociates atom pairs

[31] The distribution of k-vectors quantifying the etic energy of the atom pairs along the internuclear axis is set by the temperature of the Rb-Sr mixture and by the geometry and depth of the optical dipole trap, and is irrelevant to the assignment of quantum numbers to the detected molecular state.

[32] It is customary to use uppercase letters to denote the hyperfine quantum numbers F and m_F of a molecule, and lowercase letters for the quantum numbers f and m_f of an atom. We do not follow this convention in this section, because Rb-Sr atom pairs and weakly-bound RbSr molecular states have a very similar hyperfine structure in the electronic ground state. That is not necessarily the case in the electronic ground state of bi-alkali systems (see Chapter 5, Section 5.2) or in RbSr electronically-excited states (see Chapter 4, Section 4.4).

into electronically-excited molecules for a time T_{pulse}, which leads to loss of atoms[33]. Simultaneously, a second laser, referred to as bound-bound laser (L_{BB}), irradiates the atoms. The frequency ν_{BB} of this laser is scanned and, when its frequency matches a resonance frequency that connects the target electronically-excited molecular state of L_{FB} to a yet-undetected molecular state, it resonantly couples the two states. If L_{BB} is sufficiently intense, the two molecular states are strongly mixed. This induces an Autler-Townes-type splitting of the photoassociation line, which reduces the L_{FB}-induced photoassociation rate [63]. This decrease in photoassociation rate translates into a decrease of the photoassociation-induced losses over the course of the L_{FB} laser pulse, which can be observed experimentally and indicates the detection of a molecular state. The binding energy of the detected molecule is then given by $h \times (\nu_{\text{BB}} - \nu_{\text{FB}})$, where ν_{FB} is the (fixed) frequency of L_{FB} and ν_{BB} the resonance frequency at which the decrease of the photoassociation rate is observed.

A quick overview of two-colour spectroscopy in ultracold RbSr

In the two-colour spectroscopy experiments that we performed to probe the ground-state PEC of RbSr, the lasers L_{FB} and L_{BB} irradiate a μK-cold sample of about 10^5 Rb atoms and 10^6 Sr atoms for a time T_{pulse}. The Rb atoms are prepared in the $f = 1$ hyperfine manifold, with all $m_f = 0, \pm 1$ states almost equally populated (the quantization axis is taken along the direction of the homogeneous magnetic field of a few G that we apply during the laser pulse). The L_{FB} laser is set at a fixed frequency, and resonantly couples an initial Rb-Sr atom pair state of collisional energy $E \sim k_B \times 1.0$ μK to a target electronically-excited RbSr molecular state of energy $E_{\text{mol},2}$ close to the Rb $(^2S_{1/2}) + \text{Sr}\ (^3P_1)$ dissociation asymptote[34]. This provokes photoassociation-induced losses in a given m_f-state of Rb. All three $f = 1$, $m_f = 0, \pm 1$ states of Rb are imaged separately after the laser pulse, using Stern-Gerlach separation and atomic absorption imaging. The Rb-Sr sample is lost at this point, and another experimental cycle begins: a new Rb-Sr is prepared and another laser pulse combining L_{FB} and L_{BB} is performed. The frequency ν_{BB} of the laser L_{BB} is changed from one experimental shot to the other. When it matches a resonance frequency $\nu_{\text{BB}} = \left(E_{\text{mol},2} - E_{\text{mol},1}\right)/h$, where $E_{\text{mol},1}$ is the energy of a RbSr molecule in the electronic ground state, an Autler-Townes splitting is produced [63]. The dressing of the excited molecular state by the electronic-ground-state molecular state and one L_{BB} photon results in an avoided crossing, which pushes the excited state out of resonance from L_{FB}. The photoassociation rate is therefore reduced at the resonant L_{BB} frequency, which translates into an increase of the Rb atom number in the

[33] See Chapter 4 for more details on this photoassociation process.

[34] The reader interested in the details of this one-photon photoassociation setup is referred to Chapter 4, and in particular to Figure 4.2. In this chapter, more details are given on the preparation of the Rb-Sr sample and on the laser system and experimental conditions that we use in one-colour spectroscopy.

m_f-state subject to photoassociation. This is depicted in Figure 2.3[35], and the avoided crossing produced by L_{BB} is depicted in Figure 2.4. The binding energy $BE_{mol,1}$ of the detected molecular state is obtained by comparing the difference in frequency $\nu_{BB} - \nu_{FB}$ of the two lasers, at the L_{BB} resonant frequency where this increase in atom number is observed. It is $BE_{mol,1} = h \times (\nu_{BB} - \nu_{FB}) - E$, where E is the collisional energy E of the Rb-Sr atom pair and amounts to only a few tens of kHz at our μK temperatures ($k_B \times 1.0\,\mu\text{K} = h \times 20.8365\,\text{kHz}$)[36]. The gap $\hbar\Omega$ of the avoided crossing produced by L_{BB} is proportional to $\sqrt{I_{BB}}$, where I_{BB} is the bound-bound laser intensity — see Figure 2.4. Therefore, it is best to work with as large L_{BB} intensities as possible to maximise the decrease of photoassociation rate and thus the detection visibility.

The Rabi frequency Ω characterizes the coupling of the molecular states by the L_{BB} light, and provides information about the structure of the molecular states[37]. This Rabi frequency can be measured as follows. The L_{BB} laser is set to the resonant frequency $\nu_{BB} = \left(E_{mol,2} - E_{mol,1}\right)/h$, and the frequency of ν_{FB} is scanned around the L_{FB} photoassociation resonance frequency. The avoided crossing produced by L_{BB} leads to an Autler-Townes splitting of the L_{FB} photoassociation resonance [63], also referred to as Autler-Townes doublet [64]. Two photoassociation resonances are then observed, instead of one in the absence of L_{BB}. They occur at two distinct values of ν_{FB}, separated in frequency by $\Omega/2\pi$ (hence the term Autler-Townes splitting), and translate into two photoassociation-induced loss features that can be observed experimentally[38]. This $\Omega/2\pi$ splitting is measured at different L_{BB} intensities, which constitutes a characterization of the strength of the bound-bound transition. Examples of such measurements are presented in Ref. [52], Figure 5.16, in the context of RbSr, and we do not repeat it here. We performed this characterization for some of the RbSr molecular states that we detected, which is reported in Chapter 3, Table 3.1 (note that we report the Rabi frequency per unit square root of intensity, not the actual Rabi frequency at a given optical intensity).

The reader is referred to Chapter 3 for further details on our two-colour spectroscopy experimental setup, and on the data acquisition and analysis.

[35] The Rb absorption pictures shown in Figure 2.3 and Figure 4.2 are taken from a magnetic Feshbach spectroscopy scan, not a two-colour scan. The images obtained in the context of two-colour spectroscopy are fully analogous to the ones presented here, which were chosen for these figures because they show very clearly to the reader the effects of loss/recovery of Rb atoms on the absorption images.

[36] The typical binding energies that we measure are of a few GHz or hundred MHz, and this correction is comparatively very small — see Chapter 3, Table 3.1 where the binding energies that we measured are reported.

[37] The coupling matrix element $\langle\psi^{(1)}_{mol}|\,\hat{H}_{BB}\,|\psi^{(2)}_{mol}\rangle$, which is induced by L_{BB} and connects the two molecular states, is related to the Rabi frequency Ω through $\hbar\Omega = 2\,\langle\psi^{(1)}_{mol}|\,\hat{H}_{BB}\,|\psi^{(2)}_{mol}\rangle$, as shown in Figure 2.4. Note that the phase of this matrix element can always be chosen such that $\Omega > 0$ [64].

[38] The Rabi frequency is an angular frequency (expressed in rad.s^{-1} or rad.Hz), not an actual frequency (expressed in Hz), hence the factor 2π to relate to the optical frequencies that we use and measure.

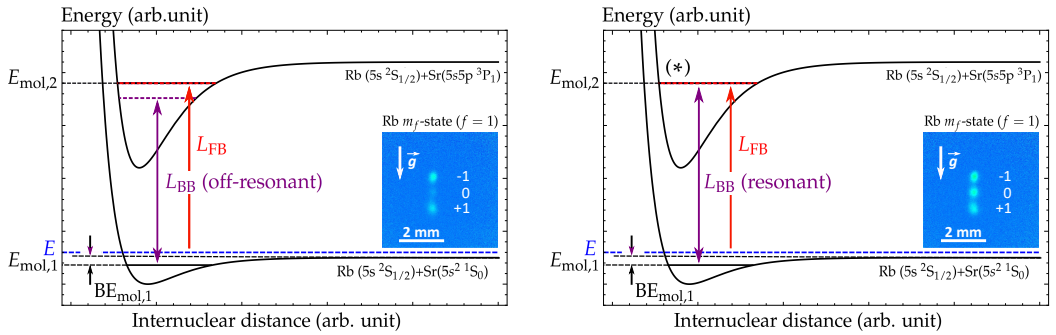

FIGURE 2.3: Principle of an ultracold Rb-Sr two-colour spectroscopy experiment close to the $^1S_0 - {}^3P_1$ intercombination line of Sr. The lasers L_{FB} and L_{BB} irradiate the Rb-Sr sample for a time T_{pulse}. The L_{FB} laser is set at a fixed frequency and produces electronically-excited molecules of energy $E_{mol,2}$, provoking photoassociation-induced losses in a given m_f-state of Rb ($m_f = 0$ in this figure). The frequency ν_{BB} is changed from one experimental shot to the other, with the goal of finding a resonance frequency at which these losses are reduced. The insets show absorption images of Stern-Gerlach-separated Rb atoms, with the direction of gravity indicated with a white arrow (Rb time of flight = 14 ms). **Left panel**: laser L_{BB} off-resonant. Strong photoassociation-induced losses are provoked in $m_f = 0$ due to L_{FB}. **Right panel**: laser L_{BB} resonant. An Autler-Townes splitting is produced (see Figure 2.4), which decreases the photoassociation rate. The number of Rb atoms imaged in $m_f = 0$ is thus increased compared to the off-resonant case. The binding energy $BE_{mol,1}$ of the detected molecular state is obtained by comparing the frequency of the two lasers, resulting in $BE_{mol,1} = h \times (\nu_{BB} - \nu_{FB}) - E$ at the resonant L_{BB} frequency. The collisional energy E is a very small correction in ultracold atom experiments.

Assignment of the quantum numbers of the detected RbSr molecular states

In the next paragraphs, we discuss the assignment of the rotational and hyperfine quantum numbers of the initial Rb-Sr atom pair state and of the detected molecular states.

As for the initial scattering state, the ^{87}Rb sample is prepared in the $f = 1$ manifold and the m_f-states affected by the photoassociation light are seen on absorption pictures using Stern-Gerlach separation. Therefore, the hyperfine contribution $|f, m_f\rangle$ of the initial state is perfectly known. The scattering cross-section is dominated by s-wave scattering, i.e. $N = 0$, in the ultracold limit. This ultracold limit is defined as $kR_e \ll 1$, where $\hbar k$ is the momentum of the collision and R_e the characteristic radius of the PEC [65]. In the case of Rb-Sr ground-state pairs we have $R_e = (\mu C_6/\hbar^2)^{1/4} \sim 70$ Å, and for our typical collisional energies $E = \hbar^2 k^2/2\mu \sim k_B \times 1.0$ μK we are working in the ultracold limit with $kR_e \sim 0.1$, as shown in Figure 2.5. However, the collisional cross-section corresponding to higher partial waves $N > 0$ is greatly enhanced in the presence of a bound state in the centrifugal barrier of the

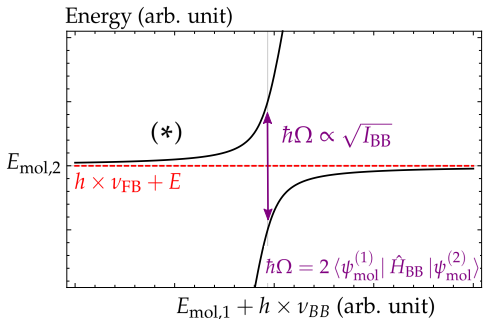

FIGURE 2.4: Avoided crossing produced by L_{BB}. At the frequency ν_{BB} at which the L_{BB} laser is resonant, an avoided crossing occurs. The excited molecular state is then "dressed" with the electronic-ground-state molecular state and one L_{BB} photon, and as a consequence the photoassociation laser L_{FB} (red dashed line) is not resonant anymore. The photoassociation-induced losses are thus canceled when the frequency ν_{BB} matches the resonance frequency. As a result, more Rb atoms are detected after Stern-Gerlach separation when L_{BB} is resonant than when it is non-resonant.

corresponding potential[39]. Such a state is present in the ^{87}Rb-^{88}Sr mixture, enhancing the p-wave scattering cross-section, which explains our ability to detect a $N = 3$ molecular state via two-colour spectroscopy — see next paragraphs.

The hyperfine contribution $|f, m_f\rangle$ of the detected molecular state is not "visible" on absorption pictures, as it is for the initial scattering state, but it can be extracted by measuring the binding energy $h \times (\nu_{BB} - \nu_{FB})$ as a function of the applied magnetic field B — see Chapter 3. At magnetic fields of a few G, the Zeeman energy associated with a single Rb atom in a given m_f state of the $f = 1$ manifold is $E_{m_f}(B) = g_f\, m_f\, \mu_B\, B$, where $\mu_B = h \times 1.3996\,\mathrm{MHz/G}$ is the Bohr magneton and $g_f \simeq -1/2$ is the $f = 1$ low-field g-factor of ^{87}Rb — see Ref. [50] and Chapter 5, Figure 5.8. The g_f-factors $g_f \simeq +1/2$ of the $f = 2$ manifold is inverted compared to $f = 1$. Accordingly, the low-field differential Zeeman shifts are respectively $h \times -0.7\,\mathrm{MHz/G}$ and $h \times +0.7\,\mathrm{MHz/G}$ between adjacent m_f-states in the $f = 1$ and $f = 2$ manifolds[40]. Thus, an ambiguity may arise: a molecular state detected by recovering losses in the $|f, m_f\rangle = |1, 0\rangle$ entrance channel and for which the measured binding energy is "moving" as $h \times +0.7$ MHz/G can be either $|1, +1\rangle$ or $|2, -1\rangle$, leading to a potential error

[39] This is referred to as a shape resonance — see Subsection 2.1.6.

[40] By differential Zeeman shift between adjacent m_f-states we mean the difference in Zeeman energy between a state of quantum number $m_f + 1$ and a state of quantum number m_f, within the same f manifold.

of $h \times 6.835$ GHz (see Figure 5.7) in the estimation of the real binding energy[41,42]. To lift this ambiguity, one has to detect the molecular state in both $f = 1$ and $f = 2$ manifolds, as we did for the rovibrational $|\nu, N\rangle = |66, 0\rangle$ bound states in the ^{87}Rb-^{87}Sr mixture and the $|\nu, N\rangle = |66, 2\rangle$ and $|\nu, N\rangle = |65, 3\rangle$ bound states in the ^{87}Rb-^{88}Sr mixture — see Table 3.2, Chapter 3.

The rotational quantum number N defines the parity $(-1)^N$ of the initial scattering state and of the detected molecular state[43]. One-photon electric dipole transitions only connect states with opposite parity, thus for the two-photon detection scheme the initial scattering state and the detected molecular state must have the same parity[44]. Therefore, we expect the change in rotational quantum number compared to the initial state to be either $\Delta N = 0, 2, 4, ...$ Note that this selection rule does not require any knowledge about the electronically excited molecular state that L_{FB} couples to the initial state. Since at our ultracold temperatures we expect the initial state to be $N = 0$, as explained above, in the early days of the ground-state spectroscopy we assumed that we couldn't detected molecular states with $N = 3$. This assumption proved wrong in the ^{87}Rb-^{88}Sr mixture, where the p-wave scattering cross-section $N = 1$ is enhanced, allowing to reach an $N = 3$ bound state with $\Delta N = 2$. This error led to the impossibility to fit a C_6 coefficient that would match the binding energies observed in all the isotopic mixtures that we investigated[45], and it took more than one year of investigation of the ^{87}Rb-^{87}Sr mixture via two-colour and Feshbach spectroscopy, and a new fit procedure, to understand and solve this discrepancy. Our message to molecular spectroscopists is thus the following. Do not overestimate your ability to attribute quantum numbers to molecular states, and do not take for granted selection rules as unexpected or even unknown phenomena — see Section 5.5 — might make you able to detect unexpected bound states.

[41] Note that the binding energy itself (defined for a molecular state of given f, m_f with respect to the atomic threshold of same f, m_f) doesn't change with the value of the magnetic field, only the two-colour detuning that we use to measure binding energies experimentally.

[42] The difference in zero-field hyperfine energy between an $f = 1$ atom pair state and an $f = 2$ molecular state is not exactly $h \times 6.835$ GHz, due to the molecular correction to the Rb hyperfine constant — see Chapter 5, Equation 5.53. However, this correction is much smaller than $h \times 6.835$ GHz, as is obvious from Figure 5.9, and the attribution of the f quantum number is thus unambiguous if both $f = 1$ and $f = 2$ molecular states are detected. The measured corrections to the atomic hyperfine energy are denoted as δE_{hf} in our paper presented in Chapter 3.

[43] The parity $\pm$ of the Hund's case (b) basis functions are $(-1)^{N+s}$ (where $+1$ and -1 indicate the parity $+$ or $-$ respectively) where $s = 0$ for Σ^+ electronic terms [57]. See Section 4.1 for a discussion on the coupling cases of ground and electronically excited RbSr.

[44] At least for electric dipole transitions. Electric quadrupole/octupole, magnetic dipole/quadrupole, ... transitions are orders of magnitude weaker and are unlikely to lead to detectable losses at our relatively low photoassociation laser intensities.

[45] More precisely: the incorrect C_6 estimated by fitting the 4 binding energies measured at the time in the ^{87}Rb-^{88}Sr and ^{87}Rb-^{84}Sr mixtures implied the presence of a bound state in the ^{87}Rb-^{87}Sr mixture, at a binding energy which we couldn't observe.

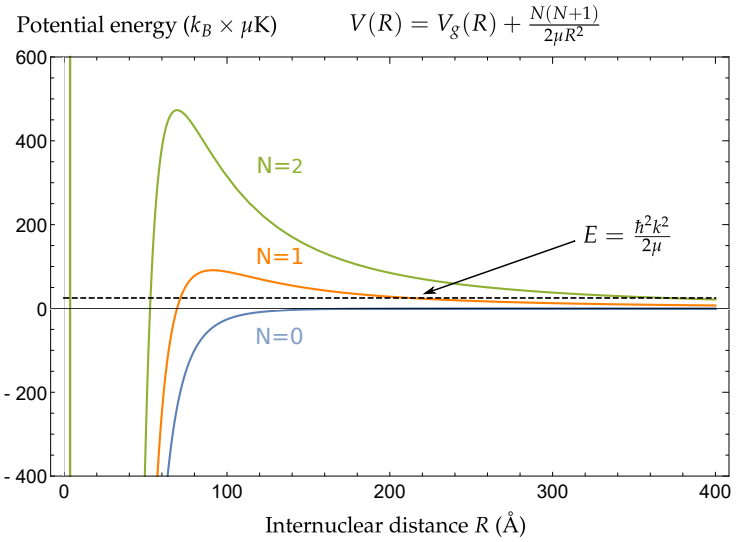

FIGURE 2.5: Potential energy experienced by a colliding ^{87}Rb-^{84}Sr atom pair with rotational quantum number N. The larger the C_6 coefficient of the PEC $V_g(R)$, the lower the height of the centrifugal $N > 0$ barriers. At our ultracold temperatures the collisional energy $E \sim k_B \times 1.0\ \mu$K is much smaller than the height of the first centrifugal barrier $N = 1$, thus the collisional cross-section is largely dominated by $N = 0$ (i.e. s-wave) scattering states. An exception arises in the ^{87}Rb-^{88}Sr mixture, for which a state bound in the $N = 1$ thermal barrier enhances the p-wave cross-section.

2.2.2 Magnetic Feshbach spectroscopy

We report in the publication presented in Chapter 6 the first observation of magnetic Feshbach resonances between alkali and closed-shell atoms (Rb and Sr respectively in our experiment). Magnetic Feshbach spectroscopy proved to be an invaluable tool in our quest of the understanding of the ground-state PEC of RbSr. Upon application of an external magnetic field B, a diatomic molecular state is brought into resonance with an atom pair scattering state: the huge increase in collisional cross-section at the crossing point between the two states leads to three-body losses that are observable experimentally. These processes are described thoroughly in Chapter 5, and the results of the Feshbach spectroscopy are discussed extensively in our publications presented in Chapter 3 and Chapter 6.

Assignment of the quantum numbers of the detected RbSr molecular states

The hyperfine contribution $|f, m_f\rangle$ of the initial scattering state is perfectly know, as in two-colour spectroscopy. The state-specific detection is obtained through Stern-Gerlach separation of the Rb atomic cloud and standard absorption imaging. The hyperfine contribution of the detected molecular state is again "invisible" on absorption pictures, and in that case has to be inferred from the Zeeman crossing diagrams shown in Chapter 6. The more resonances are measured, the less ambiguous the attribution of the molecular hyperfine quantum numbers is.

Three mechanisms that lead to Feshbach resonances in RbSr are presented in Sections 5.3, 5.4 and 5.5 respectively, and are subject to different selection rules regarding parity. Mechanism I and II couple molecular states of the same parity N, which implies that in the s-wave regime only $N = 0$ molecular states are detected through loss spectroscopy. Mechanism III, on the other hand, couples $N = 0$ scattering states to $N = 2$ molecular states only and thus only such molecular states are detected. Again, the p-wave cross-section of ^{87}Rb-^{88}Sr is enhanced. Accordingly, we should be able to detect $N = 1$ molecular states through mechanism I and II in this mixture, and $N = 1, 2$ and 3 states through the (weak) mechanism III owing to its selection rule $|N - 2| \leq N' \leq |N + 2|$. We didn't try to detect such states to this date, but will do so in the near future.

We stress again that at the start of the magnetic Feshbach spectroscopy, we didn't expect to be able to detect $N = 2$ molecular states, because we thought that only Mechanism I and II could lead to RbSr resonances. The narrow anisotropic resonances induced by Mechanism III were an experimental discovery. Therefore, at the risk of repeating ourselves: be very open-minded about the quantum numbers characterizing the molecular states you detect, because their attribution might prove non-trivial.

Chapter 3

Publication: The RbSr $^2\Sigma^+$ ground state investigated via spectroscopy of hot and ultracold molecules

Phys. Chem. Chem. Phys. **20**, 26221 (2018)

Alessio Ciamei[*a], Jacek Szczepkowski[*b], Alex Bayerle[*a], Vincent Barbé[a], Lukas Reichsöllner[a], Slava M. Tzanova[c], Chun-Chia Chen[a], Benjamin Pasquiou[a], Anna Grochola[b], Pawel Kowalczyk[d], Wlodzimierz Jastrzebski[b] and Florian Schreck[a]

Abstract

We report on spectroscopic studies of hot and ultracold RbSr molecules, and combine the results in an analysis that allows us to fit a potential energy curve (PEC) for the $X(1)^2\Sigma^+$ ground state bridging the short-to-long-range domains. The ultracold RbSr molecules are created in a μK sample of Rb and Sr atoms and probed by two-colour photoassociation spectroscopy. The data yield the long-range dispersion coefficients C_6 and C_8, along with the total number of supported bound levels. The hot RbSr molecules are created in a 1000 K gas mixture of Rb and Sr in a heat-pipe oven and probed by thermoluminescence and laser-induced fluorescence spectroscopy. We compare the hot molecule data with spectra we simulated

* Corresponding authors
[a] Van der Waals-Zeeman Institute, Institute of Physics, University of Amsterdam, Science Park 904, 1098 XH Amsterdam, The Netherlands
[b] Institute of Physics, Polish Academy of Sciences, Al. Lotnikòw 32/46, Warszawa 02-668, Poland
[c] Institut für Quantenoptik und Quanteninformation (IQOQI), Österreichische Akademie der Wissenschaften, 6020 Innsbruck, Austria
[d] Institute of Experimental Physics, Faculty of Physics, University of Warsaw, ul. Pasteura 5, 02-093 Warszawa, Poland

using previously published PECs determined by three different *ab-initio* theoretical methods. We identify several band heads corresponding to radiative decay from the $B(2)^2\Sigma^+$ state to the deepest bound levels of $X(1)^2\Sigma^+$. We determine a mass-scaled high-precision model for $X(1)^2\Sigma^+$ by fitting all data using a single fit procedure. The corresponding PEC is consistent with all data, thus spanning short-to-long internuclear distances and bridging an energy gap of about 75% of the potential well depth, still uncharted by any experiment. We benchmark previous *ab-initio* PECs against our results, and give the PEC fit parameters for both $X(1)^2\Sigma^+$ and $B(2)^2\Sigma^+$ states. As first outcomes of our analysis, we calculate the *s*-wave scattering properties for all stable isotopic combinations and corroborate the locations of Fano-Feshbach resonances between alkali Rb and closed-shell Sr atoms recently observed [66]. These results and more generally our strategy should greatly contribute to the generation of ultracold alkali – alkaline-earth dimers, whose applications range from quantum simulation to state-controlled quantum chemistry.

3.1 Introduction

Production of ultracold molecules composed of one alkali and one alkaline-earth(-like) atom is being pursued with increasing effort over the last years, boosted by the achievement of quantum degeneracy for gases of alkaline-earth atoms and atoms with similar electronic structure [67–69] These heteronuclear open-shell molecules possess a $^2\Sigma$ electronic ground state. In the rovibronic ground state, they exhibit a non-zero electronic spin angular momentum and a strong permanent electric dipole moment. These properties make them suitable for quantum simulations of magnetism and topological quantum phases mediated by the induced electric dipole-dipole interaction [32, 70–73]. Molecules with $^2\Sigma$ ground state could also be used as sensitive magnetic field sensors [74], quantum computing platforms [75], and probes of parity-violations and variation of the proton-to-electron mass ratio [76–78]. If one can produce a quantum degenerate gas of molecules, where all degrees of freedom are under control, one can study quantum chemical reactions and their dynamics at the most fundamental level, with full control over the reactants, in dependence of electromagnetic fields, and detecting reaction products [72, 73, 79–82].

In order to create molecules at ultracold temperatures and to understand quantum chemistry processes, an accurate molecular model is needed. Recently *ab-initio* calculations for alkali – alkaline-earth(-like) molecules have provided potential energy curves (PECs), permanent electric dipole moments and transition dipole moments, and a few attempts at benchmarking theories with experiments have been recorded [83–89]. The precision of *ab-initio* calculations is typically not enough to reliably predict the properties that need to be known

to form ultracold molecules, such as molecular binding energies. Theory must therefore be complemented by spectroscopy experiments.

Different spectral ranges can be explored with the help of various types of spectroscopy, three of which being relevant for the present work. Photoassociation (PA) spectroscopy of ultracold atoms provides data with precision and accuracy reaching down to the kHz level [63, 90, 91]. PA spectroscopy favours the production of weakly-bound molecules, since their wavefunction has the best overlap with the large wavefunction describing colliding atoms. Knowledge of these weakly-bound levels is sufficient to determine the long-range behaviour of the PECs [92, 93]. Thermoluminescence and laser induced fluorescence (LIF) spectroscopy in high-temperature ovens provide spectra with many optical lines at a fraction of cm^{-1} precision [83, 86, 94]. Thermoluminescence and LIF spectra are usually dominated by the radiative decay towards the most bound levels of the ground-state potential and therefore allow to determine the behaviour of the PECs in a range of internuclear distances centred around the potential equilibrium distance.

In this paper we present two independent experimental investigations of alkali – alkaline-earth RbSr molecules, two-colour PA spectroscopy of ultracold Rb - Sr mixtures, and thermoluminescence/LIF spectroscopy of hot molecules, both carried out for the first time on this system. By combining the results from both experiments in a joint analysis and exploiting three previously reported state-of-the-art *ab-initio* calculations [95, 96], we can provide a PEC for RbSr ground-state molecules representing accurately all our experimental data and smoothly bridging the gap between the two spectral ranges investigated. We also determine the molecular constants of the $X(1)^2\Sigma^+$ and $B(2)^2\Sigma^+$ states, and dispersion coefficients of the $X(1)^2\Sigma^+$ state. We use these fitted PECs to benchmark the *ab-initio* calculations, which come from three independent theoretical methods. Thanks to this analysis, we can infer the molecular spectra with sufficient accuracy to guide future experiments (e.g. STIRAP path towards rovibronic ground state [97–99]), as well as atomic properties such as scattering cross sections and magnetic Fano-Feshbach resonances.

This manuscript is structured as follows. In Section 3.2, we summarize the experimental and theoretical information currently available on molecular RbSr and we introduce the molecular potentials that we investigate. In Section 3.3, we present two-colour PA spectroscopy of three RbSr isotopologues performed on μK atomic mixtures. We use the PA spectroscopy results to fit a model from which we extract the long-range dispersion coefficients C_6 and C_8 along with the zero-energy semi-classical action. Based on this spectroscopy type alone, we calculate the *s*-wave scattering properties of all isotopic combinations of Rb and Sr, and explain the location of magnetic Fano-Feshbach resonances observed in previous work by some of the authors [66]. The Fano-Feshbach resonances are then included in the fit to provide a single comprehensive model. We corroborate this analysis by comparison

with independent cross-thermalization experiments. In Section 3.4, we present the thermoluminescence spectroscopy and LIF spectroscopy in a 1000 K heat-pipe oven. We detail the production of the molecular gas sample and its interrogation. We compare the recorded spectrum with three simulated spectra recreated starting from three *ab-initio* theory calculations. From this comparison we identify 24 band heads in the data and give the fitted Dunham coefficients, which describe the lowest vibrational energy levels of the ground and first excited $^2\Sigma^+$ states. In Section 3.5, we use the results from both types of spectroscopy to refine the three *ab-initio* ground-state potentials via a direct potential fit of an analytic function. We discuss the final results and how they compare with theory. In Section 3.6, we conclude and give an outlook.

3.2 RbSr state of the art

We first introduce the molecular structure of RbSr and the results of previous studies. RbSr has recently been the subject of theoretical works [18, 95, 96, 98, 100], two of which [95, 96] cover the spectral region that we are investigating and provide state-of-the-art PECs based on *ab-initio* calculations. In Ref. [95], Żuchowski, Guérout, and Dulieu compare two different methods. The first is a full-configuration-interaction (FCI) treatment of RbSr, represented as a molecule with 3 valence electrons subject to an effective core potential (ECP) complemented with a core polarization potential (CPP), which is referred to as FCI-ECP+CPP. The second is a spin-restricted coupled-cluster (RCC) method, applied to a 19 electron problem subject to a fully-relativistic small-core ECP with single, double and triple excitations, referred to as RCCSD(T). In Ref. [96], Pototschnig *et al.* provide PECs obtained via multiconfigurational self-consistent field calculations, involving ECP and CPP, followed by second order multireference configuration interaction, which we label MRCI in the following. For all three methods, PECs of the non-rotating molecule are calculated without or with inclusion of the fine-structure Hamiltonian, resulting in Hund case (a,b)[5] or (c) representation, respectively.

Experimental investigation of RbSr has been restricted so far to Helium-nanodroplet-assisted spectroscopy [101, 102]. In these experiments a supersonic jet of He droplets is sequentially injected into pickup cells containing Rb or Sr, which can get caught on the droplet surface and reactively collide forming a RbSr molecule. In contact with superfluid He, RbSr further relaxes to its vibronic ground state, which greatly simplifies spectroscopic studies. Extensive spectroscopy data were collected via resonance-enhanced two-photon ionization, elucidating the electronic structure of RbSr in the spectral region $11600 - 23000\,\mathrm{cm}^{-1}$, where the precision was limited by line-broadening due to the coupling of RbSr to the He droplet.

[5] Hund cases (a) and (b) are equivalent for non-rotating molecules.

Remarkably, RbSr desorbed from the droplet upon laser excitation, allowing to record fluorescence of free RbSr molecules and to extract the harmonic constant of the ground state. The experimental value was consistent with theoretical predictions, however the measurement precision was not sufficient to discriminate between the three aforementioned high-precision theoretical PECs.

The electronic states relevant to the present work are those dissociating into the two lowest atomic asymptotes $\mathrm{Rb}(5s\ ^2S) + \mathrm{Sr}(5s^2\ ^1S)$ and $\mathrm{Rb}(5p\ ^2P) + \mathrm{Sr}(5s^2\ ^1S)$, see Figure 3.1. Our thermoluminescence spectra are dominated by transitions between levels belonging to the $X(1)^2\Sigma^+$ and $B(2)^2\Sigma^+$ states. Two-colour PA spectroscopy explores the $X(1)^2\Sigma^+$ ground-state potential, by using intermediate molecular levels supported by potentials dissociating into the $\mathrm{Rb}(5s\ ^2S) + \mathrm{Sr}(5s5p\ ^3P)$ asymptote, see Figure 3.1. From our combined measurements we therefore derive quantitative information about the $X(1)^2\Sigma^+$ and $B(2)^2\Sigma^+$ states. Since for both states the projection Λ of the electronic angular momentum on the internuclear axis is zero, spin-orbit coupling vanishes and Hund case (b) is the appropriate representation for the rotating molecule [57]. The corresponding basis vectors are $|\Lambda, N, S, J\rangle$, where N is the momentum given by the coupling between the corresponding angular momentum vector of Λ and the nuclear orbital momentum, S is the electron spin and J is the total electronic angular momentum. Moreover, both the atomic and molecular levels are described by the total angular momentum of the Rb atom [66], labelled F for the molecule and f^{Rb} for the atom.

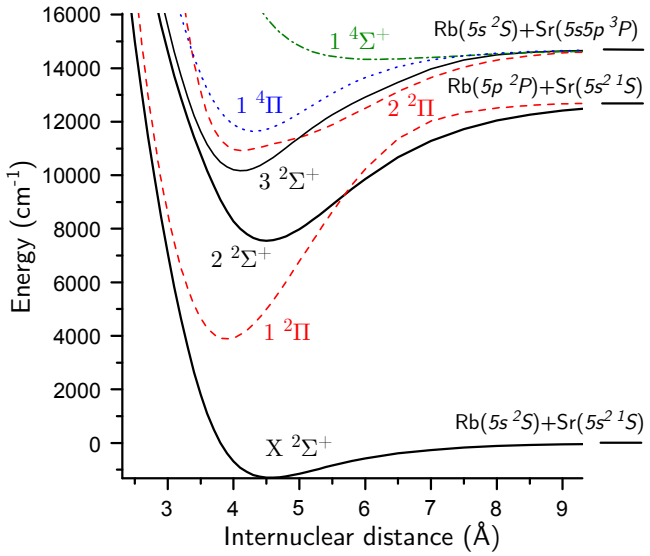

FIGURE 3.1: The potential energy curves calculated using the MRCI method [60] for all states correlating to the Rb($5s$ ^2S) + Sr($5s^2$ ^1S), Rb($5p$ ^2P) + Sr($5s^2$ ^1S) and Rb($5s$ ^2S) + Sr($5s5p$ ^3P) asymptotes. The solid black lines denote $^2\Sigma^+$ states, the dashed red lines $^2\Pi$ states, the dotted blue line a $^4\Pi$ state and the dash-dotted green line a $^4\Sigma^+$ state.

3.3 PA spectroscopy of weakly-bound levels

In this section, we study the bound levels supported by the $X(1)^2\Sigma^+$ RbSr ground-state potential close to the dissociation threshold using μK atomic clouds. We first describe the two-colour photoassociation spectroscopy we use to observe and characterize weakly-bound RbSr molecular levels. We then present the characteristics of the atomic mixture samples studied here. We give the spectroscopy results and discuss their uncertainties. We detail our data analysis and discuss the physical quantities that can readily be extracted from this type of data, such as the zero-energy semi-classical action and the van der Waals dispersion coefficients, which determine the spectrum of weakly-bound levels and the atomic scattering properties. We use our findings to confirm the identification and position of recently observed Fano-Feshbach resonances [66], and include these data into our analysis. Finally, we corroborate the overall analysis by comparing the s-wave scattering lengths inferred by our model with the results of cross-thermalization measurements.

3.3.1 Overview of two-colour photoassociation spectroscopy

We carry out two-colour PA spectroscopy to observe weakly-bound $X(1)^2\Sigma^+$ levels and measure their energies referenced to the energy of the atomic scattering state $\mathrm{Rb}(^2S_{1/2}, f^{\mathrm{Rb}} = 1)$+$\mathrm{Sr}(^1S_0)$. Two-colour PA spectroscopy exploits the presence of an optically-excited molecular level e, which is coupled to an atom-pair state a by the free-bound laser L_{FB} with frequency f_{FB}. When this laser is resonant with the a to e transition, pairs of colliding atoms a are transferred to e, from where they spontaneously decay to low-lying molecular levels, resulting in atom loss.[6] If an additional bound-bound laser L_{BB} with frequency f_{BB} is tuned on resonance with a molecular transition between e and a weakly-bound molecular level m of the $X(1)^2\Sigma^+$ ground state, a significant light shift pushes e out of resonance with L_{FB}. The loss induced by L_{FB} is then suppressed, resulting in an atom number peak when varying the frequency of L_{BB}, see the example in Figure 3.2. The energy E of the molecular level m referenced to the energy of the atom pair a is directly given at this peak by $E = h \times (f_{\mathrm{BB}} - f_{\mathrm{FB}})$, where h is the Planck constant. In the limit of low temperature and small external fields, the molecular binding energy E_b is equal to E for levels with $F = 1$, and $E_b = E + E_{\mathrm{hf}}$ for levels with $F = 2$, where E_{hf} is the Rb hyperfine splitting.

In order to detect weakly-bound levels up to the least bound ones, we exploit similarly weakly-bound levels supported by the electronically excited potentials correlating to the $\mathrm{Rb}(5s\ ^2S_{1/2}) + \mathrm{Sr}(5s5p\ ^3P_1)$ asymptote [51, 95], see Figure 3.1. These levels provide sufficient Franck-Condon factors between e and m, while the narrow linewidth of the nearby Sr

[6] We confirm that such loss originates from the formation of RbSr molecules and not Rb_2 or Sr_2 molecules, by verifying that the loss only occurs if both elements are present.

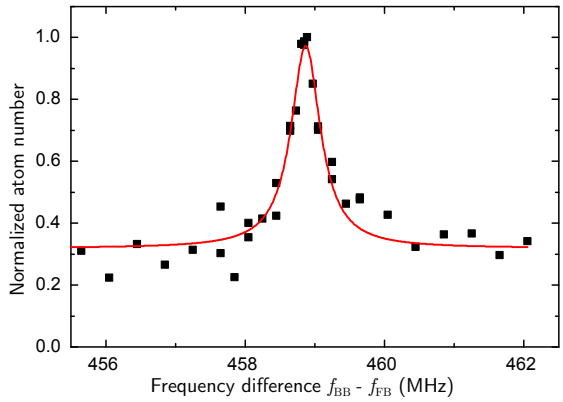

FIGURE 3.2: Typical two-colour photoassociation spectroscopy signal. The plot shows the number of Rb atoms in the $f^{Rb} = 1$, $m_f^{Rb} = 1$ level normalized to the atom number in the other two $f^{Rb} = 1$, m_f^{Rb} levels, as function of the frequency difference between L_{BB} and L_{FB}, recorded during a scan of the L_{BB} frequency, while L_{FB} is on resonance with an a to e transition. This signal corresponds to the $\{v = 66, N = 0, F = 1\}$ level of the ^{87}Rb-^{88}Sr ground-state potential, see Table 3.2.

intercombination transition results only in small losses and heating by off-resonant scattering of photons on Sr atoms.

3.3.2 Sample conditions and spectroscopy setup

We prepare the desired ultracold mixtures of Rb - Sr isotopes as in our previous works [52, 66, 103]. We keep the mixture in a crossed-beam dipole trap formed by one 1064-nm horizontal elliptical beam with a vertical waist of 19(1) μm and a horizontal waist of 313(16) μm, and one 1064-nm (or 1070-nm) vertical beam with a waist of 78(2) μm (or 90(5) μm). When studying ^{87}Sr, we add a 532-nm horizontal beam with vertical (horizontal) waist of 19(1) μm (219(4) μm) to increase the trap depth, in order to capture more Sr atoms. We prepare ^{87}Rb in its hyperfine ground level ($^2S_{1/2}$, $f^{Rb} = 1$) with almost equal population of the Zeeman sublevels $m_f^{Rb} = 0, \pm 1$. During PA spectroscopy, we measure each m_f^{Rb} population separately via time-of-flight expansion in a Stern-Gerlach magnetic field gradient. Bosonic Sr isotopes ^{84}Sr and ^{88}Sr have zero nuclear magnetic moment leading to a structureless $^1S_0$ ground state. Fermionic ^{87}Sr has a non-zero nuclear magnetic moment of $i^{Sr} = 9/2$ and is prepared in the stretched level $m_i^{Sr} = 9/2$ or $m_i^{Sr} = -9/2$ via optical pumping.

The atomic samples used to study ^{87}Rb^{84}Sr and ^{87}Rb^{88}Sr molecules have a temperature of 1.0(1) μK, average densities of $0.3 - 4 \times 10^{12}\,\mathrm{cm}^{-3}$ for Sr and $2 - 7 \times 10^{12}\,\mathrm{cm}^{-3}$ for Rb (summing over all m_f^{Rb} levels), and the trap frequencies are $\{\omega_x, \omega_y, \omega_z\} = 2\pi \times$

$\{66(6), 57(6), 560(50)\}$ Hz for Sr and $2\pi \times \{110(10), 95(9), 950(80)\}$ Hz for Rb,[78] where the z-axis is vertical. The samples used to study the fermionic ^{87}Rb^{87}Sr molecules have a temperature of $1.5(1)\,\mu$K, average densities in the range $2 - 6 \times 10^{11}\,\mathrm{cm}^{-3}$ for Sr and $0.8 - 3 \times 10^{12}\,\mathrm{cm}^{-3}$ for Rb, and trapping frequencies in the range $\{\omega_x, \omega_y, \omega_z\} = 2\pi \times \{70 - 80, 55 - 70, 590 - 640\}$ Hz for Sr and $2\pi \times \{110 - 130, 95 - 125, 820 - 930\}$ Hz for Rb.

The PA beam, containing both L_{FB} and L_{BB}, propagates horizontally at a $\sim 30^\circ$ angle from the axis of the horizontal dipole trap and has a waist of either $60(1)\,\mu$m or $110(10)\,\mu$m, depending on the transition strength and the available laser power. L_{FB} and L_{BB} are derived from the same master oscillator, either via injection-lock or beat-lock, which ensures good coherence between them (typically below 100 Hz for injection-locked and ~ 30 kHz for beat-locked lasers). We apply a homogeneous magnetic field in the range of 0 to 20 G. We vary the polarization and frequency of $L_{\mathrm{FB,BB}}$ as required to optimally detect a specific molecular level. We adjust the pulse time and power of L_{FB} in order to induce 70 to 90 % loss of Sr atoms. The L_{BB} intensity is chosen such as to obtain a good signal-to-noise ratio for the two-colour PA signal, while not being limited by off-resonant scattering of photons on Sr atoms.

3.3.3 Experimental results

We have observed a total of 10 molecular levels via two-colour PA spectroscopy, of which we report the energies E in Table 3.1. We also report the one-colour PA lines used, the type of transition induced, the angular momentum projections involved and the bound-bound Rabi frequency, if characterized. Levels with negative values of E are necessarily levels with $F = 2$. The typical error of E_b is significantly larger than the uncertainty of $h \times (f_{\mathrm{BB}} - f_{\mathrm{FB}})$, and is the result of several sources of uncertainty.

The first significant error contribution comes from the differential Zeeman shift between the atom-pair level a and the molecular level m. In order to minimize this contribution, we exploit the fact that, in the case of equal spin quantum numbers $F = f^{\mathrm{Rb}}$ and $m_F = m_f^{\mathrm{Rb}}$, this shift is vanishingly small for weak binding energy of the molecular level m, see the example of Figure 3.3. We thus drive two-colour transitions between the atom pair in $f^{\mathrm{Rb}} = 1$ and molecular levels with $F = 1$ and $m_F = m_f^{\mathrm{Rb}}$. For the example of Figure 3.3 with $m_F = m_f^{\mathrm{Rb}}$, we derive a small differential magnetic moment of $-2.0(2.0)$ kHz/G. Such shift extrapolated to all measured points results in a maximum systematic shift in the range $0.2 - 20.0$ kHz. For

[7] The error bars on the trap frequencies are dominated by the uncertainty on the waists previously stated.

[8] The sample used to detect the ^{87}Rb^{88}Sr level at a binding energy of $h \times 459$ MHz has a temperature of $1.5(1)\,\mu$K, average densities $6.4(2.2) \times 10^{12}\,\mathrm{cm}^{-3}$ for Sr and $8.4(3.0) \times 10^{11}\,\mathrm{cm}^{-3}$ for Rb, and trapping frequencies $\{\omega_x, \omega_y, \omega_z\} = 2\pi \times \{57(7), 8(1), 930(100)\}$ Hz for Sr and $2\pi \times \{97(10), 14(2), 1600(200)\}$ Hz for Rb.

TABLE 3.1: Results of two-colour PA spectroscopy. The energy E is given by the two-colour frequency detuning $E/h = \nu_{L_{\mathrm{BB}}} - \nu_{L_{\mathrm{FB}}}$ at $B = 0\,\mathrm{G}$. Δ is the detuning of L_{FB} from the Sr $^1\mathrm{S}_0 - ^3\mathrm{P}_1$ transition for bosonic molecules and from the Sr $(^1\mathrm{S}_0, f^{\mathrm{Sr}} = 9/2) - (^3\mathrm{P}_1, f^{\mathrm{Sr}} = 11/2)$ transition for ^{87}Rb^{87}Sr molecules. The column labelled "Transition" shows the type of transition addressed by both L_{FB} and L_{BB}. The labels m_f^{at} and m_F^{mol} are the projections of the total angular momentum on the quantization axis, neglecting nuclear rotation and the nuclear spin of ^{87}Sr, for the atomic and molecular levels, respectively. For some excited levels $m_F^{mol,e}$ is not known. Such levels are all high-field seeking. The last column gives the bound-bound Rabi frequencies, if measured, between molecular levels m and e in the electronic ground and excited states

Isotopologue	E/h (MHz)	Δ (MHz)	Transition	m_f^{at}, $m_F^{mol,e}$, $m_F^{mol,m}$	$\Omega/2\pi$ (kHz/$\sqrt{\mathrm{mW/cm^2}}$)
^{87}Rb^{84}Sr	29.01(3)	173.5(2), 427.8(2)	π	0, 0, 0	-, 16(1)
	744.53(3)	173.5(2), 427.8(2)	π	0, 0, 0	6.7(3), 285(10)
^{87}Rb^{87}Sr	199.97(17)	686.79(23)	σ^-	-1,-,-1	6.0(5)
	287.27(18)	686.79(23)	σ^-	-1, -, -1	22.2(2.0)
	1950.24(11)	686.79(23)	σ^-	-1, -, -1	-
^{87}Rb^{88}Sr	$-6476.80(4)$	41.39(60)	$\sigma^\pm$	0, -, 0	0.31(6)
	$-4677.78(15)$	260.54(5)	$\sigma^\pm$	0, 0, 0	-
	356.99(3)	41.39(60)	π	0, -, 0	3.39(25)
	458.90(22)	53.5(4)	π	1, -, 1	3.1(1.3)
	2153.83(15)	260.54(5)	π	0, 0, 0	0.59(13)

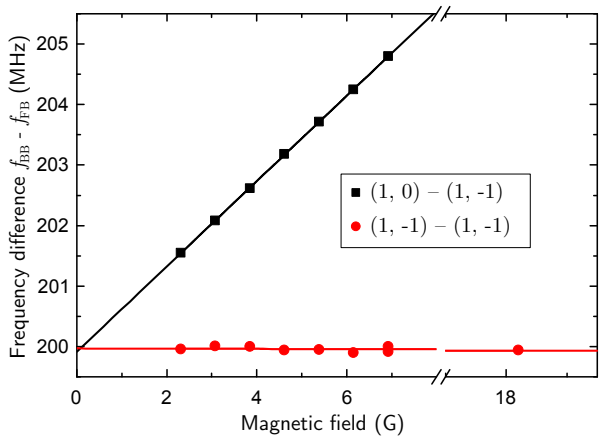

FIGURE 3.3: Molecular level energy $E = h \times (f_{BB} - f_{FB})$ as function of the magnetic field. The $(F, m_F) - (f^{Rb}, m_f^{Rb})$ transitions $(1,0) - (1,-1)$ (black squares) and $(1,-1) - (1,-1)$ (red disks) are shown together with linear fits. The error bars of the measurements are smaller than the symbol sizes.

molecular levels with $F = 2$, we drive magnetically insensitive two-colour transitions with $m_F = m_f^{Rb} = 0$. This results in a systematic shift of at the most 10 Hz for the measured points.

The second error contribution is the light shift on the two-colour transition arising from the spectroscopy lasers themselves. We have characterized it for some of the points and estimated it for the others as explained in our previous work [48]. This amounts to shifts up to 100 kHz for the typical laser powers used here.

The third error contribution is the light shift on the two-colour transition arising from the dipole trap. Similarly to the previous error contribution, it is characterized for some of the points, and estimated for the others. Given the trap used here, only the differential polarizability between atoms and molecules affecting the centre-of-mass Hamiltonian is relevant. For Sr_2 we have shown that the relative variation of the polarizability is smaller than 1 % [48]. Here we use the conservative value of 5 % to estimate the errors if not characterized.

The last error contribution comes from thermal shifts and is typically negligible, since a temperature around 1 μK corresponds to an energy of about $h \times 20$ kHz.

3.3.4 Data analysis

Line attribution and estimation of physical quantities.

The first step in a quantitative analysis of the weakly-bound spectrum probed by two-colour photoassociation is a line attribution, by which we mean the assignment of quantum numbers to both atomic and molecular levels used in the measurements of E. In particular, the angular momenta F and N of molecular levels are not known, and their proper assignment is crucial to the success of any model-fitting attempt. The angular momenta of atomic levels are partially known: we measure the Rb atomic spin angular momentum $f^{\mathrm{Rb}} = 1$ and its projection m_f, and for ^{87}Sr we measure the nuclear momentum projection m_i^{Sr}. However, despite the low temperature of the sample, the atom-pair orbital momentum is not known, but will be zero for the majority of cases. The possible molecular angular momenta can be restricted by considering the atomic angular momenta and the changes of angular momentum allowed by two-colour PA. All possible assignments of quantum numbers must then be tested by the fit in order to find the best one.

Attributing quantum numbers to molecular levels is not trivial, especially in cases of sparse spectral data like the present one. In the spectral region considered here, i.e. for $E_b << D_e$ with D_e the molecular potential depth, only universal, model-independent properties are invoked in order to attribute quantum numbers. These properties are:

1. the asymptotic behaviour of the interaction potential V_g as $V_g(r) \rightarrow -C_6/r^6$ at large internuclear distance $r \gg R_L$, where R_L is the LeRoy radius;

2. the presence of a strong repulsive wall at the inner classical turning point, i.e. $|\frac{dV_g}{dr}(R_1)| \gg |\frac{dV_g}{dr}(R_2)|$, where R_1 and R_2 are the inner and outer classical turning points for vibrational motion;

3. mass-scalability under the Born-Oppenheimer approximation, due to the presence of a single electronic state.

Property 1 implies that the semi-classical phase accumulation of the zero-energy scattering wavefunction $\Phi^0_{WKB} = \Phi_{WKB}(E_b = 0)$ is well defined. Moreover, because of both property 2 and the condition $E_b << D_e$, Φ_{WKB} is to a large extent model-independent [104]. Property 3 implies that a single-channel Hamiltonian, containing $V_g(r)$, explains all spectral data for different isotopologues via simple mass-scaling. Based on these considerations, a single well-defined value Φ^0_{WKB} referenced to an isotopologue of choice is sufficient to describe our system. In this work we choose the isotopologue with highest abundance ^{85}Rb^{88}Sr as our reference. As a consequence of these properties, we expect that two physical quantities Φ^0_{WKB} and C_6 can be extracted from our data by fitting our complete dataset and assigning

the quantum numbers consistently. We employ a simple semi-classical approach to find the correct attribution of quantum numbers F and N [105].

We use this fitting strategy on the two-colour photoassociation spectroscopy data presented in Table 3.2 (labelled as "PA" in the "Method" column). Only a single attribution of quantum numbers delivers a satisfactory fit, which we report in Table 3.2 in columns F and N. This simple fitting strategy is thus sufficient to provide an unambiguous attribution for these two quantum numbers, while the attribution of ν still presents some uncertainty. As expected, the vast majority of observed molecular levels are either $N = 0$ or $N = 2$. Even so, let us note the presence of two $N = 3$ levels for ^{87}Rb^{88}Sr, which might seem inconsistent with our ultracold sample temperature. However, due to the presence of a virtual near-threshold level in this isotopologue, the amplitude of the p-wave scattering wavefunction at the one-colour PA Condon point is less than a factor of 3 smaller than that of typical s-wave scattering states. The fit also provides a first estimation for Φ^0_{WKB} and C_6. We extract the zero-energy semi-classical action $\Phi^0_{WKB} = 67.42(1)$, which gives 67 bound levels for ^{87}Rb^{84}Sr and ^{87}Rb^{87}Sr, and 68 bound levels for ^{87}Rb^{88}Sr, and we extract the dispersion coefficient $C_6 = 1.78(2) \times 10^7$ Å^6 cm^{-1}. Both quantities are determined with better accuracy and precision in the following sections.

Extraction of physical quantities.

Based on the unambiguous quantum number attribution of F and N explained in the previous section, we check the consistency of our data with the universal long-range dispersion and extract the relevant physical quantities from a fit of a second model. We assess consistency with our data using the reduced chi-square as figure of merit:

$$\tilde{\chi}^2 = \frac{1}{\mathrm{DOF}} \times \sum_i \left(\frac{E^{exp}_{b,i} - E^{th}_{b,i}}{\Delta E^{exp}_{b,i}} \right)^2 , \tag{3.1}$$

where DOF is the number of degrees of freedom in the fit,[9] i runs over the experimentally observed levels, $E^{exp}_{b,i}$ is the i^{th} measured binding energy (BE), $E^{th}_{b,i}$ is the i^{th} predicted BE and $\Delta E^{exp}_{b,i}$ is the experimental error of $E^{exp}_{b,i}$. We consider $\tilde{\chi}^2$ to be good if close to unity, i.e. $\tilde{\chi}^2 \simeq 1$. Since probability levels can only be associated to confidence intervals if the experimental error distribution is known, we only state confidence intervals based on a given absolute variation of $\tilde{\chi}^2$, without quantitative knowledge of the associated probability level.

We fit a single-channel Hamiltonian model to our experimental data [105] in order to retrieve the relevant physical information, i.e. the zero-energy semi-classical action and dispersion coefficients. This means we require consistency between BEs measured via two-colour

[9] The DOF are defined as the number of experimental data points minus the number of fit parameters.

TABLE 3.2: List of observed molecular levels, with the experimentally determined binding energies E_b and corresponding errors approximated by the theoretically estimated shift from the variation of the hyperfine splitting δE_{hf}. The values E_b^{th} represent the binding energies given by the best fit in Section 3.3.4. The quantum numbers $\{\nu, N, F\}$ identifying each level are also shown. The vibrational quantum number ν is counted starting from the lowest level, which has $\nu = 0$. The "Method" column specifies whether the levels are determined by two-colour photoassociation (PA) or Fano-Feshbach (FFR) spectroscopy, or both

Isotopologue	E_b/h (MHz)	$\delta E_{\mathrm{hf}}/h$ (MHz)	E_b^{th}/h (MHz)	ν	N	F	Method
^{87}Rb^{84}Sr	29.01(3)	0.094	28.93	66	0	1	PA
	744.53(3)	0.82	745.27	65	0	1	PA
^{87}Rb^{87}Sr	199.97(17)	0.34	199.90	66	2	1	PA,FFR
	287.27(18)[a]	0.44	287.30	66	0	1	PA,FFR
	288.2(4)[a]	0.44	287.30	66	0	2	FFR
	1950.24(11)	1.56	1953.00	65	0	1	PA
	5991.8(1.4)	3.30	5991.64	64	2	2	FFR
	6233.8(1.0)	3.39	6232.14	64	0	2	FFR
^{87}Rb^{88}Sr	356.99(3)[a,b]	0.50	357.21	66	2	1	PA
	357.87(4)[a,b]	0.50	357.21	66	2	2	PA
	458.90(22)	0.59	459.12	66	0	1	PA
	2153.83(15)[a,b]	1.67	2158.40	65	3	1	PA
	2156.91(15)[a,b]	1.67	2158.40	65	3	2	PA
	7401.01(66)	3.80	7397.47	64	0	2	FFR

[a] For the fit, we use the mean value of each pair.
[b] We use the measured energies of these pairs to estimate δE_{hf}.

PA spectroscopy and the bound spectrum supported by the Hamiltonian

$$\widetilde{H} = \widetilde{T} + \widetilde{V}_{int} + \widetilde{V}_{rot} = -\frac{\hbar^2}{2\mu}\frac{d^2}{dr^2} + V_g(r) + \frac{\hbar^2}{2\mu}\frac{N(N+1)}{r^2}, \tag{3.2}$$

where $\widetilde{T}$ is the kinetic energy operator, μ is the reduced mass, $\widetilde{V}_{rot}$ is the rotational energy operator and $\widetilde{V}_{int}$ is the interaction operator corresponding for the ground state to V_g, which obeys the properties enumerated in Sec. 3.3.4. For simplicity, we here use the generalized Lennard-Jones model for V_g:

$$V_{LJ}(r) = \frac{C_6}{r^6} \times \left(\left(\frac{\sigma}{r}\right)^6 - 1\right) - \sum_{n\geq 2}^{N_{vdW}} \frac{C_{2(2+n)}}{r^{2(2+n)}}, \tag{3.3}$$

which contains the leading order dispersion coefficients $C_6, C_8, ..., C_{2(2+N_{vdW})}$. The maximum order N_{vdW} used in the long-range asymptotic expansion is chosen as the lowest number that is able to provide a good fit of our data by the weakly-bound spectrum supported by V_{LJ}. The parameter σ is used to tune the short-range phase accumulation.

Due to the presence of a single electronic ground state in RbSr, the simple single-channel model (3.2) with the potential of Equation 3.3 is sufficient to provide a unique attribution of the quantum numbers F, N and ν for our experimental data. However, it is in general not sufficient to fit high-resolution spectra to experimental accuracy. This is mostly due to the fact that the two $^2\Sigma^+$ PECs of $F = 1$ and $F = 2$ character are not exactly parallel [25]. At large internuclear separation r the splitting $E_{\rm hf}(r)$ between these PECs is the Rb atom hyperfine splitting, whereas it is reduced by about 10 % at the bottom of the PECs. This effect is due to the reduction of the electronic density at the Rb nucleus because of the bonding with Sr. Although extremely small, it is responsible for the strongest Fano-Feshbach resonances recently observed in RbSr [66]. In the present work, our precision and accuracy are enough to reveal hints for this effect, appearing as significant differences in the BEs of levels with the same ν and N quantum numbers but different F, see the pairs of BEs of ^{87}Rb^{88}Sr $\{\nu = 66, N = 2\}$ and $\{\nu = 65, N = 3\}$ in Table 3.2. However, our data are not sufficient to extract this shift reliably and include it in our model.[10] We therefore keep a single-channel model and take this effect into account as a systematic error contribution to $\Delta E_{b,i}$. This contribution is estimated using the aforementioned differences in BEs and knowing that the change in hyperfine splitting scales as $\delta E_{\rm hf} \propto E_b^{2/3}$ close to the dissociation threshold [26]. These estimated shifts $\delta E_{{\rm hf},i}$, which dominate the errors $\Delta E_{b,i}$, are of the same order of magnitude as the shift predictions from *ab-initio* results [25], and are listed in Table 3.2. When

[10] The two observed shifts mentioned involve rotationally excited molecular levels with unknown spin-rotation coupling, hence they do not directly yield the shift under discussion. The simplest experiment able to characterize this shift requires the measurement of pairs of rotationless levels at different BEs.

BEs of both hyperfine states are measured, the mean binding energy is used in the fit, see Table 3.2. The quality of this estimation is assessed a posteriori via the $\tilde{\chi}^2$ of the best fit, labelled $\tilde{\chi}^2_{\text{min}}$.

We fit the model Hamiltonian (3.2) to our PA spectroscopy data, using the parameters $\{\sigma, C_6, ..., C_{2(2+N_{vdW})}\}$ as independent fit parameters and we retrieve the zero-energy semi-classical action $\Phi^0_{WKB} = \Phi^0_{WKB}(\sigma, C_6, ..., , C_{2(2+N_{vdW})})$. For $N_{vdW} = 1$, 2, and 3 we obtain for the best fits $\tilde{\chi}^2_{\text{min}} = 41$, 0.24 and 0.32 respectively. This shows that the inclusion of C_6 and C_8 terms is *necessary* and *sufficient* to model our data. We obtain the best fit parameters $\sigma = 5.012941656601387\,\text{Å}$, $C_6 = 1.784438900566861 \times 10^7\,\text{Å}^6\,\text{cm}^{-1}$, $C_8 = 6.18126306008073 \times 10^8\,\text{Å}^8\,\text{cm}^{-1}$ with DOF $= 5$. The fit returns the physical quantities $C_6 = 1.784(15) \times 10^7\,\text{Å}^6\,\text{cm}^{-1}$, $C_8 = 6.2(1.1) \times 10^8\,\text{Å}^8\,\text{cm}^{-1}$, and a corresponding $\Phi^0_{WKB} = 67.4379(12)$.[11] The errors stated in brackets correspond to, somewhat arbitrarily, the joint confidence region with $\Delta\tilde{\chi}^2 = \tilde{\chi}^2 - \tilde{\chi}^2_{\text{min}} = 1$. In Figure 3.4 we show the configurations sampled by the fitting procedure that provide the evaluation of the confidence regions. The dispersion coefficients are consistent with theoretical predictions [25, 106–108].

Atomic scattering properties at a given collisional energy and in the absence of external magnetic fields can be directly derived from the fitted PEC [105]. Scattering wavefunctions are obtained by integration of the nuclear Schrödinger equation for the appropriate angular momentum N, i.e. $\widetilde{H}(N)\psi_N(r) = E_{coll}\psi_N(r)$, where $\widetilde{H}(N)$ is the fitted Hamiltonian (3.2) with explicit N-dependence and $E_{coll} = \hbar^2k^2/2\mu$ is the collisional energy with wavevector k. Of particular interest for the cold atoms community are the scattering properties in the limit $E_{coll} \to 0$, which are dominated by s-wave scattering, i.e. $N = 0$. In this limit the scattering phase shift $\delta\phi \to -ka_s$ and the cross-section $\sigma_s \to 4\pi a_s^2$ are determined by a single parameter, the s-wave scattering length a_s, which we report in Table 3.3 for all stable isotopologues of RbSr.[12]. In Figure 3.5 we show the s-wave scattering wavefunctions $\psi_0(r)$ for a collision energy $E_{coll} = k_B \times 1.0\,\mu\text{K}$, with k_B the Boltzmann constant, where the effect of the scattering length on both the asymptotic phase shift and the short-range scattering amplitude is evident. The s-wave scattering lengths derived from the fitted model for ^{87}Rb^{84}Sr and ^{87}Rb^{88}Sr are in good agreement with those extracted from the cross-thermalization measurements presented in Subsection. 3.3.5, which corroborates the overall analysis carried out to this point.

[11] The number of vibrational levels is determined without uncertainty. All isotopologues have 67 vibrational levels, except for the two with the highest mass ^{87}Rb^{88}Sr and ^{87}Rb^{87}Sr, which have 68.

[12] The s-wave scattering length a_s is calculated by fitting ψ_0 at large r with the known asymptotic behaviour $\psi_0(r) \to \alpha r + \beta$, where α and β are fit parameters. a_s is then given by $a_s = -\beta/\alpha$ [109].

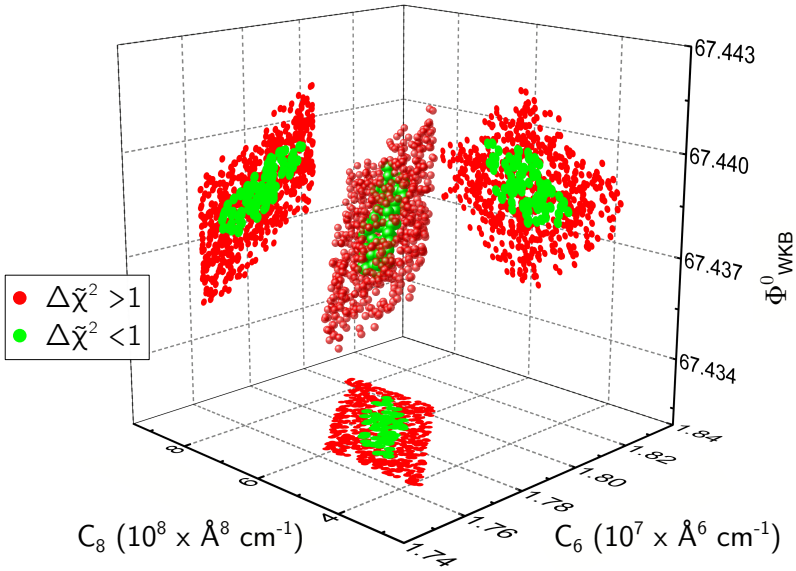

FIGURE 3.4: Confidence intervals. The plot shows $\tilde{\chi}^2$ for configurations sampled close to the best fit configuration in the fit-parameter space, with its projections on the 2D coordinate planes. The total confidence regions corresponding to $\Delta\tilde{\chi}^2 < 1$, used for error estimates, are indicated as green balls in the centre.

Validation and inclusion of Fano-Feshbach spectroscopy.

The model described in the previous section is also *sufficient* to infer within a few Gauss the resonant magnetic field of the magnetically-tunable Fano-Feshbach resonances (FFRs) present in RbSr. Let us note that we can only derive FFR locations from the fitted PEC with experimental accuracy thanks to the extreme simplicity of the $^2\Sigma^+$ ground state of RbSr [105, 110]. The existence and observability of this novel type of FFRs was theoretically predicted a few years ago [25] and recently experimentally observed by some of the authors [66].

The best fit V_{LJ} in the previous section (see Equation 3.3) predicts the location of FFRs for fermionic ^{87}Rb^{87}Sr within 10 G and has been used to infer with the same accuracy the

TABLE 3.3: Inter-species s-wave scattering lengths in units of the Bohr radius

	^{84}Sr	^{86}Sr	^{87}Sr	^{88}Sr
^{85}Rb	689(20)	90.6(2)	44.3(3)	−35.8(1.0)
^{87}Rb	92.7(2)	−43.0(1.1)	1421(98)	170.3(6)

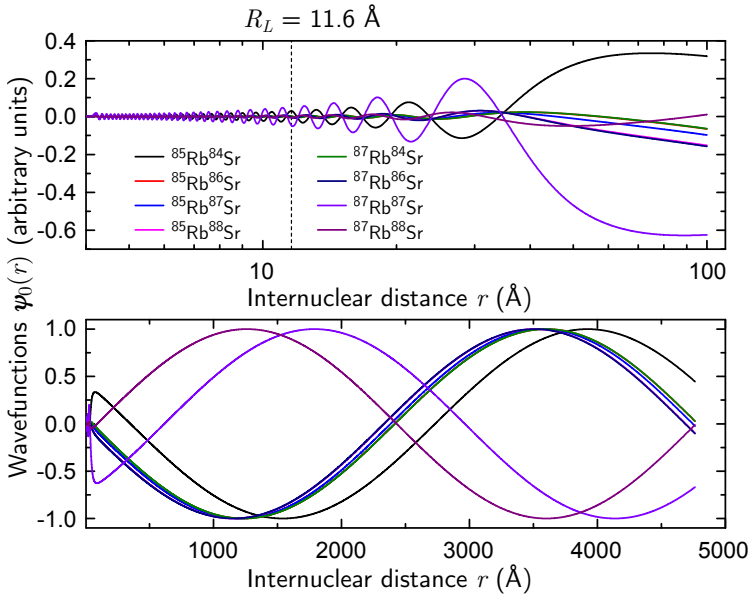

FIGURE 3.5: Atom-pair scattering wavefunctions. The top panel shows the scattering wavefunctions as function of the internuclear distance for all Rb - Sr isotopes in the range of typical PA Condon points, which are only meaningful for $r > R_L$. The bottom panel shows the scattering wavefunctions at large distance where the phase shift encodes the short-range physics. We note that two pairs of isotopes have incidentally almost the same reduced mass, hence almost overlapping wavefunctions.

location of one ^{87}Rb^{88}Sr FFR arising from the level $\{\nu = 64, N = 0, F = 2\}$, subsequently observed in an ultracold Rb-Sr mixture [66]. The BEs and corresponding quantum numbers of the bound levels inducing the observed FFRs derived with our model are reported in Table 3.2, and marked with "FFR" in the "Method" column. As a complementary check, we apply the fitting procedure to the data set including both PA and FFRs, which results in the *same unique* solution. As in the case of two-colour PA spectroscopy data alone, inclusion of C_6 and C_8 is *necessary* and *sufficient* to model the complete data set. The best fit parameters are $\sigma = 5.02477864619132$ Å, $C_6 = 1.776513404206001 \times 10^7$ Å^6 cm^{-1}, $C_8 = 6.262096495696839 \times 10^8$ Å^8 cm^{-1}, with DOF $= 8$ and $\widetilde{\chi}^2_{\text{min}} = 1.29$. The fit returns the physical quantities $C_6 = 1.777(18) \times 10^7$ Å^6\$,cm^{-1} $C_8 = 6.3(1.3) \times 10^8$ Å^8 cm^{-1}, and a corresponding $\Phi^0_{WKB} = 67.4370(13)$. There is a significant increase in our figure of merit compared to Sec. 3.3.4, which we attribute primarily to the inclusion of deeper $F = 2$ levels with rather large δE_{hf}, and secondarily to the change in DOF. The inferred s-wave scattering lengths are consistent with those presented in Table 3.5.

The ability to predict FFRs with high accuracy is extremely valuable for mixtures with one open-shell and one closed-shell atom, due to the low density of resonances in these systems, in particular in the case of zero nuclear magnetic moment for the closed-shell atom, as in bosonic RbSr isotopologues [25, 26, 111]. As an example of the outcomes of our model, Figure 3.6 shows the energy of the atomic scattering levels and molecular levels of ^{87}Rb^{84}Sr in dependence of magnetic field, and the locations of the predicted FFRs. Due to favourable scattering properties, this isotopic combination is a very good candidate for magneto-association [52].

3.3.5 An independent check of quantum number assignment: inter-species thermalization

An improper quantum number attribution strongly affects the *accuracy* of the inferred scattering lengths. We therefore experimentally characterize the thermalization of Rb atoms with a Sr cloud to measure the Rb - Sr inter-species s-wave scattering lengths, and thus confirm our quantum number attribution. The values of scattering lengths obtained by thermalization experiments suffer from low *precision*, however they constitute a useful cross-check, as they rely on simple collisional physics and are independent from our PA and Fano-Feshbach spectroscopy experiments. We present thermalization experiments done with ^{87}Rb-^{84}Sr and ^{87}Rb-^{88}Sr. Trapped ultracold mixtures of ^{87}Rb-^{87}Sr show significantly stronger 3-body losses, which limit the reliability of the data analysis for this particular mixture.

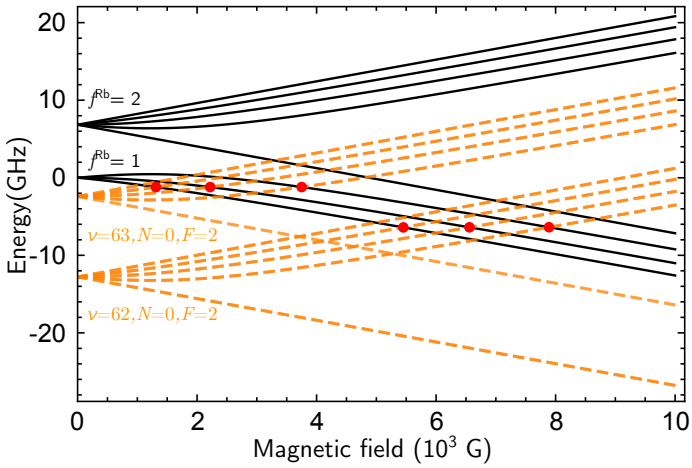

FIGURE 3.6: Zeeman sub-levels of ^{87}Rb^{84}Sr. The plot shows the energy of $f^{\mathrm{Rb}} = 1, 2$ atomic levels (black solid lines) and of $F = 2$ molecular levels (orange dashed lines, see also Table 3.7) in dependence of magnetic field. The red dots mark the location of FFRs in this magnetic field range.

Experimental setup and sample conditions.

The starting point of the thermalization measurement is an ultracold mixture composed of ^{87}Rb and either ^{84}Sr or ^{88}Sr, prepared as for spectroscopy experiments, with the addition of evaporative cooling by lowering the dipole trap potential in 6 s, followed by a 1 s re-compression of the potential, which is used to tune the atomic density and temperature. After this preparation sequence, the sample has a temperature between 200 and 400 nK and contains $1 - 1.7 \times 10^5$ atoms of ^{84,88}Sr and $50 - 70 \times 10^3$ atoms of ^{87}Rb. The typical shot-to-shot temperature fluctuation is 15 nK, while shot-to-shot atom number fluctuations are 15×10^3 and 5×10^3 for Sr and Rb, respectively. The trapping frequencies in our crossed-beam dipole trap are $\{\omega_x, \omega_y, \omega_z\} = 2\pi \times \{35 - 65, 20 - 55, 500(25)\}$ Hz for Sr and $\{\omega_x, \omega_y, \omega_z\} = 2\pi \times \{60 - 105, 35 - 90, 840(40)\}$ Hz for Rb, respectively. The frequency ranges in the horizontal x and y axes correspond to various trap re-compressions. The relative uncertainty on these frequencies is less than 5 %. The difference of trap frequencies between Sr isotopes is less than the uncertainty, hence negligible. The atomic densities used here are $n_{\mathrm{Sr}} = 0.3 - 3 \times 10^{12}\,\mathrm{cm}^{-3}$, $n_{\mathrm{Rb}} = 0.7 - 4.4 \times 10^{12}\,\mathrm{cm}^{-3}$ for the ^{87}Rb-^{84}Sr mixture and $n_{\mathrm{Sr}} = 1.7 - 4.4 \times 10^{12}\,\mathrm{cm}^{-3}$, $n_{\mathrm{Rb}} = 1.5 - 5.4 \times 10^{12}\,\mathrm{cm}^{-3}$ for the ^{87}Rb-^{88}Sr mixture. The Rb sample, as in PA spectroscopy, is prepared in $f^{\mathrm{Rb}} = 1$ and is not spin-polarized. Given the existence of a single electronic ground state, a_s can be considered independent of f^{Rb} and m_f^{Rb}.

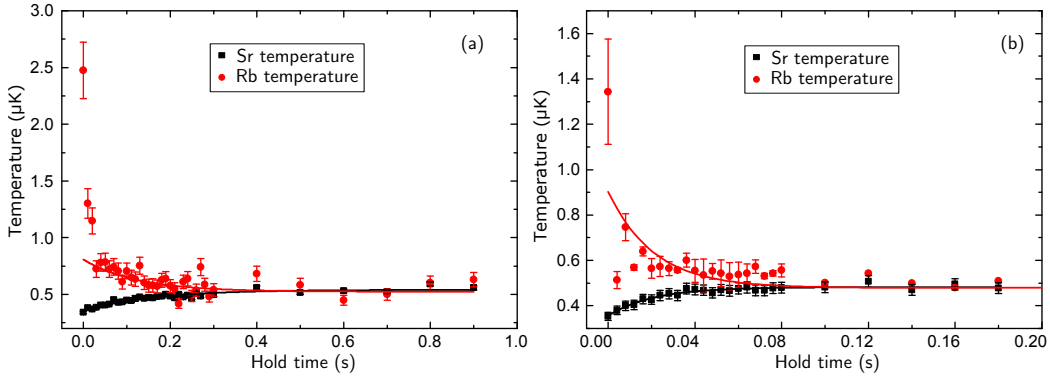

FIGURE 3.7: Inter-species thermalization. Evolution of Sr (black squares) and Rb (red circles) temperature as a function of the hold time during thermalization in (a) ^{87}Rb-^{84}Sr mixture at an effective flux of $\Phi = 7.0 \times 10^{12}\,\mathrm{s}^{-1}\,\mathrm{cm}^{-2}$ and (b) ^{87}Rb-^{88}Sr mixture at a flux of $\Phi = 1.9 \times 10^{13}\,\mathrm{s}^{-1}\,\mathrm{cm}^{-2}$. The lines are exponential fits to the data.

Measurement strategy.

In order to observe inter-species collisions, we selectively excite the cloud of one species and observe the ensuing inter-species thermalization. Since the dipole trap is roughly three times deeper for Rb than for Sr, we excite the Rb cloud by scattering photons on Rb D_2 line for a few μs. After this excitation, the mixture is kept in the trap for a variable hold time t before a 17 ms time-of-flight expansion followed by absorption imaging. From the absorption images, we extract temperatures and atom numbers of both species. The main limitations to the precision of our measurement are shot-to-shot fluctuations in atom number and temperature.

Experimental results.

We measure the evolution of temperature and atom number for each species as functions of time. In Figure 3.7 we show an example for each isotopic combination. The temperature of Sr smoothly evolves from the initial temperature $T_E^i = T_{\mathrm{Sr}}(t = 0)$ to the final equilibrium temperature $T_E^f = T_{\mathrm{Sr}}(t \to \infty)$. By contrast, the temperature of Rb shows a sharp decrease on a timescale of a few tens of ms from a temperature of a few μK down to $0.5 - 0.7\,\mu$K, after which the new equilibrium temperature $T_E^f = T_{\mathrm{Rb}}(t \to \infty) = T_{\mathrm{Sr}}(t \to \infty)$ is reached smoothly.

Extraction of collision cross sections.

We measure the thermalization time of both ^{87}Rb-^{84}Sr and ^{87}Rb-^{88}Sr mixtures. In the case of close-to-equilibrium dynamics, the evolution of temperatures $T_{\mathrm{Rb,Sr}}(t)$ is described by exponential functions with the same well-defined time constant τ. We analyse the thermalization rate τ^{-1} using a well-known model [112, 113], which we detail in Sec 3.9.1. This model gives the relation:

$$\tau^{-1} \approx \frac{1}{2.4}\,\sigma_{\mathrm{Rb-Sr}} \times \Phi, \tag{3.4}$$

where $\sigma_{\mathrm{Rb-Sr}} = 4\pi\, a^2_{\mathrm{Rb-Sr}}$ is the collision cross section dependent on the inter-species s-wave scattering length $a_{\mathrm{Rb-Sr}}$. The value 2.4 in the denominator represents the average number of collisions required for thermalization, when thermalization is fast compared to the trap frequencies. Φ is an effective flux that encompasses the kinematic contribution, see Sec 3.9.1. We fit our data for various effective fluxes and extract values for τ, shown in Figure 3.8.

The effective flux Φ is determined through the knowledge of the trap potential, atom numbers and initial temperatures. All quantities are either measured or known from calibration, with the exception of the initial temperature T^i_{Rb} of the Rb sample right after excitation. Let us note that the excitation we apply experimentally is the injection of energy in the form of both heating and displacement of the cloud. However, by assuming the regime of close-to-equilibrium dynamics, we approximate the excitation to be solely an increase in temperature. The excitation energy of Rb can be derived with good precision from the atom numbers and the temperature evolution of Sr, since the system is isolated after the excitation. The trapping potential can be approximated at these low temperatures by a three dimensional harmonic oscillator potential giving $E = 3\,k_B T$ energy per particle. The final energy in the system E^f must be equal to the initial one E^i, and under our assumptions these are $E^f = 3\,k_B T^f_E (N_{\mathrm{Sr}} + N_{\mathrm{Rb}})$ and $E^i = 3\,k_B (N_{\mathrm{Sr}} T^i_E + N_{\mathrm{Rb}} T^i_{\mathrm{Rb}})$. We thus derive $T^i_{\mathrm{Rb}} = T^f_E + \frac{N_{\mathrm{Sr}}}{N_{\mathrm{Rb}}}(T^f_E - T^i_E)$.

Fitting the data of Figure 3.8 with Equation 3.4, we obtain the inter-species scattering lengths $|a_{^{87}\mathrm{Rb}\text{-}^{84}\mathrm{Sr}}| = 103^{+15}_{-10}\,a_0$ and $|a_{^{87}\mathrm{Rb}\text{-}^{88}\mathrm{Sr}}| = 215^{+50}_{-40}\,a_0$, where a_0 is the Bohr radius, and where the errors are estimated from the residual sum of squares 5-fold increase. Let us note that the variation of the average number of collisions required for thermalization, within the meaningful range $2.4 - 3.0$ [113], leads to a variation of the scattering lengths smaller than the stated error.

While for ^{87}Rb-^{84}Sr the fit is satisfying, the fit of ^{87}Rb-^{88}Sr is worse because of the two points at highest Φ, which we include in the fit. For these two points the thermalization time is comparable with the initial fast time scale of the Rb temperature evolution (see Figure 3.7), suggesting a strong deviation from the close-to-equilibrium case, as expected from the bigger

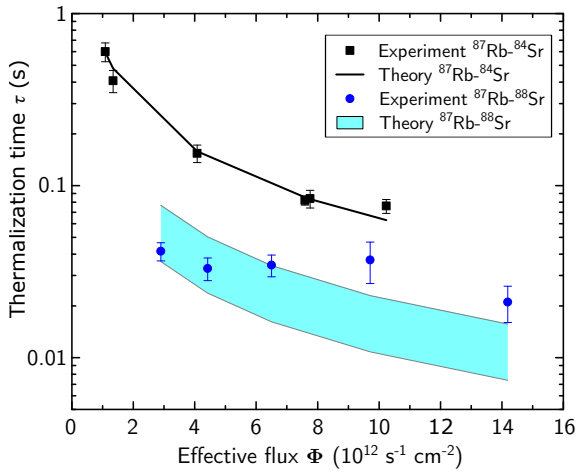

FIGURE 3.8: Thermalization time as function of the effective flux Φ (see main text) for both isotopic combinations. Black squares are data for ^{87}Rb-^{84}Sr and blue circles for ^{87}Rb-^{88}Sr. The solid black line shows the fit for ^{87}Rb-^{84}Sr using the theory described in the text. The light-blue area shows the theoretical region corresponding to the uncertainty of the fitted scattering length for ^{87}Rb-^{88}Sr.

inter-species scattering length. Nonetheless even in the latter case, a meaningful scattering length can be extracted with a correspondingly (larger) error. Finally, the ^{87}Rb-^{87}Sr mixture shows losses that we interpret as 3-body losses, which for similar densities are not observed in the other mixtures investigated. From this observation, we derive that $|a_{^{87}\mathrm{Rb}\text{-}^{87}\mathrm{Sr}}| \gg |a_{^{87}\mathrm{Rb}\text{-}^{88}\mathrm{Sr}}| \simeq 200\, a_0$.

The fitted (central) values of the inter-species scattering lengths are close to the ones inferred from spectroscopy, which is an independent confirmation of our quantum number attribution. However they are $10\,\% - 20\,\%$ higher. This is expected since the initial densities of Rb are underestimated by our model, which assumes thermalization. A Monte-Carlo trajectory simulation would most likely improve the accuracy of the scattering lengths extracted from these thermalization measurements.

3.4 Thermoluminescence and LIF spectroscopy of deeply-bound levels

In the second experiment, we study the deeply-bound levels supported by the $B(2)^2\Sigma^+$ and $X(1)^2\Sigma^+$ potentials via fluorescence spectroscopy of a 1000 K gas mixture of Rb and Sr. In this section, we first describe the experimental setup we use to record the fluorescence from RbSr molecules in a heat-pipe oven. We then explain how we simulate theoretical spectra using three published sets of potential energy curves produced by independent *ab-initio* methods [95, 96]. By comparing these spectra with our experimental data, we identify a few band heads, from which we extract Dunham coefficients describing the deepest parts of the $B(2)^2\Sigma^+$ and $X(1)^2\Sigma^+$ states. With the obtained two sets of Dunham coefficients, we repeat the comparison procedure until we identify 24 band heads and produce final sets of Dunham coefficients. Finally, we estimate the uncertainty of the Dunham coefficients resulting from our analysis by a Monte-Carlo method.

3.4.1 Experimental setup

The measurements at high temperatures were performed in two steps. In the first step, we record thermoluminescence spectra using the method and experimental setup described in Ref. [83]. We therefore provide here only information specific to this paper. We produce RbSr molecules in a dedicated dual-temperature heat-pipe oven. We place 10 g of metallic strontium in the central part of the oven, which is heated to $T_{\mathrm{Sr}} = 1000\,\mathrm{K}$, and 8 g of metallic rubidium in the outer part, heated to $T_{\mathrm{Rb}} = 800\,\mathrm{K}$. Both metals have natural isotopic composition. To ensure the stability of the heat-pipe operation, we use a buffer gas of helium at a pressure of 30 Torr. At the applied temperatures the $B(2)^2\Sigma^+$ electronic state of RbSr is thermally populated, and we record the fluorescence towards the $X(1)^2\Sigma^+$ electronic ground state using a Bruker Vertex V80 Fourier Transform Spectrometer with a spectral resolution of $0.16\,\mathrm{cm}^{-1}$ limited by its aperture size.

In the second step, we obtain spectra via laser induced fluorescence (LIF). We employ a home-made 100 mW external-cavity diode laser whose wavelength is actively stabilized using a HighFinesse WS7 wavemeter. By tuning the laser frequency to the centre of selected band heads, we excite RbSr molecules to the $B(2)^2\Sigma^+$ state and record fluorescence to the ground state with the same spectrometer as before. To increase the contrast between the LIF and thermoluminescence signals observed simultaneously, we reduce the temperature of the central part of the heat-pipe to $T_{\mathrm{Sr}} = 900\,\mathrm{K}$.

3.4.2 Simulations of the recorded spectra

In order to interpret the experimental spectra, we first simulate fluorescence spectra using PECs and transition dipole moments computed theoretically, and compare theory and experiment. The simulations start from three sets of PECs, obtained independently with FCI-ECP+CPP [95], RCCSD(T) [95], and MRCI [96] methods. We calculate the energies of rovibrational levels of the $B(2)^2\Sigma^+$ and $X(1)^2\Sigma^+$ states by solving the radial Schrödinger equation with each of the three sets of PECs. All bound levels in the $X(1)^2\Sigma^+$ and $B(2)^2\Sigma^+$ states are included in the simulations. The contribution of the $A(1)^2\Pi$ state in this spectral region was found to be negligible. In our calculation we omit the fine structure splitting of molecular levels resulting from spin-rotational coupling. Indeed, the energy difference between fine structure components with low rotational quantum numbers N' contributing to a band head formation is expected to be smaller than the spectral resolution of the measurement [94]. We assume spectral lines to have a Gaussian profile with FWHM $= 0.16\,\mathrm{cm}^{-1}$, which results from the Fourier Transform Spectrometer working parameters. Intensities of all spectral lines are calculated assuming thermal equilibrium in the central part of the heat-pipe. The simulation procedure has been described in detail by Szczepkowski *et al.* Szczepkowski *et al.*, including equations necessary to perform the calculations.

The final step of the calculations is to average the simulated spectra of the most abundant isotopologues of RbSr, weighted by their natural abundances (59.6 % for $^{85}Rb^{88}Sr$, 22.9 % for $^{87}Rb^{88}Sr$, 7.1 % for $^{85}Rb^{86}Sr$, 5.1 % for $^{85}Rb^{87}Sr$, 2.7 % for $^{87}Rb^{86}Sr$ and 1.9 % for $^{87}Rb^{87}Sr$). As a result, we obtain three sets of "theoretical spectra" to be compared with the experimental data, shown in Figure 3.9. The analysis of the spectra reveals that the positions of the observed band heads are defined by the $^{85}Rb^{88}Sr$ isotope alone, and other isotopes influence mainly the band-head widths (broadened up to $0.08\,\mathrm{cm}^{-1}$). Thus we only take into account the $^{85}Rb^{88}Sr$ isotope in the Dunham coefficients generation procedure described in the next subsection. The influence of other isotopes is included again during the error estimation process.

3.4.3 Results

In order to identify the observed band heads, we compare the thermoluminescence spectra of RbSr with the simulated spectra based on the three theoretical methods [95, 96]. Unfortunately, these simulations provide spectra of considerably different shapes for each theory (see Figure 3.9) and only few experimental band heads can be identified unambiguously as they appear in all three simulations.

To address this issue we record additional LIF spectra by tuning the excitation laser frequency to the centres of already identified band heads. These new experimental data, shown

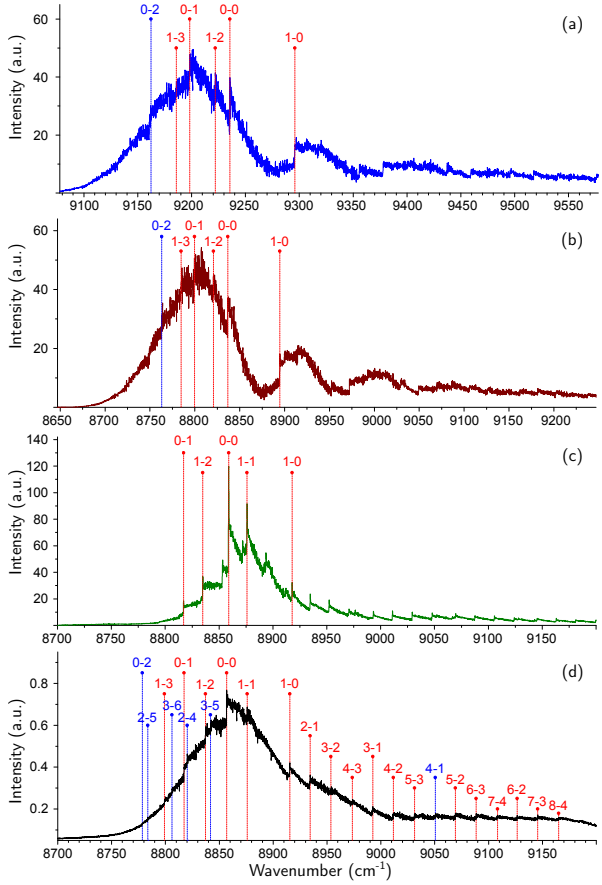

FIGURE 3.9: Simulated thermoluminescence spectra based on the three sets of theoretical PECs for the $X(1)^2\Sigma^+$ and $B(2)^2\Sigma^+$ states, calculated with (a) RCCSD [95], (b) FCI-ECP+CPP [95], and (c) MRCI [96], compared with the experimental data (d). The positions of identified band heads are marked with dashed lines and labelled with their vibrational quantum numbers $v' - v''$ (where primed and double primed symbols refer to $B(2)^2\Sigma^+$ and $X(1)^2\Sigma^+$, respectively). The wavenumber scales of theoretical spectra are adjusted in such a way that $0 - 0$ band heads are at the same position in all panels. The well-resolved band heads used in the final fit of Dunham coefficients are marked in red.

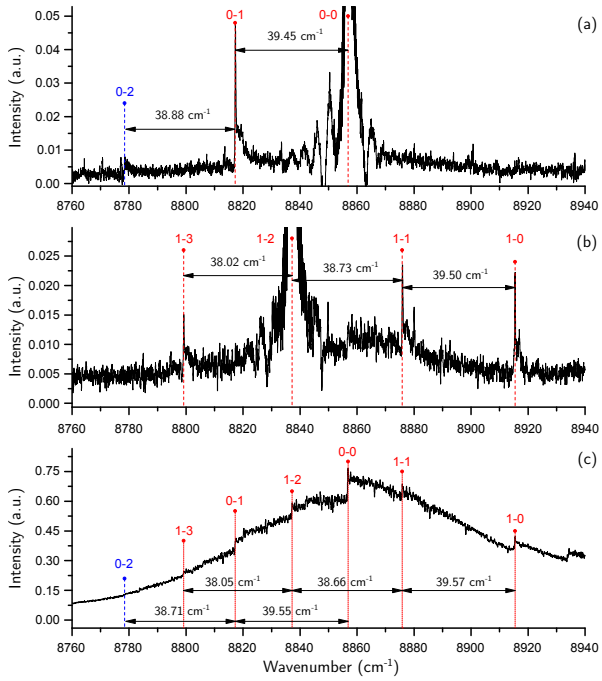

FIGURE 3.10: Comparison of band-head positions in the LIF (a) and (b), and thermoluminescence (c) spectra. The LIF spectra were obtained with the laser tuned to the centres of $v' - v''$ band heads: (a) $0 - 0$ and (b) $1 - 2$. The well-resolved band heads used in the preliminary fit of Dunham coefficients are marked in red.

in Figure 3.10, confirm the validity of the assignment in the case of six band heads. Using the energy of experimental band heads and their assignment confirmed both by thermoluminescence and LIF spectroscopy, we fit preliminary Dunham coefficients for both $X(1)^2\Sigma^+$ and $B(2)^2\Sigma^+$ electronic states. The values of the ground state rotational constants (labelled $Y_{01} \equiv B_e$) were taken from theory for each set and fixed during the fit. We thus obtain three sets of fitted coefficients, each corresponding to one theoretical method. This procedure is described in detail in Ref. [83].

These fitted Dunham coefficients allow for a new prediction of the vibrational level energies in the $X(1)^2\Sigma^+$ and $B(2)^2\Sigma^+$ states, followed by an assignment of additional band heads in the thermoluminescence spectrum. With the improved assignment a correction of Dunham coefficients becomes possible, and we repeat the whole procedure until the final identification of 24 band heads, whose energies are given in Table 3.4 as a Deslandres table. To prevent mistakes in the assignment, only the 18 strongest band heads, whose energies are written in bold in the table and whose positions are marked in red in Figure 3.9, were taken

into account in the final fit of Dunham coefficients. As the outcome of this hot gas mixture spectroscopy, the fitted coefficients describe the energies of the six lowest vibrational levels $v'' = 0 - 5$ in the ground state and the nine lowest vibrational levels $v' = 0 - 8$ of the $B(2)^2\Sigma^+$ state. The final values of the Dunham coefficients, given in Table 3.5, will be used in the next steps of our analysis described in the following section.

TABLE 3.4: Deslandres table constructed for the observed band heads in the experimental thermoluminescence spectrum of RbSr. The wavenumbers of band heads are given in cm^{-1}. The energies of the 18 strongest band heads used in the final fit are written in bold.

	$v''=0$		1		2		3		4		5		6
$v'=0$	**8856.81**	39.55	**8817.26**	38.71	8778.55								
	58.63		58.61		58.66								
1	**8915.44**	39.57	**8875.87**	38.66	**8837.21**	38.05	**8799.16**						
			58.52										
2			**8934.39**						8820.25	36.6	8783.65		
			58.18								58.2		
3			**8992.57**	38.89	**8953.68**						8841.85	35.84	8806.01
			58.06		57.92								
4			9050.63	39.03	**9011.60**	37.97	**8973.63**						
					57.6		57.53						
5					**9069.2**	38.04	**9031.16**						
					57.34		57.35						
6					**9126.54**	38.03	**9088.51**						
							57.17						
7							**9145.68**	37.33	**9108.35**				
									56.82				
8									**9165.17**				

The uncertainties of the Dunham coefficients result mainly from the determination of the positions and widths of the band heads, as many lines corresponding to transitions between different rovibrational levels of the $B(2)^2\Sigma^+$ and $X(1)^2\Sigma^+$ states overlap in the spectra, and thus only the top parts of the band heads are observed in our experiment. We use a Monte-Carlo method to find the error associated with this problem. We randomly vary the positions of individual band heads within a range of $0.46\,cm^{-1}$. The choice for this range results from the band-head half-widths, assumed arbitrarily to be $0.3\,cm^{-1}$, combined with the maximum value of the isotopic shifts. We also vary the widths of individual band heads within $0.16\,cm^{-1}$, a value that influences the number of rovibrational lines taken into consideration in each case. We determine a set of Dunham coefficients for each random combination of positions and widths. We repeat the procedure until the average values of all coefficients becomes equal to the fitted values reported in Table 3.5. The final errors are defined for each Dunham coefficient as three times their standard deviation.

TABLE 3.5: The Dunham coefficients for the $B(2)^2\Sigma^+$ and $X(1)^2\Sigma^+$ states of the $^{85}Rb^{88}Sr$ molecule based on the LIF and thermoluminescence spectra. The three sets of coefficients for each state correspond to different values of the ground state equilibrium distance r_e taken from theoretical calculations. All values are in cm^{-1}.

	MRCI [96]	FCI-ECP+CPP [95]	RCCSD(T) [95]
		$X(1)^2\Sigma^+$	
Y_{10}	40.39(72)	40.32(76)	40.31(76)
Y_{20}	−0.39(11)	−0.38(12)	−0.38(12)
$Y_{01} \times 10^2$	1.874[a]	1.84842[a]	1.79052[a]
$Y_{11} \times 10^4$	−0.8(6)	−1.1(1.1)	−0.9(1.2)
		$B(2)^2\Sigma^+$	
T_e	8847.92(80)	8847.66(80)	8847.66(80)
Y_{10}	58.96(38)	58.95(39)	58.95(39)
Y_{20}	−0.13(4)	−0.13(5)	−0.13(5)
$Y_{01} \times 10^2$	1.932(4)[b]	1.952(5)[b]	1.893(5)[b]
$Y_{11} \times 10^5$	−8.3(6.4)	−3.4(6.7)	−3.4(6.8)

[a] Values taken from theory and fixed during the fit.

[b] Values strongly correlated with Y_{01} of the $X(1)^2\Sigma^+$ state.

3.5 *Ab initio*-based PEC fit

We now combine the results from both types of spectroscopy, at μK and 1000 K temperatures, and perform a joint fit procedure in order to obtain a model representing the complete spectrum of the $X(1)^2\Sigma^+$ ground state of RbSr. In this section, we first describe the specifics of the problem we will address. We then submit and motivate our choice of representation for the potential energy curves. We next detail all steps of our fitting procedure. Finally, we present the results of our joint analysis and compare them with the predictions of the three *ab-initio* theoretical methods we selected.

3.5.1 Statement of the problem

The goal of our data analysis is to provide a representation of the complete bound spectrum of the electronic ground state. This apparently contradicts the fact that, based on the independent analyses of the weakly- and deeply-bound levels, only 15 % of the vibrational levels, corresponding to less than 25 % of the well depth, were observed. Moreover, two-colour photoassociation spectroscopy has very high accuracy and precision but only a few weakly-bound levels have been probed, while thermoluminescence spectroscopy explored a significantly bigger energy range but lacks rotational resolution and its precision is limited to 0.16 cm^{-1}. To the knowledge of the authors, such a problem has not been addressed before and requires a novel method of analysis able to exploit all information present in the two data sets at our disposal.

An examination of the methods used in the previous sections shows how to overcome this problem. The weakly-bound spectrum was analysed, without the need for *ab-initio* PECs, via a direct potential fit of an analytic PEC, with the sole requirement of a correct long-range behaviour, see Subsection 3.3.4. The deeply-bound spectrum was analysed by a fit of Dunham expansion coefficients to band heads whose rovibrational composition was determined by the simulated spectrum based on *ab-initio* PECs, see Subsections 3.4.2 and 3.4.3. Since the fitted Lennard-Jones PEC and the Dunham expansion have no predictive power beyond the corresponding regions of definition, the results of those analyses are valid separately but cannot be extrapolated to the region with missing data. However, a model originating from *ab-initio* calculations, with an appropriate PEC for the $X(1)^2\Sigma^+$ state and a correlated $B(2)^2\Sigma^+$ state is expected to be a good representation of the complete data set, capable of predictive power for the $X(1)^2\Sigma^+$ state, and easily refined in the future by inclusion of new data.

3.5.2 Representation of the $X(1)^2\Sigma^+$ and $B(2)^2\Sigma^+$ state PECs

We now choose a suitable representation of the RbSr $X(1)^2\Sigma^+$ and $B(2)^2\Sigma^+$ states. A somewhat similar problem, albeit considerably more intricate, arose in the case of the excited $1^3\Sigma_g^+$ state in the homonuclear Li_2 molecule accessed via the $1^3\Sigma_g^+ \rightarrow a^3\Sigma_u^+$ system, see Ref. [114]. In this case, Dattani and Le Roy were able to bridge a $5000\,cm^{-1}$ gap in spectroscopy data, i.e. 70 % of the well depth, by performing direct potential fit of Morse/Long-Range (MLR) functions to a rovibrationally resolved high-precision spectrum.[13] The MLR function appears to be particularly suited to represent the RbSr ground state. Indeed, since the RbSr $X(1)^2\Sigma^+$ state is a single isolated electronic state and RbSr is a heavy molecule, the MLR PEC can easily represent the long-range tail, Born-Oppenheimer breakdown effects are expected to be small [116][14], and damping functions are readily incorporated [119]. The $B(2)^2\Sigma^+$ state, relevant for thermoluminescence spectroscopy, is experimentally probed only close to its bottom, far from other electronic states, so it can be explicitly included in the analysis. However, compared to the case of Ref. [114], the precision of our thermoluminescence data is significantly lower and lacks rotational resolution. As a consequence, for reasons different from the case of Ref. [114], the fit is non-trivial and a specific method must be devised.

The version of the MLR function used in this work is the same as in Ref. [114]:

$$V_{\mathrm{MLR}}(r) = D_e\left[1 - \frac{u(r)}{u(r_e)}e^{-\beta\left(y_p(r),y_q(r)\right)\cdot y_p(r)}\right]^2, \tag{3.5}$$

$$u(r) = \sum_{i=1}^{N_u} d_{m_i}(r)\cdot\frac{C_{m_i}}{r^{m_i}}, \tag{3.6}$$

$$y_x(r) = \frac{r^x - r_e^x}{r^x + r_e^x}, \tag{3.7}$$

$$\beta\left(y_p, y_q\right) = \ln\left(\frac{2D_e}{u(r_e)}\right)\cdot y_p(r) + \left(1 - y_p(r)\right)\cdot\sum_{i=0}^{N_\beta}\beta_i\left(y_q(r)\right)^i, \tag{3.8}$$

where D_e is the well depth, r_e is the equilibrium distance, $u(r)$ is the function describing the long-range behaviour, $y_x(r)$ is an x-order effective radial variable and $\beta\left(y_p, y_q\right)$ is the exponent coefficient of the radial variable y_p[15]. The functions $d_{m_i}(r)$, explicitly included in Equation 3.6, are Douketis-type [120] damping functions $D_m^s(r)$ with $s = -1$ and adapted to

[13] Successively, the binding energies extrapolated in the gap region were experimentally confirmed within $1.5\,cm^{-1}$ [115].

[14] Adiabatic corrections are similar to those in Rb_2 [117, 118].

[15] Compared to Ref. [114] the notation is simplified because we set $r_{ref} = r_e$, i.e. all effective radial variables are referenced to r_e.

RbSr by scaling of the radial variable via atomic ionization potentials [121] as explained in Ref. [114]. The C_{m_i} coefficients in Equation 3.6 are the N_u lowest order dispersion coefficients.

In order to represent the theoretical PECs by MLR functions we choose a family of these functions and values of their parameters based on the available theoretical calculations. The family of the MLR functions is defined by the choice of N_u in Equation 3.6, N_β in Equation 3.8) and p, q. We use perturbation-theory results for C_6, C_8 and C_{10} available in the literature [106] and set $N_u = 3$. This choice implies $p > m_{last} - m_1 = 4$ and correspondingly $1 < q < p$ [114], with a contribution to the asymptotic long-range tail of order $r^{-m_1-p} = r^{-6-p}$. We resolve this indefiniteness, together with the one of N_β, by fitting the MLR function to the three point-wise representations of *ab-initio* PECs in the region $r \geq 3.0$ Å, using the unweighted $\tilde{\chi}^2$ as figure of merit, with errors set to $1.0\,\mathrm{cm}^{-1}$. In all fitted cases we obtain $\tilde{\chi}^2_{\mathrm{min}} \simeq 1.0$ with "well-behaved" PECs, i.e. with a single inflection point, already for $N_\beta = 5$, and the best fits are obtained for low values of p, q. Hence, we eventually set $N_u = 3$, $N_\beta = 5$, $p = 5$ and $q = 2$, which we hold constant during later fits. Since our data on deeply-bound levels are not rotationally resolved and since weakly-bound levels, within our experimental precision, do not carry information on the equilibrium distance r_e, we set r_e equal to the equilibrium distances from the theoretical calculations and hold it fixed during fits. The remaining parameters D_e and β_i are fitted to the three point-wise representations of *ab-initio* PECs. This provides us with the three desired MLR functions representing the PECs from the three theoretical calculations, which we later use as starting conditions for fitting our experimental data. Since harmonic and first anharmonic contributions are sufficient to represent the data, see Subsection 3.4.3, only the parameters that strongly affect the lowest derivatives at $r = r_e$ need to be fitted to the thermoluminescence data. These are the coefficients β_i with lowest i. In summary, in the following fitting procedure of all experimental data, we will treat $\beta_{0\leq i\leq 2}$, C_6, C_8 and D_e as the only fitting parameters, retaining in this way the theoretical shape of each PEC in the region where no data are available.

A well defined representation of the $\mathrm{B}(2)^2\Sigma^+$ state is needed to simulate the thermoluminescence spectrum. We adopt a point-wise representation determined both by our experiment and by theoretical calculations in the region of missing data. This is realized by initializing the PEC with the *ab-initio* predictions and adapting it to fitted Dunham coefficients via the Inverted Perturbation Approach [122], see Subsection 3.5.3. The bottom part of the potential, determined by the experiment, and the upper part, determined by theory, are matched smoothly to provide a well depth referenced to that of the ground state. Within this representation the fitting parameters are the Dunham coefficients, which provide the link between the representations of the $\mathrm{X}(1)^2\Sigma^+$ and $\mathrm{B}(2)^2\Sigma^+$ states.

3.5.3 Fit Method

We fit our model of the $X(1)^2\Sigma^+$ and $B(2)^2\Sigma^+$ states to experimental data both from two-colour photoassociation and thermoluminescence/LIF spectroscopy. In particular, the fitted experimental quantities for two-colour PA are binding energies, while in the case of thermoluminescence/LIF they are band-head wavenumbers and, with lesser precision, the overall intensity profile. We recall that the fit parameters are those defining $V_{\rm MLR}$ for the $X(1)^2\Sigma^+$ state and the Dunham coefficients of the $X(1)^2\Sigma^+ - B(2)^2\Sigma^+$ system. While the weakly-bound spectrum and the band-head positions do not determine precisely the equilibrium distances, the intensity profile carries this information together with the overall potential shapes and can be used to adjust the equilibrium distance of the $B(2)^2\Sigma^+$ state with respect to that of the $X(1)^2\Sigma^+$ state. The initial values for the fit parameters in $V_{\rm MLR}$ are defined in Subsection 3.5.2 for each *ab-initio* model, while the initial values for the Dunham coefficients are those of Table 3.5. The figure of merit used in the fit is $\widetilde{\chi}^2$, see Equation 3.1. In the following, we outline a single iteration step of our fit, which is applied to each *ab-initio* model, while a future work will provide a detailed explanation [105].

We first generate the rovibrational levels of $X(1)^2\Sigma^+$, using the fitted Dunham coefficients, for the range $v'' = 0 - 6$ for $N'' = 0$, and fit them together with the experimental weakly-bound energy levels, via a direct potential fit of our model MLR PEC [105]. We derive the $B(2)^2\Sigma^+$ state depth from the MLR D_e parameter and the Dunham coefficients. We then construct the $B(2)^2\Sigma^+$ PEC via the Inverted Pertubation Approach, using both the $B(2)^2\Sigma^+$ energy levels, generated with Dunham coefficients in the range $v' = 0 - 8$ for $N' = 0 - 44$, and the $B(2)^2\Sigma^+$ potential well depth. We simulate the thermoluminescence spectra using the resulting PECs, in order to check the agreement of the simulated band-head positions and intensity profiles with the experimental ones. Here the convergence of the fit algorithm is checked and, if met, the calculation is stopped. Otherwise, we optimize the equilibrium point of the $B(2)^2\Sigma^+$ state to maximize the agreement between the simulated intensity profile and the experimental one. During this optimization, for each change of the equilibrium point, the $B(2)^2\Sigma^+$ state is optimized against the $X(1)^2\Sigma^+$ state, which consists in fitting the Dunham coefficients of the $B(2)^2\Sigma^+$ state keeping those of the $X(1)^2\Sigma^+$ state fixed. With this new guess for the equilibrium distance of the $B(2)^2\Sigma^+$ state, we refit all Dunham coefficients of both states, see Subsection 3.4.3, and repeat the iteration step.

3.5.4 Results and discussion

The fit outlined above is performed separately starting with FCI-ECP+CPP, RCCSD(T) and MRCI *ab-initio* point-wise representations. In all cases we obtain good agreement between our best-fit model and the binding energies and band-head positions. However, while in

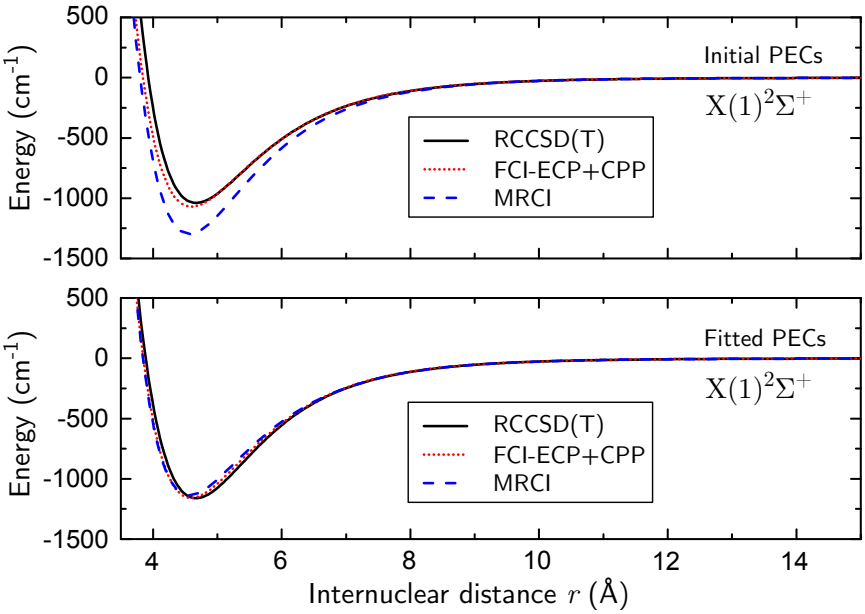

FIGURE 3.11: PECs of the $X(1)^2\Sigma^+$ state of RbSr. Top panel: theoretical PECs corresponding to the three different *ab-initio* calculations considered in this work. Bottom panel: PECs fitted to experimental data with initial fit parameters determined by each *ab-initio* method, see Subsection 3.5.3.

the case of MRCI and FCI-ECP+CPP potential energy curves, the $B(2)^2\Sigma^+$ state depth inferred after the first iteration is within 190 cm^{-1} of the *ab-initio* predictions, in the case of RCCSDS(T) the well depth is about 440 cm^{-1} away from the theoretical value. As a consequence, we observe that all *ab-initio* PECs give a sufficiently good representation of the RbSr ground state allowing for experimental fits, but only FCI-ECP+CPP and MRCI predictions are able to approximate the excited state well enough to permit its refinement by tuning its equilibrium distance. Best-fit parameters for the $X(1)^2\Sigma^+$ state MLR functions and refined point-wise representations of the $B(2)^2\Sigma^+$ state are reported in the Appendix 3.9.2. The derived Dunham coefficients for both $X(1)^2\Sigma^+$ and $B(2)^2\Sigma^+$ states are consistent with those in Table 3.5. A comparison between the initial MLR functions, fitted to *ab-initio* data, and the final MLR functions, based on *ab-initio* PECs and fitted to experimental data, is shown in Figure 3.11.

The convergence of the three PECs towards a unique solution, as illustrated in Figure 3.11, and the good agreement with our experimental data corroborate our fit method. In particular, we observe that our data are sufficient to constrain strongly the depth of the

ground state potential well to $D_e = 1152^{+9}_{-16}\,\mathrm{cm}^{-1}$.[16] The fitted PECs are consistent with the model-independent quantities derived in the previous sections up to residual model dependency. In particular, compared to those of Section 3.3.4, the dispersion coefficient C_6 and the semiclassical phase Φ^0_{WKB} are slightly bigger, which is mostly due to the inclusion of C_{10} in the MLR model,[17] while the C_8 is consistent within our relatively low precision. The fit quality of weakly-bound levels can still be assessed by the $\tilde{\chi}^2$ and DOF $= 8$ used in Section 3.3.4, since it is insensitive to β_i fitting parameters. We obtain 0.89, 0.53 and 0.99 for MRCI, FCI-ECP+CPP and RCCSD(T), respectively, which are all sufficiently good. We use the $\tilde{\chi}^2$, with DOF $= 10$ and error set to 0.16 cm^{-1}, of the distance between band-head positions in experimental and simulated thermoluminescence spectra as a second benchmark of the fitted potential energy curves. We obtain 0.83, 0.5 and 1.78 for MRCI, FCI-ECP+CPP and RCCSD(T) respectively, which shows agreement within our experimental resolution.

In Table 3.6 the experimental values of spectroscopic constants are compared with the theoretical ones. Also here the convergence of the described fitting procedure is remarkable. The final value of the vibrational constant ω_e does not depend on the starting *ab-initio* PECs used in the fit for both $X(1)^2\Sigma^+$ and $B(2)^2\Sigma^+$ states. However, the agreement between the experimental and theoretical ω_e values obtained is clearly the best for the FCI-ECP+CPP model. Similarly this model provides the best prediction of the potential well depths D_e of the investigated states and of the number of bound levels in the ground state. The experimental data also allow to determine the difference between equilibrium distances of the $X(1)^2\Sigma^+$ and $B(2)^2\Sigma^+$ electronic states, $\Delta r_e = r_{eB} - r_{eX}$, and the values obtained are almost identical when starting from theoretical PECs calculated with the FCI-ECP+CPP ($\Delta r_e = -0.086$Å) and MRCI ($\Delta r_e = -0.087$Å) methods.

Finally, we check in two ways the quality of the final fitted potential for the $X(1)^2\Sigma^+$ state. Firstly, we simulate the thermoluminescence spectrum by using the potential we obtained starting from the FCI-ECP+CPP potential, as it gives the best agreement between theoretical and experimental values of molecular constants. In Figure 3.12 we show a comparison of this simulation with the experimental results. The agreement for the band-head positions between the two spectra is almost perfect, and this allows the assignment of even more band heads. Secondly, we use the fitted $X(1)^2\Sigma^+$ state potential to calculate the positions of Fano-Feshbach resonances, which are listed in Table 3.7. At the time of the writing of this paper and thanks to these predictions, the resonances arising at about 1.3 kG for $^{87}Rb^{84}Sr$ and 1.0 kG for $^{87}Rb^{88}Sr$ have indeed been observed experimentally at the expected magnetic fields, which proves the high quality of the potential we obtained for the RbSr $X(1)^2\Sigma^+$ state.

[16] Although the depths derived from the FCI-ECP+CPP and RCCSD(T) methods are extremely close, we attribute to D_e the mean value of all three cases and the full uncertainty range.

[17] By fitting once more the weakly-bound spectrum with V_{LJ} including a C_{10} term fixed to the theoretical value, we obtain $C_6 = 1.7962010665716115 \times 10^7$ Å^6 cm^{-1}, $C_8 = 5.792504377056786 \times 10^8$ Å^8 cm^{-1} and $\Phi^0_{WKB} = 67.4386$.

TABLE 3.6: Comparison of spectroscopic constants and dispersion coefficients for the $X(1)^2\Sigma^+$ and $B(2)^2\Sigma^+$ states of the $^{85}Rb^{88}Sr$ molecule, between the present experiment-based work, the *ab-initio* calculations used here [95, 96], and other relevant works labelled as in their respective publication. Units of energy and length are cm^{-1} and Å, respectively, while Φ^0_{WKB} is dimensionless. The final errors, defined as three times the standard deviation, are given in parentheses

	D_e	ω_e	$B_e \times 10^2$	r_e [Å]	T_e	$C_6 \times 10^{-7}$	$C_8 \times 10^{-8}$	Φ^0_{WKB}
			$X(1)^2\Sigma^+$					
present[a]	1136	40.39(72)	1.874[e]	4.565[e]	0	1.81(2)	5.8(1.3)	67.4393
present[b]	1158	40.32(76)	1.848[e]	4.595[e]	0	1.80(2)	6.1(1.3)	67.4381
present[c]	1161	40.31(76)	1.791[e]	4.669[e]	0	1.81(2)	5.90(1.3)	67.4396
experimental [101]	–	42(5)	–	–	–	–	–	–
MRCI [96]	1298	42.5	1.874	4.565	0	–	–	70.7768
FCI-ECP+CPP [95]	1073.3	38.98	1.848	4.595	0	–	–	65.8890
RCCSD(T) [95]	1040.5	38.09	1.791	4.669	0	–	–	64.7252
ST [60]	1273	42.2	1.853	4.590	0	–	–	–
CCSD(T) [100]	916	36	1.75	4.72	0	–	–	–
Relativistic KR-MRCI [98]	1017.58	35.8	1.8	4.66	0	–	–	–
theory [106]	–	–	–	–	–	1.783	6.220	–
			$B(2)^2\Sigma^+$					
present[a]	5025	58.92(38)	1.946	4.478	8848.0(8)	–	–	–
present[b]	5047	58.94(39)	1.920	4.509	8847.6(8)	–	–	–
present[d]	5050	58.95(39)	1.893	–	8847.7(8)	–	–	–
MRCI [96]	5214	59.5	1.921	4.507	8830	–	–	–
FCI-ECP+CPP [95]	4982.9	58.37	1.975	4.445	8828	–	–	–
EOM-CC [95]	4609.6	60.20	1.925	4.503	9224	–	–	–
ST [60]	5078	58.5	1.899	4.533	8711	–	–	–
Relativistic KR-MRCI [98]	4683.56	58.1	1.98	4.43	9151	–	–	–
theory [106]	–	–	–	–	–	8.448	59.80	–

[a] Based on MRCI [96] *ab-initio* calculation.
[b] Based on FCI-ECP+CPP [95] *ab-initio* calculation.
[c] Based on RCCSD(T) [95] *ab-initio* calculation.
[d] Based on RCCSD(T) [95] and EOM-CC [95] *ab-initio* calculation; parameters taken from Dunham coefficients listed in Table 3.5.
[e] Fixed during the fit at the corresponding theoretical value.

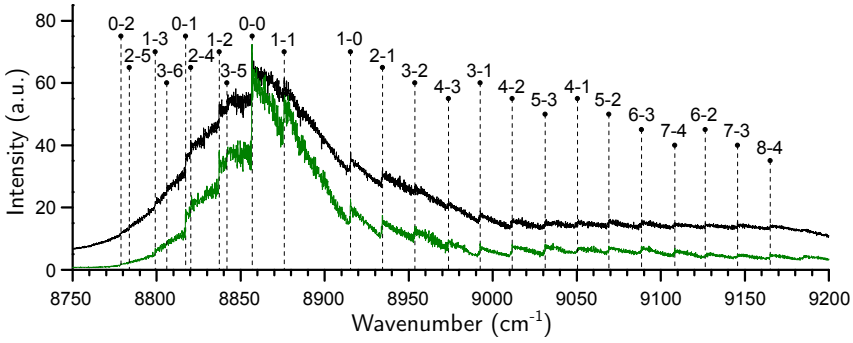

FIGURE 3.12: Comparison of the original experimental spectrum (upper curve, in black) with the spectrum simulated using the experimental potential employing the ground state r_e value from the FCI-ECP+CPP [95] calculations (lower curve, in green). The positions of identified band heads are marked with dashed lines, on top of which the assigned vibrational quantum numbers $\nu' - \nu''$ are given.

TABLE 3.7: Fano-Feshbach resonances for RbSr isotopologues due to coupling between $N = 0$ molecular levels and $N = 0$ atomic scattering levels in the magnetic field region $B < 3.0$ kG. E_b is the binding energy of the bound state, f^{Rb}, m_f^{Rb}, F and m_F are the quantum numbers defined in the main text identifying the open and closed channel, respectively. B is the resonant magnetic field, $\Delta\mu$ is the differential magnetic moment, and ΔB is the width of the resonance calculated as the avoided crossing gap divided by $\Delta\mu$. The avoided crossing gap is calculated for the two-body problem by using first order perturbation theory and the *ab-initio* coupling matrix term induced by the variation of Rb hyperfine constant [25]. The two atoms are confined in a species-independent potential well with $\omega = 2\pi \times 60$ kHz isotropic trapping frequency, which is a typical value for sites of a three-dimensional optical lattice

BE (MHz)	f^{Rb}	m_f^{Rb}	F	m_F	B (G)	$\Delta\mu$ (MHz/G)	ΔB (mG)
^{85}Rb^{84}Sr							
6644.83	2	-2	3	-2	2950.99	-2.64	31.40
6644.83	2	-1	3	-1	2500.46	-2.53	35.06
6644.83	2	0	3	0	2108.76	-2.49	31.82
6644.83	2	1	3	1	1778.42	-2.53	24.94
6644.83	2	2	3	2	1506.91	-2.64	16.03
^{85}Rb^{86}Sr							
3421.32	2	-2	3	-2	1637.55	-2.10	5.37
3421.32	2	-1	3	-1	1029.72	-1.54	5.85
3421.32	2	0	3	0	562.87	-1.29	4.03
3421.32	2	1	3	1	307.68	-1.54	1.75
3421.32	2	2	3	2	193.47	-2.10	0.63
9308.75	2	1	3	1	2799.16	-2.67	4.71
9308.75	2	2	3	2	2499.41	-2.72	3.26
^{85}Rb^{87}Sr							
78.63	2	-1	2	-2	157.16	-0.53	0
78.63	2	0	2	-1	165.59	-0.48	0
78.63	2	1	2	0	174.48	-0.43	0
78.63	2	2	2	1	183.83	-0.39	0
78.63	3	-3	3	-2	149.40	-0.59	0
78.63	3	-2	3	-1	157.41	-0.53	0
78.63	3	-1	3	0	165.88	-0.47	0
78.63	3	0	3	1	174.82	-0.43	0
78.63	3	1	3	2	184.23	-0.39	0
78.63	3	2	3	3	194.10	-0.35	0
1071.24	2	-2	3	-3	1329.33	0.56	0
1071.24	3	-3	3	-2	995.37	-1.85	0
4227.19	2	-2	3	-2	1995.89	-2.37	-5.26
4227.19	2	-2	3	-1	1741.03	-2.22	0
4227.19	2	-1	3	-2	1740.39	-2.23	0
4227.19	2	-1	3	-1	1470.84	-2.06	5.63
4227.19	2	-1	3	0	1256.20	-1.98	0
4227.19	2	0	3	-1	1255.68	-1.99	0
4227.19	2	0	3	0	1049.46	-1.95	4.51
4227.19	2	0	3	1	889.86	-1.97	0
4227.19	2	1	3	0	889.49	-1.98	0
4227.19	2	1	3	1	748.80	-2.06	2.87
4227.19	2	1	3	2	642.03	-2.19	0
4227.19	2	2	3	1	641.79	-2.19	0
4227.19	2	2	3	2	551.81	-2.37	-1.46
4227.19	2	2	3	3	482.92	-2.57	0
4227.19	3	-3	3	-2	2314.53	-2.65	0
10827.35	2	2	3	3	2916.48	-2.77	0
^{85}Rb^{88}Sr							

5128.78	2	-2	3	-2	2364.10	-2.52	8.32
5128.78	2	-1	3	-1	1879.36	-2.33	9.05
5128.78	2	0	3	0	1474.80	-2.26	7.75
5128.78	2	1	3	1	1157.32	-2.33	5.57
5128.78	2	2	3	2	920.02	-2.52	-3.24
$^{87}Rb^{84}Sr$							
9242.30	1	0	2	0	2218.82	-1.89	3.77
9242.30	1	1	2	1	1312.74	-2.15	1.69
$^{87}Rb^{86}Sr$							
12546.80	1	1	2	1	2726.72	-2.47	4.35
$^{87}Rb^{87}Sr$							
0.01	1	-1	1	0	0.18	0.70	0
0.01	1	0	1	1	0.18	0.70	0
0.01	2	-1	2	-2	0.18	0.70	0
0.01	2	0	2	-1	0.18	0.70	0
0.01	2	1	2	0	0.18	0.70	0
0.01	2	2	2	1	0.18	0.70	0
287.32	1	0	1	-1	397.14	-0.74	0
287.32	1	1	1	0	432.35	-0.62	0
287.32	2	-2	2	-1	366.06	-0.88	0
287.32	2	-1	2	0	398.65	-0.73	0
287.32	2	0	2	1	434.30	-0.62	0
287.32	2	1	2	2	473.02	-0.52	0
1952.06	2	-2	2	-1	1672.34	-1.70	0
6235.49	1	-1	2	-2	294.64	1.96	0
6235.49	1	-1	2	-1	1918.11	-0.88	-59.55
6235.49	1	-1	2	-1	519.45	0.88	16.13
$^{87}Rb^{88}Sr$							
7403.10	1	-1	2	-1	2804.54	-1.68	-8.73
7403.10	1	0	2	0	1014.50	-1.08	-5.70
7403.10	1	1	2	1	366.98	-1.68	-1.14

3.6 Conclusions and Outlook

We have performed three different types of spectroscopy experiments in order to investigate the ground and second excited electronic states, both of $^2\Sigma^+$ symmetry, of the alkali – alkaline-earth RbSr molecule. We have presented a novel procedure to connect data from two-colour photoassociation measurements, which provide information on energy levels of the $X(1)^2\Sigma^+$ state near the dissociation threshold, and low-resolution data from thermoluminescence/LIF experiments, which allow to describe the bottom of both $X(1)^2\Sigma^+$ and $B(2)^2\Sigma^+$ PECs. As the thermoluminescence spectra lack rotational resolution, the equilibrium distance between the Rb and Sr nuclei cannot be determined from our measurements and must be taken from theoretical calculations. Therefore we use three different sets of theoretical PECs, resulting from state-of-the-art *ab-initio* calculations, as starting points for the fit of potential energy curves to the experimental data. We obtain three potentials for the $X(1)^2\Sigma^+$ state, but despite significant differences between the starting potentials, the three fitted ones converge to nearly the same shape. In the region of missing experimental data the shapes of the fitted PECs stay close to the initial theoretical potentials and this region awaits future spectroscopic investigation to be refined. Although in the case of the $B(2)^2\Sigma^+$ state, the experimental data provide only information about deeply-bound energy levels, our procedure is able to reject one of the three theories that diverges too much from the experimental results.

We have demonstrated that our data analysis method is a powerful tool to obtain potential energy curves of heavy molecules, where achieving rotational resolution is difficult and investigation of the mid-range spectrum challenging. This method may find a welcome use in the field of physical chemistry, since it shows, in the simple case of diatomic molecules, that several independent sources of information, both experimental and theoretical, can be synthesized successfully. The findings of our analysis may be of interest to physicists from various fields. Indeed, calculations performed with the fitted RbSr potentials demonstrate their power to predict the positions of unassigned band heads and the intensity distribution of the spectrum, but also the positions of Fano-Feshbach resonances, some of which were later confirmed experimentally [66]. As a next step, we plan to further refine the PECs derived in this work via new LIF experiments with rotational resolution, and to characterize the effects induced by hyperfine and spin-rotation couplings via additional two-color PA. We will also use the results of this work to determine an efficient STIRAP path for RbSr molecules towards the rovibronic ground state [98]. With such molecules available, one can run quantum simulations [32, 70–72], perform fundamental tests of physics [76–78], and study chemical reactions with full control over reactants at the quantum level [72, 79–82].

3.7 Conflicts of interest

There are no conflicts of interest to declare.

3.8 Acknowledgements

This project has received funding from the European Research Council (ERC) under the European Union's Seventh Framework Programme (FP7/2007-2013) (Grant agreement No. 615117 QuantStro). B.P. thanks the NWO for funding through Veni Grant No. 680-47-438 and C.-C.C. thanks the Ministry of Education of the Republic of China (Taiwan) for a MOE Technologies Incubation Scholarship. J.S. acknowledges partial support from the Miniatura I programme founded by the National Science Centre of Poland (NCN, Grant no. 2017/01/X/ST2/00057). This work was partially supported by the National Science Centre of Poland (Grant no. 2016/21/B/ST2/02190). A.C. is grateful to Jeremy Hutson for fruitful discussions. J.S. is grateful to Olivier Dulieu and Piotr Żuchowski for fruitful discussions.

3.9 Appendix

3.9.1 Theoretical model for inter-species thermalization

A rigorous analysis of the experimental data would require a Monte-Carlo trajectory simulation taking into account the initial atomic distributions, the subsequent excitation of the Rb cloud and the elastic-scattering cross sections, both inter-species and intra-species. However, we are here only interested in a confirmation of our ground-state potential model and for that we do not require precise values for the scattering lengths. Moreover we observe that, although during the thermalization the system is out of equilibrium, it might be close enough to equilibrium to apply a very simple collision model giving the cross-thermalization rate from equilibrium statistical physics [112]. This is suggested in our case by the very fast decrease in Rb temperature compared to the cross-thermalization time. In order to clarify the analysis, we review the model here.

The temperature difference is expected to decrease exponentially to zero with an inter-species thermalization rate given by

$$\tau^{-1} = \frac{d(\Delta T)}{\Delta T dt} = \frac{d(\Delta T)}{\Delta T}\Gamma, \tag{3.9}$$

where ΔT is the temperature difference between species 1 and 2 and $dt = 1/\Gamma$ is the average collision time. The rate of inter-species collisions Γ is given by

$$\begin{aligned}\Gamma &= \sigma_{12} \times \bar{v} \times \int n_1(x)\, n_2(x)\, dx^3 = \\ &= \sigma_{12} \times \bar{v} \times N_1 N_2 \int \rho_1(x)\, \rho_2(x)\, dx^3,\end{aligned} \tag{3.10}$$

where $\sigma_{12} = 4\pi a_{12}^2$ is the inter-species cross section, $\bar{v}$ is the mean thermal relative velocity and $n_{1,2}(x)$, $\rho_{1,2}(x)$ are the atomic density distributions normalized to $N_{1,2}$ or 1, respectively. At thermal equilibrium with known trapping potential $U_{1,2}$, temperatures $T_{1,2}$, and atomic masses $m_{1,2}$, we know all the quantities in the equation above except the inter-species scattering length. In particular $\bar{v} = \sqrt{(8k_B/\pi) \times ((T_1/m_1) + (T_2/m_2))}$ and $n_{1,2}(x) \propto \exp^{-U_{1,2}(x)/k_B T_{1,2}}$.

From basic kinematics the energy transfer from species 1 to species 2 is given by

$$\begin{aligned}\Delta E_{1\to 2} &= \xi\, k_B \Delta T, \\ \xi &= \frac{4 m_1 m_2}{(m_1 + m_2)^2},\end{aligned} \tag{3.11}$$

where ξ accounts for the mass imbalance, and in our case $\xi \simeq 1$. From this we obtain

$$d(\Delta T) = \frac{\xi}{3}\frac{N_1 + N_2}{N_1 N_2}\Delta T. \tag{3.12}$$

Substituting Equation 3.12 into Equation 3.9, we get the final result

$$\tau^{-1} = \frac{\xi}{3}\frac{N_1 + N_2}{N_1 N_2}\Gamma = \frac{\xi}{3}\sigma_{12} \times (N_1 + N_2)\,\bar{v} \int \rho_1(x)\,\rho_2(x)\,dx^3 =$$

$$= \frac{\xi}{3}\sigma_{12} \times \Phi, \tag{3.13}$$

where the kinematic contribution to the rate is summarized in the effective flux Φ.

The value of 3 in the denominator of Equation 3.13 represents the average number of collisions for thermalization. Corrections to this number have been evaluated [113], and it is shown to vary within the range $2.4 - 3.4$, with 2.4 referring to fast thermalization compared to trap oscillation time and 3.4 to the opposite case.

3.9.2 Potential energy curves

In this part, we provide additional information about the fitted potentials. In Table 3.8, we give the best fit parameters for the MLR PEC describing the $X(1)^2\Sigma^+$ state. In Table 3.9 and Table 3.10 we give the point-wise representations of the fitted PECs for the $B(2)^2\Sigma^+$ state, fitted starting from the FCI-ECP+CPP and the MRCI methods, respectively. Finally, in Figure 3.13 we show a comparison of the potentials for the $B(2)^2\Sigma^+$ state before and after our fit procedure.

TABLE 3.8: Best fit parameters for the MLR PECs describing the $X(1)^2\Sigma^+$ state in the cases of the three initial *ab-initio* representations. Units of energy and length are cm^{-1} and Å, respectively. The number of digits in the presented values of parameters is necessary to reproduce band-head positions and weakly-bound energy levels with the experimental uncertainty

	MRCI [96]	FCI-ECP+CPP [95]	RCCSD(T) [95]
p	5^a	5^a	5^a
q	2^a	2^a	2^a
N_u	3^a	3^a	3^a
N_β	5^a	5^a	5^a
D_e	1136.153957156767	1158.334744879383	1161.0696743991873
r_e	4.5645^a	4.59508^a	4.66879^a
C_6	1.808868014576728	1.795668695101867	1.8134615231939677
C_8	5.792504377056786	6.148308472469144	5.870256113661574
C_{10}	2.2043858534998264^a	2.2043858534998264^a	2.2043858534998264^a
β_0	−1.2521217820591306	−1.2744532761179883	−1.2541965574219214
β_1	−2.7403962754860123	−2.6486718159733136	−2.324690124968812
β_2	−1.2388430923676004	−0.8587136858852784	−0.06921139967893859
β_3	0.8220377227516734^a	1.5773120878976061^a	0.9325813112428021^a
β_4	-2.710995726338915^a	-0.16154919058041997^a	-4.2183716802600495^a
β_5	-4.142301068756231^a	-0.8834374478517256^a	-5.290318777716273^a

[a] Held fixed during fit to experimental data.

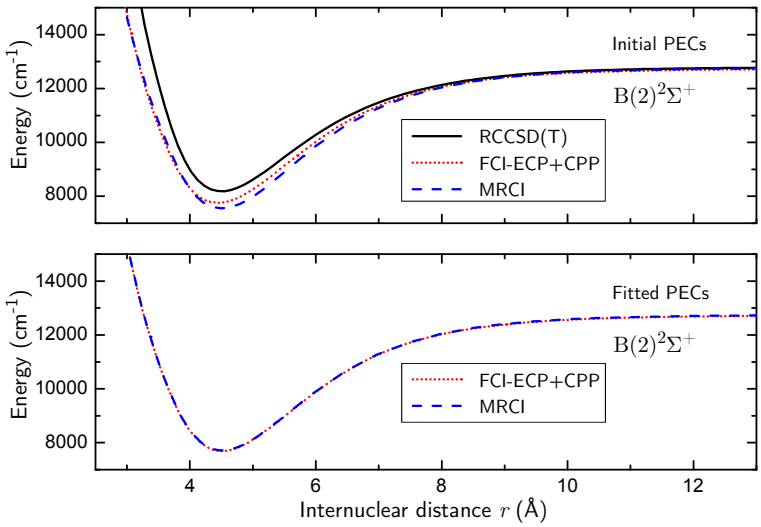

FIGURE 3.13: PECs of the $B(2)^2\Sigma^+$ state of RbSr. Top panel: theoretical PECs corresponding to the three different *ab-initio* calculations considered in this work. Bottom panel: PECs fitted to experimental data with initial fit parameters determined by the FCI-ECP+CPP and MRCI methods, see Subsection 3.5.3.

TABLE 3.9: The point-wise potential energy curve of the $B(2)^2\Sigma^+$ state obtained after the fit procedure, based on the theoretical curve calculated with the FCI-ECP+CPP method

r (Å)	E (cm^{-1})	r (Å)	E (cm^{-1})
2.68	19257.0300	8.18	12109.8735
2.78	17908.5708	8.29	12157.4315
2.89	16617.8234	8.39	12197.4666
3.00	15379.9026	8.50	12238.2371
3.10	14312.2244	8.60	12272.5381
3.21	13241.3574	8.71	12307.4494
3.31	12375.1023	8.82	12339.6227
3.42	11528.6439	8.92	12366.6696
3.52	10837.7736	9.03	12394.1795
3.63	10150.2670	9.13	12417.2977
3.74	9536.4284	9.24	12440.8047
3.84	9050.4423	9.35	12462.4492
3.95	8604.8603	9.45	12480.6336
4.05	8289.8226	9.56	12499.1204
4.16	8021.3425	9.66	12514.6521
4.27	7838.3481	9.77	12530.4436
4.37	7737.9870	9.87	12543.7127
4.48	7691.2318	9.98	12557.2074
4.58	7699.9253	10.09	12569.6388
4.69	7753.0775	10.19	12580.0904
4.79	7837.0308	10.30	12590.7265
4.90	7961.2580	10.40	12599.6736
5.32	8634.7155	10.51	12608.7842
5.43	8837.5343	10.62	12617.1902
5.54	9044.9495	10.72	12624.3507
5.64	9233.5924	10.83	12631.8586
5.75	9439.0045	10.93	12638.2067
5.85	9621.9672	11.04	12644.7041
5.96	9818.0546	11.14	12650.2014
6.06	9991.0355	11.25	12655.8314
6.17	10174.3255	11.36	12661.0571
6.28	10349.5430	11.46	12665.4829
6.38	10501.3856	11.57	12670.0202
6.49	10659.9119	11.67	12673.8658
6.59	10796.1676	11.78	12677.8112
6.70	10937.3983	11.89	12681.4802
6.81	11069.6823	11.99	12684.5934
6.91	11182.3688	12.10	12687.7911
7.02	11298.2776	12.20	12690.5065
7.12	11396.6341	12.31	12693.2978
7.23	11497.4813	12.41	12695.6701
7.33	11582.8320	12.52	12698.1107
7.44	11670.1576	12.63	12700.3871
7.55	11751.0295	12.73	12702.3241
7.65	11819.3069	12.84	12704.3196
7.76	11889.0220	12.94	12706.0191
7.86	11947.8194	13.05	12707.7714
7.97	12007.8007	13.16	12709.4095
8.08	12063.2037		

TABLE 3.10: The point-wise potential energy curve of the $B(2)^2\Sigma^+$ state obtained after the fit procedure, based on the theoretical curve calculated with the MRCI method

r (Å)	E (cm^{-1})	r (Å)	E (cm^{-1})
2.57	20015.9638	7.97	12039.5764
2.67	18623.1081	8.47	12260.0669
2.77	17378.0065	8.97	12412.7431
2.87	16227.5400	9.47	12513.9446
2.97	15164.7084	9.97	12581.4056
3.07	14191.0980	10.47	12626.6346
3.17	13301.5037	10.97	12657.3393
3.27	12484.9011	11.97	12693.3984
3.37	11729.7060	12.97	12711.7395
3.47	11028.5584	13.97	12721.6836
3.57	10381.0891	14.00	12721.9028
3.67	9791.4292	14.10	12722.6076
3.77	9271.8458	14.20	12723.2748
3.87	8816.5037	14.30	12723.9066
3.97	8486.8951	14.40	12724.5053
4.07	8191.1429	14.50	12725.0727
4.17	7968.0412	14.60	12725.6108
4.27	7821.7664	14.70	12726.1213
4.37	7739.7466	14.80	12726.6058
4.47	7711.9908	14.90	12727.0659
4.57	7729.6107	14.97	12727.3742
4.67	7784.9552	15.00	12727.5029
4.77	7871.4749	15.10	12727.9182
4.87	7983.6310	15.20	12728.3130
4.97	8116.4157	15.30	12728.6885
5.07	8265.5303	15.40	12729.0457
5.17	8430.3232	15.50	12729.3857
5.27	8609.5386	15.60	12729.7094
5.37	8792.9576	15.70	12730.0178
5.47	8981.4689	15.80	12730.3115
5.77	9548.1877	15.90	12730.5915
5.97	9908.3732	16.00	12730.8585
6.47	10690.4487	18.00	12734.2857
6.97	11287.8051	20.00	12735.7680
7.47	11725.8313		

Chapter 4

The potential energy curves of electronically-excited RbSr: theory and experiments

In this chapter I will introduce the reader to the electronically-excited PECs of RbSr, and describe the one-colour spectroscopy methods that our group developed and used to probe these PECs experimentally. Section 4.1 gives a short theoretical introduction to the PECs of electronically-excited RbSr. They are discussed succinctly in Chapter 2, Subsection 2.1.5, but in this chapter spin-orbit coupling is left undiscussed because it is extremely weak in the ground-state PEC of RbSr. The situation is very different in electronically-excited RbSr, where spin-orbit coupling is a major coupling term. Section 4.2 gives an overview of the principles underlying our one-colour spectroscopy work, and in Section 4.3 the laser system and experimental conditions for this spectroscopy are described. In the work discussed in this chapter, we produced molecules with an excitation energy close to the excitation energy of the $^1S_0 - {}^3P_1$ intercombination line of Sr, of which the wavelength is 689 nm and the natural linewidth is $\gamma/2\pi = 7.5\,\mathrm{kHz}$. The one-colour spectra that we obtained in the four isotopologue mixtures ^{87}Rb-^{87}Sr, ^{88}Rb-^{87}Sr, ^{86}Rb-^{87}Sr and ^{84}Rb-^{87}Sr are presented in Section 4.4, along with the methods that we used to analyse these data. The one-colour spectroscopy data tables are presented in Appendix B. The positions of the resonance positions that we measured in the fermionic isotopologue mixture ^{87}Rb-^{87}Sr are reported in Table B.1, and those obtained in the fermionic isotopologue mixtures ^{88}Rb-^{87}Sr, ^{86}Rb-^{87}Sr and ^{84}Rb-^{87}Sr are reported in Table B.2. The magnetic moments of the electronically-excited RbSr molecules, when measured, are reported in Table B.3. These data are subject to an ongoing theoretical analysis.

The knowledge of at least a few electronically-excited molecular states is required to perform two-colour spectroscopy and probe the ground-state PEC of RbSr, as shown in

Chapter 2, Figure2.3. Furthermore, this knowledge is required to produce molecules via STIRAP or photoassociation followed by spontaneous emission, as discussed in Chapter 1, Section 1.4. Thus, our experimental investigation of the PECs of electronically-excited RbSr was motivated by two goals. First, measuring the binding energy of molecular states in the electronic ground state, in order to constrain the fit of the long-range part of the ground-state PEC — this work led to the publication reported in Chapter 3. Second, developing methods of producing RbSr molecules in the electronic ground state.

4.1 The PECs of electronically-excited RbSr: theoretical description

In a diatomic molecule, the very strong Coulomb interaction between the electrons and the nuclei forces the electrons to follow the motion of the nuclei. The electronic motion is therefore said to be *strongly coupled to the internuclear axis*. Accordingly, we have introduced the molecule-fixed electronic coordinates $\{\vec{r}_i\}$ and the total angular momentum exclusive of spin, $\vec{N} = \vec{\ell} + \vec{L}$, which rotates the electrons along with the nuclei.

The use of molecule-fixed coordinates for the electronic spin vectors $\vec{S} = \sum \vec{s}_i$, summing over i electrons, is on the other hand justified only in presence of spin forces that force the orientation of the spins to change along with the change of orientation of the nuclei. In the electronic ground state $^2\Sigma^+$ of RbSr, the total electronic spin $\vec{S}$ is almost fully decoupled from the internuclear axis and thus $\vec{S}$ is better expressed in space-fixed coordinates[1]. Indeed, the spin-orbit interaction that couples spin and electronic degrees of freedom in the electronically-excited states of RbSr is almost absent in the ground state: the diagonal contribution of spin-orbit coupling is zero for electronic Σ terms[2], and the off-diagonal couplings of the ground state to the electronically-excited PECs are much smaller than the energetic separation between them, leading to negligibly small corrections to the binding energies of the $^2\Sigma^+$ molecular states. Effects that couple the internuclear axis to $\vec{S}$ in the electronic

[1] This case is referred to as Hund's coupling case (b). The quantum numbers that define the molecular eigenstates (neglecting the hyperfine structure) are then Λ, S, v, N, m_N and parity $\pm$ for Σ electronic terms. The diatomic Hamiltonian, Equation 2.1, is thus *mostly diagonal* in the basis $|\Lambda\ S\ v\ N\ m_N\rangle$ in the electronic subspace of the $^2\Sigma^+$ term. The off-diagonal contributions, such as the spin-rotation term discussed in this paragraph or the Coriolis terms, can be treated using perturbation theory in this basis provided they are small enough. This is in general the correct way to think about molecular structures: one must find a convenient eigenbasis in which most of the Hamiltonian is diagonal and where off-diagonal couplings can be treated perturbatively. The Hund's cases provide eigenbasis that are appropriate for common cases encountered in experimental spectroscopy.

[2] The diagonal contribution of the spin-orbit $\vec{L} \cdot \vec{S} = L_z S_z + 1/2\,[L_+ S_- + L_- S_+]$ in the $|^{2S+1}|\Lambda|\rangle = |S\Lambda\rangle$ electronic eigenbasis stems from the $L_z S_z$ operator, and $L_z\,|S\Lambda\rangle = \Lambda\,|S\Lambda\rangle = 0$ for $\Lambda = 0$.

ground state exist, though. The most important of them is the spin-rotation coupling between $\vec{N}$ and $\vec{S}$[3,4]. It is typically weak for small values of N, and we have neglected it in our work on the electronic ground state.

For the electronically-excited PECs, the situation is very different. The spin-orbit interaction $\hat{H}_{\mathrm{SO}} = A\vec{L}.\vec{S}$ couples $\vec{S}$ very strongly to the electronic orbital motion $\vec{L}$, which is itself strongly coupled to the internuclear axis. The analysis of the spin-orbit coupling interaction for electronically-excited RbSr is presented very clearly in Ref. [95], and we do not repeat it here. The result is that it couples very strongly the excited PECs of Figure 2.2, leading for instance to large avoided crossings between them. The electronically-excited PECs $U_n(R)$, obtained including $\hat{H}_{\mathrm{SO}}$ in the electronic Hamiltonian, are shown in Figure 4.1. The corresponding eigenvalue equations are

$$(\hat{H}_e + \hat{H}_{\mathrm{SO}})\psi_n^{\mathrm{el}}(\vec{r}, R) = U_n(R)\psi_n^{\mathrm{el}}(\vec{r}, R) \quad \text{with} \quad \{|n\rangle\}_n = \{|^{2S+1}|\Omega|^{\pm}\rangle\}_{S,\Omega}\,, \tag{4.1}$$

where $\hat{H}_e$ is defined as in Equation 2.16. The internuclear distance dependence $A(R)$ of the spin-orbit term was not taken into account in Ref. [95] and in the subsequent work of Ref. [53].

In presence of spin-orbit coupling, Λ ceases to be a good quantum number because $\hat{H}_e + \hat{H}_{\mathrm{SO}}$ doesn't commute with L_z. Instead, it commutes with $L_z + S_z$ and accordingly the projection $\Omega = \Lambda + \Sigma$ of the total (spin+orbital) electronic angular momentum $\vec{P} = \vec{L} + \vec{S}$ onto the internuclear axis is a good quantum number for the electronic Hamiltonian. Owing to the strong coupling of $\vec{P}$ to the internuclear axis, it is best to use molecule-fixed coordinates for both $\vec{L}$ and $\vec{S}$ for electronically-excited RbSr states. The partial operators defined by Equation 2.18 must rotate the nuclei without affecting the electronic molecule-fixed coordinates, and are therefore modified by replacing $L_{x,y,z}$ by $P_{x,y,z} = L_{x,y,z} + S_{x,y,z}$ respectively, so that both electronic positions and spin orientations are left unchanged in the molecular frame. The total angular momentum (exclusive of nuclear spin) $\vec{J} = \vec{N} + \vec{S}$ then replaces the total angular momentum exclusive of spin $\vec{N}$, and takes the same form as $\vec{N}$ does in absence of electronic spin — see Equation 2.20. In this manner, the total rotation of the

[3]Spin-rotation takes the form $\gamma(R)\vec{N}.\vec{S}$, where two physical effects contribute to $\gamma(R)$: the small magnetic moment that arises from the rotation of the nuclei and couples to the electronic spin, and a cross-term between spin-orbit coupling and rotational kinetic energy. The second contribution is typically much larger than the first one, except for very light molecules such as H_2 [57]. The interested reader is referred to the discussions of Hund's case (b) in Ref. [58] and to the analysis of the CN radical in Ref. [57], where spin-rotation in the context of electronic $^2\Sigma^+$ terms is discussed.

[4]An extra corrective term $-D_\nu N^4$ contributes to the energy of rotating molecular states. The corresponding constant D_ν is referred to as the centrifugal distortion constant of the vibrational state of quantum number ν. The total rotational plus fine structure Hamiltonian therefore takes the form $H_{rfs} = B_\nu N^2 - D_\nu N^4 + \gamma\vec{N}.\vec{S}$, where B_ν is the rotational constant of the considered vibrational state [24].

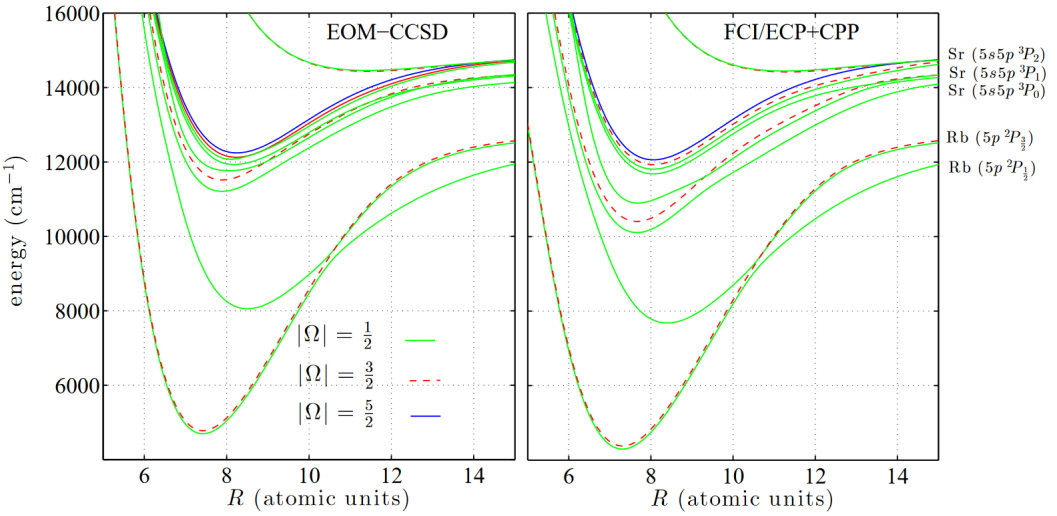

FIGURE 4.1: The RbSr potential energy curves, taking into account spin-orbit coupling, kinetic and electrostatic terms. They are calculated using the EOM-CCSD and FCI/ECP+CPP methods for all states correlating to the experimentally relevant asymptotes. From Ref. [95].

molecule including electronic spins $\vec{J}^2$ doesn't affect the electronic molecule-fixed coordinates and $\left[(\hat{H}_e + \hat{H}_{SO}), \vec{J}^2\right] = 0$. Replacing $\vec{N}$ by $\vec{J}$, the decoupling of the rotational motion from the {electronic+radial} degrees of freedom, Equations 2.34 and 2.38, is thus also obtained in presence of spin coupling to the internuclear axis. The rotational eigenfunctions $|J\ m_J\ \Omega\rangle$ of $\vec{J}^2$ have the same properties as those given in Equation 2.24, again replacing N, m_N and Λ by J, m_J and Ω respectively[5]. The nuclear Hamiltonian, Equation 2.25, takes the form

$$\hat{T}_N = \underbrace{-\frac{\hbar^2}{2\mu R^2}\frac{\partial}{\partial R}R^2\frac{\partial}{\partial R}}_{\hat{H}_{\text{vibration}}} + \underbrace{\frac{\vec{J}^2}{2\mu R^2}}_{\hat{H}_{\text{rotation}}} + \underbrace{\frac{\vec{J}^2 - 2\vec{J}\cdot\vec{P}}{2\mu R^2}}_{\hat{H}_{\text{Coriolis}}} . \tag{4.2}$$

[5]The eigenbasis obtained by diagonalizing $\hat{H}_e$ without including $\hat{H}_{SO}$, Equation 2.27, and by using $\vec{J}$ is the Hund's case (a) eigenbasis $|\Lambda\ S\ v\ J\ m_J\rangle$. It is well suited to the description of molecules where spin-orbit coupling is present but is less strong than the electrostatic interactions. In this case, spin-orbit coupling can be treated as a perturbation. The eigenbasis obtained by diagonalizing $\hat{H}_e + \hat{H}_{SO}$, Equation 4.1, is the Hund's case (c) eigenbasis $|\Omega\ S\ v\ J\ m_J\rangle$. It is well suited to the description of molecules where spin-orbit coupling is stronger than the electrostatic interactions. In this case, Ω is a good quantum number, but Λ is not. This is the case of the RbSr excited states presented here and accordingly, the term symbol $^{2S+1}|\Omega|^{\pm}$ is preferred to the $^{2S+1}|\Lambda|^{\pm}_{\Omega}$ molecular term symbol common in literature.

Therefore, the total separated Hamiltonian (neglecting hyperfine structure) takes the same form as in Equation 2.25, i.e.

$$\hat{H} = \hat{H}_{\text{vibration}} + \hat{H}_{\text{rotation}} + \hat{H}_{\text{Coriolis}} + \hat{T}_{\text{mass pol.}} + (\hat{H}_e + \hat{H}_{\text{SO}}) \,. \tag{4.3}$$

The adiabatic approximation, Equation 2.33, is excellent for the electronic ground state $^2\Sigma^+$ due to its large separation in energy with respect to the other electronic states, but is much less good for the excited RbSr states where several PECs are very close in energy. Large non-adiabatic contributions are expected to couple these PECs, especially for bound states that have a large interradial probability density $|\chi_v^{\text{vib}}(R)|^2$ (defined as the probability density of finding the two nuclei at the distance R from one another) close to the avoided crossings. The interplay between the electronic/vibrational/rotational structure with the hyperfine interactions induced by the presence of nuclear spins $\vec{I}_{\text{Rb}}$ and $\vec{I}_{\text{Sr}}$ is also a non-trivial matter[6]. The RbSr spectra that we obtained near the $^1S_0 - {}^3P_1$ intercombination line of Sr are subject to an ongoing theoretical analysis.

[6] In this thesis, The electronic and nuclear spins $\vec{S}$ and $\vec{I}$ are denoted as $\vec{s}$ and $\vec{i}$ respectively. It is customary to use uppercase letters for the quantum numbers of a molecule, and lowercase letters for those of an atom.

4.2 Photoassociation and one-colour spectroscopy of RbSr: the principles

Photoassociation is the process through which an electronically-excited molecule is created from a pair of free atoms, following the absorption of a photon. In a photoassociation experiment, a gas of atoms is irradiated with light, and molecules are formed when the frequency of the light is such that the relative kinetic energy $E = \frac{\hbar^2 k^2}{2\mu}$ of an atom pair and the energy $h \times \nu_{\text{light}}$ of one photon add up to the energy E_{mol} of an excited molecular state. Photoassociation is therefore a resonant process, and photoassociation resonances are also referred to as optical Feshbach resonances[7]. The free atom pair state is said to belong to the open channel, and the electronically-excited state to the closed channel. Complete introductions to photoassociation and optical Feshbach resonances are given in Refs. [63] and [123].

The electronically-excited PECs of RbSr, presented in Figure 4.1, can be investigated experimentally in photoassociation experiments. This technique is known as one-colour (one-photon) spectroscopy. In such experiments, an ultracold gas of Rb-Sr atoms is produced and irradiated with laser light[8], which produces electronically-excited RbSr molecules at the resonant laser frequency. The corresponding photoassociation reaction is

$$\text{Rb} + \text{Sr} + \gamma \rightarrow \text{RbSr}^*, \tag{4.4}$$

where γ is the photoassociation or free-bound (FB) laser photon[9], and RbSr^* denotes the electronically-excited RbSr molecule that has been photoassociated. The energy $h \times \nu_{\text{FB}}$ of the photoassociation photon γ is set by the frequency ν_{FB} of the photoassociation laser.

In the one-colour spectroscopy experiments that we performed to probe the electronically-excited PECs of RbSr, the laser L_{FB} has a frequency close to that of the $^1S_0$ – $^3P_1$ intercombination line of Sr, of wavelength $\lambda = 689$ nm. It irradiates a μK-cold sample of about 10^5 Rb atoms and 10^6 Sr atoms for a time T_{pulse}, and its frequency is scanned in view of finding a resonance frequency at which Rb-Sr pairs are photoassociated into molecules. An experimental run of RbSr one-colour spectroscopy is performed as follows. Copropagating atomic beams of Rb and Sr are produced by two independent ovens, heated to about $T_{\text{Sr}} = 530$ °C

[7] We discuss magnetic Feshbach resonances in depth in Chapter 5. Most of the conceptual tools used in the context of magnetic Feshbach resonance apply to optical Feshbach resonances as well. One important difference is that the Breit-Wigner energy width of a magnetic Feshbach resonance cannot be tuned with the magnetic field. The width of an optical Feshbach resonance, on the other hand, depends linearly on the electric field intensity.

[8] While photoassociation can be performed with non-laser light sources, laser light is an ideal tool for photoassociation. Its spatial coherence allows to focus high amounts of optical power onto the atomic cloud, hence maximising the probability of absorption, and its temporal coherence permits to excite molecular states with very high selectivity thanks to the narrow electric field linewidth.

[9] This notation should not be confused with the notation γ denoting the spontaneous decay rate $\gamma/2\pi$ of an excited atom or molecule.

and $T_{\mathrm{Rb}} = 200\ ^{\circ}\mathrm{C}$ respectively. The beams are slowed down by a common Zeeman slower, and captured in independent MOTs. The Sr atoms are then cooled down to about $1\,\mu$K using the narrow $^1S_0 - {}^3P_1$ intercombination line of Sr. The Rb atoms are prepared in the $f = 1$ hyperfine manifold using optical pumping and are sympathetically cooled to μK-cold temperatures through elastic collisions with Sr. Then, both species are loaded in a crossed-beam optical dipole trap with a depth of a few ten $k_B \times \mu$K. The production of such Rb-Sr mixtures takes 10 to 25 seconds in our photoassociation experiments[10]. The resulting Rb-Sr photoassociation sample consists of a few 10^5 Rb atoms and a few 10^6 Sr atoms, trapped in a crossed-beam optical dipole trap at a temperature of a few μK. The Rb atoms are prepared in the $f = 1$ hyperfine manifold, using optical pumping, and all three $m_f = 0, \pm 1$ states are almost equally populated[11]. Further details on the Rb-Sr sample are given in Subsection 4.3.2.

Once the Rb-Sr sample is ready, an homogeneous magnetic field of magnitude B is applied, and the photoassociation laser beam is shone onto the atoms for a time $\mathrm{T_{pulse}}$. The application of a magnetic field of a few G permits to increase dramatically the photoassociation detection sensitivity, as explained in Subsection 4.3.3 below, and the direction of this field sets the m_f-state quantization axis for the photoassociation process. If the frequency ν_{FB} matches a photoassociation resonance frequency, it couples an initial atom pair state of collisional energy $E \sim k_B \times 1.0\,\mu$K to an electronically-excited state of energy $E_{\mathrm{mol},2}$ close to the Rb $(^2S_{1/2}) + \mathrm{Sr}\ (^3P_1)$ dissociation asymptote. Rb-Sr pairs are then photoassociated into RbSr* molecules. If the laser L_{FB} is instead off-resonant, no molecule is formed. At the end of the laser pulse, the population in each m_f-state of Rb is measured by switching off the dipole trap and letting the atoms fall in presence of a magnetic field gradient. After typically 7 ms of time of flight, Rb atoms in different m_f states are Stern-Gerlach separated, and undergo another 7 ms of free fall in absence of a gradient. They are then imaged using standard laser absorption imaging on the D_2 line of Rb, and the corresponding atom numbers are recorded[12]. The photoassociated RbSr* atoms do not appear on the absorption

[10] This timescale is set by the natural abundance of the Sr isotope investigated in the one-colour experiment, which defines the flux of Sr atoms coming from the oven and captured in the MOT. The lower the abundance, the more one needs to accumulate Sr atoms in the $^1D_2$ magnetic reservoir during the first-stage cooling cycle — see Refs. [103, 124], and is described in Refs. [52, 103] and in our publications presented in Chapter 3 and 6. The natural abundances of the ^{84}Sr, ^{86}Sr, ^{87}Sr and ^{88}Sr isotopes are 0.56, 9.86, 7.00 and 82.58% respectively [124]. It is therefore much faster to prepare a Rb-^{88}Sr sample (less than 10 s) than a Rb-^{84}Sr (up to 25 s).

[11] In absence of polarization that favors any projection with respect to a given quantization axis, the Rb ensemble is a statistical mixture of all possible F projections along any axis.

[12] We also image Sr using absorption imaging, but we do not perform Stern-Gerlach separation. The bosonic isotopes of Sr, ^{84}Sr, ^{86}Sr and ^{88}Sr, have neither electronic nor nuclear spin and thus are insensitive to Stern-Gerlach separation. The fermionic isotope of Sr, ^{87}Sr, has a nuclear spin but we do not resolve the corresponding Stern-Gerlach separation, owing to the very small gyromagnetic ratio of ^{87}Sr — see Chapter 5, Equations 5.46. Note that optical Stern-Gerlach separation is in principle possible with this isotope [125].

pictures[13], therefore a decrease of the Rb atom number is observed in the m_f states subject to photoassociation, as compared to the off-resonant case — see Figure 4.2. Such decrease in the Rb atom number indicates that the frequency ν_{FB} is resonant, and that an excited molecular state has been detected. Conversely, no photoassociation-induced loss indicates off-resonant laser light. The Rb-Sr sample is lost at the end of each experimental sequence, which ends with atom absorption imaging. A new experimental cycle then begins: a new Rb-Sr sample is created, the frequency of the photoassociation laser ν_{FB} is changed, and another photoassociation sequence is performed[14]. The frequency ν_{FB} is changed in steps from one experimental shot to the other, with a resolution of up to 1 MHz for coarse scans, and down to a few kHz for the investigation of narrow spectroscopic features. Due to the Rb-Sr sample preparation time, typically a 1 GHz-wide spectroscopic search with MHz resolution will last several hours.

In the one-colour spectroscopy work presented in this chapter, we produced molecules with an excitation energy close to the excitation energy of the $^1S_0$ – $^3P_1$ intercombination line of Sr, of which the wavelength is 689 nm and the natural linewidth is $\gamma/2\pi = 7.5\,\mathrm{kHz}$. The optical frequency of reference for the one-colour spectroscopy presented in this chapter is thus the frequency of the $^1S_0$ – $^3P_1$ electronic transition of Sr. The frequency of the photoassociation light is detuned by an amount Δ compared to this atomic reference frequency, as shown in Figure 4.2. In a one-colour spectroscopy scan, this detuning is changed in steps from one experimental shot to the other. The spectroscopy laser system and the methods used to produce this detuning Δ are detailed in Subsection 4.3.1.The one-colour spectroscopy spectra are produced by reporting the Rb population $p(m_f)$ in each m_f-state as a function of the detuning Δ — Subsection 4.4, Figure 4.3.

[13]The RbSr* molecules will typically decay very fast to the electronic ground state after emission of a photon (see Chapter 1, Subsection 1.4.3), populating molecular states that are not resonantly coupled to the atomic imaging laser beams.

[14]This process is quite different from that of MOT or atomic beam spectroscopy, where the photoassociation laser is continuously irradiating the sample. In that case the frequency of the laser is changed continuously over time, and the change of recorded fluorescence at the correct laser frequency indicates that a molecular state has been detected.

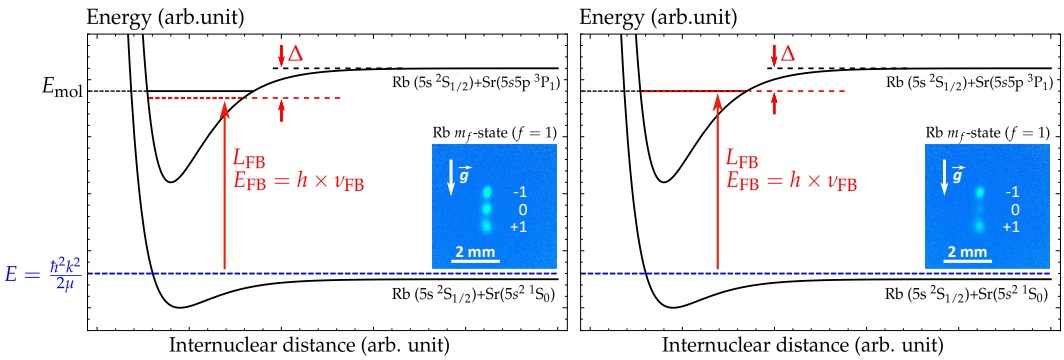

FIGURE 4.2: Principle of an ultracold Rb-Sr photoassociation experiment close to the $^1S_0 - {}^3P_1$ intercombination line of Sr. The laser L_{FB} irradiates the Rb-Sr sample for a time T_{pulse} and its frequency ν_{FB} is changed from one experimental shot to the other, with the goal of finding a resonance frequency at which Rb losses occur. The insets show absorption images of Stern-Gerlach-separated Rb atoms, where the direction of gravity is indicated with a white arrow (Rb time of flight = 14 ms). **Left panel**: laser L_{FB} off-resonant. There is no photoassociation-induced loss, therefore the imaged Rb atom number is almost the same in each m_f state, as is the case in absence of L_{FB}. **Left panel**: laser L_{FB} resonant. Excited RbSr molecules are photoassociated, which decreases the number of Rb atoms imaged in the m_f-state(s) coupled to the excited state (here $m_f = 0$). Note that the depicted pictures are simplified, because three different PECs correlate to the Rb $(^2S_{1/2}) + \text{Sr}\ (^3P_1)$ asymptote (two $|\Omega| = 1/2$ and one $|\Omega| = 3/2$ PEC — see Figure 4.1. Furthermore, the other PECs correlating to the Rb $(^2S_{1/2}) + \text{Sr}\ (^3P_{0,\,2})$ and Rb $(^2P_{1/2,\,3/2}) + \text{Sr}\ (^1S_0)$ asymptotes lie reasonably close in energy to the Rb $(^2S_{1/2}) + \text{Sr}\ (^3P_1)$ asymptote Therefore, a given excited molecular state may arise from the mixing of different PECs.

4.3 Laser system and experimental conditions for one-colour spectroscopy

4.3.1 The laser system: frequency tuning close to the $^1S_0$ – $^3P_1$ intercombination line of Sr

The optical frequency of reference for the RbSr one-colour spectroscopy presented in this chapter is the frequency of the $^1S_0$ – $^3P_1$ electronic transition of Sr. We use the same transition to laser cool Sr atoms to μK temperatures. Therefore, the cooling laser system and the photoassociation laser system can share the same master laser. This master laser is a 689-nm Toptica DLpro with an intrinsic linewidth of about 1 MHz, locked to a high-finesse optical cavity to reduce its short-term linewidth to a few kHz. The master laser frequency is actively stabilized onto the $^1S_0$ – $^3P_1$ absorption signal of a Sr spectroscopy cell, which provides the absolute frequency reference $\nu_{^1S_0-{}^3P_1,\,^{88}\mathrm{Sr}}$ for long-term frequency stability[15]. The transition of ^{88}Sr is used for long-term stabilization, since it is by far the most abundant isotope of Sr and thus gives the strongest absorption signal for modulation transfer spectroscopy. In the next paragraphs, the photoassociation laser system is described, whereas further details of the laser cooling system are given in Ref. [124].

The photoassociation laser light must be frequency-shifted with respect to the master light, for two reasons. First, the absolute frequency of the $^1S_0$ – $^3P_1$ transition of Sr depends on the considered isotope, and we investigated all stable isotopes of Sr in our Rb-Sr photoassociation experiments. Therefore, the isotopic shifts of the $^1S_0$ – $^3P_1$ transitions of ^{84}Sr, ^{86}Sr and ^{87}Sr compared to ^{88}Sr have to be compensated. The shift in frequency of the $^1S_0$ – $^3P_1$ transitions of ^{84}Sr and ^{86}Sr compared to the ^{88}Sr transition are -351.49 MHz and -163.81 MHz respectively. The fermionic isotope ^{87}Sr has non-zero nuclear spin, therefore the hyperfine structure of its $^3P_1$ manifold has to be taken into account (the $^1S_0$ ground state has only one manifold: $f = i = 9/2$). The shifts are 1352.0, 221.7 and -1241.4 MHz for the hyperfine manifolds $f = 7/2, 9/2$ and $11/2$ respectively [124]. Second, the photoassociation frequency ν_{FB} must be detuned by an amount Δ with respect to the frequency of the $^1S_0$ – $^3P_1$ transition of the chosen isotope of Sr, as is clear from Figure 4.2. We use two (complementary) methods to achieve this frequency tuning, as described below.

In the first years of the experiment, we used acousto-optic modulators (AOMs), of which the input frequencies are produced by direct digital synthesizers (DDS). The frequency of the photoassociation laser, shifted from the source frequency by a single AOM is given by $\nu_{\mathrm{FB}} = \nu_{^1S_0-{}^3P_1,\,^{88}\mathrm{Sr}} + n \times f_{\mathrm{AOM}}$, where n is the AOM diffraction order that we use (typically

[15] The master light is actually stabilized with an AOM-generated 80-MHz offset compared to the atomic transition, for practical reasons (see Ref. [124]).

± 1 or ± 2, the diffraction efficiency dropping dramatically for the higher diffraction orders) and f_{AOM} the RF input of the AOM. Obviously, it is possible to use several AOMs in series to shift the laser frequency further than allowed by the bandwidth of an individual AOM. The frequency of the photoassociation laser is then $\nu_{\mathrm{FB}} = \nu_{1_{S_0}-{}^3P_1,\,{}^{88}\mathrm{Sr}} + \sum_i n_i \times f_{\mathrm{AOM}\,i}$, where the sum is taken over all AOMs. However, this method comes with severe drawbacks. The cost of the system increases rapidly with the number of AOMs, which are costly devices (about 2000€ per AOM), and the total output power available for photoassociation is diminished by each of the AOMs in the optical path due to their limited diffraction efficiency[16]. Furthermore, and even more importantly, the experimental setup has to be rearranged once the available range of binding energies allowed by the bandwidth of the AOMs (typically a few ten or hundred MHz per AOM) is reached, which prohibits long and uninterrupted spectroscopic searches.

In order to perform the GHz-wide spectroscopic scans that are presented in Subsection 4.4 of this chapter, we used tunable frequency offset locking [126] instead of AOM chains. The output light of the photoassociation laser, a DL100 Toptica laser, is superimposed with the master laser light (frequency-shifted by AOMs if necessary) on an home-built photodiode. The beat signal between the photoassociation and master laser is recorded, and the resulting beat frequency $\Delta\nu = |\nu_{\mathrm{FB}} - \nu_{\mathrm{master}}|$ is compared with an external local oscillator (LO) produced by a DDS. An error signal is produced from this beat signal, as explained in Refs. [51, 126], and is fed back to the photoassociation laser using a Toptica FALC 110 proportional–integral–derivative controller (PID). In this scheme, the locking point that sets ν_{FB} is tuned by varying the DDS frequency f_{LO}, within the 500 MHz range allowed by our DDSs. In order to extend this range even further, we use a fiber-coupled electro-optic modulator (EOM)[17] that produces sibebands in the spectrum of the master light, allowing to shift the master laser frequency by several GHz. The frequency of the master laser light is then given by $\nu_{\mathrm{master}} = \nu_{1_{S_0}-{}^3P_1,\,{}^{88}\mathrm{Sr}} + \sum_i n_i \times f_{\mathrm{AOM}_i} + m \times f_{\mathrm{EOM}}$, where m denotes the order of the sideband produced by the EOM[18], and the frequency of the photoassociation laser is $\nu_{\mathrm{FB}} = \nu_{\mathrm{master}} \pm f_{\mathrm{LO}} + f_{\mathrm{offset}}$, where $f_{\mathrm{offset}} = 12.05(5)$ MHz is an electronic offset inherent to the locking scheme, set by the polarity of the PID[19]. A schematic of the laser setup can be

[16] We often overcome our limited resources in 689-nm optical power by injection-locking DL100 Toptica lasers with the seeding light of the reference laser. The injection-locked lasers then act as a optical amplifiers. This process fully conserves the coherence of the reference laser, and we use it extensively for out 689-nm MOT beams and our photoassociation beams. When more than 30 mW of optical power are needed, a tapered amplifier can be used.

[17] The fiber-coupled EOM that we use is a lithium niobate phase modulator, model PM-0K5-10-PFU-PFU-830 produced by EOSpace, with a 3 dB bandwidth of about 12 GHz. We drive it with a Rhode and Schwartz SMB100A 9 kHz – 3.2 GHz frequency generator.

[18] We can use up to the third sideband to lock our system, corresponding to $m = \pm 3$ where the + and - signs indicate the blue and red sidebands respectively. Sideband generation is very inefficient for the sidebands of higher orders, leading to error signals too small to be used with our available RF amplifying systems.

[19] The sign of $\pm f_{\mathrm{LO}}$ is chosen by locking on the error signal produced by the condition $\nu_{\mathrm{FB}} > \nu_{\mathrm{master}}$ or $\nu_{\mathrm{FB}} < \nu_{\mathrm{master}}$ respectively.

found in Ref. [51]. This technique allowed us to apply detunings Δ of up to $h \times 10$ GHz compared to the $^1S_0 - {}^3P_1$ transition frequency of Sr — see Subsection 4.4.

4.3.2 The Rb-Sr photoassociation sample: densities, temperature, internal states

The Rb-Sr photoassociation sample consists of a few 10^5 Rb atoms and a few 10^6 Sr atoms, trapped in a crossed-beam optical dipole trap at a temperature of a few μK. The crossed-beam dipole trap, or "science trap", is based on laser beams of wavelength 1064 nm and (optionally) 532 nm. This trap is described in our publications presented in Chapter 3 and Chapter 6, and it is subject to regular adjustments of beam waists, intensity, geometry, ... to match the desired experimental conditions. The general principles underlying the production of μK-cold Rb-Sr samples are not specific to photoassociation experiments, and they are described in Refs. [52, 103] and in Chapter 3 and 6. The actual densities and temperatures that we used for the one-colour spectroscopy presented in this chapter are given at the end of this subsection, for each Rb-Sr isotopologue that we investigated. In the next paragraphs, we discuss the photoassociation-specific choices that we made to optimize the probability of observing Rb-Sr photoassociation events.

The first thing that has to be considered is the appropriate choice of atomic densities and temperatures. The goal is to maximise the amount of Rb atoms lost per unit time due to photoassociation, so that a large loss signal can be detected. Over the course of a photoassociation pulse, the evolution of the Rb atom number N_{Rb} (and the Sr atom number N_{Sr}) is given by

$$\begin{aligned} \frac{d}{dt}N_{\mathrm{Rb}} &= -K_{\mathrm{PA}}(I_p)\,\eta_{\mathrm{PA}}(T)\,N_{\mathrm{Rb}}N_{\mathrm{Sr}} \\ \frac{d}{dt}N_{\mathrm{Sr}} &= -K_{\mathrm{PA}}(I_p)\,\eta_{\mathrm{PA}}(T)\,N_{\mathrm{Rb}}N_{\mathrm{Sr}}\,, \end{aligned} \tag{4.5}$$

where only photoassociation-induced losses are taken into account. The local and peak photoassociation rates $K_{\mathrm{PA}}(I(\vec{r}))$and $K_{\mathrm{PA}}(I_p)$ do not depend on the Rb-Sr conditions of density and temperatures, and we discuss these terms in Subsection 4.4. The quantity $\eta_{\mathrm{PA}}(T)$ parametrizes the overlap of the Rb and Sr clouds with each other and with the photoassociation beam. It is given by $\eta_{\mathrm{PA}}(T) = (N_{\mathrm{Rb}}N_{\mathrm{Sr}} \times I_p)^{-1} \int n_{\mathrm{Rb}}(T,\vec{r}) \times n_{\mathrm{Sr}}(T,\vec{r}) \times I(\vec{r})\, d\vec{r}$, where $n_{\mathrm{Rb}}(T,\vec{r})$ and $n_{\mathrm{Sr}}(T,\vec{r})$ are the local temperature-dependent Rb and Sr densities, and $I(\vec{r})$ and $I_p = 2P/\pi\omega^2$ are the local and peak intensities of the photoassociation laser beam respectively. The quantity $\eta_{\mathrm{PA}}(T)$ is independent of the atom numbers N_{Rb} and N_{Sr}. However, it depends on T, because the Rb and Sr density distributions are Boltzmann distributions that

depend on the temperature (and on the trapping potential) — see Ref. [127], Equation (33). From Equations 4.5, the strategy is clear: to maximise the loss of Rb atoms, one needs to maximise N_{Sr} and $\eta_{\mathrm{PA}}(T)$[20]. In other words, one needs to maximise the spatial overlap of the Rb and Sr clouds (and align properly the photoassociation beam onto these clouds) and the amount of Sr atoms. That is the strategy we adopted. We typically load just enough Rb to get a clear absorption signal for each m_f-state, and load as much Sr as possible in the crossed-beam dipole trap. The resulting sample contains a few 10^4 Rb atoms in each m_f state, and at least a few 10^6 Sr atoms. As for the overlap, the gravitational sags of both Rb and Sr is negligible at the trap depths that we use, and the clouds are thus centered onto one another. They do not overlap perfectly though, since Rb and Sr experience different trapping potential, and thus different density profiles, due to their different polarisabilities $\alpha(\lambda)$ at the wavelength(s) of the laser beams of the crossed-beam dipole trap (see Appendix A for a discussion of optical dipole traps in the context of RbSr). However, they largely overlap at the center of the trap, where the trap potential is the strongest.

As for the temperature, we chose to work at the μK-temperatures that we obtain from laser cooling on the $^1S_0 - {}^3P_1$ transition of Sr, and subsequent thermalization with Rb. However, one can also perform photoassociation at lower or higher temperature. On the lower-temperature side, we could in principle perform evaporation of the Rb and Sr gases. Over the course of the evaporation process, the peak atomic density increases with decreasing atom number and decreasing temperature, ultimately forming Bose-Einstein condensates (or a Fermi sea in the case of fermionic ^{87}Sr). This is a technique that we use routinely in the laboratory. Such quantum-degenerate gases are denser than the μK-cold gases that we use for photoassociation, and thus provide in principle a better Rb-Sr photoassociation sample[21]. However, evaporation to quantum degeneracy takes between 5 and 10 s typically in

[20] Note that one could also detect the photoassociation-induced losses of Sr, instead of Rb. From Equations 4.5, one should then maximise N_{Rb} , i.e. load as much Rb as possible in the crossed-beam dipole trap. There are two important drawbacks to this approach. First, m_f-state renormalization is not possible in Sr, which limits severely the achievable detection sensitivity. Second, the frequency of the photoassociation beam is close to that of the $^1S_0 - {}^3P_1$ atomic transition of Sr. This leads to loss of Sr by off-resonant scattering, especially for small Δ, as discussed in Subsection 4.3.4 (this can be taken explicitly into account by adding the corresponding loss rate to the evolution of the Sr atom number over the course of the photoassociation pulse). Therefore, the Sr atom number varies with Δ, which makes it very inconvenient to use it as a probe of photoassociation events (Rb is not affected by this off-resonant scattering, and thus provides a stable baseline). To perform Rb-Sr photoassociation spectroscopy close to the D_1 line of Rb instead, where off-resonant scattering affects Rb but not Sr, it might be better to use Sr as a probe and to load as much Rb as possible into the trap. In this case, the dipole selection rules for the D_1 transition might provide good guidelines for the choice of magnetic field, light polarization and atomic polarization (i.e. Rb m_f-state preparation).

[21] At the end of evaporation, the dipole trap potential is very shallow (the trap depth in the gravity direction is of order $h \times 100\,\mathrm{kHz}$ for Sr, after evaporation to BEC) and the gravitational sags of the Rb and Sr gases are significant, which compromises their overlap. Furthermore, they quantum-degenerate gases might not be miscible, depending on their interspecies scattering length depending on the interspecies scattering length of the chosen Rb-Sr isotopologue. The gravitational sags can be canceled by ramping up the potential depth after evaporation. Furthermore, the immiscibility of the two gases can be avoided by matching exactly the trap frequencies of Rb and

our experiments, and for a 1 GHz spectroscopy scan at MHz resolution (i.e., 1000 experimental cycles) this amounts to a few extra hours of scan, compared to without evaporation. We prefer to avoid loosing that much time, given that these spectroscopy scans are already very time-consuming. On the higher-temperature side, we could choose to work with samples at a few ten or hundred μK. This permits the thermal broadening of the photoassociation lines, a technique which is useful to create broad loss features out of narrow resonances. The detection of RbSr magnetic Feshbach resonances, for instance, was facilitated by the thermal broadening of our Rb-Sr sample — see our publication presented in chapter 6. The thermal width of a given resonance feature is of the order of the temperature, which according to $k_B \times 1.0\ \mu\text{K} = h \times 20.8365\,\text{kHz}$ leads to a broadening of about 20 kHz at 1 μK and 2 MHz at 100 μK. The main drawback of this method is that the photoassociation signal is weaker for larger thermal broadening. Indeed, within the Rb-Sr atom pair thermal distribution of collisional energies, the proportion of atom pairs that are resonantly coupled to the electronically-excited molecular state at a given photoassociation frequency ν_{FB} decreases as the distribution gets larger. We chose not to compromise signal strength for increased broadening, and thus worked at μK temperatures. The typical $\sim h\times$ MHz molecular linewidths that we observed are anyway naturally rather broad, compared to the narrow linewidth of the $^1S_0 - {}^3P_1$ intercombination line of Sr[22] — see Tables B.1 and B.2.

Another important aspect of the preparation of the Rb-Sr photoassociation sample is the choice of the internal states of both Rb and Sr. As for ^{87}Rb, it is produced in its hyperfine ground state $f = 1$ using optical pumping, with each one of the m_f-states $m_f = 0, \pm 1$ equally populated. In the first stage of the experimental sequence, the strong magnetic field gradient of the 461-nm Sr MOT quadrupole field (55 G.cm^{-1} in the axial direction) depletes the $m_f = +1$ high-field-seeking state of Rb, and favors the retention of the low-field-seeking $m_f = -1$ during the experimental sequence. This results in a strong imbalance in the m_f-state distribution. To compensate for that, we "scramble" the m_f-states by performing several non-adiabatic RF sweeps across the $m_f = 0 - m_f = -1$ and $m_F = 0 - m_f = +1$ transitions[23]. We made attempts at spectroscopy scans with a Rb sample prepared in the $f = 2$ manifold, but we couldn't observe any photoassociation lines in the ^{87}Rb-^{87}Sr mixture over a few hundred MHz, in a range of detunings Δ where loss features could be observed in the $f = 1$ manifold[24]. As for Sr, the bosonic Sr isotopes ^{84,86,88}Sr have no nuclear spin

Sr, which we can do by using a bichromatic 1064/532 nm optical dipole trap. The reader interested in these matters is referred to Ref. [52].

[22] In the case of very narrow molecular lines, the thermal spread can easily dominate. This is the case in Sr_2 for instance, in which typical linewidths are of the order of a few ten kHz only close to the $^3P_1$ dissociation asymptote [128].

[23] The Rb absorption pictures shown in Figure 4.2 were taken without such compensation, hence the clear imbalance in the m_f-state populations.

[24] This could indicate broadening of the photoassociation lines, due to predissociation of the electronically-excited state into lower-lying hyperfine manifolds.

($i = 0$), which results in only one, non-magnetic $m_i = 0$ state in the electronic ground state $^1S_0$. The fermionic ^{87}Sr isotope, on the other hand, has a nuclear magnetic moment $i = 9/2$ and is prepared in its stretched state $m_i = -9/2$ via optical pumping, where m_i is the projection of the nuclear spin i onto the quantization axis provided by the external magnetic field [125]. This preparation in a stretched nuclear spin state proved essential to observe ^{87}Rb-^{87}Sr photoassociation-induced losses, as discussed in Subsection 4.3.3.

Temperature and densities Rb-Sr samples used in one-colour spectroscopy

The bosonic isotopologue mixtures ^{87}Rb-^{84,86,88}Sr have a temperature of 1.0(1) μK, with average densities of $0.3 - 4 \times 10^{12}$ cm^{-3} for Sr and $2 - 7 \times 10^{12}$ cm^{-3} for Rb (summing over all Rb m_f-states). The (angular) trap frequencies $\{\omega_x, \omega_y, \omega_z\}$ are $2\pi \times \{66(6), 57(6), 560(50)\}$ Hz for Sr and $2\pi \times \{110(10), 95(9), 950(80)\}$ Hz for Rb. Here z is the direction of gravity and y the propagation direction of the horizontal optical dipole trap, which provides the restoring force against gravity. The fermionic isotopologue mixture ^{87}Rb-^{87}Sr has a temperature of 1.5(1) μK, average densities of $2 - 6 \times 10^{11}$ cm^{-3} for Sr and $0.8 - 3 \times 10^{12}$ cm^{-3}. The trap frequencies are $2\pi \times \{76(6), 65(8), 612(25)\}$ Hz for Sr and $2\pi \times \{125(17), 110(13), 874(51)\}$ Hz for Rb.

4.3.3 The photoassociation magnetic field and light polarization

At the time of the photoassociation pulse, an homogeneous magnetic field B is applied onto the Rb-Sr samples. This field is set to $B = 2.15$ G for ^{87}Rb-^{84}Sr, $B = 4.61$ G for ^{87}Rb-^{86,88}Sr, and $B = 2.15 - 2.73$ G for ^{87}Rb-^{87}Sr in the experiments presented in this chapter. The photoassociation laser light propagates colinearly to the applied magnetic field B and it is left-circularly polarized with respect to the magnetic field direction. In the next two paragraphs, we indicate the reasons for these experimental choices.

The application of a magnetic field during photoassociation serves two purposes. First, it lifts the degeneracy of the m_f states of both the initial scattering Rb-Sr state and the detected RbSr* molecule. At magnetic fields of a few G, the Zeeman energy associated with a single Rb atom in a given m_f state of the $f = 1$ manifold is $E_{m_f}(B) = g_f \, m_f \, \mu_B \, B$, where $\mu_B = h \times 1.3996$ MHz/G is the Bohr magneton and $g_f \simeq -1/2$ is the $f = 1$ low-field g-factor of ^{87}Rb — see [50] and Chapter 5, Figure 5.8. This energy defines the internal energy of the initial Rb-Sr pair, because the ground-state Sr magnetic sensitivity is almost null[25]. The RbSr* detected state is associated with the effective F_{exc}-number[26], and the associated Zeeman energies are

[25] Only the fermionic isotopes ^{87}Sr has a magnetic sensitivity, due to its non-zero nuclear spin, and it is very small compared to that of Rb — see Chapter 5, Equations 5.46.

[26] It is customary to use uppercase letters to denote the quantum numbers F and m_F of a molecule, and lowercase letters for the quantum numbers f and m_f of an atom.

$E_{\mathrm{mol},\,m_{F_{\mathrm{exc}}}} = E_{\mathrm{mol}}(0\,G) + g\; m_{F_{\mathrm{exc}}}\; \mu_B\; B$, where g is the g-factor of the excited molecule and $m_{F_{\mathrm{exc}}}$ can take the values $m_{F_{\mathrm{exc}}} = -F_{\mathrm{exc}}, -F_{\mathrm{exc}}+1, ..., F_{\mathrm{exc}}$. The g-factor is unknown prior to the detection and characterization of the excited molecular state (see Appendix B, Table B.3 in which the results of such a characterization is presented), and in general both F_{exc} and g are different from the f and g_f of the Rb-Sr atom pair state. Therefore in presence of the magnetic field, the Rb loss features induced by the detection of a given molecular state occur at different detunings Δ for different m_f states. Only a few G of magnetic field are necessary to shift these transitions by a few MHz from one another. We exploit this to cancel the detrimental effect of the overall Rb atom number fluctuations from one experimental run to the other. Instead of analysing the raw atom number N_{m_f} of each m_f state, subject to shot-to-shot fluctuation, we instead analyse the relative population $p(m_f)$ in each state, defined as the atom number in the m_f-state of interested divided by the sum of all other Rb atoms. The loss features are then resolved independently for each m_f-state. This renormalization, permitted by the combination of the Stern-Gerlach separation and of the applied magnetic field B at the time of photoassociation, improves dramatically the one-colour spectroscopy signal-to-noise, hence improving the detection sensitivity. This technique proved crucial to detect very weak photoassociation signals.

The second purpose of the magnetic field is to define a quantization axis for the photoassociation transitions, with respect to which the laser light polarization has to be set such that it maximises the probability of photon absorption. The dipole selection rules for electronic transitions of atoms gives guidelines for the choice of polarization and magnetic field axis, although they might not always apply to photoassociation transitions[27]. Since the photoassociation laser has its frequency close to the excitation frequency of the $^1S_0$ – $^3P_1$ atomic transition of Sr, we use the selection rules for this transition as guidelines. This is in general not a correct molecular spectroscopy approach, because the mixing of atomic orbitals in electronically-excited molecular states may modify these selection rules. However, it constitutes a good starting point, and we could detect many RbSr one-colour resonances based on these guidelines. They proved very important to detect ^{87}Rb^{87}Sr resonances, where the non-zero nuclear spin of ^{87}Sr imposes constraints on the polarization of the light (see the following lines) and on the polarization of the Sr atoms (see Subsection 4.3.2). In our experiments, the photoassociation laser light propagates colinearly to the applied magnetic field B and is left-circularly polarized with respect to the magnetic field direction. Therefore, in terms of single-atom electronic transitions, it maximises the absorption cross-section of the σ^- $|^1S_0, m_J = 0\rangle$ – $|^3P_1, m_J = -1\rangle$ transition of

[27] The simple parity selection rules that apply to electronic states of atoms can get more complicated when it comes to molecules with a vibrational and rotational structure, which couples to the electronic and hyperfine degrees of freedom.

Sr[28]. For the bosonic isotopes ^{88}Sr, ^{86}Sr and ^{84}Sr, the π, σ^- and σ^+ transitions have the same strength, and therefore any choice of polarization/quantization axis is as good as the others, as far as maximising the absorption cross-section goes. However, the definition of the quantization axis by the magnetic field is critical in the case of the fermionic isotope ^{87}Sr, which has a nuclear spin $i = 9/2$. This is because, in ^{87}Sr, the only fully-closed transitions are the σ^- $|^1S_0, i = 9/2, m_i = -9/2\rangle$ – $|^3P_1, f = 11/2, m_f = -11/2\rangle$ transition and the σ^+ $|^1S_0, i = 9/2, m_i = +9/2\rangle$ – $|^3P_1, f = 11/2, m_f = +11/2\rangle$ transition . Therefore, only these two transitions display a Clebsch-Gordan coefficient CG = 1 maximising the absorption cross-section[29]. All other transitions, including all transitions involving a non-stretched $m_i = -7/2, -5/2, ..., +7/2$ initial state have CG < 1 due to the possibility for the excited atom to decay back into a different m_i state than the initial one. Therefore, for these transitions the absorption cross-section is suppressed. The polarization of our ^{87}Sr sample in the stretched $m_f = -9/2$ state of the $^1S_0$ manifold was of critical importance to observe ^{87}Rb^{87}Sr resonances, as well as the choice of left-circularly polarized photoassociation light to drive "σ^--like" molecular transitions[30]. We couldn't observe any photoassociation-induced loss signal during our first attempts at photoassociating ^{87}Rb and ^{87}Sr using an unpolarized ^{87}Sr sample and arbitrary light polarization.

4.3.4 The lifetime of the Rb-Sr sample and the choice of pulse time and laser intensity

The irradiation time T_{pulse} and the intensity of the photoassociation laser should always be maximised in order to maximise the probability of observing photoassociation events. However, the limited lifetime of the Rb-Sr sample also has to be considered in order to make the proper choices, as we explain in the next paragraphs.

[28] We refer here to the angular contribution of the cross-section, which sets the selection rules for dipolar electronic transitions. According to these rules the polarization of light has to be linear and parallel to the quantization axis of the magnetic field to drive π transitions with a Clebsch-Gordan coefficient CG = 1, and left/right circular and perpendicular to the quantization axis to drive σ^-/σ^+ transitions with CG = 1.

[29] We remind the reader that the electronically-excited $^3P_1$ manifold of Sr is associated with the orbital electronic angular momentum $L = 1$, the total electronic spin $S = 1$ and the total electronic angular momentum $J = 1$. The fermionic isotope has a nuclear spin $i = 9/2$, in contrast to the bosonic isotopes, which results in the splitting of the $^3P_1$ manifold into three $f = 7/2, 9/2$ and $11/2$ hyperfine manifolds. See Subsection 2.1.5 for a presentation of atomic and molecular term symbols.

[30] We could achieve similar results with the $m_i = +9/2$ state of the $^1S_0$ manifold, using right-circularly polarized photoassociation light. Note that the CG = 1 condition cannot be achieved for the excited $|^3P_1, f = 9/2\rangle$ and $|^3P_1, f = 7/2\rangle$ atomic manifolds, irrespective of light and atomic polarization conditions. Furthermore, a ^{87}Sr ground-state Sr atom polarized in $m_i = -9/2$ cannot be coupled to these manifolds through a σ^- transition (there is no $m_f = -11/2$ state in any of these two manifolds). This might contribute to explain the relative weakness of the photoassociation signals that we observed below these asymptotes compared to the $|^3P_1, f = 11/2\rangle$ manifold. Additionally, the molecular states that lie above the $|^3P_1, f = 11/2\rangle$ asymptote might predissociate quickly into the corresponding continuum of excited atom pairs, leading to a broadening of the molecular transition and therefore to a dilution of the signal strength.

The lifetime of the atomic sample is limited by two factors. The first one is the loss of Rb and Sr atoms by inelastic three-body losses, where the collision of three atoms leads to the formation of a diatomic molecule and to the transfer of the corresponding binding energy to the molecule and to the third atom in the form of kinetic energy. The energy released is typically much higher than the trap depth, and leads to the loss of both molecule and atom from the trap. The three-body loss coefficient scales as $K_3 \propto a_s^4$ where a_s is the s-wave scattering length [129][31]. Correspondingly, we observe strong three-body losses in the ^{87}Rb-^{87}Sr mixture, which has a very large interspecies scattering length ($a_s = 1421(98)\ a_0$, as shown in Table 1.1). This limits the lifetime of the ^{87}Rb-^{87}Sr sample to a few hundred ms, and we do no observe any photoassociation events after about 400 ms of laser irradiation, because the Sr atom number N_{Sr} becomes too small. In the mixtures ^{87}Rb-^{84,86,88}Sr, the Rb-Sr s-wave scattering length is more reasonable and leads to negligible three-body losses over several seconds, at least at the densities we use for photoassociation. Accordingly, we set T_{pulse} to 400 ms for ^{87}Rb-^{87}Sr and to several seconds for the ^{87}Rb-^{84,86,88}Sr mixtures.

The second factor that limits the Rb-Sr sample lifetime is the loss of Sr atoms due to off-resonant absorption of photons from the photoassociation beam. The photon scattering rate of Sr is $\frac{\gamma}{2}\frac{s}{1+s+4(\Delta/\gamma)^2}$ where $s = I/I_{\mathrm{sat}}$ is the saturation parameter, $I_{\mathrm{sat}} = 3.0\ \mu\mathrm{W.cm}^{-2}$ the saturation intensity, $\gamma = 2\pi \times 7.50\,\mathrm{kHz}$ the linewidth of the $^1S_0$ – $^3P_1$ transition and $\Delta = \nu_{^1S_0 - {}^3P_1} - \nu_{\mathrm{FB}}$ the detuning of the photoassociation laser frequency from the frequency of the $^1S_0$ – $^3P_1$ Sr transition. Each absorption event leads to a momentum kick in the direction of propagation of the photoassociation beam. The corresponding recoil energy is $E_r = \hbar^2 k^2/2m_{\mathrm{Sr}} = h \times 4.8 - 5\,\mathrm{kHz}$, where m_{Sr} is the mass of the Sr atom (which is slightly different for each Sr isotope) and $k = 2\pi/\lambda$, with $\lambda = 689$ nm the wavevector magnitude of the photoassociation light. When the energy accumulated by a Sr atom due to successive absorption events becomes comparable with the trap depth, the atom leaves the trap and is lost. At our typical trap depths of $h \times 100$ – $500\,\mathrm{kHz}$, this corresponds to the scattering of a few ten photons[32]. We set the intensity such that the remaining Sr atom number seen on absorption pictures after the photoassociation pulse is within 10 – 30 % of the initial atom number. We leave this residual atom number to verify that we didn't loose the capability of producing a Sr sample, due to experimental issues[33], while the typically hours-long spectroscopy scan was executed. The peak intensity $I_0 = 2P/\pi\omega^2$ of the photoassociation beam,

[31] Taking into account the actual molecular structure, corrections can be made to this scaling. In particular, the s-wave scattering length for which three-body losses are maximally suppressed is not exactly $a_s = 0$ — see Equation (7.6) and its discussion in Ref. [129]. They result in a shift of the maximum of losses with respect to the scattering length and are irrelevant to our discussion.

[32] The photoassociation beam propagates in the horizontal plane, where the dipole trap confinement is the weakest.

[33] Typically including laser delocks, electronics failures, broken shutters blocking laser cooling light, ...

set by its total optical power P and its Gaussian beam waist $\omega = 110(10)$ μm[34], is adapted accordingly by using low intensities in the scan regions of small Δ and large intensities in the regions of large Δ. In deep regions of the target potential, where Δ is very large, the off-resonant scattering is negligible and it is best to use maximum optical intensity to maximise the coupling between atom pair and molecular state. The laser intensities that we used are in the range 0.01 – 100 W.cm^{-2} and in the regions of large Δ they were limited by the available optical power of our photoassociation laser.

[34]The waist of the photoassociation beam has been chosen such that it overlaps largely with the Rb cloud, which is more compressed than the Sr cloud in the $1064 - 1070$ nm optical dipole traps.

4.4 The experimental data and their analysis

The Rb-Sr photoassociation spectra obtained closed to the $^1S_0 - {}^3P_1$ asymptote of Sr are presented in Figure 4.3 and in Tables B.1 and B.2 of Appendix B, for all four isotopologues that we investigated: ^{87}Rb^{84}Sr, ^{87}Rb^{86}Sr, ^{87}Rb^{87}Sr and ^{87}Rb^{88}Sr. These spectra were obtained using the methods described in the previous sections[35]. The gap in the ^{87}Rb^{86}Sr spectrum is due to the presence of a strong Sr_2 resonance at $\Delta = 3.15(20)$ GHz, which depletes the Sr cloud and prevents Rb-Sr photoassociation. The gap in the ^{87}Rb^{84}Sr was scanned using the same Rb-Sr sample as discussed previously, but with different laser irradiation conditions, and no loss signal was observed in that range. For each isotopologue, the zero of the frequency axis is the zero-magnetic-field resonance frequency of the atomic $^1S_0 - {}^3P_1$ transition of Sr, which we measure experimentally for each isotope of Sr. In order to cancel thermal broadening, which would otherwise limit the accuracy of this reference, the transition frequency is measured in a Sr BEC for all bosonic isotopes of Sr, and in a very cold gas of a very hundred nK for the fermionic isotope ^{87}Sr. These measurements are performed at extremely low laser intensities to avoid any power-broadening[36]. The $^1S_0 - {}^3P_1$ transition has a linewidth of $\gamma/2\pi = 7.5$ kHz, and we measure this transition frequency with an accuracy of about 30 kHz (this number was most likely limited by magnetic and/or laser frequency noise at the time of data taking). The molecular structure properties that we extracted from the one-colour RbSr spectra are presented and discussed below.

Three parameters are especially important in view of understanding the excited molecular potentials probed by one-colour spectroscopy: the resonance positions Δ_{PA} — where the subscript PA stands for photoassociation, and the position is given with respect to the Rb ($^1S_0$)+Sr ($^3P_1$) dissociation asymptote, as shown in Figure 4.2[37] — , the spontaneous decay rate $\gamma/2\pi$ of the detected molecular states and the number of Zeeman sublevels of the detected states and the associated g-factors. In the following paragraphs we explain how to extract each one of these parameters from the experimental spectra.

The resonance positions of the photoassociation lines Δ_{PA} are obtained by fitting the Rb loss features observed in the spectra with Lorentzian fit functions. A magnetic field of a

[35] We remind the reader that the Rb sample is prepared in the $f = 1$ manifold, with all three $m_f = 0, \pm 1$-states almost equally populated. The bosonic ^{84}Sr, ^{86}Sr and ^{88}Sr atom have $i = f = 0$ in the ground state $^1S_0$. The fermionic isotope ^{87}Sr has $i = f = 9/2$ in $^1S_0$, and it is prepared in the stretched state $m_i = -9/2$.

[36] The saturation intensity of the $^1S_0 - {}^3P_1$ transition of Sr is $I_{sat} = 3.0\ \mu$W.cm^{-2}, and the peak laser intensity is $I_0 = 2P/\pi\omega^2$, where ω is the waist of the laser beam and P the optical power. This means that with the beam waist $\omega = 110(10)\ \mu$m of our photoassociation beam, optical powers of less than 1 nW have to be used to avoid power-broadening.

[37] The fermionic isotope ^{87}Sr has a nuclear spin $i = 9/2$, which splits the $^3P_1$ fine-structure manifold into three $f = 7/2, 9/2$ and $11/2$ non-degenerate hyperfine manifolds. The corresponding resonance positions are given with respect to the $f = 7/2$ threshold, which has the highest energy.

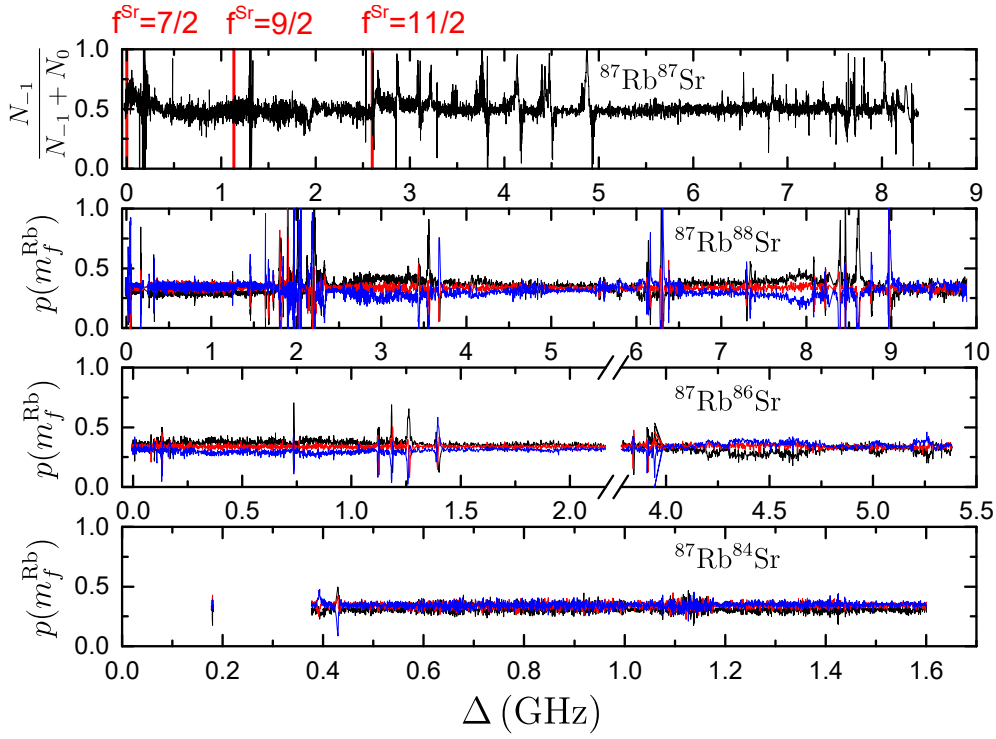

FIGURE 4.3: Results of the RbSr one-colour spectroscopy searches for the ^{87}Rb^{87}Sr, ^{87}Rb^{88}Sr, ^{87}Rb^{86}Sr and ^{87}Rb^{84}Sr isotopologues. The Rb population in the states $f = 1, m_f = -1$ (black squares), $m_f = 0$ (red circles), and $m_f = +1$ (blue triangles) are displayed as a function of the detuning Δ of the photoassociation laser frequency with respect to the Sr $^1S_0$ – $^3P_1$ atomic transition. The zero of the frequency axis is the zero-field $^1S_0$ – $^3P_1$ transition of Sr. The three hyperfine manifolds associated with $^3P_1$ in ^{87}Sr (not to be confused with the $f = 1$ manifold of Rb) are indicated in red letter, and the associated atomic transitions are marked by red lines. For this isotope the zero of the frequency axis is the $(^1S_0, i = 9/2)$ – $(^3P_1, f = 7/2)$ transition. Data taken by V. Barbé and A. Ciamei, figure created by A. Ciamei.

few G is applied during the photoassociation pulse, which enhances dramatically the detection sensitivity of the one-colour spectroscopy scans, as explained in Subsection 4.3.3. However, we are interested in the zero-magnetic-field resonance positions. We used two methods to extract them. The first is to locate the resonance detected during the one-colour spectroscopy scan, in presence of the magnetic field, and then to measure each one of these resonances again at zero magnetic field (i.e. $B < 30\,\mathrm{mG}$, which is the best precision we achieved on the magnetic field magnitude at the time of data taking). The raw atom number N_{m_f} is then used for fitting the loss features, instead of the populations $p(m_f)$. The detection sensitivity is of course degraded in absence of m_f-state renormalization, but since the resonance has been detected already it is not a problem. The second method is to measure the resonances corresponding to one given molecular state at several values of the magnetic field, and then extrapolate the zero-field resonance position from the observed magnetic behaviour. Such measurements are shown in Ref. [52], Figure 5.7, in the context of Rb-Sr photoassociation also. Both methods are time-consuming, especially the second one. All resonances positions reported for the bosonic isotopologues, Table B.1, correspond to the extracted zero-magnetic-field positions. The resonance positions of the ^{87}Rb-^{87}Sr fermionic isotopologue, on the other hand, were not extracted at zero magnetic field. There are so many of such resonances that it would have been extremely time-consuming to do so, and we didn't have a good reason to perform this characterization. We instead estimated the ^{87}Rb-^{87}Sr zero-magnetic-field resonance positions, and the corresponding error bars, based on the value of the magnetic field during photoassociation and the average magnetic moment that we measured for all ^{87}Rb^{87}Sr molecular states that we characterized (see Table B.3). These resonance positions are reported in Table B.2.

The spontaneous decay rates $\gamma/2\pi$ of the detected molecular states are obtained by fitting the Rb loss features with a model fit function more specific to photoassociation processes, Equation 4.8 given below. The measured decay rates are typically of order MHz, as reported in Table B.3[38]. To construct the fit function, we assume that the loss of Rb atoms

[38]We didn't expect such broad linewidths, owing to the narrow $\gamma/2\pi = 7.5\,\mathrm{kHz}$ linewidth of the Sr $^1S_0 - {}^3P_1$ atomic transition. This might be caused by the mixing of the excited potentials correlating to $^3P_1$ with the ones correlating to the Rb asymptotes — the D_1 and D_2 lines of Rb have respectively $\gamma/2\pi = 5.746(8)$ MHz and $\gamma/2\pi = 6.065(9)$ MHz [50] —, or to predissociation of the atom pair into the $^3P_0$ continuum of scattering states Rb ($^2S_{1/2}$) + Sr ($^3P_0$).

over the course of the photoassociation pulse is dominated by two mechanisms: Rb-Sr photoassociation and three-body losses[39]. Furthermore, we assume for simplicity that the three-body losses are induced by Sr-Sr-Rb collisions[40]. The temporal evolution of the Rb atom number N_{Rb} is then

$$\frac{d}{dt}N_{\mathrm{Rb}} = -K_{\mathrm{PA}}(I_p)\,\eta_{\mathrm{PA}}(T)\,N_{\mathrm{Rb}}N_{\mathrm{Sr}} - K_3\,\eta_3(T)\,N_{\mathrm{Rb}}N_{\mathrm{Sr}}^2\,. \tag{4.6}$$

The K_3 coefficient is the three-body Sr-Sr-Rb loss coefficient[41]. The quantities $\eta_3(T)$ and $\eta_{\mathrm{PA}}(T)$ parametrize the overlap of the Rb and Sr clouds with each other and with the photoassociation beam, for three-body loss and photoassociation-induced loss processes respectively. The former is given by $\eta_3(T) = (N_{\mathrm{Rb}}N_{\mathrm{Sr}}^2)^{-1}\int n_{\mathrm{Rb}}(T,\vec{r})\times n_{\mathrm{Sr}}^2(T,\vec{r})\,d\vec{r}$, where $n_{\mathrm{Rb}}(T,\vec{r})$ and $n_{\mathrm{Sr}}(T,\vec{r})$ are the local temperature-dependent Rb and Sr densities. The latter is given by $\eta_{\mathrm{PA}}(T) = (N_{\mathrm{Rb}}N_{\mathrm{Sr}}\times I_p)^{-1}\int n_{\mathrm{Rb}}(T,\vec{r})\times n_{\mathrm{Sr}}(T,\vec{r})\times I(\vec{r})\,d\vec{r}$, with $I(\vec{r})$ and $I_p = 2P/\pi\omega^2$ the local and peak intensities of the photoassociation laser beam respectively. Both $\eta_3(T)$ and $\eta_{\mathrm{PA}}(T)$ are independent of the atom numbers N_{Rb} and N_{Sr}. However, they depend on the temperature T, because the Rb and Sr density distributions are Boltzmann distributions that depend on the temperature (and on the trapping potential) — see Ref. [127], Equation (32). The local and peak photoassociation rates $K_{\mathrm{PA}}(I(\vec{r}))$ and $K_{\mathrm{PA}}(I)$ have a Lorentzian lineshape, given by

$$K_{\mathrm{PA}}(I(\vec{r})) = c_1 \times \frac{\gamma}{(\gamma/2)^2 + (\Delta - \Delta_{\mathrm{PA}})^2} \times \frac{I(\vec{r})}{I_p}\,, \tag{4.7}$$

where c_1 is a constant, which carries the information about the transition dipole moment induced between the scattering and molecular states by the photoassociation light — see

[39] The rate of collisions of Rb atoms with particles from the background gas of the vacuum chamber depends quality of the vacuum. Our vacuum-limited lifetime is $\tau \sim 30$ s, as measured from the 1/e lifetime of a Sr BEC in an optical dipole trap. It is therefore much larger than the photoassociation pulse time T_{pulse}, which is 400 ms for ^{87}Rb-^{87}Sr and a few seconds for the other isotopic mixtures — see Subsection 4.3.4. Collisions with the background gas and the associated one-body losses can thus be safely neglected over the course of the photoassociation pulse.

[40] At the densities we use for photoassociation, we observe no Rb atom loss over the course of several seconds, if only Rb is in the trap. Therefore Rb-Rb-Rb collisions can be neglected here. In the case of the fermionic mixture ^{87}Rb-^{87}Sr, on the other hand, the very large s-wave interspecies scattering length ($a_s = 1421(98)\ a_0$) leads to strong three-body losses and a rapid decrease of the Rb atom number. These losses are induced by either Rb-Rb-Sr or Rb-Sr-Sr collisions, which we cannot distinguish experimentally here. The three-body losses give rise to only small corrections of the fitted spontaneous decay rates $\gamma/2\pi$, therefore it was chosen to consider only Sr-Sr-Rb events for simplicity. This choice simplifies the expression of the Rb atom number, Equation 4.8, which we use for fitting the loss features.

[41] See for instance Ref. [130] for rate equations analogous to Equation 4.6, in the context of a Rb three-body loss study.

Ref. [53], Equation (4.25) and Ref. [123]. This constant is therefore sensitive to the polarization of the light, as discussed in Subsection 4.3.3. We further assume that the temperature of the atoms doesn't change during the photoassociation pulse[42], and that N_{Sr} is not affected by photoassociation events[43]. Setting $c_2 = \int_0^{T_{\mathrm{pulse}}} c_1\ K_{\mathrm{PA}}(I_p)\ \eta_{\mathrm{PA}}(T)\ N_{\mathrm{Sr}}\ dt$ and $c_3 = \int_0^{T_{\mathrm{pulse}}} K_3\ \eta_3(T)\ N_{\mathrm{Sr}}^2\ dt$[44], the Rb atom number is then

$$N_{\mathrm{Rb}}(t) = N_{\mathrm{Rb}}(0) \times \exp\left(-c_2\ \frac{\gamma}{(\gamma/2)^2 + (\Delta - \Delta_{\mathrm{PA}})^2} - c_3\right)\ , \tag{4.8}$$

which is the model fit function we used to fit the experimental loss features and extract γ. Complementary information about this fitting procedure can be found in Ref. [51]. Importantly, the measured γ and Δ_{PA} are different from their "bare" values, due to the photoassociation light. The spontaneous decay rate $\gamma/2\pi$ is broadened due to the stimulated emission width, and Δ_{PA} is subject to a light shift[45], as is clear from Equation (4.25) of Ref. [53]. We investigated these effects on the resonances from which $\gamma/2\pi$ was extracted, by measuring the corresponding loss features as a function of laser power, and concluded that they are not broadened under our experimental conditions. We also measured the light shift of several resonances with the same method, and these shifts were of 100 kHz at most at our laser intensities. Note that the full width at half maximum of the Lorentzian fit used to extract Δ_{PA} slightly overestimates γ, as shown in Tables B.1 and B.2.

The number of Zeeman sublevels and the associated g-factor are obtained by measuring Δ_{PA} at several values of the magnetic field B, for a given excited molecular state. At zero magnetic field, all resonances induced by the presence of the detected molecular state are degenerate. At $B > 0\,\mathrm{G}$, however, the Zeeman sublevels split according to $\Delta E(B) = E(0\,\mathrm{G}) + \mu_{\mathrm{exc}}\ B = E(0\,\mathrm{G}) + g\ m_{F_{\mathrm{exc}}}\ \mu_B\ B$, where $\mu_B = h \times 1.3996\,\mathrm{MHz/G}$ is the Bohr magneton, μ_{exc} the magnetic moment of the excited molecular state, $m_{F_{\mathrm{exc}}}$ the projection of its total angular momentum F_{exc} along the B-field axis and g the associated g-factor[46]. Since we have

[42] This is in general not true. Photoassociation is stronger where the Rb and Sr densities are the largest, which is at the center of the optical dipole trap. Atoms in this region have less potential energy than the atoms at the edges of the trap, therefore their depletion leads to anti-evaporation and to heating of the gas. However we do not measure huge changes in the temperature of the clouds on absorption pictures, and we dismissed such effects from the fitting procedure. The absolute values of c_2 and c_3 are anyway irrelevant to the extraction of γ.

[43] This is a legitimate assumption, since we typically load about ten times more Sr atoms than Rb atoms into the optical dipole trap (see Subsection 4.3.2).

[44] Note that N_{Sr} depends on t due to the Sr off-resonant scattering of photons over the course of the photoassociation pulse (see Subsection 4.3.2). However, the knowledge of the temporal evolution of N_{Sr} is not needed here, since the absolute values of c_2 and c_3 are irrelevant to the extraction of γ.

[45] This shift of the optical Feshbach resonance is completely analogous to the shift of magnetic Feshbach resonances — see Chapter 5, Equation 5.8.

[46] Note that the magnetic behaviour, which does not always lead to energy shifts that scale linearly with the magnetic field, is not fully captured by the g-factor in all cases. In particular, states with only one Zeeman sublevel, i.e. $m_{F_{\mathrm{exc}}} = 0$, can exhibit a non-zero magnetic moment. See for instance the ^{87}Rb^{84}Sr molecular state detected at $\Delta_{\mathrm{PA}} = 173.50\,\mathrm{MHz}$, Table B.3.

full knowledge of the magnetic moment of the initial scattering state (see Subsection 2.2.1 in this chapter), it is possible to "track" the $m_{F_{\text{exc}}}$ states of the excited molecular state with the magnetic field, and to see them merge at zero magnetic field. This magnetic characterization method is beautifully explained in the PhD thesis of my predecessor Alex Bayerle, where examples of measured RbSr Zeeman diagrams are presented — see Ref. [52], Figure 5.9. The number of Zeeman levels of the detected molecular states, their magnetic moment μ_{exc} and the associated g-factor are presented in Table B.3[47].

[47] We only report the g-factor of the states for which there is no uncertainty on the total number of Zeeman sublevels and for which there is more than one sublevel.

Chapter 5

Magnetic Feshbach Resonances in RbSr

The first experimental observation of Feshbach resonances between alkali and closed-shell atoms, Rb and Sr respectively in our experiment, is to be considered one of the major results of this PhD thesis. In Section 5.1, we present the general physics of magnetic Feshbach resonances and show how such resonances can be used to magnetoassociate atom pairs into weakly-bound molecules in an optical lattice. The reference review of Feshbach resonances in ultracold atom experiments is given in Ref. [131], and the reader is encouraged to read it in complement to this chapter. Section 5.2 is dedicated to the physics of magnetic Feshbach resonances in bi-alkali systems, owing to their importance in the ultracold atom community. Special attention is given to Rb_2, which is of relevance for RbSr experiments. Sections 5.3, 5.4 and 5.5 are dedicated to the physics of RbSr Feshbach resonances, which arise from coupling mechanisms that are much weaker than the ones found in bi-alkali systems[1]. Mechanisms I and II, which lead to the strongest RbSr Feshbach resonances, are presented in Sections 5.3 and 5.4 respectively. Our theory collaborators were the first to predict the existence of such resonances [25, 26], and we were the first experimental group to observe them. This discovery led to the publication presented in Chapter 6. Section 5.5 is dedicated to extremely narrow RbSr Feshbach resonances, induced by mechanism III, which we discovered experimentally and which triggered a subsequently-published theoretical work [132].

[1] As should be clear from the reading of this chapter, the broad magnetic resonances that involve the exchange interaction between the two valence electrons in bi-alkali systems are simply absent in pairs of an alkali and a closed-shell atom, because they exhibit only one valence electron (the one of the alkali atom). Similarly, electronic spin-spin dipole interactions that give rise to narrow resonances in bi-alkali systems are absent. However, there exist anisotropic resonances that arise from nuclear and electronic spin dipole interactions, and are conceptually very similar to the electronic spin-spin interactions of bi-alkali systems. This type of extremely narrow RbSr resonances, that we discovered experimentally, is the subject of Section 5.5.

5.1 Magnetic Feshbach resonances and ultracold molecules: a general perspective

Feshbach resonances, or Fano-Feshbach resonances, arise when a continuum of scattering states couples resonantly to a discrete bound state. The resonant coupling results in a rapid change of the long-range phase of the scattering states across the resonance, and consequently to drastic changes in both elastic and inelastic scattering cross-sections.

The original work of Fano was performed in the context of helium autoionization in electron scattering experiments [133]. The highly asymmetric lineshapes obtained in Helium experiments were successfully explained by Fano, who indicated it to be the result of the coupling of the electronically doubly excited state of helium 2s2p, with binding energy $E_b \sim$ 60 eV, to the continuum of 2s ionized helium scattering states above the first-ionization energy of $\sim$ 24 eV. The characteristic lineshape associated with this process was named "Fano profile" after him. The RbSr photoassociation spectra that we obtained and that are presented in Section 4.2 and Figure 4.2 provide another example of Feshbach resonances: a discrete, electronically excited RbSr molecular state is resonantly coupled to the continuum of Rb-Sr atom pair scattering states in the RbSr electronic ground state by a laser photon. Such resonances are referred to as optical Feshbach resonances and are reviewed in Ref. [63].

In this chapter we focus on the case of magnetic Feshbach resonances, for which the resonance condition between continuum and molecular state is achieved through the application of an external magnetic field.

5.1.1 Magnetic Feshbach resonances

Magnetic Feshbach resonances, which are the subject of this chapter, arise when a molecular state of magnetic moment μ_{mol} and of internal energy E_{mol} is set close in energy to an atom pair scattering state of magnetic moment μ_{E} and of collisional energy $E = \hbar^2 k^2 / 2\mu$ (where μ is the reduced mass of the pair) upon application of an external magnetic field.

The channel to which the scattering state $|E\rangle$ of interest belongs is referred to as channel 1, also referred to as open channel[2] or background channel. It is defined by a potential energy curve (PEC)[3] and by a set of hyperfine quantum numbers that we will make explicit in the

[2]The terminology "open" and "closed" indicates the respective positions of the zero-collisional energy thresholds of the channels 1 and 2 with respect to the collisional energy of interest E. The threshold of the closed channel 2 lies higher in energy than $|E\rangle$, therefore it is energetically inaccessible — see Figure 5.1. On the other hand, the molecular states $|\psi^{(1)}_{\mathrm{mol}}\rangle$ and the scattering states $|E'\rangle$ with $E' < E$ of the open-channel PEC can be reached from $|E\rangle$ by releasing internal energy from the system. This situation arises for instance when three-body losses occur in the gas; the internal energy is then transferred to center-of-mass kinetic energy.

[3]An introduction to the concept of PEC and to the associated scattering and molecular eigenstates is given in Subsections 2.1.5 and 2.1.6, in the context of RbSr.

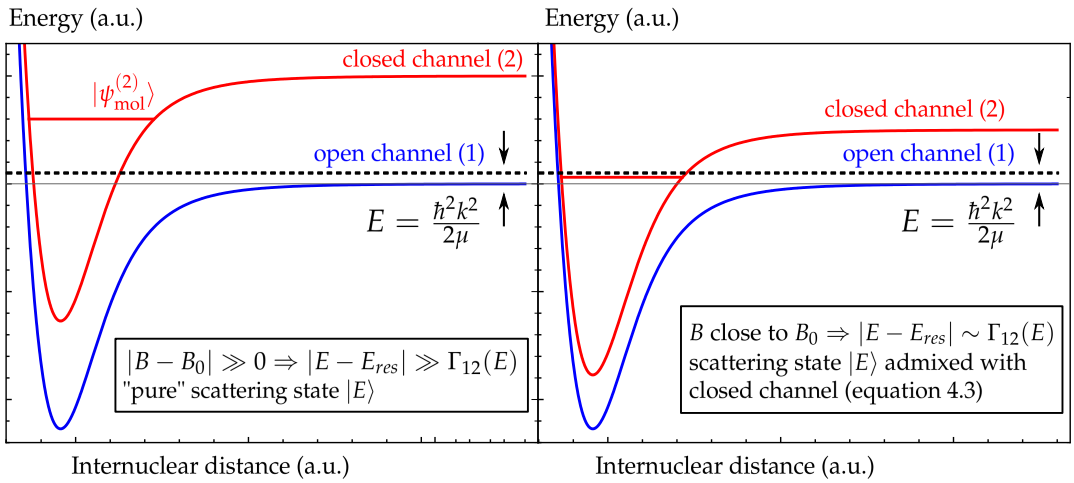

FIGURE 5.1: Magnetic Feshbach resonance. Upon application of an external magnetic field of magnitude B, a molecular state belonging to the closed channel (2) is brought close to degeneracy with a scattering state of collisional energy E belonging to the open channel (1) scattering threshold. At the resonance position both channels get mixed and the scattering phase of the open channel state is modified by the admixture with the closed channel.

cases of Rb_2 and RbSr in the next sections. The channel to which the resonant molecular state $|\psi^{(2)}_{\rm mol}\rangle$ of energy $E_{\rm mol,2}$ belongs is referred to as channel 2, or closed channel. The zero of energy of the system is defined to be the zero-collisional energy threshold $k = 0$ of the open channel, and therefore depends on the external magnetic field[4].

In the ultracold limit, the scattering states are predominantly s-wave (see Figure 2.5), corresponding to $N = 0$ in Equation 2.41 and are characterized by a collisional energy $E = \hbar^2 k^2/2\mu$ and by a radial scattering wavefunction $\chi^{\rm scat}_{k,N}(R)$. Importantly, while for molecular states $\chi^{\rm vib}_{\nu,N}(R) \to 0$ for $R \to \infty$ and thus unit-normalization $\langle \chi^{\rm vib}_{\nu,N}(R)|\chi^{\rm vib}_{\nu,N}(R)\rangle$=1 is possible, in absence of external confinement the scattering wavefunctions are not square-integrable and must be energy-normalized according to $\langle E|E'\rangle = \delta(E - E')$. We go back to this point in Subsection 5.1.2. The s-wave (i.e. $N = 0$) scattering radial wavefunctions have the asymptotic behaviour

$$\chi^{\rm scat}_{k,N=0}(R) \xrightarrow[R\to\infty]{} \sqrt{\frac{2\mu}{\pi k}} \sin(kR + \delta_{\rm bg}) \,, \tag{5.1}$$

[4]The magnetic moment of the open channel is "absorbed" in this definition: the energy of the open channel reduces to the collisional energy, and the magnetic energy of the closed channel state is given by the relative magnetic moment $\delta\mu = \mu_{\rm mol,2} - \mu_{\rm E}$.

where the asymptotic phase shift δ_{bg} is a property of the open-channel PEC [56]. It defines the background s-wave scattering length a_{bg} (typically expressed in units of the Bohr radius[5]) and thus the elastic s-wave collision cross-section $\sigma = 4\pi a^2$ through[6]

$$-ka_{\mathrm{bg}} = \tan(\delta_{\mathrm{bg}})\,. \tag{5.2}$$

The existence of a coupling term $\hat{V}_{12}$ between the closed and open channels admixes $|\psi^{(2)}_{\mathrm{mol}}\rangle$ with the scattering states of the open channel. As a result of this coupling, a scattering state $|E\rangle$ is transformed into the state of same energy E according to[7]

$$|E\rangle \to \sin(\delta_{\mathrm{res}})\frac{1}{\pi\,\langle E|\,\hat{V}_{12}\,|\psi^{(2)}_{\mathrm{mol}}\rangle}\left(|\psi^{(2)}_{\mathrm{mol}}\rangle + P\int_0^\infty \frac{\langle E'|\,\hat{V}_{12}\,|\psi^{(2)}_{\mathrm{mol}}\rangle}{E-E'}\,|E'\rangle\,dE'\right) - \cos(\delta_{\mathrm{res}})\,|E\rangle\ , \tag{5.3}$$

where the term in parenthesis is the molecular state $|\psi^{(2)}_{\mathrm{mol}}\rangle$ modified by the admixture with the scattering states of the open channel [56, 133]. The Cauchy principal value symbol P indicates that the integral is taken over all energies E' with the exception of $E' = E$. The asymptotic behavior of this modified scattering state is

$$\chi^{\mathrm{scat}}_{k,N=0}(R) \xrightarrow[R\to\infty]{} \sqrt{\frac{2\mu}{\pi k}}\sin(kR + \delta_{\mathrm{bg}} + \delta_{\mathrm{res}})\,, \tag{5.4}$$

where it is seen that the interaction with the molecular state $|\psi^{(2)}_{\mathrm{mol}}\rangle$ of channel 2 results in a change of the asymptotic phase shift of the scattering states $|E\rangle$ of channel 1. The asymptotic phase shift modified by this interaction is

$$\delta_{\mathrm{res}} = -\tan^{-1}\left(\frac{1}{2}\frac{\Gamma_{12}(E)}{E-E_{\mathrm{res}}}\right)\,. \tag{5.5}$$

Accordingly, the s-wave scattering length a becomes, owing to $-ka = \tan(\delta_{\mathrm{bg}} + \delta_{\mathrm{res}})$,

$$a(E) = a_{\mathrm{bg}} + \frac{1}{k}\frac{\Gamma_{12}(E)/2}{E-E_{\mathrm{res}}}\,. \tag{5.6}$$

The Breit-Wigner energy width of the Feshbach resonance is given by

[5] The Bohr radius is $a_0 = \frac{4\pi\epsilon_0\hbar^2}{m\,e^2} = 0.529177210$ Å, where m and e are the mass and charge of the electron respectively.

[6] The expression $\sigma = 4\pi a^2$ for s-wave collisions ($N = 0$) is valid for distinguishable particles, such as Rb-Sr or for identical bosons in different $|f, m_f\rangle$ states, such as two Rb atoms. For identical bosons in the same quantum state, such as two ^{84}Sr atoms, it is $\sigma = 8\pi a^2$. For identical fermions in the same quantum state, such as two ^{87}Sr atoms in the same $|I, m_I\rangle$ state s-wave collisions are prohibited by Pauli principle.

[7] Due to the $\sin(\delta_{\mathrm{res}})$ dependence, the relative contribution of the molecular state to the coupled scattering state is not symmetric across $\delta_{\mathrm{res}} = 0$. This asymmetry is characteristic of the Fano profile.

$$\Gamma_{12}(E) = 2\pi |\langle E| \hat{V}_{12} |\psi_{\text{mol}}^{(2)}\rangle|^2 , \tag{5.7}$$

and the position of the resonance is

$$E_{\text{res}} = E_{\text{mol},2} + E_{\text{shift},12} \quad \text{with} \quad E_{\text{shift},12} = P \int_0^\infty \frac{|\langle E'| \hat{V}_{12} |\psi_{\text{mol}}^{(2)}\rangle|^2}{E - E'} dE' . \tag{5.8}$$

These two parameters (Breit-Wigner width and position) are the most important quantities that characterize the Feshbach resonance. The Breit-Wigner width quantifies the range of collisional energies E for which the continuum is strongly coupled to $|\psi_{\text{mol}}^{(2)}\rangle$, across the position E_{res} — see Figure 5.1. The position E_{res} is shifted compared to the energy of the "bare" molecular state $E_{\text{mol},2}$, owing to its admixtures with the other scattering states $|E'\rangle \neq |E\rangle$ of the open channel, as seen from Equation 5.3.

At the position $E = E_{\text{res}}$, the s-wave scattering length diverges and so does the elastic s-wave collision cross section. The gas is strongly interacting, with an enormous amount of scattering events per unit time. In this regime, typically not only the elastic s-wave cross-section but also inelastic losses and three-body recombination rates are dramatically enhanced[8]. This is for us experimentalists both a blessing and a curse. A blessing, because it allows to perform Feshbach spectroscopy by inferring in a simple manner the binding energy of molecular bound states from the positions where inelastic losses occur — see Chapter 6. A curse, because close to the crossing point the gas might get destroyed before molecule association could be achieved.

Importantly, for low-energy scattering states with $E \to 0$ and thus $k \to 0$, the E-dependence of the Breit-Wigner width, Equation 5.7, follows the Wigner threshold law

$$\begin{aligned} \Gamma_{12}(E) &\propto \sqrt{E} \\ \Gamma_{12}(E) &\propto k . \end{aligned} \tag{5.9}$$

Therefore, the Breit-Wigner width can be expressed conveniently as $\Gamma_{12}(E) \xrightarrow{k\to 0} 2ka_{\text{bg}}\Gamma_{12}^0$, where Γ_{12}^0 is an energy-independent constant [131, 134]. The s-wave scattering length is thus

$$a(E) = a_{\text{bg}} \left(1 + \frac{\Gamma_{12}^0}{E - E_{\text{res}}}\right) . \tag{5.10}$$

[8] Far from any resonance, two-body collisions (elastic and inelastic) dominate in the low-density gases of our experiments — see Chapter 1, Section 1.1. Two-body inelastic collisions (aka, spin-exchange collisions) are completely absent in ground-state Sr but are present in ^{87}Rb. The corresponding spin-exchange rates are very low, as discussed in Subsection 5.2.2, but can be greatly enhanced close to a Feshbach resonance.

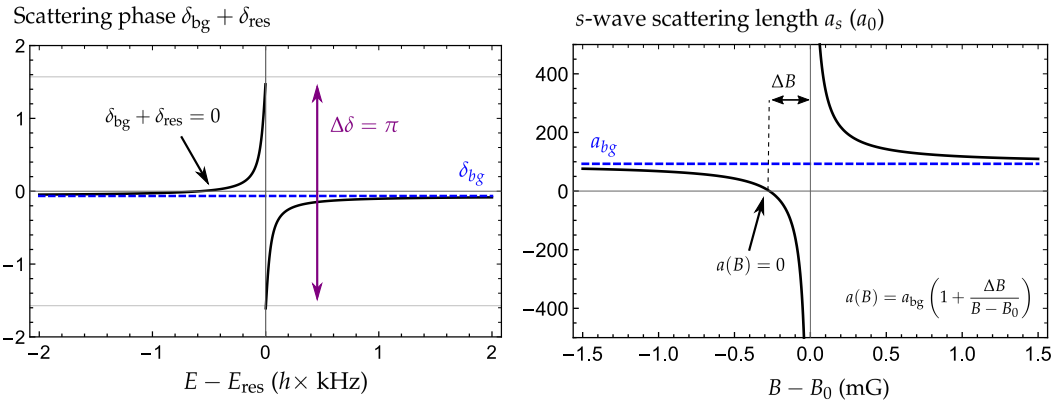

FIGURE 5.2: Scattering phase and s-wave scattering length near a magnetic Feshbach resonance. **Left panel:** Variation of the scattering phase shift across the $B_0 = 1311\,\mathrm{G}$ ^{87}Rb^{84}Sr s-wave Feshbach resonance. Across the resonance position, the phase shift varies rapidly between $+\pi/2$ and $-\pi/2$, and at the zero crossing the scattering phase shift cancels out due to the interference of the resonant and background scattering waves. **Right panel**: corresponding change in s-wave background scattering length in Bohr radius (a_0) units. At the resonance position the diverging scattering cross-section leads to three-body losses that are observable experimentally. The plotted s-wave scattering state has $E = \frac{\hbar^2 k^2}{2\mu} = k_B \times 1.0\ \mu$K, and the parameters of the resonance are $a_{bg} = 93\ \mathrm{a_0}$, $\Delta B = 0.27\,\mathrm{mG}$, $\delta\mu/h = 2.15\,\mathrm{MHz/G}$ and $\Gamma_{12}^0 = \Delta B/\delta\mu = h \times 0.58\,\mathrm{kHz}$.

In the context of magnetic Feshbach resonances, both $|E\rangle$ and $|\psi_{\text{mol}}^{(2)}\rangle$ have a magnetic moment and their relative energy can be tuned by applying an external magnetic field B. The magnetic moments $\mu_E(B)$ and $\mu_{\text{mol},2}(B)$ are in general B-field dependent themselves, in particular in the important case of hyperfine states $|f, m_f\rangle$ of alkali atoms[9]. Equation 5.10 then becomes

$$a(B) = a_{\text{bg}}\left(1 + \frac{\Delta B}{B - B_0}\right) \quad \text{with} \quad \begin{cases} B_0 = B_c + \delta B \\ \Delta B \propto \Gamma_{12}^0 \end{cases}, \tag{5.11}$$

which is the celebrated expression for the B-field dependent s-wave scattering near a magnetic Feshbach resonance. B_c is the magnetic field at which the molecular state would enter the continuum in absence of coupling between closed and open channel. The magnetic resonance shift δB can be reduced to the simple expression given in Equation 5.13, and is very small for resonances with small ΔB, such as RbSr resonances. ΔB quantifies the magnetic-field separation between the pole $a(B) \to \pm\infty$ and the zero crossing $a(B) = 0$, as shown in Figure 5.2. However, the physical quantity that is really of interest to quantify the strength of the molecule-continuum coupling is the Breit-Wigner width, not ΔB[10]. In particular, we require the Breit-Wigner width to be large for magnetoassociation purposes — see Subsection 5.1.2.

Magnetic Feshbach resonances thus arise under two conditions. First, that a molecular state $|\psi_{\text{mol}}^{(2)}\rangle$ can be set close to resonance with an atom pair scattering state $|E\rangle$ upon application of an external magnetic field[11]. Second, that a coupling term $\hat{V}_{12}$ exists between the open and closed channel and gives a non-zero value to the Breit-Wigner width, Equation 5.7.

Feshbach resonance shifts in RbSr

The initial treatment of Fano didn't include the interaction of the bound state $|\psi_{\text{mol}}^{(2)}\rangle$ with the bound states of the open channel, only its interaction with the continuum. In ultracold atom experiments, it can happen that a molecular bound state in the open channel lies close in

[9] The ^{87}Rb^{84}Sr resonance located at $B = 1311$ G involves the crossing of the ^{87}Rb^{84}Sr $|\nu = -4, N = 0\rangle$ vibrational state, which belongs to the closed channel $|f, m_f\rangle = |2, +1\rangle$ and has a magnetic moment $\mu_{\text{mol},2}$ given by $\mu_{\text{mol},2}/h = 1.075$ MHz/G at $B = 1311$ G, and of the atom pair state which belongs to the open channel $|f, m_f\rangle = |1, +1\rangle$ and has a magnetic moment μ_E given by $\mu_E/h = -1.077$ MHz/G at $B = 1311$ G.

[10] As is clear from the relation $\Gamma_{12}(E) \xrightarrow{k\to 0} 2ka_{\text{bg}}\Gamma_{12}^0$, for s-wave scattering the product $a_{\text{bg}}\Delta B$ is a good estimator of the strength of a Feshbach resonance. Therefore, ΔB can be used to compare the strength of resonances occurring in the same open channel PEC, since in that case the background s-wave scattering length a_{bg} is uniquely defined. This is for instance the case of the ^{87}Rb$_2$ resonances reported in Figure 5.6, taken from Ref. [135]. All resonances reported in the right table occur in the same open channel: same Rb atoms, same partial wave (s-wave) and same hyperfine states. Therefore, their relative strength can be compared by comparing their ΔB.

[11] That requires, in all cases known to the author, the set of hyperfine quantum numbers of the open and closed channel to be different. This is necessary for the magnetic moments of the two channels to differ.

energy to the resonance and shifts the resonance position[12]. This is simply taken into account by adding the interaction of the resonant molecular state $|\psi_{\text{mol}}^{(2)}\rangle$ with the open channel $|\psi_{\text{mol}}^{(1)}\rangle$ bound states to the expression of the shift. This leads to

$$E_{\text{shift}}^{(E,2)} = \int_0^\infty \frac{|\langle E'|\hat{V}_{12}|\psi_{\text{mol}}^{(2)}\rangle|^2}{E-E'}dE' + \sum \frac{|\langle \psi_{\text{mol}}^{(1)}|\hat{V}_{12}|\psi_{\text{mol}}^{(2)}\rangle|^2}{E-E_{\text{mol},1}}\,, \tag{5.12}$$

where the sum is taken over all open-channel bound states $|\psi_{\text{mol}}^{(1)}\rangle$, and only bound states close to the resonance contribute significantly to the shift. Remarkably, it has been shown that in the limit where the Wigner-threshold law applies, the magnetic shift is

$$\delta B = \frac{r_{\text{bg}}(1-r_{\text{bg}})}{1+(1-r_{\text{bg}})^2}\Delta B\,, \tag{5.13}$$

where $r_{\text{bg}} = a_{\text{bg}}/\bar{a}$ is the dimensionless background scattering length, renormalized by the mean scattering length $\bar{a} = 0.477989(2\mu C_6/\hbar^2)^{1/4}$ as defined by Gribakin and Flambaum [109, 136].

The strongest shifts we expect for the s-wave RbSr Feshbach resonances data presented in Chapter 6 occur in the ^{87}Rb^{87}Sr mixture, for which the last vibrational state has a very small binding energy $E_b < 40$kHz. Consequently, this mixture exhibits a very large s-wave background scattering length $a_{\text{bg}} = 1421(98)\ a_0$ where a_0 is the Bohr radius. Given the C_6 coefficient of RbSr in its electronic ground state ($1.784(15)\times 10^7$ Å^6 cm^{-1}, see Chapter 3), the mean ^{87}Rb^{87}Sr scattering length is $\bar{a} \simeq 74\ a_0$[13]. For the resonance with the largest ΔB that we observed (3.5 mG, see Table 6.1 in Chapter 6), this corresponds to a shift of less than 5 mG. Such shifts are well below the experimental resolution of our Feshbach spectroscopy (the experimental three-body loss width is for instance $\delta = 366(3)$ mG for the same resonance, owing to thermal broadening), and thus was not taken into account in our analysis for the fit of the ground-state PEC of RbSr.

5.1.2 Magnetoassociation in an optical lattice

Magnetic Feshbach resonances have been widely used in the cold atom community to produce ultracold molecules. Trapping the atoms in an optical lattice prior to molecule formation has several advantages: the suppressed center-of-mass motion prevents the molecules from chemically reacting with one another, since they are "pinned" on individual lattice sites,

[12] An extreme example of this is presented in Ref. [131], Figure 13. A molecular state of the closed channel crosses a weakly-bound open-channel molecular, at a slightly lower magnetic field than the field at which it crosses the zero-energy open-channel threshold. This creates an avoiding crossing and the open-channel bound state, "dressed" with the closed-channel molecular state is pushed towards the threshold where it creates a Feshbach resonance.

[13] This estimation is made using $a_0 \simeq 0.53$ Å and 1 cm$^{-1} = h \times 30$ GHz.

and the compression of the relative motion radial wavefunction of the atom pair increases the strength of the atom to molecule coupling compared to untrapped atoms. The original theoretical paper that investigated molecule formation using Feshbach resonances in an optical lattice is Ref. [136], and an excellent discussion of heteronuclear molecules in optical lattices can be found in Ref. [137].

The confining potential of the optical lattice site has to be added to the diatomic Hamiltonian[14], Equation 2.3, which leads to

$$\hat{H} = \hat{H}_{\text{rel}} + \hat{T}_c + \hat{\Delta}_{\text{trap}} \tag{5.14}$$

$$\hat{H}_{\text{rel}} = \hat{H}_{\text{vibration}} + \hat{H}_{\text{rotation}} + \hat{H}_{\text{Coriolis}} + \hat{T}_{e-N} + \hat{H}_e + \frac{1}{2}\mu{\omega_{\text{rel}}}^2 R^2 \tag{5.15}$$

$$\hat{T}_c = -\frac{\hbar^2}{2M}\vec{\nabla}_c^2 + \frac{1}{2}M{\omega_C}^2{R_C}^2 \tag{5.16}$$

$$\hat{\Delta}_{\text{trap}} = \hat{V}_{\text{anharm}}(\vec{R_C}, \vec{R}) + \mu{\Delta_\omega}^2\vec{R_C}\cdot\vec{R}\,. \tag{5.17}$$

The terms in blue refer to the effect of the trapping potential, and the harmonic angular frequencies for the relative and center-of-mass motion are $\omega_{\text{rel}} = \sqrt{\frac{M_A{\omega_B}^2 + M_B{\omega_A}^2}{M_A+M_B}}$ and $\omega_C = \sqrt{\frac{M_A{\omega_A}^2 + M_B{\omega_B}^2}{M_A+M_B}}$ respectively [56]. The trapping potential is thus decomposed into the sum of two harmonic terms, and of the corrections $\hat{\Delta}_{\text{trap}}$. The first of these corrections accounts for the non-harmonicity of the trapping potential, and the second for the differences $\Delta\omega^2 = |{\omega_A}^2 - {\omega_B}^2|$ in angular trap frequencies between the two atoms A and B on a lattice site[15]. These trap frequencies are set by the lattice depth s experienced by the particles A and B, which is defined as the ratio of the dipolar potential created by the lattice beams divided by the recoil energy of the particle at the lattice wavelength — see Section A.2 of the appendix. In our experiments, A and B are Rb and Sr and the lattice wavelength is 1064 nm. The lattice depth s depends linearly on the lattice beams intensity. Rb and Sr have almost the same mass, therefore their recoil energies are almost identical (see Equations A.11). However, they have different polarisabilities $\alpha(\lambda)$ at the wavelength $\lambda = 1064\,\text{nm}$. The ratio of their polarisabilities is $\alpha^{\text{Rb}}(1064\,\text{nm})/\alpha^{\text{Sr}}(1064\,\text{nm}) = 3.2$ (see Equations A.5). Therefore, at a given optical intensity the lattice depth s is about three times as high for Rb as it is for Sr, and the corresponding trap frequencies $\omega \propto \sqrt{s}$ are about 1.8 times larger for Rb than for Sr[16].

[14] We remind the reader that the diatomic Hamiltonian is the sum of the center-of-mass motion and of the relative motion, as shown in Equation 2.26.

[15] Angular trap frequencies and Gaussian waists of laser beams are denoted by the same symbol ω in this thesis. That's how these two quantities are usually referred to in the literature.

[16] The approximation $\omega \propto \sqrt{s}$ is valid for large lattice depth, and is typically very accurate for $s > 20$.

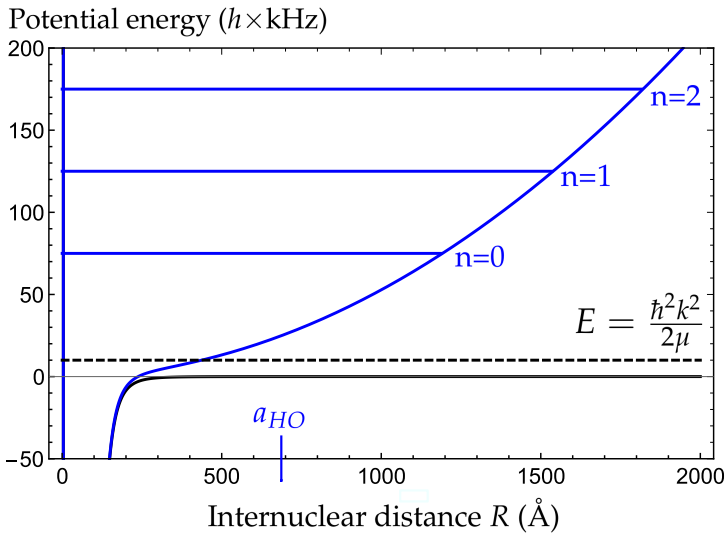

FIGURE 5.3: Free-space (black line) and optical lattice (blue line) situations for the relative motion of an atom pair of ^{87}Rb and ^{84}Sr. In the free space case, the s-wave scattering eigenstates are energy-normalized and constitute a continuum of positive collisional energy E above the dissociation threshold. In the optical lattice case, here displayed for a perfectly harmonic 3D isotropic lattice with $\omega_{\rm rel} = 2\pi \times 50\,$kHz, the atom pair eigenstates are unit-normalized and constitute a discrete set of energies $E = (3/2 + n)\hbar\omega_{\rm rel}$ and of relative spacing $\hbar\omega_{\rm rel}$, proportional to $\sqrt{I(x,y,z)}$ where $I(x,y,z)$ is the local lattice intensity. On-site interaction corrections are of order $\sim h\times$kHz for ^{87}Rb-^{84}Sr and are not depicted here. The harmonic oscillator length $a_{\rm HO}$ is set by $\omega_{\rm rel}$ and is much larger than the ^{87}Rb-^{84}Sr s-wave scattering length $a_S = 49$ Å $(93\,a_0)$. Therefore, the coupling between center-of-mass and relative motions induced by the difference in trap frequencies of ^{87}Rb and ^{84}Sr at $\omega_{\rm rel} = 2\pi \times 50\,$kHz is very small.

The corrective terms $\hat{\Delta}_{\text{trap}}$ couple the center-of-mass and relative motions[17]. In particular, the molecular vibration gets coupled to the lattice motion. This effect can in principle induce the decay of weakly-bound states (in particular our target molecular state for Feshbach association) to deeper-bound molecular states, accompanied with release of energy towards motional lattice states [J. Hutson, private communication]. We argue in the next paragraph that the anharmonic term $\hat{V}_{\text{anharm}}(\vec{R_C}, \vec{R})$ is small in the ground state of the center-of-mass motion. The second term $\mu {\Delta_\omega}^2 \vec{R_C} \cdot \vec{R}$ is non-zero in our case, because Rb and Sr have different polarisabilities at $\lambda = 1064$ nm and thus have different trap frequencies in our optical lattice — see Equation A.5. According to Ref. [56], this term is weak for $a_s / a_{\text{HO}} \ll 1$, where a_s is the s-wave scattering length for the atom pair and $a_{\text{HO}} = \sqrt{\frac{\hbar}{\mu \omega_{\text{rel}}}}$ is the harmonic oscillator length of the relative motion as defined by the trapping potential[18]. The largest lattice depths we ever reached in our experiments are approximately $s = 260$ for Sr and $s = 863$ for Rb, which correspond to $\omega_{\text{Sr}} = 2\pi \times 66$ kHz and $\omega_{\text{Rb}} = 2\pi \times 117$ kHz respectively. This leads to $\omega_{\text{rel}} = 2\pi \times 94$ kHz in a 3D isotropic lattice. The associated harmonic oscillator length, $a_{\text{HO}} = 948\ a_0$, is much larger than the s-wave scattering length $a_s = 92.7(2)\ a_0$ of ^{87}Rb-^{84}Sr, even in this very deep lattice regime. Therefore, the effect of this second term should also be small in the context of our ^{87}Rb^{84}Sr association experiments[19]. We neglect $\hat{\Delta}_{\text{trap}}$ in the following, which leads to a separation of the center-of-mass and relative motions. The eigenstates of the diatomic system then read $|\psi_{\text{tot}}\rangle = |\psi_C\rangle\,|\psi_{\text{rel}}\rangle$.

The center-of-mass harmonic motion is quantized according to the 3D harmonic oscillator energy structure $E_C = (\frac{3}{2} + N_C)\hbar\omega_C$, where N_C is a positive integer. In the regime where the lattice is present but the on-site atomic tunneling rates to other lattice sites are significant (i.e., below the Mott insulator transition or for $N_C > 0$), the harmonic approximation is poor and the motion of the particles is better described using the band index n_{band} and the pseudo-momenta q of the center of mass[20]. For very deep lattices though, where tunneling is suppressed, the motion is almost perfectly harmonic in the ground state $N_C = 0$ and $\hat{V}_{\text{anharm}}(\vec{R_C}, \vec{R})$ can be neglected[21].

[17] Center-of-mass and relative motion are uncoupled in the case of perfectly harmonic motion. This ideal behaviour is reached in two extreme limits: in total absence of external confinement, and in a perfectly harmonic trap where both atoms experience the same trapping potential.

[18] Note that when the two masses are almost identical, as is the case of ^{87}Rb and ^{84}Sr, the harmonic frequencies of the center-of-mass and relative motions are also almost identical.

[19] It was advised to us to decrease the lattice depth in case we couldn't observe molecule formation, in order to be in a regime where a_{HO} is not close to a_s [G. Shlyapnikov, private communication]. According to this estimation, we should be safe in this respect.

[20] A good estimator of the quality of the harmonic approximation in a given band is the band width, which is the spread in energy of all quasi-momentum states of the band. In the perfectly harmonic case this spread is null, i.e. $E_C(q) = E_C(0)$, independently of the value of the quasi-momentum q. The tunneling rates J, set by the depth of the lattice, are proportional to the energy width of the band.

[21] In other words: in the very high lattice intensity limit, the Wannier function for the ground-state of center-of-mass motion is well approximated by the Gaussian ground-state wavefunction of a perfect harmonic oscillator. In

The relative motion wavefunctions, Equation 2.38, are changed due to the presence of the trapping potential. This change is qualitatively different for molecular bound states and for positive-energy atom pair states. The molecular bound states are mostly defined by the PEC of the system, and stand almost unaffected by the trapping potential. This is due to the very different ranges of the molecular and trapping potentials, evident from Figure 5.3. The atom pair states, on the contrary, are strongly altered. In field-free space, the potential energy of the relative motion becomes constant at large distances, thus the radial scattering wavefunctions $\chi^{\text{scat}}_{k,N}(R)$ have a constant amplitude for $R \to +\infty$. They are therefore not square-integrable and must be energy-normalized according to $\langle E|E'\rangle = \delta(E-E')$[22]. On one site of an optical lattice, on the other hand, the continuum of scattering states $|E;k\rangle$ with collisional energy $E = \hbar^2k^2/2\mu$ is replaced by a quantized set of trap states $|E;n\rangle$, where n denote the quantum numbers appropriate to the description of the states. These states have a vanishing amplitude at large internuclear distances, and are thus unit-normalized according to $\langle E;n|E;n\rangle$=1. For a perfectly harmonic potential, Equation 5.15, they exhibit the harmonic energy structure $E = (\frac{3}{2}+n)\hbar\omega_{\text{rel}}$ up to small corrections related to the molecular potential[23], where $n = 2M+N$ is a positive integer (M also) and N is the considered partial wave Ref. [56][24]. Therefore the ground state of relative motion is isotropic, with $N = 0$ and $n = 0$ and an energy of $E = \frac{3}{2}\hbar\omega_{\text{rel}}$, while the next trap state has $N = 1$ with energy $E = \frac{5}{2}\hbar\omega_{\text{rel}}$. The subsequent states $n > 1$ of energies $E = \frac{7}{2}\hbar\omega_{\text{rel}}, \frac{9}{2}\hbar\omega_{\text{rel}}, \ldots$ exhibit degeneracies, with even (odd) n corresponding to even (odd) partial waves sets N respectively. The corresponding eigenfunctions are the well-known eigenfunctions for a quantum harmonic oscillator. Dismissing on-site interaction corrections, the radial ground-state wavefunction is

$$\chi^{\text{trap}}_{n,N=0}(R) = \frac{2}{\pi^{1/4}}(\mu\omega_{\text{rel}}/\hbar)^{3/4}\ \exp\left(-\frac{\mu\omega_{\text{rel}}}{2\hbar}R^2\right). \tag{5.18}$$

In an optical lattice, a Feshbach resonance induces an *avoided crossing* at the crossing point between an atom trap state and a molecular state. This situation is pictured in Figure 5.4. At

this regime the energy of the lowest band of the lattice is "flat", in the sense that it doesn't depend on the quasi-momentum q. The energy of the system is completely dominated by the potential of the lattice and the kinetic energy doesn't contribute. Therefore, the band width is very small and the tunneling rates are suppressed. The harmonic approximation gets worse with increasing N_C, for which the Wannier functions have a non-negligible overlap with neighbouring lattice sites.

[22] This is of course an idealization. In a real experiment, the particles are always subject to a repulsive potential of some sort, be it the walls of our our glass cell or other. However the range of such confinement is orders of magnitude larger than chemical and scattering length scales, hence the quantization of the continuum plays no role.

[23] The most important of these corrections is the on-site interaction energy of the pair of atoms onto the lattice site. It is the lattice counterpart to the phase shit $\delta_{\text{bg}} = \tan^{-1}(ka_{\text{bg}})$ for untrapped states (see Equation 5.1) and lies in the $h\times$ kHz range for ^{87}Rb^{84}Sr at our typical trap frequencies.

[24] Note that the quantum number n quantifies the relative motion: it is not the band index n_{band} that quantifies the center-of-mass motion.

the position of the resonance, which is shifted according to Equation 5.12, where the integral is replaced by a sum over all discrete trap states of the open channel, an energy gap opens. The width of this gap is $\hbar|\Omega|$, where Ω is set by the off-diagonal coupling matrix element given by[25,26]

$$\frac{\hbar\Omega}{2} = \langle E;n|\,\hat{V}_{12}\,|\psi^{(2)}_{\rm mol}\rangle\,. \tag{5.19}$$

Close to the resonance, the atom-pair trap state of the open channel 1 is admixed with the molecular state of the closed channel 2 according to

$$|\psi_{\rm rel}\rangle = \alpha\,|E;n\rangle + \beta\left[|\psi^{(2)}_{\rm mol}\rangle + \sum_{n'\neq n} a_{n',\rm mol\,2}\,|E;n'\rangle + \sum a_{\rm mol\,1,mol\,2}\,|\psi^{(1)}_{\rm mol}\rangle\right]\,, \tag{5.20}$$

which is the discrete counterpart of the free-space Equation 5.3, with unit-normalization $\langle\psi_{\rm rel}|\psi_{\rm rel}\rangle = 1$. The sums are taken over all eigenstates $|E;n\rangle$ and $|\psi^{(1)}_{\rm mol}\rangle$ of the background open channel, and account for the modification of the "bare" molecular state $|\psi^{(2)}_{\rm mol}\rangle$ due its admixing with the background channel. Accordingly, they induce a shift of the position of the avoided crossing. This shift is typically very close to the free-space shift δB given in Equation 5.13, and as such is negligible for the RbSr resonances with very small ΔB. Note that while the molecular states are barely affected by the trapping potential, the energy of the trap pair states varies with $\omega_{\rm rel} \propto \sqrt{I(x,y,z)}$, where $I(x,y,z)$ is the local lattice beam intensity — see Appendix A, Equation A.13. Accordingly, the magnetic field at which the avoided crossing occurs depends on the optical lattice intensity. In the situation where the coupled states $|E;n\rangle$ and $|\psi^{(2)}_{\rm mol}\rangle$ are well-separated in energy compared to the coupling terms $\langle E;n'|\,\hat{V}_{12}\,|\psi^{(2)}_{\rm mol}\rangle$ and $\langle\psi^{(1)}_{\rm mol}|\,\hat{V}_{12}\,|\psi^{(2)}_{\rm mol}\rangle$, Equation 5.20 reduces to the two-level admixing of the pure trap and molecular states. It is then

$$|\psi_{\rm rel}\rangle = \alpha\,|E;n\rangle + \beta\,|\psi^{(2)}_{\rm mol}\rangle\,, \tag{5.21}$$

and in that case $|\alpha|^2 + |\beta|^2 = 1$. Starting from an atom pair in the $|E;n=0\rangle$ ground state of relative motion of the lattice, the molecular state component β can be changed from 0 to unity by ramping down the external magnetic field B from above the Feshbach resonance — see Figure 5.4. Molecules are then produced very efficiently from the trapped atom pairs.

[25] We dismiss the rotational quantum number N in $|E;n,N\rangle$ in the following equations for ease of reading. It is zero in the ground state of the lattice.

[26] The off-diagonal matrix element is typically expressed in terms of the Rabi frequency Ω (expressed in rad.s^{-1} or rad.Hz), which is convenient to work with energies expressed in frequency units. We follow this convention here. The off-diagonal matrix element is then $\hbar\frac{\Omega}{2}$ and the energy gap at the position of the avoided crossing is $\hbar\Omega$. Ω can be either positive or negative, but this is irrelevant to the present discussion.

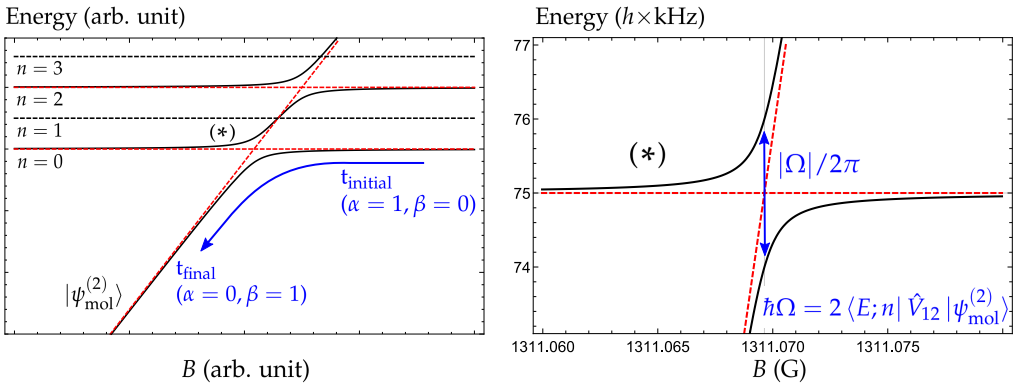

FIGURE 5.4: Magnetoassociation in a 3D isotropic optical lattice, using the ^{87}Rb^{84}Sr Feshbach resonance at $B = 1311$ G. **Left panel:** Principle of a magnetoassociation ramp. Starting from an atom pair ($\alpha = 1$) in the ground state of relative motion $n = 0$, the B-field is ramped adiabatically across the lowest avoided crossing. The probability density is thus entirely transferred to the molecular state ($\beta = 1$), transforming the atom pair into a Feshbach molecule. The black (red dashed) lines indicate the energy eigenvalues of the molecular closed-channel state and of the open-channel trap states in presence (absence) of coupling $\hat{V}_{12}$ between the two channels. Mechanism I, which produces the RbSr Feshbach resonance, is isotropic and thus couples the $|\nu = -4, N = 0\rangle$ resonant molecular state to trap states of even parity n only — see Section 5.3. Therefore, the states of odd n do not lead to avoided crossings. **Right panel:** Avoided crossing between the ^{87}Rb-^{84}Sr open-channel $|f, m_f\rangle = |1, +1\rangle$ trap state $|E; n = 0\rangle$ and the closed-channel $|f, m_f\rangle = |2, +1\rangle$ molecular state $|\nu = -4, N = 0\rangle$ at $B = 1311$ G. The gap at the position of the avoided crossing is estimated to be $|\Omega|/2\pi \simeq 2$ kHz at $\omega_{\text{rel}} = 2\pi \times 60$ kHz [P. Żuchowski, private communication].

This process is known as magnetoassociation (in an optical lattice) and in the next three paragraphs, we discuss the requirements for near-unity magnetoassociation. We give particular attention to the case of ^{87}Rb^{84}Sr, which is the molecule we aim to produce in the laboratory.

First, to perform magnetoassociation as depicted in Figure 5.4, it is necessary to load atom pairs in the ground state of relative and center-of-mass motion of the optical lattice[27]. The beauty of cold atom experiments is that one can produce a Bose-Einstein condensate (BEC) — or two, in the case of heteronuclear bosonic systems such as ^{87}Rb^{84}Sr — in the ground state of both relative and center-of-mass motions using standard laser and evaporative cooling techniques. The BECs constitute macroscopic ensembles of cold atoms in a well-defined state of relative motion, which is the state of zero relative momentum $\hbar k = 0$.

[27] The lattice ground state in which the atoms are loaded has $N_C = 0$ and $n = 0$, corresponding to a total energy of $E_C + E = \frac{3}{2}\hbar(\omega_C + \omega_{\text{rel}})$ (neglecting the on-site interaction corrections to the relative energy.)

These ensembles are then loaded adiabatically into the ground state of relative and center-of-mass motion of the optical lattice[28], by gradually ramping up the lattice light intensity. The atoms undergo the superfluid-to-Mott insulator transition upon increase of the lattice depth, and the double BEC is transformed adiabatically into a double Mott insulator. This double Mott insulator is characterized by a very low tunneling rate across the lattice, and by the suppression of atom number fluctuation on the lattice sites. Ideally, as many lattice sites as possible should be filled with exactly one Rb and one Sr atom in the ground state of relative and center-of-mass motion, in order to maximise the amount of molecules that can be produced. The preparation of such a double Mott insulator is essential to the success of RbSr magnetoassociation.

Second, it is essential that the two-level approach of Equation 5.21 is valid. Otherwise, the undesired mixing of the target molecular state with adjacent open- and closed-channel states makes unit-probability transfer much harder or even impossible. The Feshbach resonance we want to use to magnetoassociate ^{87}Rb^{84}Sr is located at $B = 1311\,\mathrm{G}$, and gives rise to an avoided crossing between the ^{87}Rb-^{84}Sr ground state of relative motion of our optical lattice ($n = 0$), belonging to the open channel $|f, m_f\rangle = |1, +1\rangle$, and the molecular state $|\nu = -4, N = 0\rangle$, belonging to the closed channel $|f, m_f\rangle = |2, +1\rangle$. This avoided crossing is correctly described as a two-level process, as we argue in the next lines. This resonance is induced by mechanism I, which is produced by the perturbation $\hat{V}_{12}$ given in Section 5.3, Equation 5.55. This mechanism is isotropic and therefore couples atom pair states to states of the same rotational quantum number N only. Thus, at the position of the avoided crossing, the closest open-channel states that are coupled to $|\psi^{(2)}_{\mathrm{mol}}\rangle = |\nu = -4, N = 0\rangle\,|2, +1\rangle$ by mechanism I are the trap states $n = 2$ of energy $\frac{7}{2}\hbar\omega_{\mathrm{rel}}$[29], which are separated by more than $h \times 40\,\mathrm{kHz}$ from the ground state at our typical trap frequencies $\omega_{\mathrm{rel}} > 2\pi \times 20\,\mathrm{kHz}$. Since the coupling matrix element is $\langle E; n = 0|\,\langle 1, +1|\,\hat{V}_{12}\,|\nu = -4, N = 0\rangle\,|2, +1\rangle \sim h \times 1\,\mathrm{kHz}$ [P. Żuchowski, private communication], and gets smaller at higher n[30], these open-channel states can be considered decoupled from the two-level system. The closest open-channel molecular state that is coupled to $|\psi^{(2)}_{\mathrm{mol}}\rangle$ by mechansim I is the $|\nu = -1, N = 0\rangle$ state, which has a binding energy of $E_b = h \times 29\,\mathrm{MHz}$. Since $\langle \nu = -4, N = 0|\,\langle 2, +1|\,\hat{V}_{12}\,|\nu = -1, N = 0\rangle\,|1, +1\rangle \simeq h \times 200\,\mathrm{kHz}$ [M. Frye, private communication], the separation of energies is also legitimate for this closed-channel state. Therefore, the ^{87}Rb^{84}Sr Feshbach resonance crossing at $B = 1311\,\mathrm{G}$ is correctly described as a two-level process.

Third, and last, the energy gap $\hbar\Omega$ at the position of the avoided crossing sets limits on

[28] Provided that the BECs are void of any center-of-mass excitations prior to loading, which requires careful alignment of the optical dipole trap, in which the initial BECs are located, and of the lattice beams.

[29] Note that a total of 6 states have $n = 2$: five ($N = 2, M = 0$) states and one ($N = 0, M = 1$) state. Only the latter is coupled to the incoming $N = 0$ by mechanism I.

[30] This is due to the radial overlap integral, Equation 5.62, which gets smaller for higher-n trap states.

the speed at which the magnetoassociation ramp can be performed[31] and on the stability of the magnetic field. The fraction η of the ensemble that has been transferred to the bound state at the end of the ramp is simply given by the two-level Landau Zener probability

$$\eta = 1 - \exp\left[-2\pi \frac{(\hbar\Omega/2)^2}{\hbar\delta\mu \frac{dB}{dt}}\right], \tag{5.22}$$

where $\delta\mu$ is the relative magnetic moment between the atom pair and molecular states. The larger $|\Omega|$, the faster one can transfer the atoms into the molecular state. Any effect that leads to either loss of the created molecules (i.e. scattering of photons from the lattice light, decay to deeper-bound molecular states through uncontrolled molecular effects,...) or decoherence of the superposition 5.21 (induced by fluctuations of the magnetic field B most importantly, but also intensity fluctuations in the lattice beams that lead to changes of ω_{rel} and thus to changes of the atom pair state relative energy $E = \frac{3}{2}\hbar\omega_{\text{rel}}$) lead to decrease of the transfer efficiency η. The ^{87}Rb^{84}Sr avoided crossing located at $B = 1311\,\text{G}$ exhibits $\delta\mu/h = 2.153\,\text{MHz/G}$ ($1\,\text{G} = 10^{-4}\,\text{T}$), with a gap of $|\Omega|/2\pi \simeq 2\,\text{kHz}$ at $\omega_{\text{rel}} = 2\pi \times 60\,\text{kHz}$ [P. Żuchowski, private communication]. The strength of the coupling goes as $\Omega \propto \omega_{\text{rel}}^{3/4}$ [132][M. Frye & P. Żuchowski, private communication] and our current lattice beams allow us to reach $\omega_{\text{rel}} = 2\pi \times 44\,\text{kHz}$, which therefore corresponds to $|\Omega|/2\pi = 1.6\,\text{kHz}$ [32]. Transferring more than 99% of the atoms into the molecular state requires $\eta > 0.99$, hence $\frac{dB}{dt} < 2.5\,\text{G/s}$. For instance, a sweep $\Delta B = 100\,\text{mG}$ spanning $h \times 215\,\text{kHz}$ in energy across the resonance requires a minimum of $T_{\text{sweep}} = 40\,\text{ms}$. During these 40 ms the external B-field (as well as the ambiant B-field and the intensities of the lattice beams) has to be stabilized to a level comparable to the magnetic coupling width $\hbar|\Omega|/\delta\mu = 0.8\,\text{mG}$, which requires a 10^{-6} relative precision at $B = 1311\,\text{G}$. Challenge accepted.

[31] Note that this is a more severe requirement than it looks. If a ramp of a few hundred ms is required, then all processes that lead to the loss of molecules must happen on a longer timescale. Otherwise, one cannot observe the molecules even if they are formed. The smoking-gun measurement used to prove the formation of molecules in all experiments similar to ours consists in performing two consecutive ramps of the magnetic field. The first ramp, from above to below the resonance position, forms the molecules. The absorption imaging signal of the atoms then decreases, because the formed molecules are not imaged by the imaging beams — this negative signal can indicate molecule formation, but also loss induced by undesired processes. The second ramp is performed from below to above the resonance position, and dissociates the molecules back into atom pairs. The atom pairs contribute to the imaging signal, leading to an increase in the absorption signal compared to the end of the first ramp. This positive signal is a definitive proof of the formation of molecule. See Ref. [138], Figure 4 in which KRb formation is observed using this method.

[32] The maximum depth that we can achieve for Sr is $s = 60$. For our optical lattice wavelength of 1064 nm, this corresponds to a depth of $s = 196$ for Rb (see Equations A.5 and A.11 in the appendix). The corresponding (angular) trap frequencies are $\omega_{\text{Sr}} = 2\pi \times 30.2\,\text{kHz}$ and $\omega_{\text{Rb}} = 2\pi \times 54.7\,\text{kHz}$.

The case of a non-isotropic lattice

As we have shown, in the 3D isotropic case the relative motion energy eigenvalues are given by $E = (\frac{3}{2} + n)\hbar\omega_{\text{rel}}$ and are proportional to $\sqrt{I(x,y,z)}$ where $I(x,y,z)$ is the local optical lattice intensity — see Appendix A, Equation A.13. If the three lattice beams have different intensities, then these eigenvalues are replaced by $E = \sum (\frac{1}{2} + n_i)\hbar\omega^i_{\text{rel}}$, where the sum runs over the three orthogonal directions of the lattice beams $i \in \{x,y,z\}$ and n_i are positive integers. Therefore, while the excited states $n_i > 0$ exhibit lifting of degeneracies, the ground state of the relative motion is still uniquely defined with $n_x = n_y = n_z = 0$, associated with the energy $E = \frac{1}{2}\hbar(\omega_x + \omega_y + \omega_z)$. In the context of magnetoassociation, the separation of energy between the open- and closed-channel states involved in the avoided crossing and the other open channel states holds under the same conditions as discussed previously in this subsection.

5.2 Magnetic Feshbach resonances in Rb_2 and in other bi-alkali systems

At the heart of the physics of Feshbach resonances in bi-alkali systems lies the interplay between two physical mechanisms: the exchange interaction and the hyperfine interactions. In this section we present the molecular physics that underlies these phenomena, and give examples of both broad and narrow Feshbach resonances in the Rb_2 case of interest for RbSr.

The Hamiltonian describing the collision of an alkali atom 1 with another alkali atom 2 in their electronic ground-state is

$$\hat{H} = \frac{1}{2\mu}\left[-\hbar^2\frac{\mathrm{d}^2}{\mathrm{d}R^2} + \frac{\hat{N}^2}{R^2}\right] + \hat{V}_{\mathrm{PEC}}(R) + \hat{H}_1 + \hat{H}_2\,, \tag{5.23}$$

using the same notation as introduced in Chapter 2. It is the sum of the molecular Hamiltonian, as obtained in Equation 2.43 within the adiabatic approximation (the ground-state PEC $\hat{V}_g$ of RbSr has been replaced by the appropriate bi-alkali PEC(s)), and of the single-atom Hamiltonians $\hat{H}_1$ and $\hat{H}_2$. The single-atom Hamiltonians are

$$\begin{aligned}\hat{H}_1 &= \zeta_1\hat{i}_1\cdot\hat{s}_1 - \left(\gamma_{i,1}\,\hat{i}_{1,z} + \gamma_S\,\hat{s}_{1,z}\right)B\\ \hat{H}_2 &= \zeta_2\hat{i}_2\cdot\hat{s}_2 - \left(\gamma_{i,2}\,\hat{i}_{2,z} + \gamma_S\,\hat{s}_{2,z}\right)B\,,\end{aligned} \tag{5.24}$$

where $\gamma_S/2\pi = h\times -2.8025$ MHz/G is the electron gyromagnetic ratio (divided by 2π), and $\gamma_{i,1}$ and $\gamma_{i,2}$ are the gyromagnetic ratios of the nuclear spins of the nuclei 1 and 2 — see Equation 5.46 for the corresponding values in Rb. The electronic and nuclear spin operators are denoted as $\hat{s}_1$, $\hat{s}_2$ and $\hat{i}_1$, $\hat{i}_2$ respectively, and the associated projection operators are denoted as $\hat{s}_{1,z}$, $\hat{s}_{2,z}$, $\hat{i}_{1,z}$ and $\hat{i}_{2,z}$. The projection is taken along the quantization axis z defined by the direction of the applied magnetic field B. The eigenstates of the single-atom Hamiltonians $\hat{H}_1$ and $\hat{H}_2$ are the (B-field dependent) hyperfine coupled-basis states $|f_1, m_{f_1}\rangle$ and $|f_2, m_{f_2}\rangle$ respectively. Therefore $\hat{H}_1 + \hat{H}_2$ is diagonal in the hyperfine basis $|f_1, m_{f_1}\rangle\,|f_2, m_{f_2}\rangle$ of the atom pair. A complete introduction to the physics of the ground-state Rb hyperfine Hamiltonian is given in Subsection 5.3.1 in the context of RbSr Feshbach resonances.

In bi-alkali systems two PECs correlate to the electronic ground-state dissociation limit $^2S_{1/2} + {}^2S_{1/2}$, in contrast with RbSr for which the electronic ground state is uniquely defined by the single PEC of molecular term $^2\Sigma^+$. These two PECs are associated with the two possible values of the total electronic spin $S = 0$ and $S = 1$ obtained from the combination $\vec{S} = \vec{s}_1 + \vec{s}_2$ of the individual spins $s_1 = s_2 = 1/2$ of each atom of the pair. The total electronic

spin is a good quantum number of the molecule if the hyperfine structure $\hat{H}_1, \hat{H}_2$ is not included, and the molecular eigenfunctions $\psi_n^{\mathrm{el}}(\vec{r}, R)$ and the two PECs $U_n(R)$ obtained in the cases $S = 0$ and $S = 1$ in the electronic ground state are very different — see Equation 2.27 and Figure 5.5. In particular, they support different sets of vibrational and rotational molecular states, and different s-wave scattering lengths[33]. The molecular terms corresponding to the singlet and triplet PECs are $^1\Sigma^+$ and $^3\Sigma^+$ respectively[34], associated with the singlet and triplet potentials $V_{^1\Sigma^+}(R)$ and $V_{^3\Sigma^+}(R)$. Accordingly, the total Hamiltonian is

$$\hat{H} = \frac{1}{2\mu}\left[-\hbar^2\frac{\mathrm{d}^2}{\mathrm{d}R^2} + \frac{\hat{N}^2}{R^2}\right] + \sum_S \hat{V}_S(R)\,|S\rangle\langle S| + \hat{H}_1 + \hat{H}_2\,. \tag{5.25}$$

where $|S\rangle\langle S|$ are the projectors onto the subspaces of total value S of the Hilbert space, with $V_{S=0}(R) = V_{^1\Sigma^+}(R)$ and $V_{S=1}(R) = V_{^3\Sigma^+}(R)$. The individual atomic spins $s_1 = s_2 = 1/2$ are always good quantum numbers such that $\langle \vec{s}_{1/2}{}^2\rangle = (1/2)(1/2+1)\hbar^2 = 3\hbar^2/4$ for any state of motion. Therefore, using the relations $S^2\,|S, m_S\rangle = S(S+1)\hbar^2\,|S, m_S\rangle$[35] and $\vec{S}^2 = \vec{s}_1{}^2 + \vec{s}_2{}^2 + 2\,\vec{s}_1\cdot\vec{s}_2 = 3\hbar^2/2 + 2\,\vec{s}_1\cdot\vec{s}_2$, the total spin projection operators can be written as

$$\begin{aligned} |0\rangle\langle 0| &= \frac{1}{4} - \frac{1}{2\hbar^2}\vec{s}_1\cdot\vec{s}_2 \\ |1\rangle\langle 1| &= \frac{3}{4} + \frac{1}{2\hbar^2}\vec{s}_1\cdot\vec{s}_2\,, \end{aligned} \tag{5.26}$$

The total Hamiltonian then reads

$$\hat{H} = \frac{1}{2\mu}\left[-\hbar^2\frac{\mathrm{d}^2}{\mathrm{d}R^2} + \frac{\hat{N}^2}{R^2}\right] + \hat{V}_D(R) + \hat{V}_E(R)\,\frac{\vec{s}_1\cdot\vec{s}_2}{\hbar^2} + \hat{H}_1 + \hat{H}_2\,, \tag{5.27}$$

where V_D and $V_E(R)$ are the direct and exchange potentials[36], respectively [140]. They are defined as

$$\begin{aligned} V_D(R) &= \frac{1}{4}\left[V_{^1\Sigma^+}(R) + 3V_{^3\Sigma^+}(R)\right] \\ V_E(R) &= \frac{1}{2}\left[V_{^3\Sigma^+}(R) - V_{^1\Sigma^+}(R)\right]\,. \end{aligned} \tag{5.28}$$

[33] The ^{87}Rb atom is exceptional in this respect, because its singlet and triplet s-wave scattering lengths $a_{S=0} = 90\ a_0$ and $a_{S=1} = 99\ a_0$ are almost identical [118]. The spin-exchange rates are therefore very low — see Ref. [139] and Subsection 5.2.2.

[34] In the case of identical boson pairs, such as $^{87}Rb_2$, the valence electron of the single-atom ground state term lies in an s orbital, which implies a *gerade* symmetry for the singlet term, and an *ungerade* symmetry for the triplet term [57]. The corresponding molecular terms are denoted as $^1\Sigma_g^+$ and $^3\Sigma_u^+$.

[35] The hats of the $\hat{\vec{s}}_1$ and $\hat{\vec{s}}_2$ operators are omitted for ease of reading.

[36] Note that these potentials are *not* PECs in the chemical sense of the term.

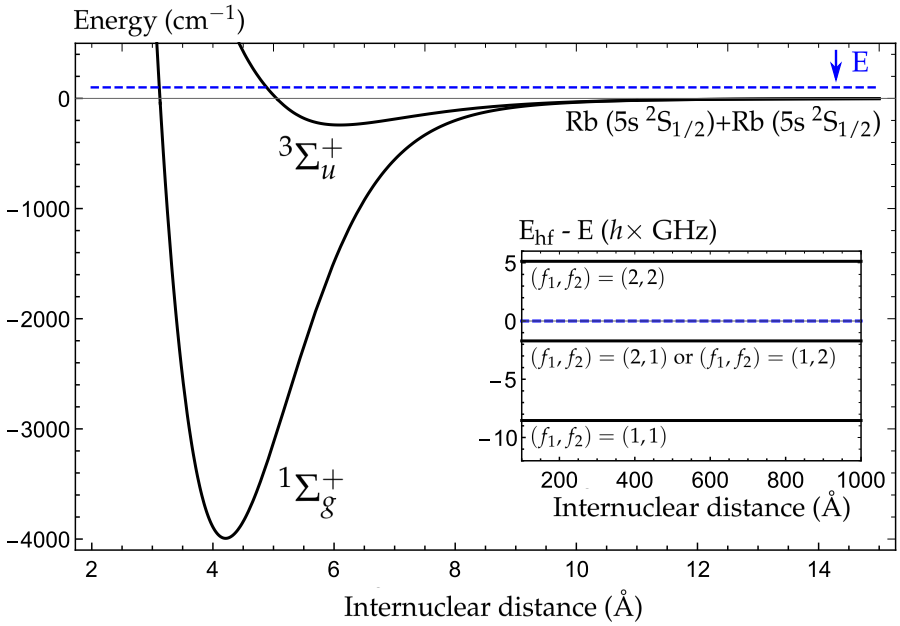

FIGURE 5.5: Singlet and Triplet interaction potentials of a pair of ground-state Rb atoms. Owing to the very large exchange energy, the singlet PEC is much deeper than the triplet PEC. The hyperfine structure of a ^{87}Rb-^{87}Rb atom pair of collisional energy E, as defined by the single-atom Hamiltonians $\hat{H}_1$ and $\hat{H}_2$ in absence of magnetic field (single-atom Zeeman splittings at $B > 0$ G are shown in Figure 5.8) is displayed on a different (much smaller) energy scale. Note that for non-identical alkali atoms the hyperfine constants ζ_1 and ζ_2 are different, giving rise to four non-degenerate manifolds instead of three. The exchange interaction doesn't alter the hyperfine structure of the scattering states, but perturbs it significantly in the case of weakly-bound molecular states — see Figure 5.6.

The asymptotic behaviour of these potentials is

$$\begin{aligned} V_D(R) &\xrightarrow[R\to\infty]{} -\frac{C_6}{R^6} - \frac{C_8}{R^8} - \frac{C_{10}}{R^{10}} - \dots \\ V_E(R) &\xrightarrow[R\to\infty]{} -a(R)\exp\left(-bR\right), \end{aligned} \tag{5.29}$$

where a is an algebraic function of R and b a positive constant [118, 141]. The direct potential is independent of spin and defines the dispersive tail of the potential, as discussed in Subsection 2.1.7 in the context of RbSr, and the spin-dependent exchange potential falls off rapidly at large internuclear distances.

Importantly, the spin operator $\vec{s}_1 \cdot \vec{s}_2$ of the exchange interaction is *not* diagonal in the hyperfine basis $|f_1, m_{f_1}\rangle |f_2, m_{f_2}\rangle$ of the two alkali atoms. In other words, $\hat{H}_1 + \hat{H}_2$ and $\vec{s}_1 \cdot \vec{s}_2$ do not commute. The competition between the hyperfine interaction and the exchange interaction leads to the broadest Feshbach resonances in bi-alkali systems, as we show below.

5.2.1 Broad resonances: competition between the exchange and hyperfine interactions

The total Hamiltonian, Equation 5.27, can be decomposed into two parts. The first part encompasses the hyperfine structure and defines the open and closed channel. It is

$$\hat{H}_D = \frac{1}{2\mu}\left[-\hbar^2 \frac{\mathrm{d}^2}{\mathrm{d}R^2} + \frac{\hat{N}^2}{R^2}\right] + \hat{V}_D(R) + \hat{H}_1 + \hat{H}_2 \,. \tag{5.30}$$

The second part is the exchange part, which acts as a coupling term between the two channels. It is

$$\hat{V}_{12} = \hat{V}_E(R)\, \frac{\vec{s}_1 \cdot \vec{s}_2}{\hbar^2} \,. \tag{5.31}$$

The open-channel scattering eigenstates of the Hamiltonian defined by Equation 5.30 are of the form $|E\rangle = |\chi^{\mathrm{scat}}_{k,N}(R)\rangle\, |N, m_N\rangle\, |f_1, m_{f_1}, f_2, m_{f_2}\rangle$, as given in Equation 2.41. They are defined by their collisional energy $E = \hbar^2 k^2/2\mu$, their rotational quantum numbers N, m_N and their hyperfine contribution $|f_1, m_{f_1}, f_2, m_{f_2}\rangle$. The closed-channel molecular eigenstates are of the form $|\psi_{\mathrm{mol}}\rangle = |\chi^{\mathrm{vib}}_{\nu,N'}(R)\rangle\, |N', m_{N'}\rangle\, |f_1', m_{f_1'}, f_2', m_{f_2'}\rangle$ and are defined similarly, with the vibrational quantum number ν replacing the collisional energy defined by k.

In that picture the open and closed channel differ only by their respective hyperfine contributions $|f_1, m_{f_1}, f_2, m_{f_2}\rangle$[37]. These contributions differ depending on whether the two atoms are identical bosons, identical fermions, or distinguishable particles [141]. They are given by

$$|f_1, m_{f_1}, f_2, m_{f_2}\rangle = \begin{cases} c\left[\,|f_1, m_{f_1}\rangle\, |f_2, m_{f_2}\rangle + (-1)^N\, |f_2, m_{f_2}\rangle\, |f_1, m_{f_1}\rangle\,\right] & \text{bosons} \\ c\left[\,|f_1, m_{f_1}\rangle\, |f_2, m_{f_2}\rangle + (-1)^{N+1}\, |f_2, m_{f_2}\rangle\, |f_1, m_{f_1}\rangle\,\right] & \text{fermions} \\ |f_1, m_{f_1}\rangle\, |f_2, m_{f_2}\rangle \quad \text{distinguishable particles}\,, \end{cases} \tag{5.32}$$

where $|f_1, m_{f_1}\rangle$ and $|f_2, m_{f_2}\rangle$ are the single-atom contributions upon which the operators $\vec{s_1}, \vec{s_2}, \vec{i_1}, \vec{i_2}, \ldots$ act, with $c = \sqrt{\frac{1}{2}}$ or $c = \frac{1}{2}$ in the cases $|f_1, m_{f_1}\rangle \neq |f_2, m_{f_2}\rangle$ and $|f_1, m_{f_1}\rangle =$

[37] That is not the case if one defines the open and closed channel as the singlet and triplet PECs respectively, for in that case also the vibrational and rotational contributions differ.

$|f_2, m_{f_2}\rangle$ respectively. From that symmetrization it is clear that identical bosons (fermions) in identical $|f, m_f\rangle$ states only collide through $N = 0, 2, 4, ...$ ($N = 1, 3, 5, ...$) partial waves. The same applies to the corresponding molecular states.

The exchange interaction $\hat{V}_{12} = \hbar^{-2} \times \hat{V}_E(R)\ \vec{s}_1 \cdot \vec{s}_2$ is not diagonal in the eigenbasis of $\hat{H}_D$. The spin operator $\vec{s}_1 \cdot \vec{s}_2$ is off-diagonal with respect to the hyperfine basis defined by Equation 5.32, and the radial operator $\hat{V}_E(R)$ is off-diagonal with respect to the vibrational/rotational basis of $\hat{H}_D$. Therefore, the exchange interaction introduces large off-diagonal coupling terms between molecular states and between scattering and molecular states[38]. The Breit-Wigner width of a Feshbach resonance at the crossing of an open-channel scattering state $|E\rangle$ with a closed-channel molecular state $|\psi^{(2)}_{\text{mol}}\rangle$ is

$$\Gamma_{12}(E) = 2\pi |\langle E|\, \hat{V}_{12}\, |\psi^{(2)}_{\text{mol}}\rangle\, |^2\,, \tag{5.33}$$

as given previously in Equation 5.7. The coupling matrix element introduced by the exchange interaction is

$$\langle E|\, \hat{V}_{12}\, |\psi^{(2)}_{\text{mol}}\rangle = I_{\text{radial}}\ I_{\text{spin}}(B)\ \delta_{N,N'}\ \delta_{m_N, m_{N'}}\,, \tag{5.34}$$

where the associated radial and spin overlap integrals are[39]

$$\begin{aligned} I_{\text{radial}} &= \langle \chi^{\text{scat}}_{k,N}(R)|\, \hat{V}_E(R)\, |\chi^{\text{vib}}_{\nu,N'}(R)\rangle \\ I_{\text{spin}}(B) &= \hbar^{-2} \times \langle f_1, m_{f_1}, f_2, m_{f_2}|\, \vec{s}_1 \cdot \vec{s}_2\, |f_1', m_{f_1'}, f_2', m_{f_2'}\rangle\ . \end{aligned} \tag{5.35}$$

The value of the radial integral is set by the difference between triplet and singlet potentials and can be very large — see Equation 5.28 and Figure 5.5. Furthermore, it gets larger for molecular states of higher vibrational quantum number ν, because such states display larger interradial probability density $|\chi^{\text{vib}}_{\nu,N}(R)|^2$ in regions of smaller R and thus larger $V_E(R)$. This coupling mechanism is fully isotropic, because $V_E(R)$ does not depend on the angular orientation (θ, ϕ) of the molecule. Therefore, it cannot couple scattering and molecular states with different rotational quantum numbers N, N'. In the ultracold limit, where the scattering partial waves $N = 0$ dominate (for bosons and distinguishable particles), the largest observable Feshbach resonances are thus induced by $N = 0$, non-rotating molecular states — see the table of Figure 5.6, where l indicates N and v indicates the vibrational quantum

[38] It also adds diagonal corrections $\langle \psi_{\text{mol}}|\, \hat{V}_{12}\, |\psi_{\text{mol}}\rangle$ to the binding energies of the molecular states. These corrections are quite large even for weakly-bound states, far from any molecule/molecule or scattering threshold/molecule crossing — this is clear from Figure 5.6. We do not discuss this matter here since we are primarily interested in the off-diagonal couplings responsible for Feshbach resonances.

[39] The notation $I_{\text{spin}}(B)$ is a reminder that the $|f, m_f\rangle$ states are B-field dependent — see Subsection 5.3.1. We do not discuss this dependence here, but it is crucial in the context of RbSr Feshbach resonances.

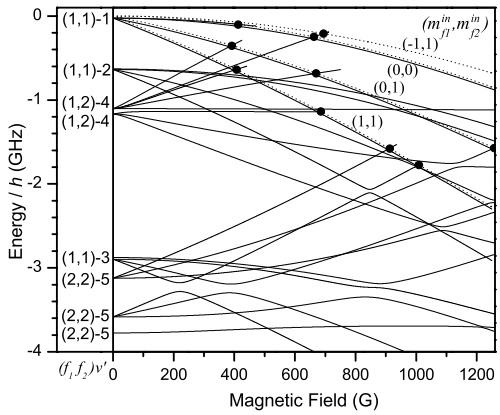

B_{exp} (G)	B_{th} (G)	d (%)	Δ (mG)	$l(f_1,f_2)v',m_F$	F	m_{f1},m_{f2}
406.23	406.6	57	0.4	0 (1,2)-4, 2		0,2
685.43	685.8	78	17	0 (1,2)-4, 2		1,1
911.74	911.7	72	1.3	0 (2,2)-5, 2	4	
1007.34	1008.5	64	170	0 (2,2)-5, 2	2	
···	377.2	···	$\ll 0.1$	2 (1,1)-2, 0		−1,1
···	395.0	···	$\ll 0.1$	2 (1,1)-2, 0		0,0
856.85	857.6	<10	$\ll 0.1$	2 (1,1)-2, 1	2	0,1
···	249.1	···	$\ll 0.1$	2 (1,2)-4, 1		−1,2
306.94	306.2	34	$\ll 0.1$	2 (1,2)-4, 0		−1,1
319.30	319.7	54	<0.1	2 (1,2)-4, 2		0,2
387.25	388.5	53	<0.1	2 (1,2)-4, 1		0,1
391.49	392.9	63	0.3	2 (1,2)-4, 3	3	1,2
532.48	534.2	57	<0.1	2 (1,2)-4, 0		0,0
551.47	552.0	66	0.2	2 (1,2)-4, 2		1,1
819.38	819.3	29	<0.1	2 (1,2)-4, 1		1,0

FIGURE 5.6: Magnetic Feshbach resonances in ^{87}Rb. **Left panel:** $^{87}Rb_2$ Feshbach resonances (black spots) arising at the crossing between s-wave scattering states (dashed lines) and $N = 0$ molecular states (solid lines). The scattering hyperfine sublevels are indicated on the graph as (m^{in}_{f1},m^{in}_{f2}) and the hyperfine (f_1,f_2) manifolds of the molecular states, within which lifting of degeneracies induced by the exchange energy occur, are indicated on the left together with their vibrational quantum number v. **Right panel**: Selection of experimentally-observed $^{87}Rb_2$ Feshbach resonances, occurring in the s-wave $|f_1, m_{f_1}\rangle\,|f_2, m_{f_2}\rangle = |1,+1\rangle\,|1,+1\rangle$ open channel. The indicated quantum numbers are those of the resonant molecular states that produce the Feshbach resonances. The rotational number l is denoted as N in this thesis. The broadest resonances are provoked by $N = 0$ molecular states through the isotropic exchange interaction, and the narrow ones are produced by $N = 2$ states due to the weaker and anisotropic spin-spin dipole interaction and second-order spin-orbit interaction. From Ref. [135].

numbers v. The spin integral defines the selection rules for the existence of resonances. The operator $\vec{s}_1 \cdot \vec{s}_2 = \hat{s}_{1,z}\hat{s}_{2,z} + \frac{\hat{s}_{1,+}\hat{s}_{2,-}+\hat{s}_{1,-}\hat{s}_{2,+}}{2}$ does not change the total spin projection $m_S = m_{s_1} + m_{s_2}$ along the B-field axis, therefore it also leaves the total electronic+nuclear spin projection $m_{f_1} + m_{f_2} = m_{s_1} + m_{s_2} + m_{i_1} + m_{i_2}$ unchanged[40]. Feshbach resonances thus arise only at the crossings between scattering and molecular states with identical total projections $m_{f1} + m_{f_2} = m_{f'_1} + m_{f'_2}$.

The physics we have presented here is universal in bi-alkalis and leads to the largest Feshbach resonances in these systems, with a qualitatively different situation for relatively

[40]The electronic spin raising and lowering operators $\hat{s}_{1,\pm} = \hat{s}_{1,x} \pm i\,\hat{s}_{1,y}$ and $\hat{s}_{2,\pm} = \hat{s}_{2,x} \pm i\,\hat{s}_{2,y}$ fulfill the standard angular momentum properties $\hat{s}_{1,\pm}\,|s_1\,m_{s_1}\rangle = \sqrt{s_1(s_1+1) - m_{s_1}(m_{s_1}\pm 1)}\hbar\,|s_1\,(m_{s_1}+1)\rangle$ and $\hat{s}_{2,\pm}\,|s_2\,m_{s_2}\rangle = \sqrt{s_2(s_2+1) - m_{s_2}(m_{s_2}\pm 1)}\hbar\,|s_2\,(m_{s_2}+1)\rangle$ respectively. They are designed to act on the $|s_1, s_2, m_{s_1}, m_{s_2}\rangle\,|i_1, i_2, m_{i_1}, m_{i_2}\rangle$ spin basis in which all angular momenta are explicitly decoupled. Note that each hyperfine-basis state $|f_1, m_{f_1}\rangle\,|f_2, m_{f_2}\rangle$, and each state of the basis $|S, m_S, s_1, s_2\rangle\,|i_1, m_{i_1}, i_2, m_{i_2}\rangle$ that couples the two electronic spins can be written as a linear combination of $|s_1, s_2, m_{s_1}, m_{s_2}\rangle\,|i_1, i_2, m_{i_1}, m_{i_2}\rangle$ states.

heavy and light species. For heavy species such as Rb_2 [135] or RbCs [142], the typical vibrational spacing close to threshold is smaller than the hyperfine splittings[41]. Therefore, the weakly-bound molecular states of such dimers are approximately well described in the spin basis $|f_1, m_{f_1}\rangle\,|f_2, m_{f_2}\rangle$ of the atomic hyperfine f_1 and f_2 quantum numbers — the exchange $\hat{V}_{12} = \hbar^{-2} \times \hat{V}_E(R)\ \vec{s}_1 \cdot \vec{s}_2$ plays the role of a perturbation in the structure $\hat{H}_D$ defined by Equation 5.30. For light species such as H_2 or Li_2, the vibrational spacing is much larger than the hyperfine splittings[42], therefore the molecular states of the closed channel typically have very strong singlet or triplet character, and are much better described in terms of the $|S, m_S, s_1, s_2\rangle\,|i_1, m_{i_1}, i_2, m_{i_2}\rangle$ spin basis in which the exchange $\vec{s_1}.\vec{s_2}$ is diagonal[43]. The hyperfine Hamiltonian then acts as the perturbation $\hat{V}_{12} = \hat{H}_1 + \hat{H}_2$ of the main structure $\hat{H}_E$ defined by the exchange interaction. This conceptually symmetric approach is taken in Refs. [144] and [140] in the context of $^6Li_2$ and $^6Li^{40}K$ respectively.

5.2.2 Narrow resonances: spin-spin dipole interaction and second-order spin-orbit interaction

Feshbach resonances in bi-alkali systems are also mediated by weak additional terms in the Hamiltonian given in Equation 5.27. Two of them have received special attention in theoretical and experimental literature: the magnetic dipole-dipole interaction $\hat{H}_{ss}$ between the two electronic spins $\vec{s_1}$ and $\vec{s_2}$, and second-order spin-orbit coupling. The former takes the general form of the interaction between two magnetic momenta [145, 146]. It is

$$\begin{aligned}\hat{H}_{ss} &= -\frac{\mu_0 \gamma_{s_1} \gamma_{s_2}}{4\pi\, R^3}\ T^2(C) \cdot T^2(\vec{s_1}, \vec{s_2}) \\ &= -\frac{\mu_0 \gamma_{s1} \gamma_{s2}}{4\pi\, R^3} \sqrt{\frac{4\pi}{5}} \sum_{q=-2}^{+2} (-1)^q\ Y_2^{-q}(\theta, \phi)\ \hat{T}_2^q(\vec{s_1}, \vec{s_2})\ ,\end{aligned} \tag{5.36}$$

where $\gamma_{s_1} = \gamma_{s_2} = \gamma_S$ is the electronic spin gyromagnetic ratio, of which the value is

[41] In Rb_2 the single-atom hyperfine splitting between the $F = 1$ and the $F = 2$ manifolds is $h \times 6.835\,\text{GHz}$, while the binding energy of the first vibrational state $v = -1$ is $E_b < h \times 100\,\text{MHz}$, and the $v = -2$ and $v = -3$ states have $E_b \simeq h \times 600\,\text{MHz}$ and $E_b \simeq h \times 2.2\,\text{GHz}$ respectively — see Figure 5.6.

[42] In $^6Li_2$ the single-atom hyperfine splitting between the $F = 1/2$ and the $F = 3/2$ manifold is $h \times 228\,\text{MHz}$ [143], while the binding energy of the first vibrational state $v = -1$ is $E_b \simeq h \times 1.38\,\text{GHz}$ in the singlet potential $S = 0$, and $E_b \simeq h \times 24\,\text{GHz}$ in the triplet potential $S = 1$ [131]. In $^2H_2$ the triplet potential is so shallow that it doesn't support any bound state.

[43] In this basis the electronic spins $s_1 = 1/2$ and $s_2 = 1/2$ are coupled to obtain the total electronic spin S, with $S = 0$ or 1 — see Subsection 5.2.2.

$\gamma_S/2\pi = h \times -2.8025$ MHz/G — see Equation 5.46[44]. The spin-spin dipole interaction involves the dot product of the two rank-2 tensors $T^2(C)$ and $T^2(\vec{s_1}, \vec{s_2})$[45] and is therefore sometimes referred to as a "tensor interaction". The components of the angular tensor $T^2(C)$ are the renormalized spherical harmonics $\hat{T}_2^{\,q} = \sqrt{4\pi/5}\,(Y_2^{\,q}(\theta,\phi))^* = (-1)^q\sqrt{4\pi/5}\,Y_2^{-q}(\theta,\phi)$. Consequently, $\hat{H}_{ss}$ is anisotropic and can couple different partial waves N, N'. The components of the tensor $T_2(\vec{s_1}, \vec{s_2})$ are the operators $\hat{T}_2^q(\vec{s_1}, \vec{s_2})$ and act on the electronic spins according to

$$\begin{aligned}
\hat{T}_2^0 &= 2\, s_{1,z}s_{2,z} - (s_{1,-}s_{2,+} + s_{1,+}s_{2,-})/2 \\
\hat{T}_2^{\pm 1} &= \mp\sqrt{\frac{3}{2}}\,(s_{1,\pm}s_{2,z} + s_{1,z}s_{2,\pm}) \\
\hat{T}_2^{\pm 2} &= \sqrt{\frac{3}{2}}\,s_{1,\pm}s_{2,\pm}\,.
\end{aligned} \tag{5.37}$$

All components of $T_2(\vec{s_1}, \vec{s_2})$ are off-diagonal in the hyperfine basis $|f_1, m_{f_1}\rangle\,|f_2, m_{f_2}\rangle$[46]. Approximating the open-channel scattering states and the resonant closed-channel state by the eigenstates of the Hamiltonian defined by Equation 5.30 — i.e., neglecting the exchange interaction —, the coupling matrix element that gives rise to Feshbach resonances is of the form

$$\langle E|\,\hat{V}_{12}\,|\psi_{\rm mol}^{(2)}\rangle = I_{\rm radial}\; I_{\rm spin+rotation}(B)\,, \tag{5.38}$$

where the overlap integrals are

$$\begin{aligned}
I_{\rm radial} &= -\frac{\mu_0\gamma_{s1}\gamma_{s2}}{4\pi}\,\langle\chi_{k,N}^{\rm scat}(R)|\,R^{-3}\,|\chi_{v,N'}^{\rm vib}(R)\rangle \\
I_{\rm spin+rotation}(B) &= \sqrt{\frac{4\pi}{5}}\sum_{q=-2}^{+2}\Big[(-1)^q\;\langle N, m_N|\,Y_2^{-q}(\theta,\phi)\,|N', m_{N'}\rangle \\
&\qquad \times \langle f_1, m_{f_1}, f_2, m_{f_2}|\,\hat{T}_2^{\,q}\,|f_1', m_{f_1'}, f_2', m_{f_2'}\rangle\Big]\,.
\end{aligned} \tag{5.39}$$

[44] In atomic units, the prefactor $\frac{\mu_0\gamma_{s1}\gamma_{s2}}{4\pi}$ reduces to α^2 where $\alpha \simeq \frac{1}{137}$ is the fine structure constant.

[45] We adopt the notation of Ref. [132].

[46] Note that $\hat{T}_2^0$ is diagonal in the $|S, m_S, s_1, s_2\rangle\,|i_1, m_{i_1}, i_2, m_{i_2}\rangle$ basis in which the exchange interaction is diagonal. The corresponding eigenvalues are $\hat{T}_2^0\,|S, m_S, s_1, s_2\rangle = \frac{1}{2}(3{m_S}^2 - S(S+1))\,|S, m_S, s_1, s_2\rangle$, as can easily be checked using Equation 5.37 and the decomposition $|S, m_S\rangle = \sum c\,|m_{s_1}, m_{s_2}\rangle$ with $|0,0\rangle = (|1/2,-1/2\rangle - |-1/2,1/2\rangle)/\sqrt{2}$, $|1,0\rangle = (|1/2,-1/2\rangle + |-1/2,1/2\rangle)/\sqrt{2}$ and $|1,\pm1\rangle = |\pm1/2,\pm1/2\rangle$, where $|S, m_S, s_1, s_2\rangle \equiv |S, m_S\rangle$ and $|s_1, s_2, m_{s_1}, m_{s_2}\rangle \equiv |m_{s_1}, m_{s_2}\rangle$ are the coupled and uncoupled basis for the electronic spins. This diagonal, or *direct* contribution to the spin-spin dipole interaction is sometimes referred to as the spin-spin dipole interaction itself in the literature.

The angular integrals $\langle N, m_N | \, Y_2^{-q}(\theta,\phi) \, | N', m_{N'} \rangle$ are integrals over the three spherical harmonics $Y_N^{m_N\,*} = (-1)^{m_N} Y_N^{-m_N}$, Y_2^{-q} and $Y_{N'}^{m_{N'}}$. They are therefore proportional to the corresponding $3j$ symbols, i.e.

$$\langle N, m_N | \, Y_2^{-q}(\theta,\phi) \, | N', m_{N'} \rangle \propto \begin{pmatrix} N & 2 & N' \\ -m_N & -q & m_{N'} \end{pmatrix} . \tag{5.40}$$

These $3j$ symbols are null if the triangle inequality $|N-2| \leq N' \leq |N+2|$ doesn't hold, therefore only d-wave ($N'=2$) molecular states can be coupled to incoming $N=0$ scattering states through the spin-spin dipole interaction[47]. Many resonances of this kind are reported in Ref. [135], as shown in Figure 5.6, and we observed many of them in our own experiments with ^{87}Rb[48].

The second type of small, anisotropic Feshbach resonances arises from the spin-orbit coupling $\hat{H}_{\mathrm{SO}}$. As discussed in Section 4.1, diagonal spin-orbit coupling is always null for a Σ electronic term, such as the $^3\Sigma^+$ and $^1\Sigma^+$ triplet and singlet terms of the bi-alkali PECs. However the off-diagonal contributions, which are taken into account only in second (and higher) order in perturbation theory, couple these terms to the $^1\Pi$, $^3\Pi$, $^5\Pi$ and $^3\Sigma^+$ higher-excited electronic terms. As is clear from Equation 5.37, the spin-spin dipole interaction only couples the initial state to states with $\Delta S = -1, 0$ or $+1$. Remarkably, second-order spin-orbit coupling can be formalized as an effective spin-spin dipole interaction of the same form as given in Equation 5.36, where the R-dependence depends on the details of the coupling matrix elements [139]. Therefore, it is subject to the same selection rules and produces Feshbach resonances by admixing d-wave molecular states with s-wave scattering states. These two mechanisms are not distinguishable in experimental data such as the ones presented in the table of Figure 5.6.

These two effects, spin-spin dipole interaction and second-order spin-orbit coupling, are also responsible for a very important phenomenon in ultracold atom gases: dipolar relaxation. For ^{87}Rb the spin exchange rates are very low[49]. Accordingly we simply refer the

[47] While the exchange interaction, Equation 5.31, admixes different hyperfine states in dependence of their decomposition onto the $|S, m_S, s_1, s_2\rangle \, |i_1, m_{i_1}, i_2, m_{i_2}\rangle$ basis, it doesn't change this selection rule because the triangle condition imposed by the rank 2 of the tensor $\hat{T}_2^{\,q}$ is independent of q. Therefore only $N=2$ molecular states can be coupled to s-wave scattering states, in heavy and light bi-alkali systems alike.

[48] Note that in non-alkali systems with valence electrons, but no nuclear spin, the spin-spin dipole interaction is the primary source of Feshbach resonances. That is the case of bosonic Cr, which has $i_1 = i_2 = 0$ and $s_1 = s_2 = 3$ in the electronic ground state, leading to seven PECs $^1\Sigma^+, ^3\Sigma^+, ..., ^{13}\Sigma^+$ corresponding to $S = 0, 1, ..., 6$ respectively but no hyperfine interaction [147].

[49] This is the reason why one can produce a BEC in an arbitrary state of ^{87}Rb, including the hyperfine states of the $f=2$ manifold. Spin exchange collisions induce changes of the $|f, m_f\rangle$ states of the two colliding atoms. The difference in internal energy between the initial pair $|f_1, m_{f_1}\rangle \, |f_2, m_{f_2}\rangle$ and the final pair $|f_1', m_{f_1'}\rangle \, |f_2', m_{f_2'}\rangle$ is transferred into relative kinetic energy and leads to two-body loss from the trap. In ^{133}Cs where the spin-exchange rates are high, BECs are typically produced in the lowest-lying hyperfine state $|f, m_f\rangle = |3, +3\rangle$ where no release of internal energy is possible.

interested reader to the beautiful work of Ref. [139], where these rates are estimated theoretically.

5.3 Magnetic Feshbach resonances in RbSr: mechanism I

The strongest interaction term that couples Rb-Sr atom pairs to RbSr molecular states is the perturbation of the Rb hyperfine structure due to the presence of Sr. It is referred to as "mechanism I" in our publication presented in Chapter 6, and in the subsequently published Ref. [27]. In the next subsections we remind the reader about the physics underlying the hyperfine structure of Rb, and show in which conditions its perturbation in presence of Sr leads to Feshbach resonances.

The Hamiltonian describing the collision of an alkali atom a and a closed-shell atom b in their electronic ground state is

$$\hat{H} = \frac{1}{2\mu}\left[-\hbar^2\frac{\mathrm{d}^2}{\mathrm{d}R^2} + \frac{\hat{N}^2}{R^2}\right] + \hat{V}_g(R) + \hat{H}_a + \hat{H}_b\,, \tag{5.41}$$

using the same notation as introduced in Chapter 2. It is the sum of the molecular Hamiltonian, as obtained in Equation 2.43 within the adiabatic approximation, and of the single-atom Hamiltonians $\hat{H}_a$ and $\hat{H}_b$. The single-atom Hamiltonians are

$$\hat{H}_a = \zeta_a \hat{i}_a \cdot \hat{s} - \left(\gamma_{i,a}\,\hat{i}_{a,z} + \gamma_S\,\hat{s}_z\right) B \tag{5.42}$$

$$\hat{H}_b = -\gamma_{i,b}\,\hat{i}_{b,z} B\,, \tag{5.43}$$

where the electronic and nuclear spin operators are denoted as $\hat{s}$ and $\hat{i}_a$, $\hat{i}_b$ respectively, and the associated projection operators are denoted as $\hat{s}_z$, $\hat{i}_{a,z}$ and $\hat{i}_{b,z}$. The projection is taken along the quantization axis z defined by the direction of the applied magnetic field B. We follow the notation of Ref. [26], where the indices a and b represent the Rb and Sr atoms respectively, as indicated below.

$$a = \mathrm{Rb} \qquad b = \mathrm{Sr} \tag{5.44}$$

The term $\zeta_a \hat{i}_a \cdot \hat{s}$ is the *scalar* or *Fermi contact* hyperfine interaction between the electronic and nuclear spins of Rb[50]. The hyperfine constants for the two naturally-occurring isotopes of Rb are [50, 148]

$$\begin{aligned} \zeta_{^{87}\mathrm{Rb}} &= h \times 3.41734130545\ \mathrm{GHz} \\ \zeta_{^{85}\mathrm{Rb}} &= h \times 1.0119108\ \mathrm{GHz}\,. \end{aligned} \tag{5.45}$$

[50] The other relevant type of hyperfine interaction is the dipolar hyperfine interaction, discussed in Section 5.5.

The terms $-\left(\gamma_{i,a}\,\hat{i}_{a,z}+\gamma_S\,\hat{s}_z\right)B$ and $-\gamma_{i,b}\,\hat{i}_{b,z}B$ define the *Zeeman Hamiltonian* in presence of an external magnetic field of magnitude B. They are induced by the interactions $-\vec{\mu}\cdot\vec{B}$ of the magnetic moments of each particle (electrons and nuclei) with the field. The corresponding gyromagnetic ratios are[51]

$$\begin{aligned}\gamma_S/2\pi &= h\times -2.8025\,\mathrm{MHz/G}\\ \gamma_{i,^{87}\mathrm{Rb}}/2\pi &= h\times \quad 1.39282\,\mathrm{kHz/G}\\ \gamma_{i,^{85}\mathrm{Rb}}/2\pi &= h\times \quad 0.410985\,\mathrm{kHz/G}\\ \gamma_{i,^{87}\mathrm{Sr}}/2\pi &= h\times -0.183999\,\mathrm{kHz/G}\,.\end{aligned} \tag{5.46}$$

Note that of the four naturally-occurring stable isotopes of Sr, only ^{87}Sr has a non-zero nuclear spin $i_{\mathrm{Sr}}=9/2$ and it has a very small, but non-zero gyromagnetic ratio. From these values it is clear that the dominating contribution to the Zeeman shifts stems from the spin of the valence electron of Rb. As shown in Figure 5.8, the relative contribution of a state of given spin projection m_S to a given $|f,m_f\rangle$ eigenstate of $\hat{H}_a$ changes with the value of the applied magnetic field B. Therefore the magnetic moment of a Rb atom, and of a Rb-Sr pair, depends on the value of B. Furthermore, in Rb-^{87}Sr the Zeeman energy is set mostly by the $|f,m_f\rangle$ state of Rb, not by the $|i,m_i\rangle$ state of the Sr atom which has a very small magnetic sensitivity.

In the case of bosonic Sr we have $i_b=i_{b,z}=0$, therefore the contribution of the single-atom Hamiltonians reduces to the Rb Hamiltonian $\hat{H}_a$.

5.3.1 The Rb Hamiltonian in absence and in presence of an external magnetic field

Rb has one valence electron with spin $s=1/2$ and a nuclear spin $i_{\mathrm{Rb}}=3/2$ for ^{87}Rb and $i_{\mathrm{Rb}}=5/2$ for ^{85}Rb, which leads to two hyperfine manifolds $f=i_{\mathrm{Rb}}-s$ and $f=i_{\mathrm{Rb}}+s$. The total angular momentum $\vec{f}$, sum of the electronic and nuclear spin is[52]

$$\vec{f}=\vec{s}+\vec{i}\,. \tag{5.47}$$

[51] In the convention adopted in Refs. [50, 148], the g-factors of the electron and of the nuclei i are defined by $\gamma_S=-\mu_B g_S/\hbar$ and $\gamma_i=-\mu_B g_i/\hbar$ respectively, where $\mu_B=h\times 1.3996\,\mathrm{MHz/G}$ is the Bohr magneton. In this convention the electron g-factor $g_l=2.00231930436$ is thus positive. The CODATA recommendation is to define it negative instead. Note that the electron orbital g_l factor (irrelevant to the electronic ground state of alkali and closed-shell atoms) is $g_l\simeq 1$ and corresponds to $\gamma_l/2\pi\simeq -1.40\,\mathrm{MHz/G}$, half the electronic spin gyromagnetic ratio.

[52] In the general case the total angular momentum is $\vec{f}=\vec{l}+\vec{s}+\vec{i}$, where $\vec{l}$ is the orbital electronic momentum. In the ground state $^2S_{1/2}$ of the Rb atom, there is no orbital electronic excitation therefore $\vec{l}=\vec{0}$.

The quantum numbers s, i, f and m_f define a complete basis of states for the Rb atom, known as the *coupled basis*[53], and fulfill the angular momentum properties

$$\begin{aligned} \hat{\vec{f}}^{\,2} \left| s i f, m_f \right\rangle &= f(f+1)\, \hbar^2 \left| s\, i\, f, m_f \right\rangle \\ \hat{f}_z \left| s\, i\, f, m_f \right\rangle &= m_f\, \hbar \left| s\, i\, f, m_f \right\rangle \ . \end{aligned} \tag{5.48}$$

The hyperfine interaction $\zeta_a \hat{i}_a \cdot \hat{s}$ is diagonal in the coupled basis. This is clear from the identity $\vec{f}^{\,2} = (\vec{i}+\vec{s})^2 = \vec{i}^{\,2} + \vec{s}^{\,2} + 2\,\vec{i}\cdot\vec{s}$, which implies

$$\begin{aligned} \vec{i}\cdot\vec{s} \left| s\, i\, f\, m_f \right\rangle &= \frac{\vec{f}^{\,2} - \vec{s}^{\,2} - \vec{i}^{\,2}}{2} \left| s\, i\, f, m_f \right\rangle \\ &= \frac{f(f+1) - s(s+1) - i(i+1)}{2} \left| s\, i\, f, m_f \right\rangle \ . \end{aligned} \tag{5.49}$$

In absence of an external magnetic field, $B = 0$ G, only the hyperfine interaction contributes to the internal energy of the Rb atom and the Rb Hamiltonian is fully diagonal in the coupled basis. This is expressed by the commutation relations $[\hat{H}_a, \hat{\vec{f}}^{\,2}] = \zeta_a \times [\hat{i}_a \cdot \hat{s}, \hat{\vec{f}}^{\,2}] = 0$ and $[\hat{H}_a, \hat{f}_z] = \zeta_a \times [\hat{i}_a \cdot \hat{s}, \hat{f}_z] = 0$. Therefore, f and m_f are good quantum numbers in absence of magnetic field.

In presence of an external magnetic field, $B \neq 0$ G, the Zeeman energies of the electron and of the nucleus are added to the hyperfine interaction — see Equation 5.42. The eigenstates of the system are then not anymore eigenstates of $\hat{\vec{f}}^{\,2}$, but are still eigenstates of $\hat{f}_z$ [54]. This is expressed by the (non-)commutation relations

$$\begin{aligned} [\hat{H}_a, \vec{f}^{\,2}] &= [\zeta_a \vec{i}\cdot\vec{s}, \vec{f}^{\,2}] + [\left(\gamma_{i,a}\hat{i}_z + \gamma_S \hat{s}_z\right) B, \vec{f}^{\,2}] \\ &= 0 + [\left(\gamma_{i,a}\hat{i}_z + \gamma_S \hat{s}_z\right) B, \vec{i}^{\,2} + \vec{s}^{\,2} + 2\,\vec{i}\cdot\vec{s}] \\ &= \gamma_{i,a} B\, i\hbar \left(\hat{i}_y \hat{s}_x - \hat{i}_x \hat{s}_y\right) + \gamma_S B\, i\hbar \left(\hat{i}_x \hat{s}_y - \hat{i}_y \hat{s}_x\right) \\ &\neq 0 \end{aligned} \tag{5.50}$$

and

[53] This name indicates the vectorial coupling of $\vec{s}$ and $\vec{i}$ by the hyperfine interaction. Note that s and i fulfill the properties $\hat{\vec{s}}^{\,2} \left| s\, i\, f, m_f \right\rangle = s(s+1)\, \hbar^2 \left| s\, i\, f, m_f \right\rangle$ and $\hat{\vec{i}}^{\,2} \left| s\, i\, f, m_f \right\rangle = i(i+1)\, \hbar^2 \left| s\, i\, f, m_f \right\rangle$, and are always good quantum numbers since $[\hat{H}_a, \hat{\vec{s}}^2] = [\hat{H}_a, \hat{\vec{i}}^2] = 0$ for any value of the magnetic field.

[54] Equations 5.50 and 5.51 are obtained using the standard angular momentum equalities for the electron spin $[\vec{s}^2, s_i] = 0$ and $[s_i, s_j] = i\hbar\epsilon_{i,j,k}\, s_k$ and their nuclear spin counterparts. The indices denote Cartesian coordinates $i, j, k \in \{x, y, z\}$ and $\epsilon_{i,j,k} = -1/+1$ for odd/even permutations of x, y, z respectively. We denote the nuclear spin of Rb $\hat{i}_a \equiv \hat{i}$ and omit the hats of vectorial operators for ease of reading.

$$\begin{aligned}[\hat{H}_a, \hat{f}_z] &= [\zeta_a \vec{i} \cdot \vec{s} + \left(\gamma_{i,a}\hat{i}_z + \gamma_S \hat{s}_z\right) B, \hat{f}_z] \\ &= [\zeta_a \left(\hat{\vec{f}}^{\,2} - \hat{\vec{s}}^{\,2} - \hat{\vec{i}}^{\,2}\right)/2, \hat{f}_z] + [\left(\gamma_{i,a}\hat{i}_{a,z} + \gamma_S \hat{s}_z\right) B, \hat{i}_z + \hat{s}_z] \\ &= \zeta_a \left([\hat{\vec{f}}^{\,2}, \hat{f}_z] - [\hat{\vec{s}}^{\,2}, \hat{i}_z + \hat{s_z}] - [\hat{\vec{i}}^{\,2}, \hat{i}_z + \hat{s_z}]\right)/2 + 0 \\ &= 0\,,\end{aligned} \tag{5.51}$$

respectively. The total projection of the angular momentum $m_f = m_s + m_i$ onto the magnetic field axis is therefore always a good quantum number, whereas f is a good quantum number only in absence of magnetic field. The convention adopted in the literature is to label the eigenstates of the system as $|s\ i\ f, m_f\rangle \equiv |f, m_f\rangle$ even in presence of a magnetic field, because denoting an eigenstate by the hyperfine manifold f to which it correlates at $B = 0$ G and by its projection m_f is unambiguous. Using this convention, the eigenstates of the system $|f, m_f\rangle$ fulfill Equations 5.48 and 5.49 only at $B = 0$ G, whereas for increasing values of magnetic field the hyperfine interaction $\zeta_a \hat{i}_a \cdot \hat{s}$ becomes increasingly off-diagonal in this basis[55]. This competition between the Zeeman energy and the hyperfine interaction is at the core of mechanism I, leading to Feshbach resonances in RbSr.

5.3.2 The perturbation of the Rb hyperfine structure due to the presence of Sr (mechanism I)

In this subsection, we discuss how the Rb hyperfine structure is perturbed by Sr and under which conditions this may lead to RbSr Feshbach resonances. The strength of the scalar hyperfine interaction in the electronic ground state of Rb, the first term of Equation 5.42, is set by the electronic density $|\psi_e(0)|^2$ (i.e. the probability of presence per unit volume) of the Rb valence electron at the position of the nucleus. This term is also referred to as the Fermi contact interaction, and the corresponding Hamiltonian is

[55] In the low magnetic-field limit, the hyperfine interaction dominates and the Zeeman Hamiltonian can be treated as a perturbation of the hyperfine Hamiltonian. That is how the g_f-factors describing the low magnetic field behaviour of the $|f, m_f\rangle$-states are derived. In the high-field limit, on the contrary, the Zeeman energy dominates and the best basis to describe the system is the *uncoupled basis* $|s\ m_s\ i\ m_i\rangle$ that accounts for the individual interaction of the angular momenta i and s with the magnetic field. In between these two limits, the interplay between the hyperfine and Zeeman interactions leads to the "bending" of the energy curves of several $|f, m_f\rangle$ states, due to the very strong repulsion of levels with same m_f projections but belonging to different f manifolds — see Figure 5.7. The change of magnetic moment of the Rb eigenstates with changing magnetic field is due to the change of the relative contribution of each uncoupled state $|s\ m_s\ i\ m_i\rangle$ to the coupled states $|f, m_f\rangle$ that diagonalize $\hat{H}_a$.

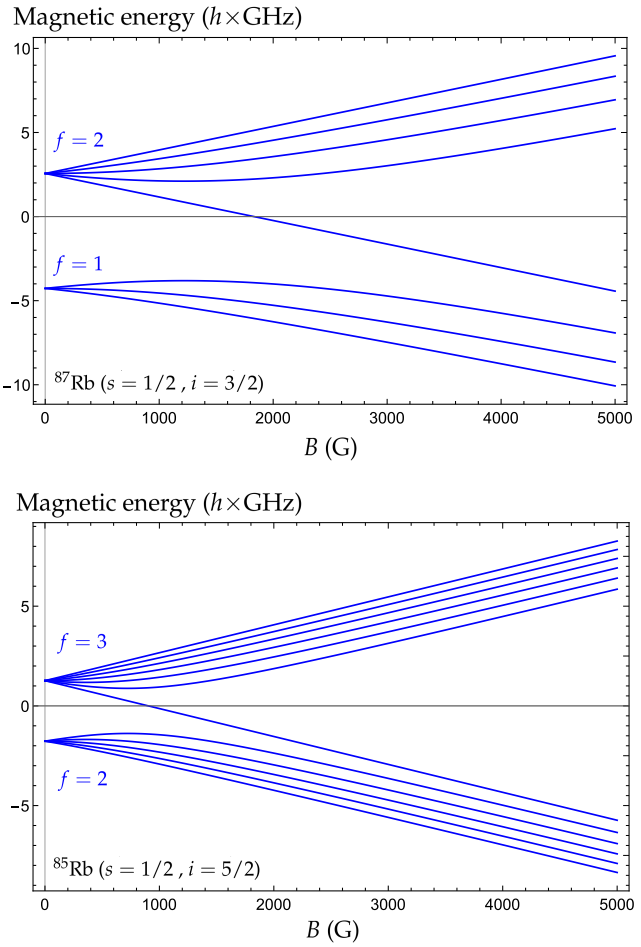

FIGURE 5.7: Zeeman diagrams of the single-atom ^{87}Rb and ^{85}Rb Hamiltonians, associated with the hyperfine constants of Equation 5.45, which define the zero-field splitting, and the gyromagnetic ratios of Equation 5.46, which define the Zeeman energy in presence of the magnetic field B. The f quantum number is a good number only at $B = 0$ G, while its projection m_f along the axis of the magnetic field is always a good quantum number. The bending of the Zeeman curves indicates that the Zeeman energy becomes comparable or larger than the hyperfine energy.

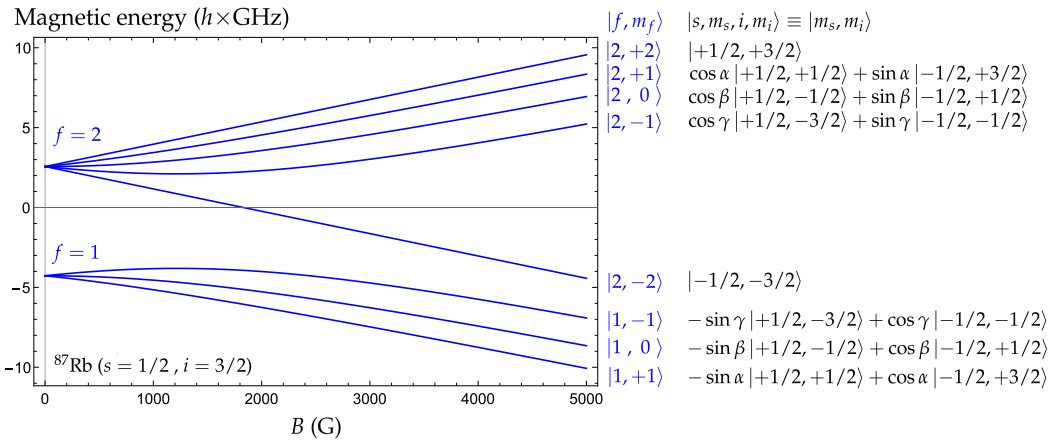

FIGURE 5.8: Single-atom eigenstates of ^{87}Rb as a function of the external magnetic field B. The $|f, m_f\rangle$ eigenstates are decomposed into the uncoupled-basis states $|s, m_s, i, m_i\rangle$ of the individual electronic spin and nuclear angular momenta, which define the magnetic behaviour of the atom. The relative contribution of each of the uncoupled states to a given $|f, m_f\rangle$-state varies with B, due to the changing contribution of the Zeeman energy to the total energy of the system. Accordingly, the magnetic moment of a given $|f, m_f\rangle$-state is a function of B. The limiting behaviour is $\sin\alpha, \sin\beta, \sin\gamma \to 0$ at $B \to \infty$ and $\sin^2\alpha, \sin^2\beta, \sin^2\gamma \to 3/4, 2/4, 1/4$ at $B \to 0$ [146]. The hyperfine operator $\zeta_a \hat{i}_a \cdot \hat{s}$ is only diagonal in the $|f, m_f\rangle$ eigenbasis at $B = 0\,$G. This is essential to mechanism I, which leads to RbSr Feshbach resonances.

$$\begin{aligned}\hat{H}_{\text{Fermi}} &= \zeta_a \hat{i}_a \cdot \hat{s} \\ &= \frac{2}{3}|\psi_e(0)|^2 |\gamma_S| \gamma_{i,a} \times \hat{i}_a \cdot \hat{s}\,,\end{aligned} \tag{5.52}$$

where γ_S and $\gamma_{i,a}$ are the gyromagnetic ratios of the electron spin and of the nuclear spin of a respectively — see Subsection 5.3.1. The value of $\gamma_{i,a}$ depends on the nucleus considered and its sign defines the sign of the hyperfine coupling constant ζ_a. The physical meaning of Equation 5.52 is clear: the larger the overlap between the electronic and nuclear wavefunctions, the stronger the interaction between the nuclear spin and electronic spin.

In presence of a Sr atom at a given internuclear distance R from Rb, the Coulomb repulsion between the electronic cloud of Sr and the valence electron of Rb leads to a decrease of the electronic density $|\psi_e(0)|^2$ at the position of the nucleus, which can be modelled by an R-dependent Rb hyperfine constant. The modified hyperfine constant is

$$\zeta_a(R) = \zeta_a + \Delta\zeta_a(R)\,. \tag{5.53}$$

The Hamiltonian of the system may therefore be written as the sum of a zeroth-order term $\hat{H}^0$, which contains the Rb and Sr single-atom Hamiltonians given in Equations 5.42 and 5.43, and of the perturbation $\hat{H}'$ introduced by the R-dependence of the hyperfine constant. It reads

$$\hat{H}^0 = \frac{1}{2\mu}\left[-\hbar^2\frac{\mathrm{d}^2}{\mathrm{d}R^2} + \frac{\hat{N}^2}{R^2}\right] + \hat{V}_g(R) + \zeta_a \hat{i}_a \cdot \hat{s} - \left(\gamma_{i,a}\,\hat{i}_{a,z} + \gamma_S\,\hat{s}_z\right) B \tag{5.54}$$

$$\hat{H}' = \Delta\zeta_a(R)\hat{i}_a \cdot \hat{s}\,. \tag{5.55}$$

The unperturbed Hamiltonian, Equation 5.54, is the sum of the molecular Hamiltonian and the Rb single-atom Hamiltonian, given in Equations 2.43 and 5.42 respectively. It supports molecular bound states as well as atom pair scattering states. The corresponding molecular eigenstates have radial nuclear wavefunctions $\chi^{\text{vib}}_{\nu,N}(R)/R$ that are set by $V_g(R)$ and denoted by the vibrational quantum number ν, and their rotational nuclear motion and hyperfine contribution are described by the basis sets $|N, m_N\rangle \equiv Y^{\text{rot}}_N(\theta,\phi)$ and $|f, m_f\rangle$ respectively — see Equations 2.39 and 5.3.1. In absence of external confinement, the scattering eigenstates have energy-normalized radial internuclear wavefunctions $|\chi^{\text{scat}}_{k,N}(R)\rangle \equiv \chi^{\text{scat}}_{k,N}(R)/R$, of which the asymptotic behaviour is given by Equation 5.1, and their rotational nuclear motion and hyperfine contribution are described by the same basis sets $|N, m_N\rangle$ and $|f, m_f\rangle$ as the molecular states. Importantly, the eigenstates of $\hat{H}^0$ are by definition orthogonal with

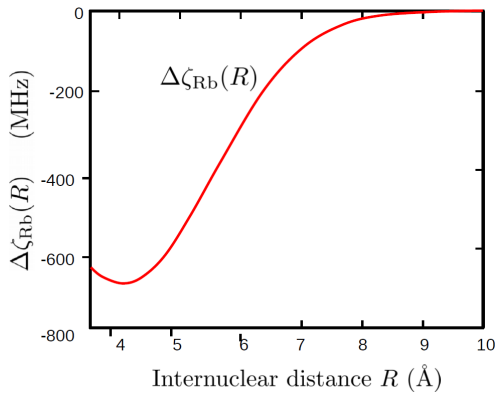

FIGURE 5.9: Variation of the hyperfine constant of ^{87}Rb as a function of the internuclear distance between Rb and Sr. This variation defines the strength of the radial coupling between atom pair states and molecular states in the context of mechanism I, which leads to RbSr Feshbach resonances. The single-atom ^{87}Rb hyperfine constant itself is $\zeta_{^{87}\mathrm{Rb}} = h \times 3.417...$ GHz, therefore this relatively small R-dependent variation can be treated as a perturbation. Calculated by Piotr Żuchowski.

respect to one another. In particular, scattering states $|E;k,N\rangle = |\chi^{\mathrm{scat}}_{k,N}(R)\rangle\,|N,m_N\rangle\,|f,m_f\rangle$ and molecular states $|\psi_{\mathrm{mol}}\rangle = |\chi^{\mathrm{vib}}_{v,N'}(R)\rangle\,|N',m_{N'}\rangle\,|f',m_{f'}\rangle$ are orthogonal[56], as expressed by

$$\begin{aligned}\langle E;k,N|\psi_{\mathrm{mol}}\rangle &= \langle\chi^{\mathrm{scat}}_{k,N}(R)|\chi^{\mathrm{vib}}_{v,N'}(R)\rangle\,\langle N,m_N|N',m_{N'}\rangle\,\langle f,m_f|f',m_{f'}\rangle \\ &= 0\,.\end{aligned} \tag{5.56}$$

Furthermore, the eigenstates are subject to the orthogonality relations[57,58]

[56] $|E;k,N\rangle$ denotes the scattering state of collisional energy $E = \hbar^2k^2/2\mu$ and of rotational quantum number N — see Subsection 5.1.1. In the ultracold limit, the scattering cross-section is largely dominated by s-wave scattering states ($N = 0$). An interesting exception to that is the ^{87}Rb^{88}Sr mixture for which the p-wave ($N = 1$) scattering cross-section is enhanced by a virtual molecular state close to the zero-energy p-wave threshold — see Chapter 3.

[57] The spherical harmonics $|N,m_N\rangle$ are joint, normalized eigenstates of $\hat{N}^2$ and $\hat{N}_z$ and as such fulfill the properties $\hat{N}^2\,|N,m_N\rangle = N(N+1)\hbar^2\,|N,m_N\rangle$, $\hat{N}_z\,|N,m_N\rangle = m_N\hbar\,|N,m_N\rangle$ and $\langle N,m_N|N',m_{N'}\rangle = \delta_{N,N'}\,\delta_{m_N,m_{N'}}$ — see Subsection 2.1.6.

[58] Note that in general $\langle\chi^{\mathrm{scat}}_{k,N}(R)|\chi^{\mathrm{vib}}_{v,N'}(R)\rangle \neq 0$ for $N \neq N'$. Indeed, in that case the radial contributions $|\chi^{\mathrm{scat}}_{k,N}(R)\rangle$ and $|\chi^{\mathrm{vib}}_{v,N}(R)\rangle$ are eigenfunctions of different radial equations, as defined by Equation 2.42. The corresponding molecular and scattering states are still orthogonal, but the orthogonality condition is provided by the orthogonality of the rotational contributions, Equation 5.58.

$$\begin{aligned}\langle \chi^{\text{scat}}_{k,N}(R)|\chi^{\text{vib}}_{\nu,N'}(R)\rangle &= \int_0^\infty R^{-2}\,\chi^{\text{scat}}_{k,N}(R)\chi^{\text{vib}}_{\nu,N'}(R)R^2dR \\ &= 0 \quad \text{for} \quad N = N'\end{aligned} \tag{5.57}$$

$$\begin{aligned}\langle N, m_N|N', m_{N'}\rangle &= \int_{\phi=0}^{2\pi}\int_{\theta=0}^{\pi}(Y^{\text{rot}}_N(\theta,\phi))^*\,Y^{\text{rot}}_{N'}(\theta,\phi)\sin(\theta)d\theta d\phi \\ &= \delta_{N,N'}\,\delta_{m_N,m_{N'}}\end{aligned} \tag{5.58}$$

$$\langle f, m_f|f', m_{f'}\rangle = \delta_{f,f'}\,\delta_{m_f,m_{f'}}\,. \tag{5.59}$$

The perturbation of the Rb hyperfine structure, Equation 5.55, breaks this orthogonality, thereby producing Feshbach resonances by inducing coupling between specific sets of free atom states and molecular states. The R-dependent hyperfine constant mixes the radial nuclear wavefunctions of these eigenstates, while the $\hat{i}_a \cdot \hat{s}$ operator mixes their hyperfine contributions. The matrix elements associated with this mixing are

$$\begin{aligned}\langle E;k,N|\,\hat{H}'\,|\psi_{\text{mol}}\rangle &= \langle \chi^{\text{scat}}_{k,N}(R)|\,\Delta\zeta_a(R)\,|\chi^{\text{vib}}_{\nu,N'}(R)\rangle\,\langle N, m_N|N', m_{N'}\rangle\,\langle f, m_f|\,\hat{i}_a\cdot\hat{s}\,|f', m_{f'}\rangle \\ &= I_{\text{radial}}\,I_{\text{spin}}(B)\,\delta_{N,N'}\,\delta_{m_N,m_{N'}}\,,\end{aligned} \tag{5.60}$$

and the Feshbach resonance Breit-Wigner width, Equation 5.7, associated with the mixing of one atom pair state with a molecular state is

$$\Gamma_{12}(E) = 2\pi|\,\langle E;k,N|\,\hat{H}'\,|\psi_{\text{mol}}\rangle\,|^2\,. \tag{5.61}$$

Importantly, the perturbation of Equation 5.55 does *not* couple different partial waves $|N, m_N\rangle$ and $|N', m_{N'}\rangle$, for it is isotropic and therefore doesn't act on the angular degrees of freedom (θ,ϕ). The radial overlap integral I_{radial} depends on the magnitude of the change of the hyperfine structure with the internuclear distance R, and on the shape of the radial atomic and molecular nuclear wavefunctions. It reads

$$\begin{aligned}I_{\text{radial}} &= \langle \chi^{\text{scat}}_{k,N}(R)|\,\Delta\zeta_a(R)\,|\chi^{\text{vib}}_{\nu,N'}(R)\rangle \\ &= \int_0^\infty \chi^{\text{scat}}_{k,N}(R)\Delta\zeta_a(R)\chi^{\text{vib}}_{\nu,N'}(R)dR\,.\end{aligned} \tag{5.62}$$

The spin integral $I_{\text{spin}}(B)$ is a purely atomic quantity. It depends on the value of the external magnetic field B, for the $|f, m_f\rangle$-states themselves are B-dependent, as explained in Subsection 5.3.1. More precisely, this integral depends on the value of the Rb nuclear and electronic spin projection $m_{i,a}$ and m_s onto the magnetic field axis. Thus, since the contribution of a given uncoupled state $|s, m_s, i, m_i\rangle$ to a given $|f, m_f\rangle$-state is a function of B — see Figure 5.8 —, so is $I_{\text{spin}}(B)$. This spin integral quantifies the off-diagonal nature of the hyperfine interaction in the $|f, m_f\rangle$ basis, induced by its competition with the Zeeman energy. It is non-zero only in presence of an external magnetic field, as shown in Figure 5.10, and only in the case $\Delta m_f = m_{f'} - m_f = 0$. The latter property is readily understood by writing the hyperfine operator as $\hat{i}_a \cdot \hat{s} = \hat{i}_{a,z}\hat{s}_z + \frac{\hat{i}_{a,+}\hat{s}_- + \hat{i}_{a,-}\hat{s}_+}{2}$, where $\hat{i}_{a,+}$ and $\hat{i}_{a,-}$ are the nuclear spin projection raising and lowering operators respectively, and $\hat{s}_+$ and $\hat{s}_-$ their electronic spin counterparts[59]. The operator $\hat{i}_a \cdot \hat{s}$ produces either $\Delta m_{i,a} = \Delta m_s = 0$ or $\Delta m_{i,a} = +1/-1$ and $\Delta m_s = -1/+1$, leaving the total projection $m_f = m_{i,a} + m_s$ unchanged[60]. The selection rules associated with the spin integral are thus

$$I_{\text{spin}}(B) = \langle f, m_f | \, \hat{i}_a \cdot \hat{s} \, | f', m_{f'} \rangle \neq 0 \iff B > 0\,\text{G} \quad \text{and} \quad \Delta m_f = 0\,. \tag{5.63}$$

The perturbation of the Rb hyperfine structure therefore produces Feshbach resonances at the crossing of molecular and atom pair states with identical quantum numbers N and m_f. Since an atom pair state and a weakly-bound molecular state with identical hyperfine contribution $|f, m_f\rangle$ have the same magnetic moment[61] and therefore cannot cross, this situation arises only when an atom pair state crosses a molecular state belonging to a different f manifold. There are not so many of such crossings. In the ^{87}Rb-^{84}Sr mixture, which is of interest to us because we can produce double BECs of ^{87}Rb-^{84}Sr, there is only one resonance arising in the range $0 - 2000\,\text{G}$[62]. It involves the crossing of an atom pair state in the

[59] The nuclear and electronic spin raising and lowering operators $\hat{i}_\pm = \hat{i}_x \pm i\,\hat{i}_y$ and $\hat{s}_\pm = \hat{s}_x \pm i\,\hat{s}_y$ are designed to act on the uncoupled basis and fulfill the properties $\hat{i}_\pm \, |s, m_s, i, m_i\rangle = \sqrt{i(i+1) - m_i(m_i \pm 1)}\hbar \, |s, m_s, i, (m_i + 1)\rangle$ and $\hat{s}_\pm \, |s, m_s, i, m_i\rangle = \sqrt{s(s+1) - m_s(m_s \pm 1)}\hbar \, |s, (m_s + 1), i, m_i\rangle$.

[60] The sum of the projections of *all* angular momenta of an isolated quantum system along a given axis is always conserved. That is simply one of the many consequences of momentum conservation. In the present case only the nuclear spin and the electronic spin are involved, therefore the sum of their projection must be conserved. In the context of mechanism III that is anisotropic and thus can couple states of different rotational momentum N and projection m_N, the sum of m_N and of the projection of all nuclear and electronic spins is conserved — see Section 5.5, Equation 5.76.

[61] The molecular correction to the hyperfine structure $\Delta\zeta_a(R)$ actually leads to a very small differential magnetic moment between molecular and atom states with same $|f, m_f\rangle$. However, this correction is orders of magnitude too small to allow the crossing of such states at experimentally achievable magnetic fields.

[62] We remind the reader that in the ultracold limit, the scattering cross-section is largely dominated by s-wave scattering. Therefore, the open channel states that we consider here are s-wave atom pair states ($N = 0$).

open channel $|f, m_f\rangle = |1, +1\rangle$ with the molecular state $|\nu = -4, n = 0\rangle$ in the closed channel $|f, m_f\rangle = |2, +1\rangle$, at a field of $B = 1311\,\mathrm{G}$. The binding energy of this molecular state is $E_b = 9239(3)\,\mathrm{MHz}$. This is the Feshbach resonance we are currently investigating for the magnetoassociation of ^{87}Rb^{84}Sr.

In our 1064 nm optical lattice, the spin integral is left unchanged but the radial integral is modified compared to the free-space case — see Subsection 5.1.2. The Breit-Wigner width is replaced by the energy gap $\hbar|\Omega|$, associated with the coupling matrix element defined as

$$\begin{aligned} \frac{\hbar\Omega}{2} &= \langle E; n, N| \hat{H}' |\psi_{\mathrm{mol}}\rangle \\ &= I_{\mathrm{radial}}\, I_{\mathrm{spin}}(B)\, \delta_{N,N'}\, \delta_{m_N, m_{N'}}\,. \end{aligned} \tag{5.64}$$

This coupling matrix element is related to the Landau-Zener molecule formation efficiency η as in Equation 5.22. The larger $|\Omega|$, the faster and easier magnetoassociation is. The spin and angular integrals are the same as in Equation 5.61, but the radial integral now reads

$$I_{\mathrm{radial}} = \langle \chi^{\mathrm{trap}}_{n,N}(R)|\, \Delta\zeta_a(R)\, |\chi^{\mathrm{vib}}_{\nu,N'}(R)\rangle \quad \propto \omega_{\mathrm{rel}}^{3/4} \quad \text{for} \quad N = N' = 0\,. \tag{5.65}$$

We aim at using the ^{87}Rb^{84}Sr Feshbach resonance arising at $B = 1311\,\mathrm{G}$ for magnetoassociation, as mentioned in Subsection 5.1.2. The gap associated with the coupling matrix element, Equation 5.64, is estimated to be $|\Omega|/2\pi \simeq 2\,\mathrm{kHz}$ at $\omega_{\mathrm{rel}} = 2\pi \times 60\,\mathrm{kHz}$ for this resonance [P. Żuchowski, private communication]. Furthermore, the strength of the coupling goes as $\Omega \propto \omega_{\mathrm{rel}}^{3/4}$ in the ground state $n = N = 0$ of the lattice [132][M. Frye & P. Żuchowski, private communication]. Our current lattice beams allow to reach $\omega_{\mathrm{rel}} = 2\pi \times 44\,\mathrm{kHz}$, bringing us to a maximum of $|\Omega|/2\pi = 1.6\,\mathrm{kHz}$. The relative magnetic moment $\delta\mu$ of the atom pair and molecular states is given by $\delta\mu/h = 2.153\,\mathrm{MHz/G}$ at $B = 1311\,\mathrm{G}$. This corresponds to a magnetic window of $\hbar|\Omega|/\delta\mu = 0.8\,\mathrm{mG}$ within which the two states are strongly mixed. This 0.8 mG window defines the level at which we need to stabilize the $B = 1311\,\mathrm{G}$ magnetic field to perform efficient magnetoassociation.

There are two more ^{87}Rb^{84}Sr Feshbach resonances induced by the $|\nu = -4, N = 0\rangle$ molecular state. They are located at $B = 2217\,\mathrm{G}$ and $B = 3749\,\mathrm{G}$, in the open channels $|f, m_f\rangle = |1, 0\rangle$ and $|1, -1\rangle$ respectively, and it is worth checking whether they might prove easier to use for magnetoassociation. The radial integral is the same for these resonances and for the $B = 1311\,\mathrm{G}$ resonance, because they involve the same vibrational state. However, their spin integral differ, as well as the relative moment of the atom pair and molecular states at the position of the crossing. The corresponding values are

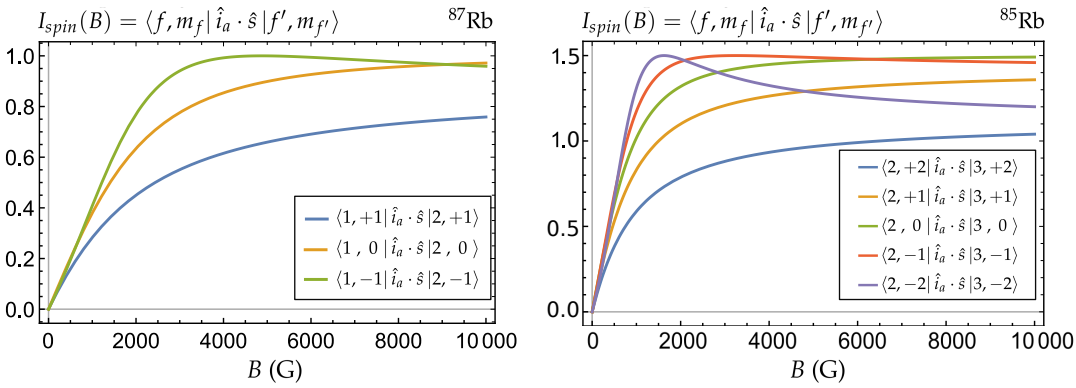

FIGURE 5.10: Non-zero spin integrals of ^{87}Rb and ^{85}Rb as a function of the magnetic field B. Together with the radial overlap integral, these spin integrals define the coupling strength of mechanism I, which produces RbSr Feshbach resonances. Calculated by the author.

$$
\begin{aligned}
I_{\text{spin}}(B) &= \langle 1, +1 | \hat{i}_a \cdot \hat{s} | 2, +1 \rangle = 0.34 \quad \text{with} \quad \delta\mu/h = 2.15\,\text{MHz/G} \quad \text{at} \quad B = 1311\,\text{G} \\
I_{\text{spin}}(B) &= \langle 1, \ \ 0 | \hat{i}_a \cdot \hat{s} | 2, \ \ 0 \rangle = 0.67 \quad \text{with} \quad \delta\mu/h = 1.89\,\text{MHz/G} \quad \text{at} \quad B = 2217\,\text{G} \\
I_{\text{spin}}(B) &= \langle 1, -1 | \hat{i}_a \cdot \hat{s} | 2, -1 \rangle = 0.99 \quad \text{with} \quad \delta\mu/h = 2.15\,\text{MHz/G} \quad \text{at} \quad B = 3749\,\text{G}\,.
\end{aligned}
\tag{5.66}
$$

At $\omega_{\text{rel}} = 2\pi \times 43.4\,\text{kHz}$, this results in magnetic windows of $\hbar|\Omega|/\delta\mu = 0.8, 1.7$ and $2.2\,\text{mG}$ at $B = 1311, 2217$ and $3749\,\text{G}$ respectively. The technological requirements to stabilize B at the mG level are more demanding at $2217\,\text{G}$ and $3749\,\text{G}$ than they are at $1311\,\text{G}$, and such a slight increase of the coupling width does not justifies using either of these two extra resonances for magnetoassociation.

5.4 Magnetic Feshbach resonances in RbSr: mechanism II

The second interaction term that couples Rb-Sr atom pairs to RbSr molecular states is the scalar hyperfine interaction that couples the nuclear spin of fermionic ^{87}Sr to the electronic spin of Rb. It is referred to as mechanism II in our publication presented in Chapter 6, and in the subsequently published Ref. [27]. This mechanism doesn't exist for bosonic isotopes of Sr for which the nuclear spin is zero.

In presence of a Rb atom at a given internuclear distance R from Sr, the nuclear spin $\vec{i}_b$ of ^{87}Sr couples to the electronic spin $\vec{s}$ of the valence electron of Rb, inducing an effective hyperfine structure in the Sr atom. This effect is isotropic and is stronger for smaller internuclear distances R, for which the electronic density of Rb is larger at the position of the Sr nucleus. Therefore, it can be modelled as an R-dependent ^{87}Sr hyperfine constant, in full analogy with Equation 5.9. The Sr hyperfine constant, induced by the valence electron of Rb, is

$$\zeta_b(R) = \Delta\zeta_b(R)\,. \tag{5.67}$$

The Hamiltonian describing the collision of the Rb atom a and the ^{87}Sr atom b in their electronic ground state may therefore be written as the sum of a zeroth-order term $\hat{H}^0$, which contains the Rb and Sr single-atom Hamiltonians given in Equations 5.42 and 5.43, and of the perturbation $\hat{H}'$ defined by the hyperfine interaction between the Sr nuclear spin and the Rb electronic spin. It reads

$$\hat{H}^0 = \frac{1}{2\mu}\left[-\hbar^2\frac{\mathrm{d}^2}{\mathrm{d}R^2} + \frac{\hat{N}^2}{R^2}\right] + \hat{V}_g(R) + \hat{H}_a + \hat{H}_b \tag{5.68}$$

$$\hat{H}' = \Delta\zeta_b(R)\hat{i}_b \cdot \hat{s}\,. \tag{5.69}$$

The scattering states and molecular eigenstates supported by $\hat{H}^0$ (in absence of external confinement) may be written $|E;k,N\rangle = |\chi^{\mathrm{scat}}_{k,N}(R)\rangle\,|N,m_N\rangle\,|f,m_f\rangle\,|i_b,m_{i_b}\rangle$ and $|\psi_{\mathrm{mol}}\rangle = |\chi^{\mathrm{vib}}_{v,N}(R)\rangle\,|N',m_{N'}\rangle\,|f',m_{f'}\rangle\,|i'_b,m'_{i_b}\rangle$ respectively, where the $|f,m_f\rangle$ hyperfine contribution of Rb and the $|i_b,m_{i_b}\rangle$ nuclear spin contribution of ^{87}Sr factor out as a product of states. These eigenstates are by definition orthogonal to one another, i.e. $\langle E;k,N|\psi_{\mathrm{mol}}\rangle = 0$. The perturbation induced by the valence electron of the Rb atom, Equation 5.69, breaks this orthogonality, thereby producing Feshbach resonances by inducing coupling between specific sets of free atoms states and molecular states. The R-dependent hyperfine constant mixes the radial nuclear wavefunctions of these eigenstates, while the $\hat{i}_b \cdot \hat{s}$ operator mixes their hyperfine and nuclear contributions. The matrix elements associated with this mixing are

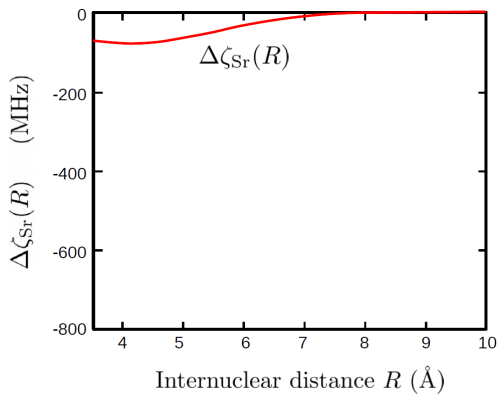

FIGURE 5.11: Variation of the hyperfine constant quantifying the interaction between the ^{87}Rb electronic spin and the ^{87}Sr nuclear spin, as a function of the internuclear distance between Rb and Sr. This variation defines the strength of the radial coupling between atom pair states and molecular states in the context of mechanism II, which produces RbSr Feshbach resonances. This coupling is weaker than its mechanism I counterpart. Calculated by Piotr Żuchowski.

$$\begin{aligned}\langle E;k,N|\,\hat{H}'\,|\psi_{\mathrm{mol}}\rangle &= \langle\chi^{\mathrm{scat}}_{k,N}(R)|\,\Delta\zeta_b(R)\,|\chi^{\mathrm{vib}}_{\nu,N'}(R)\rangle\,\langle N,m_N|N',m_{N'}\rangle \\ &\qquad\times\langle i_b,m_{i_b}|\,\langle f,m_f|\,\hat{i}_b\cdot\hat{s}\,|f',m_{f'}\rangle\,|i'_b,m'_{i_b}\rangle \\ &= I_{\mathrm{radial}}\;I_{\mathrm{spin}}(B)\;\delta_{N,N'}\;\delta_{m_N,m_{N'}}\,,\end{aligned} \tag{5.70}$$

and the Feshbach resonance Breit-Wigner width associated with the mixing of one atom pair state with a molecular state is

$$\Gamma_{12}(E) = 2\pi|\,\langle E;k,N|\,\hat{H}'\,|\psi_{\mathrm{mol}}\rangle\,|^2\,. \tag{5.71}$$

As with mechanism I, the perturbation $\hat{H}'$ does *not* couple different partial waves $|N,m_N\rangle$ and $|N',m_{N'}\rangle$, for it is isotropic and therefore doesn't act on the angular degrees of freedom (θ,ϕ). The radial overlap integral I_{radial} depends on the magnitude of the Sr hyperfine constant $\zeta_b(R)$ as a function of R, Equation 5.67, and on the shape of the radial atomic and molecular nuclear wavefunctions. It reads

$$\begin{aligned} I_{\text{radial}} &= \langle \chi^{\text{scat}}_{k,N}(R) |\, \Delta\zeta_b(R)\, | \chi^{\text{vib}}_{\nu,N'}(R) \rangle \\ &= \int_0^\infty \chi^{\text{scat}}_{k,N}(R) \Delta\zeta_b(R) \chi^{\text{vib}}_{\nu,N'}(R) dR\,. \end{aligned} \tag{5.72}$$

The spin integral $I_{\text{spin}}(B)$ is a purely atomic quantity. It depends on the value of the external magnetic field B, for the $|f, m_f\rangle$ states themselves are B-dependent, as explained in Subsection 5.3.1. More precisely, this integral doesn't depend on the value of the Rb nuclear spin projection $m_{i,a}$ onto the magnetic field axis, since only the Rb electronic spin s is involved in the coupling. Thus, since the contribution of a given uncoupled state $|s, m_s, i, m_i\rangle$ to a given $|f, m_f\rangle$ state is a function of B — see Figure 5.8 —, so is $I_{\text{spin}}(B)$. Writing the hyperfine coupling operator as $\hat{i}_b \cdot \hat{s} = \hat{i}_{b,z}\hat{s}_z + \frac{\hat{i}_{b,+}\hat{s}_- + \hat{i}_{b,-}\hat{s}_+}{2}$, where $\hat{i}_{b,+}$, $\hat{i}_{b,-}$, $\hat{s}_+$ and $\hat{s}_-$ are the Sr nuclear spin projection raising and lowering operators, and the corresponding Rb electronic spin operators respectively, one sees that it can produce either $\Delta m_{i,b} = \Delta m_s = 0$ or $\Delta m_{i,b} = +1/-1$ and $\Delta m_s = -1/+1$. Therefore, the total Rb spin projection $m_f = m_s + m_{i,a}$ may change as $\Delta m_f = 0$ or $\Delta m_f = -1/+1$, leaving the total projection $m_s + m_{i,a} + m_{i,b}$ unchanged. The selection rules associated with the spin integral are thus

$$I_{\text{spin}}(B) = \langle i_b, m_{i_b} |\, \langle f, m_f |\, \hat{i}_b \cdot \hat{s}\, | f', m_{f'} \rangle\, | i'_b, m'_{i_b} \rangle \neq 0 \iff \Delta m_f = 0, -1 \text{ or } +1\,. \tag{5.73}$$

These conditions are much less stringent than the $\Delta m_f = 0$ condition required to observe Feshbach resonances induced by mechanism I. Accordingly, we observed many more resonances in the fermionic ^{87}Rb-^{87}Sr mixture than in the bosonic ones[63], which made Feshbach spectroscopy of the ^{87}Rb-^{87}Sr mixture an invaluable probe of the RbSr ground state potential. Note that at $\Delta m_f = \Delta N = 0$ crossings both mechanism I and II produce Feshbach resonances.

Importantly, $I_{\text{spin}}(B) \neq 0$ even at $B = 0$ G in the case of mechanism II. Indeed, the hyperfine coupling operator $\hat{i}_b \cdot \hat{s}$ is off-diagonal in the $|i_b, m_{i,b}\rangle\, |f, m_f\rangle$ basis even in absence of magnetic field, whereas in the case of mechanism I the hyperfine coupling operator $\hat{i}_a \cdot \hat{s}$ is diagonal in the $|f, m_f\rangle$ basis at $B = 0$ G. This stems from the different physical mechanism at play in these two coupling schemes. Indeed, while mechanism II requires the coupling of the Rb electronic spin s to the Sr nuclear spin i_b, which is present even in absence of magnetic

[63] We measured one resonance in the ^{87}Rb-^{84}Sr mixture, and two in the ^{87}Rb-^{88}Sr mixture. According to our model of the RbSr ground state PEC, these are the only resonances available in the range $0 - 1500$ G (at least for s-wave atom pair states; more resonances might be observed in entrance channels of higher N, as discussed in Subsection 2.2.2). We observed seven resonances induced by mechanism II (one of them, the largest, overlapping with a mechanism I resonance) in the narrower $0 - 550$ G range in the ^{87}Rb-^{87}Sr mixture, and more are predicted to arise at higher fields.

field — in complete analogy with the hyperfine structure of Rb —, mechanism I requires the disruption of the Rb hyperfine structure by the Zeeman energy, which is achieved only in presence of a magnetic field. An interesting consequence of the $\hat{i}_b \cdot \hat{s}$ coupling at play in mechanism II is that the degeneracy of the $|f, m_f\rangle$-states of a given f manifold of Rb is lifted in presence of Sr, even at $B = 0$ G. We tried to observe this effect by measuring the binding energy of the $|v = 66, N = 0, f = 1\rangle$ ^{87}Rb^{87}Sr molecular state[64], using the two-colour spectroscopy method presented in 2.2, in the cases $m_f = m_{f'} = 0$ and $m_f = m_{f'} = -1$ close to $B = 0$ G. The lifting of degeneracy, which we expected from theoretical considerations to be of the order of $h \times 30$ kHz, proved too small to be reliably measured with this method. Such a shift should be very easily measurable using molecular states that are much more bound and for which the shift is expected to be in the MHz or tens of MHz range.

[64] This state is bound by $h \times 287.27(18)$ MHz — see Chapter 3.

5.5 RbSr resonances induced by anisotropic terms: mechanism III

While investigating magnetic Feshbach resonances in the fermionic ^{87}Rb-^{87}Sr mixture, we were surprised to discover extremely weak loss features, strikingly narrower than we expected from thermal broadening at the temperature of the RbSr sample (a few μK). These features didn't seem to be artifacts, since they were obtained at magnetic fields matching exactly the binding energy of a molecular state that we detected previously through two-colour spectroscopy. Based on our understanding of the ground-state PEC of RbSr at the time, we attributed this resonance to a rotating $N = 2$ state, for which neither mechanism I nor mechanism II predicts any coupling to atom pair scattering states in the s-wave ($N = 0$) regime.

The theoretical explanation of these features was given to us by Piotr Żuchowski in a private communication. The dipolar hyperfine interaction between the Rb electronic spin $\vec{s}$ and the nuclear spin $\vec{i_b}$ of ^{87}Sr leads to an anisotropic coupling between s-wave scattering states and $N = 2$ molecular states[65]. This dipolar coupling is of the same form as the dipolar electronic spin-spin interaction, Equation 5.36, where the rank-2 tensors $T^2(\vec{s_1}, \vec{s_2})$ are replaced by their hyperfine counterpart $T^2(\vec{s}, \vec{i_b})$. It reads

$$\hat{H}' = t_{\mathrm{Sr}}(R)\ \sqrt{6}\ T^2(C)\ \cdot T^2(\vec{s}, \vec{i_b})\ , \tag{5.74}$$

where the radial prefactor $t_{Sr}(R)$ is the product of two terms. The first is the classical dipole-dipole $1/R^3$ term, given in Equation 5.36. The second term is an extra R-dependent term, that largely dominates the radial integral I_{radial} and quantifies the anisotropic distortion of the Rb electronic cloud as Sr is approaching — much analogously to its isotropic counterpart $\Delta\zeta_b(R)$[66]. The spin tensor $T^2(\vec{s}, \vec{i_b})$ is defined as in Equation 5.37, i.e

$$\begin{aligned}
\hat{T}_2^0 &= 2\, s_z i_{b,z} - (s_- i_{b,+} + s_+ i_{b,-})/2 \\
\hat{T}_2^{\pm 1} &= \mp\sqrt{\frac{3}{2}}\,(s_\pm i_{b,z} + s_z i_{b,\pm}) \\
\hat{T}_2^{\pm 2} &= \sqrt{\frac{3}{2}}\, s_\pm i_{b,\pm}\ .
\end{aligned} \tag{5.75}$$

[65] The total hyperfine interaction is in general the sum of the contact interaction and the dipolar hyperfine interactions [146]. At long internuclear distances the contact interaction largely dominates the hyperfine shift.

[66] Note that this phenomenon likely has its counterpart in bi-alkali mixtures, although it is not discussed in the literature known to the author.

The rank-2 tensorial nature of this interaction imposes the selection rule $|N-2| \leq N' \leq |N+2|$, owing to Equation 5.40. Thus, in the s-wave regime it leads to Feshbach resonances only at the crossing with $N = 2$ molecular states. Furthermore, the spin+rotation operator $T^2(C) \cdot T^2(\vec{s}, \vec{i_b})$ imposes the projection of the total angular momentum along the quantization axis, $m_f + m_{i_b} + m_N$, to be conserved. The selection rules associated with this dipolar hyperfine interaction are thus

$$\begin{aligned} I_{\text{spin+rotation}}(B) = \langle N, n_N | \langle i_b, m_{i_b} | \langle f, m_f | \, T^2(C) \cdot T^2(\vec{s}, \vec{i_b}) \, | f', m_{f'} \rangle \, | i'_b, m'_{i_b} \rangle \, | N', n_{N'} \rangle \neq 0 \\ \iff \Delta(m_f + m_{i_b} + m_N = 0) \quad \text{and} \quad N' = 2 \, (\text{for } N = 0) \, . \end{aligned} \tag{5.76}$$

Interestingly, many resonances may arise from open-channel states defined by the same hyperfine contribution $|f, m_f\rangle$ but different Sr nuclear spin contribution $|i_b, m_{i_b}\rangle$. Accordingly, P. Żuchowski predicted that in our unpolarized sample of ^{87}Sr containing all 10 $m_{i_b} = -9/2, -7/2, ..., +9/2$ spin projections, we should observe several resonances, spaced in magnetic field according to the projection m_{i_b} of the scattering incoming state. We investigated the loss features further and could indeed measure "bunches" of resonances as shown in Chapter 6 (green loss features), spaced by a few ten $h\times$ kHz as expected from the small ^{87}Sr nuclear spin gyromagnetic $\gamma_{i,^{87}\text{Sr}}/2\pi = h \times -0.183999$ kHz/G — see Equations 5.46 — around the resonant fields $B = 278.2$ G and $B = 295.1$ G. This coupling mechanism, together with the dipolar interaction between the Rb electronic spin and the Sr nuclear spin (much smaller than the one previously discussed), was called mechanism III. Note that mechanism II, presented in Section 5.4, also leads to multiple loss features. However, we couldn't resolve them in that case, due to the large thermally-broadened loss profiles. The features induced by this anisotropic mechanism, though, were surprisingly narrow and we could resolve them[67]. The narrowness of the loss features, expected by us to be as broad as the other RbSr Feshbach resonances due to thermal broadening, remains a mystery.

The discovery of these resonances triggered theoretical work, published in Ref. [132]. In this work many additional small coupling terms are included and analyzed in the context of CsYb[68]. Among them, the abovementioned dipolar coupling between the Rb electronic and nuclear spin (dipolar counterpart to the Rb contact hyperfine interaction), the interaction between the nuclear electric quadrupole tensors and the distance-dependent electric

[67] The $B = 420.9$ G resonance is induced by mechanism III but is not narrow. One reason could be that the coupling strength for this resonance is much larger than the $B = 278.2$ G and $B = 295.1$ G resonances — these two resonances involve a different radial overlap integral than the one at $B = 420.9$ G because they involve the vibrational $\nu = -2$ and the $\nu = -4$ vibrational states respectively.

[68] The CsYb molecule, composed of an alkali (Cs) and a closed-shell atom (Yb), is a heavy open-shell, dipolar molecule similar to RbSr.

gradient tensor at the nuclei due to the electrons, and the spin to molecular rotation coupling discussed in Chapter 4, Subsection 4.1. This was a time of great scientific effervescence and expansion of knowledge, with theoretical predictions leading to new measurements and new measurements leading to new predictions.

If anything should be retained from this chapter, it is that the RbSr experiment would not stand where it stands now without the constant work and support of Piotr Żuchowski, Jeremy Hutson, Matthew Frye and their collaborators. Many thanks to them, we hope to keep working together in the future.

Chapter 6

Publication: Observation of Feshbach resonances between alkali and closed-shell atoms

Nat. Phys. **14**, 881 (2018)

Vincent Barbé[1,4], Alessio Ciamei[1,4], Benjamin Pasquiou[1], Lukas Reichsöllner[1], Florian Schreck[1,*], Piotr. S. Żuchowski[2] and Jeremy M. Hutson[3]

Magnetic Feshbach resonances allow control of the interactions between ultracold atoms [131]. They are an invaluable tool in studies of few-body and many-body physics [149, 150], and can be used to convert pairs of atoms into molecules [151, 152] by ramping an applied magnetic field across a resonance. Molecules formed from pairs of alkali atoms have been transferred to low-lying states, producing dipolar quantum gases [153]. There is great interest in making molecules formed from an alkali atom and a closed-shell atom such as ground-state Sr or Yb. Such molecules have both a strong electric dipole and an electron spin; they will open up new possibilities for designing quantum many-body systems [32, 71] and for tests of fundamental symmetries [154]. The crucial first step is to observe Feshbach resonances in the corresponding atomic mixtures. Very narrow resonances have been predicted theoretically [25, 26, 111], but until now have eluded observation. Here we present the observation of magnetic Feshbach resonances of this type, for an alkali atom, Rb, interacting with ground-state Sr.

[1] Van der Waals-Zeeman Institute, Institute of Physics, University of Amsterdam, Amsterdam, The Netherlands
[4] These authors contributed equally: Vincent Barbé, Alessio Ciamei.
[*]e-mail: RbSrFR@strontiumBEC.com
[2]Institute of Physics, Faculty of Physics, Astronomy and Informatics, Nicolaus Copernicus University, Torun, Poland
[3]Joint Quantum Centre (JQC) Durham-Newcastle, Department of Chemistry, Durham University, Durham, UK

A magnetic Feshbach resonance arises when a pair of ultracold atoms couples to a near-threshold molecular state that is tuned to be close in energy by an applied magnetic field. Magnetoassociation at such a resonance coherently transfers the atoms into the molecular state [155, 156]. In a few cases, near-threshold molecules formed in this way have been transferred to their absolute ground states [9, 11, 157], allowing exploration of quantum gases with strong dipolar interactions [153]. However, this has so far been achieved only for molecules formed from pairs of alkali atoms.

Mixtures of closed-shell alkaline-earth atoms with open-shell alkali atoms have been studied in several laboratories [87, 158–161]. No strong coupling mechanism between atomic and molecular states exists in systems of this type, but theoretical work has identified weak coupling mechanisms that should lead to narrow Feshbach resonances, suitable for magnetoassociation [25, 26, 111]. In this letter we describe the detection of Feshbach resonances in mixtures of ^{87}Sr or ^{88}Sr with ^{87}Rb. The coupling between atomic and molecular states arises from two mechanisms previously predicted [25, 26, 111] and an additional, weaker mechanism that we identify here.

The experimental signature of a Feshbach resonance is field-dependent loss of Rb atoms. This may arise from either 3-body recombination or inelastic collisions, both of which are enhanced near a resonance. We perform loss spectroscopy using an ultracold Rb-Sr mixture, typically consisting of 5×10^4 Rb atoms mixed with 10^6 ^{87}Sr or 10^7 ^{88}Sr atoms at a temperature of 2 to 5 μK (see Methods). Figure 6.1 shows the observed loss features, eleven arising in the ^{87}Rb-^{87}Sr Bose-Fermi mixture and one in the ^{87}Rb-^{88}Sr Bose-Bose mixture. Ten loss features consist of a single, slightly asymmetrical dip with FWHM between 200 and 400 mG. The loss features labelled [1,0]a and [1,1]a each consist of several dips with a width of 20 to 60 mG at a spacing of 80 mG. We fit each dip with a Gaussian and give the resulting positions and widths in Table 6.1. None of these Rb loss features arises in the absence of Sr, proving that they depend on Rb-Sr interactions.

Both the atomic and molecular states are described by the total angular momentum of the Rb atom, f, and its projection m_f onto the magnetic field. Where necessary, atomic and molecular quantum numbers are distinguished with subscripts at and mol. In addition, the molecule has a vibrational quantum number n, counted down from $n = -1$ for the uppermost level, and a rotational quantum number L, with projection M_L. ^{88}Sr has nuclear spin $i_{\mathrm{Sr}} = 0$, whereas ^{87}Sr has $i_{\mathrm{Sr}} = 9/2$ and a corresponding projection $m_{i,\mathrm{Sr}}$.

The Rb-Sr atom-pair states and the near-threshold molecular states lie almost parallel to the Rb atomic states as a function of magnetic field — see Supplementary Information. We can therefore use the Breit-Rabi formula of Rb for both the atom-pair states and the molecular states. This allows us to extract zero-field binding energies E_{b} of the molecular states responsible for the resonances, giving the values in Table 6.2. The crossing atomic and

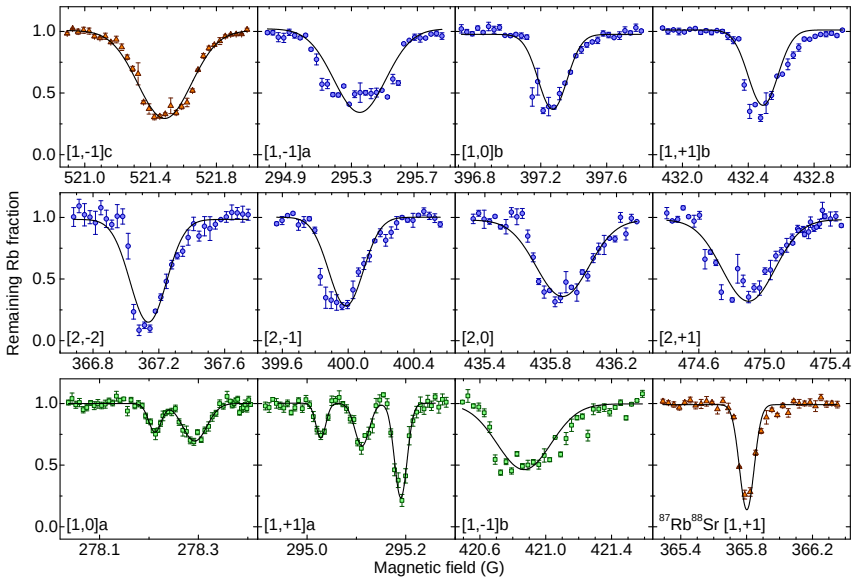

FIGURE 6.1: **Detection of Rb-Sr Feshbach resonances by field-dependent loss of Rb.** The fraction of Rb atoms remaining in state (f, m_f) after loss at each observed Feshbach resonance, normalised to unity far from the loss feature. Eleven loss features are observed in ^{87}Rb-^{87}Sr mixtures and one in ^{87}Rb-^{88}Sr (lower right panel). The loss features are labelled by $[f,m_f]j$, where $j \in$ {a,b,c} is an index used when losses due to several molecular states are observed at the same atomic threshold. Most loss features show a single dip in the atom number, whereas [1,0]a and [1,1]a show several. Each dip is fit by a Gaussian (black line), with results shown in Table 6.1. The color and shape of symbols indicates the coupling mechanism for the Feshbach resonance: mechanism I (orange triangles), II (blue circles), or III (green squares). The resonance near 521 G also has a contribution from mechanism II. The magnetic field uncertainty is 0.4 G and the noise is less than 40 mG. Error bars represent the standard error of three or more data points.

molecular levels are shown in Figures 6.2 and 6.3, with filled symbols where we observe loss features.

To verify the bound-state energies and validate our model of Feshbach resonances, we use two-photon photoassociation (PA) spectroscopy. We detect the two $n = -2$ states (with $L = 0$ and 2) below the lower ($f = 1$) threshold of ^{87}Rb-^{87}Sr (states E and F in Table 6.2) at almost exactly the energies deduced from the resonance positions. All the states observed through Feshbach resonances (B to F) also arise to within 2 MHz in a more complete model of the Rb-Sr interaction potential, as described below.

Three different coupling mechanisms are responsible for the observed loss features. The first mechanism was proposed in Ref. [25] and relies on the change of the Rb hyperfine

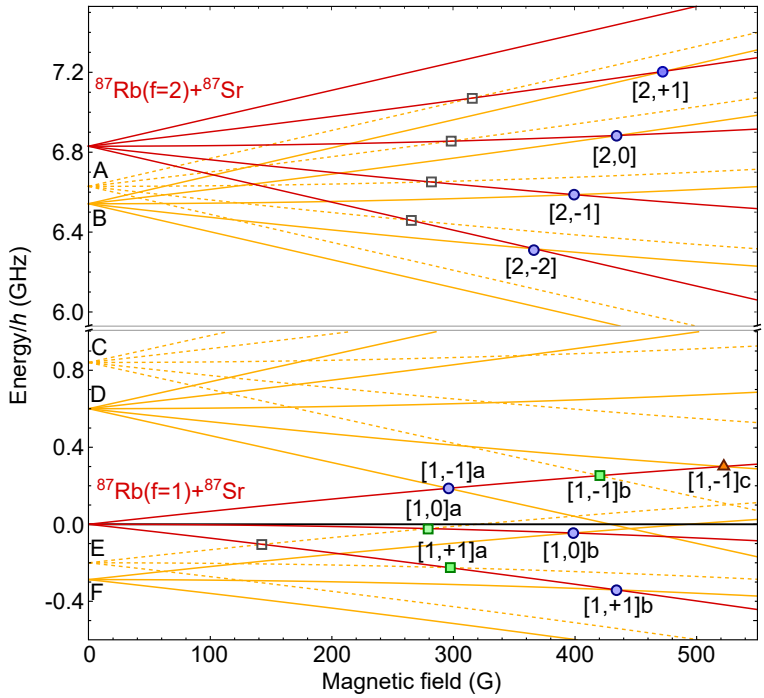

FIGURE 6.2: **Origin of the ^{87}Rb-^{87}Sr Feshbach resonances.** Energies of atomic (red) and molecular (orange) states as functions of magnetic field, shown with respect to the zero-field $f = 1$ atomic level. Molecular states are labelled as in Table 6.2 and shown dashed if rotationally excited ($L = 2$). Observed Feshbach resonances are labelled as in Figure 6.1 and marked by filled symbols (orange triangles, blue circles or green squares for coupling mechanism I, II or III, respectively). Hollow symbols mark further, weak resonances predicted by our model, which could not be observed under our measurement conditions — see Supplementary Information.

splitting when the Rb electron distribution is perturbed by an approaching Sr atom. Its coupling strength is proportional to the magnetic field in the field region explored here [26]. The coupling conserves m_f and L and there are no crossings between atomic and molecular states with the same f and m_f. This mechanism therefore produces Feshbach resonances only at crossings between atomic states with Rb in $f = 1$ and molecular states with $f = 2$. We observe one such resonance for each of ^{87}Sr and ^{88}Sr.

The second mechanism involves hyperfine coupling of the Sr nucleus to the valence electron of Rb and was first proposed in Ref. [111]. Since only fermionic ^{87}Sr has a nuclear magnetic moment, this can occur only in Rb-^{87}Sr collisions. This coupling conserves L and $m_f + m_{i,\mathrm{Sr}}$, with the selection rule $m_{f,\mathrm{at}} - m_{f,\mathrm{mol}} = 0, \pm 1$. Crossings that fulfil these conditions occur also for molecular states with the same f value as the atomic state, which makes

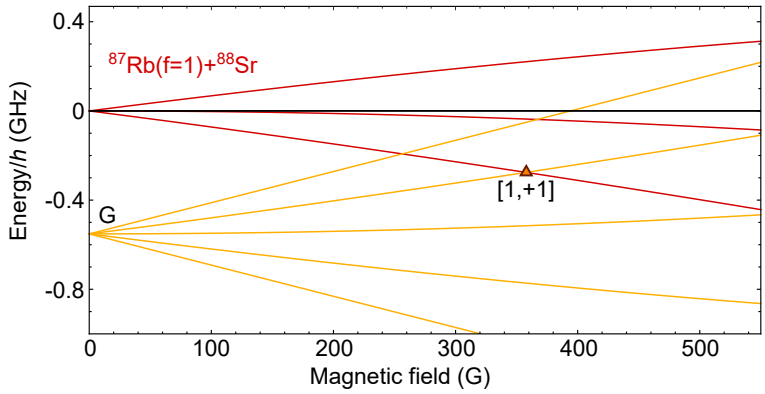

FIGURE 6.3: **Origin of the ^{87}Rb-^{88}Sr Feshbach resonance.** Energies of atomic (red) and molecular (orange) states as functions of magnetic field, shown with respect to the zero-field $f = 1$ atomic level. Only one Feshbach resonance has been observed, produced by coupling mechanism I. Since ^{88}Sr has zero nuclear spin, mechanism II is absent.

them much more abundant than crossings obeying the selection rules of the first mechanism. Feshbach resonances belonging to different $m_{i,\mathrm{Sr}}$ are slightly shifted with respect to one another because of the weak Zeeman effect on the Sr nucleus and the weak Sr hyperfine splitting. However, since the shift is only 10 mG for neighboring $m_{i,\mathrm{Sr}}$, much smaller than the width of the loss features of typically 300 mG, we do not resolve this splitting.

The third mechanism is the anisotropic interaction of the electron spin with the nucleus of either Rb or fermionic Sr. This mechanism can couple the s-wave atomic state to molecules with rotational quantum number $L = 2$. As usual, the total angular momentum projection (now $m_f + m_{i,\mathrm{Sr}} + M_L$) is conserved. If the Sr nucleus is involved, an additional selection rule is $\Delta m_f = \pm 1$. By contrast, if the Rb nucleus is involved, the selection rule is $\Delta m_f = -\Delta M_L$. These loss features are made up of many (m_f, M_L) components, split by several hyperfine terms [24]; in some cases the components separate into groups for different values of M_L. Three loss features are attributed to this mechanism and two of them ([1,1]a and [1,0]a) indeed show a structure of two or three dips.

To create a model of the Rb-Sr Feshbach resonance locations we start with a RbSr ground-state potential that we have previously determined by electronic structure calculations [95]. This will be described in detail in a future publication [110][4]. We carry out a three-parameter fit to adapt the model potential to match the molecular binding energies determined by two-photon photoassociation in three Rb-Sr mixtures (^{87}Rb-^{84,87,88}Sr), supplemented by binding energies determined from the Feshbach resonance positions. The parameters adjusted are two long-range coefficients, C_6 and C_8, and a short-range well depth. The molecular bound

[4] A/N: this work has been published in 2018, following the publication of the present article.

TABLE 6.1: **Properties of observed Feshbach resonances.** For resonances with many components, the theoretical width is the largest calculated value.

$[f, m_f]j$	(mol. state, m_f, M_L)	B (G)	δ (mG)	Δ (mG)	cpl. mech.
		^{87}Rb^{87}Sr			
[2,+1]	(B, +2, 0)	474.9(4)	373(7)	0.095	II
[2,0]	(B, +1, 0)	435.9(4)	378(7)	0.14	II
[2,−1]	(B, 0, 0)	400.0(4)	247(4)	0.14	II
[2,−2]	(B, −1, 0)	367.1(4)	260(5)	0.095	II
[1,−1]a	(D, −2, 0)	295.4(4)	372(10)	0.73	II
[1,−1]b	(C, −2, mix)	420.9(4)	386(11)	0.025	III
[1,−1]c	(D, −1, 0)	521.5(4)	366(3)	3.5	I,II
[1,0]a	(E, −1, −1)	$B_1 = 278.2(4)$	30(3)	0.0012	III
	(E, −1, −2)	$B_1 + 0.081(2)$	58(4)	0.0015	III
[1,0]b	(F, −1, 0)	397.3(4)	207(4)	0.048	II
[1,+1]a	(E, 0, 0)	$B_2 = 295.0(4)$	24(3)	0.0002	III
	(E, 0, −1)	$B_2 + 0.083(2)$	35(3)	0.0014	III
	(E, 0, −2)	$B_2 + 0.162(2)$	30(1)	0.0016	III
[1,+1]b	(F, 0, 0)	432.5(4)	213(6)	0.048	II
		^{87}Rb^{88}Sr			
[1,+1]	(G, +1, 0)	365.8(4)	105(2)	0.05	I

TABLE 6.2: **Molecular states responsible for Feshbach resonances.** Binding energies obtained from observed Feshbach resonances, E_b^{FR}, and from two-photon photoassociation, E_b^{PA}. The experimental uncertainties in E_b^{FR} arise principally from the magnetic field measurement.

label	n	F	L	E_b^{FR}/h (MHz)	E_b^{PA}/h (MHz)
			^{87}Rb -^{87}Sr		
A	−2	2	2	-	-
B	−2	2	0	288.2(4)	-
C	−4	2	2	5992(1)	-
D	−4	2	0	6234(1)	-
E	−2	1	2	200.0(3)	200.0(3)
F	−2	1	0	287.3(3)	287.3(2)
			^{87}Rb -^{88}Sr		
G	−4	2	0	7401.0(7)	-

states obtained from the model are within 2 MHz of the measured values, and the resonance positions are within 2 G. Scattering calculations on this potential give interspecies scattering lengths $a_{87,87} = 1600(+600, -450)\, a_0$ and $a_{87,88} = 170(20)\, a_0$ for ^{87}Rb-^{87}Sr and ^{87}Rb-^{88}Sr, where a_0 is the Bohr radius. Our model also predicts the background scattering lengths and Feshbach resonance positions for all other isotopic Rb-Sr mixtures. For example, we predicted the position of the ^{87}Rb-^{88}Sr resonance after initially fitting the model only on photoassociation results for three isotopic mixtures and ^{87}Rb-^{87}Sr Feshbach resonances. This resonance was subsequently observed within 10 G of the prediction.

An understanding of resonance widths is crucial to molecule formation. However, the widths δ of the experimental loss features are dominated by thermal broadening, with relatively little contribution from the true resonance widths Δ. We obtain theoretical widths Δ from the Golden Rule approximation [26] and include them in Table 6.1. Δ depends on the amplitude of the atomic scattering function at short range; it is largest when the background scattering length a is large, and is proportional to a in this regime [26]. This effect enhances all the resonance widths for ^{87}Rb-^{87}Sr.

In summary, we have observed Feshbach resonances in mixtures of Rb alkali and Sr alkaline-earth atoms. Similar resonances will be ubiquitous in mixtures of alkali atoms with closed-shell atoms, particularly when the closed-shell atom has a nuclear spin. Magnetoassociation using resonances of this type should be feasible — see Supplementary Information — and offers a path towards a new class of ultracold molecules, with electron spin and strong electric dipole moment. These molecules are expected to have important applications in quantum computation, many-body physics and tests of fundamental symmetries.

acknowledgments

This project has received funding from the European Research Council (ERC) under the European Union's Seventh Framework Programme (FP7/2007-2013) (Grant agreement No. 615117 QuantStro). B.P. thanks the NWO for funding through Veni grant No. 680-47-438. P.S.Ż. thanks the National Science Center for support from grant 2017/25/B/ST4/01486. J.M.H. thanks the UK Engineering and Physical Sciences Research Council for support under Grant No. EP/P01058X/1.

Author contributions

V.B., A.C. and L.R. performed the experiments. B.P. and F.S. supervised the experimental work. P.S.Ż. and J.M.H. contributed theoretical analysis. All authors were involved in analysis and discussions of the results and contributed to the preparation of the manuscript.

Supplementary Information

A magnetic Feshbach resonance arises when a pair of ultracold atoms couples to a near-threshold molecular state. All magnetic Feshbach resonances observed before our work occur for atomic pairs that interact to form multiple electronic states. This occurs if both atoms have electron spin or at least one of them is orbitally degenerate. Examples are alkali pairs [131] and mixtures of electronically excited (open-shell) Yb with either Li [162, 163] or ground-state Yb [164, 165]. Strong Feshbach resonances occur in these systems because the atom-pair state and the molecular state are different superpositions of the electronic states. By contrast the Rb-Sr system has only one relevant electronic state. There is also no magnetic dipole interaction, which can cause additional weak resonances between atoms such as alkalis, Cr [147], Er [166], and Dy [167]. The usual mechanisms that give rise to magnetic Feshbach resonances are therefore absent in Rb-Sr. Our work shows that all the same magnetic Feshbach resonances do occur. In the following we first discuss the unusual coupling mechanisms that give rise to these resonances. We then give details of our ground-state potential model, which fits the locations of the observed Feshbach resonances and predicts further resonances in all isotopic Rb-Sr mixtures. Finally we discuss the suitability of Feshbach resonances in Rb-Sr for magnetoassociation of atom pairs into molecules.

Coupling mechanisms and resonance widths

The Hamiltonian for the interaction of Rb and Sr atoms may be written

$$\hat{H} = -\frac{\hbar^2}{2\mu R^2}\left[\frac{d^2}{dR^2} - \frac{\hat{L}^2}{R^2}\right] + \hat{H}_{\mathrm{asym}} + \hat{U}(R), \tag{6.1}$$

where R is the internuclear distance, μ is the reduced mass, and $\hat{L}^2$ is the operator for end-over-end rotation of the two atoms about one another. $\hat{H}_{\mathrm{asym}}$ is the asymptotic hyperfine Hamiltonian[5],

$$\hat{H}_{\mathrm{asym}} = \zeta_{Rb}\hat{\mathbf{i}}_{\mathrm{Rb}}\cdot\hat{\mathbf{s}} + (g_{\mathrm{Rb}}\mu_{\mathrm{N}}\hat{i}_{z,\mathrm{Rb}} + g_{\mathrm{Sr}}\mu_{\mathrm{N}}\hat{i}_{z,\mathrm{Sr}} + g_{\mathrm{e}}\mu_{\mathrm{B}}\hat{s}_z)B. \tag{6.2}$$

The operator $\hat{U}(R)$ includes all R-dependent interactions,

$$\begin{aligned}\hat{U}(R) = \Delta\zeta_{\mathrm{Rb}}(R)\hat{\mathbf{i}}_{\mathrm{Rb}}\cdot\hat{\mathbf{s}} + \Delta\zeta_{\mathrm{Sr}}(R)\hat{\mathbf{i}}_{\mathrm{Sr}}\cdot\hat{\mathbf{s}}\, t_{\mathrm{Rb}}(R)\,\sqrt{6}\,T^2(\mathbf{s},\mathbf{i}_{\mathrm{Rb}})\cdot T^2(C) \\ + t_{\mathrm{Sr}}(R)\,\sqrt{6}\,T^2(\mathbf{s},\mathbf{i}_{\mathrm{Sr}})\cdot T^2(C) + V(R),\end{aligned} \tag{6.3}$$

[5] AN: vector operators are written in bold letter in this section.

where T^2 indicates a spherical tensor of rank 2. $T^2(C)$ has components $C^2_q(\theta,\phi)$, where C is a renormalised spherical harmonic and θ,ϕ are the polar coordinates of the internuclear vector. In Eq. (6.3) the first and second terms represent interaction-induced change of the scalar hyperfine coupling of the nuclear spins of Rb and Sr with the electron spin, the third and fourth terms represent the dipolar interaction between the electron spin and the nuclear spins of ^{87}Rb and ^{87}Sr, and the last term is the Born-Oppenheimer electronic interaction potential. The first two terms correspond to coupling mechanisms I and II discussed in the paper. The third and fourth terms correspond to mechanism III, though for RbSr the dipolar coupling involving the ^{87}Rb nucleus is very weak and the resonances due to this mechanism alone have not been observed. Note that $i_{\mathrm{Sr}} = 0$ for bosonic Sr isotopes (^{84,86,88}Sr), so that mechanism II is absent in Rb-Sr mixtures containing these isotopes. The couplings responsible for all three mechanisms were obtained from density-functional calculations of the molecular electronic structure using the same methods as in Ref. [168].

The scattering length $a(B)$ around a narrow Feshbach resonance is described by

$$a(B) = a_{\mathrm{bg}}\left(1 - \frac{\Delta}{B - B_{\mathrm{res}}}\right), \tag{6.4}$$

where a_{bg} is the background scattering length, B_{res} is the resonance position and Δ is its width (in magnetic field). The width Δ is related to the width $\Gamma(k)$ (in the energy domain) of the state above threshold,

$$\Delta = \lim_{k\to 0} \frac{\Gamma(k)}{2ka_{\mathrm{bg}}\delta\mu_{\mathrm{res}}}, \tag{6.5}$$

where $k = \sqrt{2\mu E_{\mathrm{coll}}/\hbar^2}$ is the wavevector and $\delta\mu_{\mathrm{res}}$ is the difference between the magnetic moments of the atomic pair and the bound state. In the present work we obtain the width $\Gamma(k)$, from Fermi's Golden Rule,

$$\Gamma(k) = 2\pi|\langle\alpha' n|\omega_i(R)\hat{\Omega}_i|\alpha k\rangle|^2, \tag{6.6}$$

where $\omega_i(R)\hat{\Omega}_i$ is the coupling corresponding to one of mechanisms I to III, α and α' label eigenstates of H_{asym} and $|\alpha k\rangle$ and $|\alpha' n\rangle$ are the scattering and bound-state wavefunctions, respectively. Equation 6.6 factorizes into spin-dependent and radial parts [26],

$$\Gamma(k) = 2\pi I_{\alpha,\alpha'}(B)^2 I^2_{k,n}, \tag{6.7}$$

where

$$I_{\alpha,\alpha'}(B) = \langle\alpha'|\hat{\Omega}_i|\alpha\rangle; \tag{6.8}$$

and

$$I_{k,n} = \int_0^\infty \psi_n(R)\omega_i(R)\psi_k(R)dR. \tag{6.9}$$

The values of $I_{\alpha,\alpha'}(B)$ are obtained here as the off-diagonal matrix elements of the operators $\hat{\mathbf{i}}_{\mathrm{Rb}} \cdot \hat{\mathbf{s}}$, $\hat{\mathbf{i}}_{\mathrm{Sr}} \cdot \hat{\mathbf{s}}$ and $T^2(\hat{\mathbf{i}}_{\mathrm{Sr}}, \hat{\mathbf{s}})$, transformed to the basis set of asymptotic eigenfunctions of H_{asym}, while $I_{k,n}$ was evaluated numerically for limitingly small values of k.

Predicted Feshbach resonances

Our model predicts further Feshbach resonances, in addition to the ones we have observed, in all isotopic Rb-Sr mixtures [110]. A few additional ^{87}Rb-^{87}Sr resonances occur in the magnetic field accessible to us ($< 550\,\mathrm{G}$), as indicated by hollow symbols in Figure 6.2. We searched for loss features corresponding to those resonances, but found that they are not observable under our experimental conditions. The $L = 2$ Feshbach resonances in Rb $f = 2$ are quite weak and hard to observe for two reasons. First, they coincide with broad, known Rb Feshbach resonances [135]. Secondly, our Rb $f = 2$ samples have a lower atom number per m_f state and a shorter lifetime than $f = 1$ samples. The Rb $f = 1$ resonance at 130 G is predicted to be two orders of magnitude narrower than the broadest coupling mechanism III resonance observed.

In addition, the large positive scattering length for ^{87}Rb-^{87}Sr will produce a least-bound molecular state with binding energy $h \times 25(15)$ kHz, which leads to Feshbach resonances at low magnetic field. However, bound states very near dissociation exist mostly at long range, and produce resonances with widths proportional to $|E_b|^{2/3}$ [26]. The widths of resonances due to the least-bound states are expected to be at least two orders of magnitude narrower than those due to deeper states. Therefore we do not expect to observe loss features corresponding to these resonances.

Prospect for magnetoassociation

Magnetoassociation uses magnetic Feshbach resonances to form molecules from pairs of atoms [131]. At a Feshbach resonance the atom-pair state $|a\rangle$ and the molecular state $|m\rangle$ couple, producing an avoided crossing. The strength of this crossing depends on the product $a_{\mathrm{bg}}\Delta$. A common way to perform magnetoassociation is to ramp the magnetic field across the resonances such that $|a\rangle$ evolves adiabatically into $|m\rangle$. Even quite weak resonances, comparable in coupling strength to the strongest Rb-Sr resonances, have been used for magnetoassociation, starting from a BEC [169] or atom pairs on the sites of a lattice [170]. Our Rb-Sr Feshbach resonance model identifies several promising paths to form RbSr molecules

from atoms, either in free space or in an optical lattice. We have already created a Mott insulator with 3×10^4 sites occupied by one atom of each, ^{87}Rb and ^{84}Sr [52]. Our model predicts suitable resonances in this and several other isotopic mixtures.

The experimental discovery of Feshbach resonances in Rb-Sr also validates the theory predicting Feshbach resonances in other mixtures of closed-shell atoms with alkalis. Several such mixtures are currently under experimental investigation, such as Li-Yb [158, 159], Rb-Yb [87, 160], and Cs-Yb [171]. It should be possible to identify magnetic Feshbach resonances in these mixtures using two-photon photoassociation and Feshbach spectroscopy. Identifying these resonances would give further opportunities to create molecules with a strong electric dipole and an electron spin.

Chapter 7

Outlook

The production of ultracold RbSr molecules in the rovibronic ground state is the primary goal of the RbSr laboratory. For the first step, which consists in forming weakly-bound molecules out of atom pairs, three experimental routes can be chosen: STIRAP, magnetoassociation and photoassociation followed by spontaneous emission — see Chapter 1, Section 1.4. The route that was chosen before this PhD work was STIRAP, using an electronically-excited molecular state of energy close to the Rb $(^2S_{1/2}) + \text{Sr}\ (^3P_1)$ dissociation asymptote. We temporarily abandoned this line of research after the results of the one-colour spectroscopy, for the reasons exposed in Section 1.4. We are focussing now on magnetoassociation, rendered possible by the detection of a suitable magnetic Feshbach resonance in ^{87}Rb^{84}Sr at $B = 1311$ G. Two experimental requirements have to be met to magnetoassociate RbSr molecules in an optical lattice: a low-entropy double Mott insulator, i.e. an optical lattice filled with many Rb-Sr atom pairs, and a ppm-level magnetic field stability at $B = 1311$ G — see Chapter 5, Section 5.1.2. Our attempts at magnetoassociation have been unsuccessful to this date. To maximise our chances to succeed in the near future, we chose to improve both the optical lattice and magnetic field setups. The related progress that we made and the preliminary results that we obtained are presented succinctly in Sections 7.1 and 7.2 respectively. Our prospects of performing one-colour RbSr spectroscopy close to the D_1 line of Rb, necessary in view of performing STIRAP transfer to the rovibronic ground state after weakly-bound molecule association, are discussed in Section 7.3. In this last section we also mention the molecule association scheme based on photoassociation followed by spontaneous emission, which is an alternative route for weakly-bound molecule formation. This is a promising line of research, which needs to be explored and for which the laser system is ready.

7.1 Double Mott insulator production

The production of a double Mott insulator requires careful design of the optical lattice system. The number of Rb-Sr atom pairs that we obtain in the double Mott insulator should be maximised, so as to produce as many molecules as possible. This number is the result of the balance between the external confinement of the dipole traps and lattice beams — see Appendix A, Equation A.15 —, and the on-site interaction energies of Rb-Rb, Rb-Sr and Sr-Sr atom pairs. The on-site interaction energies are set by the intraspecies and interspecies s-wave scattering lengths of Rb and Sr, which are discussed in Chapter 1, Subsection 1.2.3, and by the local depth of the lattice site for each species. Therefore, they depend on the intensity and on the wavelength λ_{lattice} of the lattice laser, because the depth felt by each atom depends on its DC-polarisability $\alpha(\lambda_{\text{lattice}})$ (see Appendix A). We chose to work at $\lambda_{\text{lattice}} = 1064\,\text{nm}$, wavelength at which one can buy very powerful and coherent laser sources. The external confinement is set by the power, a wavelength and geometry of the dipole traps and of the lattice beams. Accordingly, it can be modified by changing the waists of the corresponding laser beams, thus changing the spatial geometry of the dipolar potential — see Equation A.1. We use numerical simulations to infer how many Rb-Sr atom pairs we should expect to create for given Rb and Sr atom numbers in the initial double BEC, and for given optical powers and waists of the dipole traps and lattice beams.

Based on measurements performed before this PhD work, it was concluded that a double Mott insulator filled with up to 3×10^4 ^{87}Rb-^{84}Sr pairs had been obtained in the laboratory [52]. The rather short, $130(30)\,\text{ms}$ lifetime of these Rb-Sr pairs was attributed to the photoassociation of these pairs by the lattice light, leading to the formation and loss of electronically-excited molecules. That could be true. However, it seemed to the author of this thesis that three-body losses could explain these losses equally well, especially since the loss timescale was comparable to that of the three-body Rb-Rb-Rb and Sr-Sr-Sr losses that we observe in the lattice. To test this hypothesis, we adjusted the experimental loading conditions and showed that it was possible to obtain a signal indicative of Rb-Sr pairs even after a few seconds in the lattice. This results contradicted the former hypothesis of loss through photoassociation. We also performed a new set of numerical simulations, spotted mistakes in the previous ones, and concluded from the new measurements and the new simulations that three-body losses were more likely than two-body photoassociation. We also concluded that the optical lattice setup presented in Ref. [52] is far from optimal: the waists of both dipole trap and lattice beams are too small to populate the lattice with more than 10^4 atom pairs. Accordingly, we kept the overall design of the optical setup the same[1], but changed

[1] In particular, we still use a combination of 532 nm and 1064 nm dipole traps to cancel the relative gravitational sag of Rb and Sr, as exposed in Ref. [52].

the beam waists of all lattice beams to about 400 μm each and expanded by a factor two the waists of the elliptical dipole traps. The new 532 and 1064 dipole traps have a waist of about 40 μm in the vertical direction, and we kept the same ellipticity ratio as before (i.e. the ratio of the horizontal and vertical waists are the same, which is about 17 for 1064 nm and 14 for 532 nm). According to our simulations[2] — the new ones and the corrected previous simulations —, this new lattice setup should be able to support up to $4.0 - 5.0 \times 10^4$ Rb-Sr pairs loaded in the ground state of relative motion of the optical lattice.

To estimate experimentally the number of Rb-Sr pairs that we actually produce in the double Mott insulator, we use the same method as in Ref. [52]. Our preliminary results indicate that we can produce up to 1.8×10^4 long-lived Rb-Sr pairs. However, this statement must be taken carefully. The method of Ref. [52] relies on the use of a Rb-Sr one-colour resonance close to the $^1S_0 - {}^3P_1$ transition of Sr, which produces photoassociation losses on lattice sites occupied by Rb-Sr pairs. However, this technique is prone to create artifacts. First, the photoassociation beam also induces losses on sites with more than two atoms. This is not a huge problem, because these sites decay fast due to three-body losses anyway and one can decouple the three- and two-body dynamics rather easily. Second, it can photoassociate atoms that have been incorrectly loaded into the lattice. Indeed, such atoms will occupy excited bands, not the ground state of the lattice. Therefore, they can tunnel across lattice sites, collide with other atoms and produce photoassociation signals that are not indicative of ground-state Rb-Sr pairs. The RbSr photoassociation probe is thus a useful tool, but it has limitations and doesn't give a fully satisfactory proof that a Rb-Sr double Mott insulator has been achieved. Another method for the estimation of Rb-Sr pairs produced in the ground state of the lattice is lattice-depth modulation spectroscopy. In this method, the depth of the lattice is modulated at the frequency corresponding to the on-site interaction energy of Rb-Sr, creating particle-hole excitations and thus detectable heating — see Ref. [129], Figure (5.10). However, we could never observe a signal indicative of the Rb-Sr on-site interaction energy using this method. One reason might be that the expected heating at the correct modulation frequency, which matches the Rb-Sr on-site interaction energy, could not be resolved due to other forms of heating. Another issue is that the on-site interaction energies of ^{87}Rb-^{84}Sr and ^{84}Sr-^{84}Sr are almost identical at our lattice depths and wavelength, and thus can hardly be distinguished.

In conclusion, we think that the current optical lattice system can support up to 1.8×10^4 long-lived Rb-Sr pairs or more, which is supported by simulations and experimental data, but more characterization is required. Furthermore, we have implemented recently an intensity stabilization scheme, based on a digital PID loop, to actively stabilize the intensity

[2] These simulations assume an entropy-free sample, i.e. $T = 0$. This is close to what we achieve with our BECs but a small residual thermal cloud always remains, with a temperature of a few ten nK typically.

of the lattice beams. This will result in a minimization of lattice heating effects, and allow us to optimize even further the loading of double BECs of ^{87}Rb-^{84}Sr in the optical lattice.

7.2 Magnetic field stabilization

Producing a $B = 1311\,\mathrm{G}$ static magnetic field with mG stability is not a trivial task. We use two sets of coils in Helmoltz configuration to produce a homogeneous magnetic field at the position of the atoms, with a current-to-field characteristic of about $3.3\,\mathrm{G/A}$. To this date, no commercial power supply can produce the ~ 400 A that we require to reach $B = 1311\,\mathrm{G}$ with ppm-level current stability. Therefore, we built our own low-noise power supply with the help of the electronics workshop of the University of Amsterdam and of the Dutch company Ideetron. This power supply will be the object of a publication in the near future and we do not describe it here. In the following paragraphs the performances that we could achieve with this setup are discussed.

The best tool we have at hand to measure the stability of the magnetic field at the position of the atoms is the ultracold atom sample itself. We start by creating a BEC of ^{87}Rb atoms in the $|F, m_F\rangle = |1, 0\rangle$ state. Then we ramp up the field to $B = 1311\,\mathrm{G}$, a field at which the energy difference between the states $|1, 0\rangle$ and $|1, -1\rangle$ is about $h \times 920\,\mathrm{MHz}$ — see Figure 5.7. Then, we irradiate the Rb cloud with RF radiation, of a frequency close to $\mathrm{f_{RF}} = 920\,\mathrm{MHz}$ in order to resonantly drive the $|1, 0\rangle$ – $|1, -1\rangle$ transition. At the end of the irradiation, we separate the atoms remaining in $|1, 0\rangle$ from the atoms transferred to $|1, -1\rangle$ by Stern-Gerlach separation, perform absorption imaging and infer the relative Rb population in each state after the RF pulse. This detection technique is the same as the one described in Chapter 2, Subsection 4.3.2, and presented in Figure 4.2 in the context of one-colour spectroscopy. The outcome of such a measurement is shown on Figure 7.1, left panel. The relative population as a function of the RF irradiation frequency is indicative of the magnetic field stability, and two important informations can be extracted from it. First, the shifts in the central frequency (i.e. the RF frequency at which the maximal transfer efficiency is observed) are indicative of changes in the ambient magnetic field offset and/or changes in the power supply behaviour. Second, the width of the transfer curve is indicative of the short-term noise of the field, integrated over the RF pulse time T_{RF} (a few ms to a few hundred ms in our case)[3]. From

[3]The effects that contribute to the observable width, aside from magnetic noise, are the natural linewidth of the transition, differential BEC mean-field shifts, Doppler broadening, and the avoided-crossing gap $2\Omega_{\mathrm{RF}} \propto \sqrt{I_{\mathrm{RF}}}$ between the two coupled states, which is set by the intensity I_{RF} of the RF pulse. The $|1, 0\rangle$ – $|1, -1\rangle$ transition is essentially infinitely narrow (the $|1, -1\rangle$ never decays back to the $|1, 0\rangle$ through spontaneous emission of a RF photon), therefore it doesn't contribute to the width. Doppler broadening is almost absent in a BEC, and even in a non-condensed thermal gas with a temperature of a few μK the Doppler effect leads to sub-Hz broadening. Indeed, the first-order Doppler shift is $\Delta\mathrm{f} = \mathrm{f_{RF}} \times (v/c)$, where $c = 299792458\,\mathrm{m.s^{-1}}$ is the speed of light in vacuum and v is the speed of the considered atom. In an atom gas at thermal equilibrium, the most probable velocity v is given by

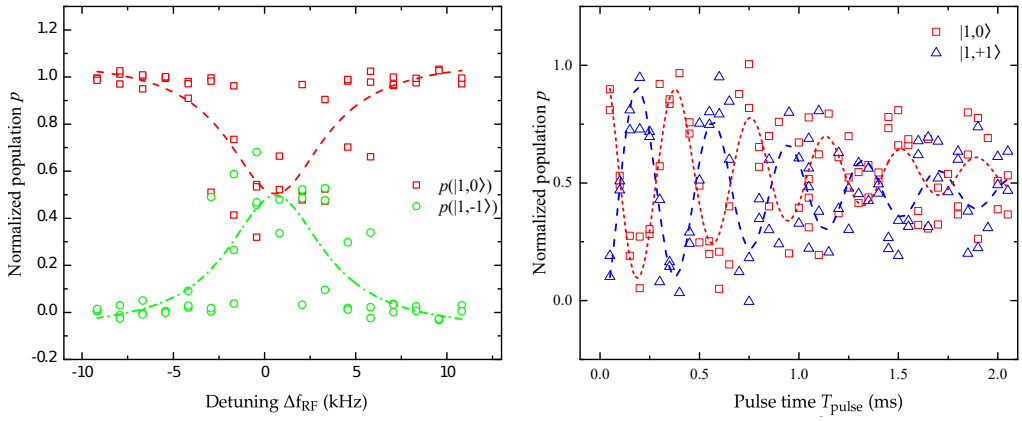

FIGURE 7.1: Magnetic field stability and noise characterization. **Left panel:** RF-spectroscopy of the Rb $|1,0\rangle$ – $|1,-1\rangle$ transition at a magnetic field of $B = 1311\,\mathrm{G}$. The squares (circles) show the normalized population p in the state $|F,m_F\rangle = |1,0\rangle$ ($|1,-1\rangle$). The dashed (dash-dotted) line are Lorentzian fits to the $|1,0\rangle$ ($|1,-1\rangle$) data. From the FWHM value and the relative magnetic moment of the two states, $\delta\mu = h \times 604\,\mathrm{kHz/G}$, we derive a magnetic field stability of about 10 mG over more than half an hour. **Right panel:** Coherent Rabi flops of Rb for the $|1,0\rangle$ – $|1,+1\rangle$ transition at $B = 127\,\mathrm{G}$. The squares (triangles) show the normalized population p in the state $|F,m_F\rangle = |1,0\rangle$ ($|1,+1\rangle$). The dashed (short-dashed) line are exponentially decaying sine fits to the $|1,0\rangle$ ($|1,+1\rangle$) data. The fitted exponential time constant is 0.94 ms.

such measurement we could infer that, close to $B = 1311\,\mathrm{G}$, the magnetic field drifts by no more than 25 mG over the course of several hours, with an 100 ms-integrated noise of about 10 mG. This is already an excellent result, but we want to push it further to ensure that we can achieve ^{87}Rb^{84}Sr magnetoassociation.

The stability of the magnetic field over the course of the magnetoassociation process determines the atom-to-molecule transfer efficiency. If the magnetic field fluctuates too much during the B-field association ramp, the coherence of the atom-molecule superposition is compromised and the transfer efficiency decreases — see Chapter 5, Subsection 5.1.2. Overall offsets in the magnetic field are in principle not detrimental, as long as the Feshbach

$\frac{1}{2}mv^2 = k_B T$, i.e. a few tens of mm.s^{-1} only at a temperature of a few μK. This leads to Doppler of the order of a few ten mHz. Differential BEC mean-field shifts are very small in ^{87}Rb, because the difference between the ^{87}Rb singlet and triplet s-wave scattering length is very small. The RF intensity I_{FB} defines the width of the feature in the limit where the Rabi frequency Ω_{RF} and $|1,-1\rangle$ states is larger than the other contributions to the width. We can reach Rabi frequencies of the order of a few kHz (see Figure 7.1, right panel), comparable to magnetic noise, therefore one has to be careful and work at relatively low intensity to perform measurements such as the one presented in Figure 7.1, left panel. If that is the case, magnetic noise is the main contribution to the width of the experimental feature and the measurement is meaningful.

resonance position is captured by the magnetic field ramp, as depicted in Figure 5.4. We believe that the short-term ($\sim$ ms) stability of the magnetic field is better than 10 ppm, for two reasons. First, we can reduce the width of the RF-spectroscopy features, such as the one shown in the left panel of Figure 7.1, by reducing the amount of data points taken during a spectroscopy scan and by decreasing T_{RF} to 5 ms. In these conditions we fit a FWHM of 1.0(2) kHz. Given the relative magnetic moment $\delta\mu = h \times 604\,\mathrm{kHz/G}$ between the $|1,-1\rangle$ and $|1,0\rangle$ states at $B = 1311\,\mathrm{G}$, this corresponds to a 5 ms-integrated magnetic noise of about 1.7(3) mG. However, by increasing the amount of data points taken we see that after a few points the resonance shifts to a different central frequency, within a window of 25 mG. Second, we can observe about five Rabi flops over the course of 2 ms, by driving the $|1,0\rangle$ – $|1,+1\rangle$ transition at $B = 127\,\mathrm{G}$ and $\mathrm{f_{RF}} = 88\,\mathrm{MHz}$. This indicates that the overall field offset is stable at $B = 127\,\mathrm{G}$, because the phase of the Rabi flops is conserved over many measurements. For these reasons we do believe that the short-term noise at $B = 1311\,\mathrm{G}$ is better than 10 ppm, but that residual magnetization shifts create shot-to-shot drifts of the magnitude of the magnetic field, artificially broadening the width of the spectroscopy features and prohibiting the observation of Rabi flops at this field[4]. Indeed, in contrast to the relatively small field of $B = 127\,\mathrm{G}$, the large field of $B = 1311\,\mathrm{G}$ magnetizes objects and materials around the vacuum chamber. We see this effect clearly from the regular shifts of our Sr red MOT position, which are indicative of changes in the vertical magnetic field offset (the coils that we use to create the homogeneous magnetic field for Feshbach association produce a field oriented in the vertical direction) and which we monitor by monitoring the Sr loading efficiency into our crossed-beam optical dipole trap of wavelength 1064 nm[5].

[4] We observe Rabi-flopping for two to five measurements consecutively. Then the phase of the Rabi flops seems to change, which is most likely due to a change of magnetization offset. This prohibits the observation of a complete set of uninterrupted Rabi flops.

[5] We monitor these shifts as follows. In the last stages of laser cooling of Sr, down to a few μK, the quadrupole gradient of the MOT is of few $\mathrm{G.cm^{-1}}$ only, and the red cooling light is very close to resonance and has very low intensity (about 1 I_{sat}, i.e. $3\,\mu\mathrm{W.cm^{-2}}$). In these conditions, the Sr MOT has a very small vertical radius of about 200 μm (see Ref. [124], Figure (2.7)). Therefore, its vertical position, which is set by the vertical magnetic field offset, has a large impact of the efficiency of the Sr loading into the crossed-beam dipole trap, because this trap has a vertical waist of about 40 μm only. Even of few mG of change in the vertical magnetic field offset can affect the number of atoms loaded into the trap. To monitor this vertical magnetic field offset, we use another coil to produce a vertical homogeneous magnetic field offset (of which we know the value) at the position of the atoms and check at which applied offset the loading efficiency is the best (i.e., at which offset the largest amount of atoms are loaded into the trap). We monitor the value of this offset on a daily basis. Changes of this value are indicative of a change of the vertical magnetic field offset by the corresponding amount. Using this method, we can resolve shifts as small as 10 mG in the vertical magnetic field offset. From the day when we started to produce homogeneous magnetic of a few hundred G for Feshbach spectroscopy (see chapter 6), at about 300 G, to the day when we finished this spectroscopy, using fields up to 500 G, we could observe a total change of about 350 mG in the vertical offset magnetic field, which we attribute almost entirely to magnetization induced by these large fields. Since then we have since even more change due to our daily use of fields up to 1500 G. Note that magnetization induced by our large homogeneous fields is the leading effect for such changes, but that also external sources (for instance, large fields being produced in neighbouring laboratories) contribute. Nowadays, we apply a very large field of $B = 1500\,\mathrm{G}$ for a few hundred ms at the end of each experimental sequence, to fix the vertical magnetization offset and avoid erratic loading of the Sr cloud from one experimental shot to the other. This compensates from the

Therefore, it could be that the magnetic field is already suitable for ^{87}Rb^{84}Sr magnetoassociation with a magnetic coupling width of $h \times 2|\Omega|/\delta\mu = 0.8\,\mathrm{mG}$, as discussed at the end of Subsection 5.1.2. Furthermore, reaching ppm-level is required to achieve close-to-unity transfer efficiency using an adiabatic transfer (see Equation 5.22), but even with a noise in the ten-ppm range it should be possible to magnetoassociate about 50 % of the ^{87}Rb-^{84}Sr pairs into molecules, using quick and incoherent magnetic sweeps across the Feshbach resonance. However, we do not want to take any risk. We want to perform adiabatic association ramps of a few ten or hundred ms, and from the measurements discussed above there is no clear proof that the noise averaged over 10 or 100 ms is at the ppm level — it is for sure in the 10 ppm range, but that might still not be good enough for very efficient association. Therefore, we are now implementing an active magnetic field stabilization system, with which we can estimate the absolute field at the position of the atoms and cancel ambient offsets and low-frequency noise, such as the 50 Hz noise of the power grid. Using this additional stabilization system, we might be able to observe several consecutive Rabi flops at $B = 1311\,\mathrm{G}$ and prove that we reached ppm-level noise and accuracy.

7.3 One-colour spectroscopy close to the D_1 line of Rb and alternative method for molecule formation

Once weakly-bound molecules will have been formed by magnetoassociation or another method, one needs to transfer them to the rovibronic ground state. In all bi-alkali, this is done using STIRAP, and this know-how should translate very simply to RbSr. Devolder et al. theoretically predicted the most promising STIRAP paths and the corresponding pump and dump laser wavelengths in ^{87}Rb^{84}Sr — see Ref. [53], Table IV. The first STIRAP scheme involves a pump laser at the wavelength $\lambda_{\mathrm{pump}} = 2.0\ \mu$m and a dump laser at $\lambda_{\mathrm{dump}} = 1.7\ \mu$m[6], which are both quite far on the infrared side and are very inconvenient from the technological point of view. The same is true of the second STIRAP scheme, which requires $\lambda_{\mathrm{pump}} = 1.4\ \mu$m and $\lambda_{\mathrm{dump}} = 1.2\ \mu$m. The third, and last, proposed STIRAP scheme instead involves the visible wavelength $\lambda_{\mathrm{pump}} = 860\,\mathrm{nm}$ and $\lambda_{\mathrm{pump}} = 809\,\mathrm{nm}$. That's the STIRAP path we chose.

We built a 795-nm laser system to perform one-colour spectroscopy of RbSr close to the D1 line, which is required to precisely measure the binding energies of the states we want to exploit for the pump leg of STIRAP. This laser will also be used, after a slight change

small magnetization drifts induced by the 1311 G field that we use in each ^{87}Rb-84Sr experimental run related to Feshbach association.

[6] This is assuming we start with the weakly-bound $v = -4$ molecular state, which is the target state of our magnetoassociation scheme at $B = 1311\,\mathrm{G}$ in ^{87}Rb^{84}Sr.

of wavelength, as the dump laser for STIRAP. We also built a 860-nm laser system for the pump leg of STIRAP. The 795-nm photoassociation laser is currently referenced to the D1 line through modulation transfer spectroscopy on a Rb spectroscopy cell, combined with a tunable frequency offset locking technique and a fiber EOM. The setup is very similar to the one described in Chapter 2, Subsection 4.3.1, which we used for one-colour RbSr spectroscopy close to the $^1S_0 - {}^3P_1$ intercombination line of Sr. With this spectroscopy setup, we can scan a few tens of GHz below the $(^2P_{1/2}) + \mathrm{Sr}\ (^1S_0)$ dissociation asymptote. Once we will have detected the first molecular states, close to 795 nm, our colleagues of the group of Olivier Dulieu should be able to accurately predict the binding energies of new molecular states. We will then change the 795-nm laser wavelength, or use the 860-nm laser to detect these new states, and through iterative steps find the suitable molecular state for the pump leg of STIRAP at about 860 nm.

As a side benefit of performing this one-colour spectroscopy, we can use the molecular lines detected close to the $(^2P_{1/2}) + \mathrm{Sr}\ (^1S_0)$ dissociation asymptote to form RbSr molecules in the electronic ground state, using the method of photoassociation followed by spontaneous emission described in Ref. [53] and in Chapter 1, Subsection 1.4.3. An important asset of this method is that it should allow us to produce molecules much faster than by using magnetoassociation, at ms timescales [54]. Therefore, if the reason why we didn't observe molecules so far is that they get destroyed during the long magnetoassociation ramps[7,8], this technique might allow us to see molecules for the first time and to understand their loss dynamics in the lattice.

[7] The magnetoassociation ramps are typically a few ten or hundred ms-long, because the small ∼kHz energy gap at the resonance position imposes a slow ramp to maintain adiabaticity — see Chapter 5, Subsection 5.1.2.

[8] The molecules could for instance get photoassociated by the 1064 nm lattice light at ms timescales or below. This is what our group experienced with Sr_2 in a 532 nm optical lattice, where the molecules had sub-ms lifetimes. Switching to a 1064 nm lattice, the molecules could live for a few minutes.

Appendix A

Optical lattices and dipole traps for RbSr: formulas

A.1 Optical dipole traps

In the following, the reader will find all equations that can be used to compute depth and trap frequencies for Rb and Sr optical lattices and dipole traps, as well as alignment and calibration procedures. The polarisabilities are given for the two wavelengths of interest of our experiment, i.e. $\lambda = 1064$ nm and $\lambda = 532$ nm. All values are given in SI units[1].

The intensity $I(x, y, x)$ of a Gaussian laser beam is

$$I(x,y,z) = \frac{2P}{\pi w_z(y) w_x(y)} \exp\left[-2\left(\left(\frac{z}{w_z(y)}\right)^2 + \left(\frac{x}{w_x(y)}\right)^2\right)\right], \tag{A.1}$$

where P is total optical power in the beam (in Watts), y is the direction of propagation of the light and x, z the transverse directions in which the electric field oscillates. The transverse profile of the optical beam is related to the waists w_x and w_z, with $w_x = w_z$ for a round-shaped beam, and to the Rayleigh ranges $z_{R,x}$ and $z_{R,z}$ in the x and z directions through the relations

$$\begin{aligned} w_z(y) &= w_z\sqrt{1 + (y/z_{R,z})^2} \quad \text{with} \quad z_{R,z} = \frac{\pi w_z(0)^2}{\lambda} \\ w_x(y) &= w_x\sqrt{1 + (y/z_{R,x})^2} \quad \text{with} \quad z_{R,x} = \frac{\pi w_x(0)^2}{\lambda}. \end{aligned} \tag{A.2}$$

The maximum intensity at the waist position $z = 0$ is found at $x = y = 0$ and is

[1] Polarisabilities are often written in atomic units in the literature. In this system of units $\hbar = 4\pi\epsilon_0 = m = e = 1$, where m and e are the electron mass and charge respectively. Therefore the appropriate unit of length in this system is the Bohr radius $a_0 = \frac{4\pi\epsilon_0\hbar^2}{m\,e^2} = 0.529177210$ Å.

$$I_0 = I(0,0,0) = \frac{2P}{\pi w_z w_x} \,. \tag{A.3}$$

Note that these formulas assume that the positions of both waists are the same: $z = 0$. This is in general not true if the difference of dimensions between the two waists is produced by a single cylindrical telescope, which is not perfectly afocal and thus produces astigmatism; we are aware of such discrepancies in our experiments. The dipolar potential imposed on the atoms by the laser beam is

$$U(x,y,z) = -\frac{1}{2\epsilon_0\, c}\alpha(\lambda) I(x,y,z) \,, \tag{A.4}$$

where the polarisabilities of the atoms at the optical frequency λ are[2]

$$\begin{aligned} &\alpha^{\mathrm{Sr}}(1064\,\mathrm{nm}) = 234 \times 4\pi\epsilon_0\, a_0^{-3} \quad \text{and} \quad \alpha^{\mathrm{Sr}}(532\,\mathrm{nm}) = 687 \times 4\pi\epsilon_0\, a_0^{-3} \\ &\alpha^{\mathrm{Rb}}(1064\,\mathrm{nm}) = 752.3 \times 4\pi\epsilon_0\, a_0^{-3} \quad \text{and} \quad \alpha^{\mathrm{Rb}}(532\,\mathrm{nm}) - 248.7 \times 4\pi\epsilon_0\, a_0^{-3} \,. \end{aligned} \tag{A.5}$$

The dipolar potential is attractive for $\alpha(\lambda) > 0$ (i.e. atoms are pushed towards the focus, where the intensity is maximal), repulsive for $\alpha(\lambda) < 0$ (the atoms are pushed away from the focus).

The trap frequencies $f_x, f_y, f_z = (\omega_x, \omega_y, \omega_z)/2\pi$ in the x, y and z directions are harmonic frequencies, and are computed assuming that close to the waist(s) the potential behaves as a $3D$ harmonic oscillator. They read

$$\begin{aligned} U(x,0,0) &\underset{x\to 0}{=} U_0 + \frac{1}{2} m {\omega_x}^2 x^2 \quad \text{with} \quad \omega_x = \sqrt{\frac{-4U_0}{m w_x^2}} \\ U(0,0,z) &\underset{z\to 0}{=} U_0 + \frac{1}{2} m {\omega_z}^2 z^2 \quad \text{with} \quad \omega_z = \sqrt{\frac{-4U_0}{m w_z^2}} \\ U(0,y,0) &\underset{y\to 0}{=} U_0 + \frac{1}{2} m {\omega_y}^2 y^2 \quad \text{with} \quad \omega_z = \sqrt{\frac{-\lambda^2 U_0}{m\pi^2}\left[\frac{1}{w_x^4} + \frac{1}{w_z^4}\right]} \,, \end{aligned} \tag{A.6}$$

where m is the mass of either Rb or Sr. The depth of the dipole trapping potential U_0 is

$$U_0 = U(0,0,0) = -\frac{1}{2\epsilon_0\, c}\alpha(\lambda) I_0 \,. \tag{A.7}$$

[2]The symbol a_0 represents the Bohr radius, see previous footnote.

Since $U_0 \propto P$, all trap frequencies should verify $f_i = \omega_i/2\pi \propto \sqrt{P}$ in the harmonic approximation. The trap frequency in the propagation direction y is always much smaller than in the other directions x, y and doesn't provide much confinement[3].

The expressions above are valid for the attractive case $\alpha(\lambda) > 0$. In the anti-trapping case each $U_0 + \frac{1}{2}m{\omega_i}^2 i^2$ is simply replaced by $U_0 - \frac{1}{2}m{\omega_i}^2 i^2$, and U_0 is replaced by $-U_0$ in the expression of each of the corresponding angular frequencies ω_i. The harmonic approximation is very good for a BEC in the ground-state of a high-intensity optical trap. However when the trapping potential is shallow (i.e. at low optical intensities), it competes with the gravitational force pulling the BEC towards the ground: in that case deviations to harmonicity are to be expected, with lower effective trap frequencies than expected from a purely harmonic behavior.

Since we cannot install beam-imaging cameras in the vacuum of the glass cell where the atoms lie, we measure the actual waists of our laser beams at the position of the atoms via trap frequency measurements. One method, the most precise, consists in measuring the center-of-mass oscillation of a BEC in one direction of the dipole trap after excitation[4], using standard absorption imaging to track the spatial displacements of the BEC. These oscillations have the same frequency f_i as the trapping potential, and this measurement method is valid for a thermal gas of atoms[5] as well as for a BEC. The second method consists in modulating the trap intensity. In that case, one needs to distinguish between the case of a thermal gas of atoms and a BEC. For a thermal gas of atoms, parametric oscillations lead to observable losses at the modulation frequency $2 \times f_i$, as is expected from classical physics. A BEC will instead exhibit monopole, quadrupole, or higher order breathing oscillations at $\sqrt{X} \times$

[3] At least at our optical lattice working conditions, where the laser source is used to produce thousands of trapping sites. In optical tweezers experiments, on the other hand, an enormous amount of laser power can be focussed to produce a trap for a single atom. In that case, the trap frequency in the propagation direction of the laser beam is not negligible.

[4] In the gravity direction, the excitation is provided by switching off the dipole trap for a short period (∼ms) to provoke falling of the BEC, and then switch on the trap again to recapture the BEC. The momentum acquired by the BEC during its fall makes it oscillate in the trap after recapture. Note that this is also possible in the non-vertical directions, but it works only if the laser beam is slightly tilted with respect to the horizontal plane, which is not our case because we carefully align the dipole beams as horizontally as possible. To measure the trap frequencies in the non-vertical directions, there is a second, better method: a thermal gas of atoms is loaded "from the side" into the dipole trap. The gas acquires momentum when it enters the trap because it is attracted towards the focus of the laser beam. This produces center-of-mass oscillations in the direction where the gas was loaded from the side. A third method is to modulate the intensity of the dipole trap with a frequency close to the trap frequency of interest. Due to the slight fall of the BEC when the trap intensity decreases in a modulation cycle, the motion of the center of mass of the BEC is resonantly excited. In my experience the first and second method are easier to use, and give better results than the third.

[5] What we call a thermal gas of bosonic atoms is a gas of thermal energy much greater than the chemical potential μ (not to be confused with μ, the reduced mass of an atom pair, introduced in Chapter 2), i.e. $k_B T \gg \mu$. In this regime the effects of bosonic statistics are irrelevant, at least to the present discussion, and the gas may be treated as a classical gas at thermal equilibrium. Expressions for the chemical potential of bosons in an optical dipole trap are given in Ref. [124]. We typically have $\mu \ll 10 - 100\,\mathrm{nK}$ in our ^{84}Sr and ^{87}Rb experiments, therefore a gas with $T \geq 1.0\,\mu\mathrm{K}$ can be considered thermal gas. For a gas of identical fermions, such as spin-polarized ^{87}Sr, the temperature of the gas must be compared to the Fermi temperature instead.

f_i, where X is a rational number depending on the trap geometry [172, 173]. The waists x, y are inferred from the measured optical power P, the frequencies are measured with either method and Equations A.6. These methods are especially precise when measurements are made at several optical powers P and the data subsequently fitted and compared with Equations A.6.

For low optical intensities, gravity has to be taken into account. This is done very simply by adding the gravitational potential energy $E = mgu$, where u is the direction of gravity, to $U(x, y, z)$ and by performing similar expansions as given in Equations A.6 around the equilibrium position defined by both trapping and gravitational potentials. In the special (and important) case where the beam propagates in the horizontal plane, perpendicular to the direction $u = z$ (with z chosen to be the direction of gravity), the effect of gravity is to shift the equilibrium position from $(0, 0, 0)$ to $(0, 0, z = z_{\mathrm{eq}})$. The shift z_{eq} in equilibrium position is called *gravitational sag* and is defined by

$$\frac{\partial}{\partial z}\left(U(x, y, z) + mgz\right) = 0 \quad \text{at} \quad z = z_{\mathrm{eq}}\,. \tag{A.8}$$

Accordingly, in the harmonic approximation A.6 the gravitational sag is

$$z_{\mathrm{eq}} = \frac{g}{{\omega_z}^2}\,, \tag{A.9}$$

where $g = 9.81\ \mathrm{m.s}^{-2}$ is the gravitational constant. The trap frequencies in the horizontal plane are then corrected by changing $U(x, 0, 0)$ and $U(0, y, 0)$ to $U(x, 0, z_{\mathrm{eq}})$ and $U(0, y, z_{\mathrm{eq}})$ in Equation A.6. Note that any tilt in the propagation axis y of the trap will lead to coupling of the propagation axis y to gravity, and induce a shift in position in the y directions analogous to that of Equation A.9 — the BEC "falls" along the direction of the tilt. Furthermore, these shifts in equilibrium position (gravitational sags+tilts) are different for Rb and Sr. This is because they have different polarisabilities, as shown in Equations A.5[6]. For theses reasons loading a (double) BEC from a shallow dipole trap into an optical lattice requires very careful optical alignment.

A.2 Optical lattices

An optical lattice is obtained by retro-reflecting a laser beam onto itself, given that the coherence length of the laser is much larger than the relative optical path between the two beams at the interfering point. The intensity pattern produced by the interference of the two counterpropagating beams is

[6] The difference in mass also contributes to the difference in equilibrium positions, but ^{87}Rb and ^{84}Sr have very similar masses.

$$I_{\text{lattice}}(x,y,z) = \left|\sqrt{I(x,y,z)}\exp\left(-iky+i\phi\right)+\sqrt{I(x,y,z)R}\exp\left(+iky+i\phi+i\delta\phi\right)\right|^2 \\ = 4R\times I(x,y,z)\times\cos^2(ky-i\delta\phi/2)+(1-R)^2\times I(x,y,z)\,, \tag{A.10}$$

where y is the axis of propagation of the beams, $k=\frac{2\pi}{\lambda}$ the light wave vector magnitude and $I(x,y,z)$ the beam intensity given in Equation A.1 — it is assumed here that the two beams have the same spatial geometry at the position of the atoms, which requires careful optical design (the waists of both beams have to be at the same place). Furthermore, both beams need to share the same linear polarization for Equation A.10 to be valid. The lattice wells, defined by their position at the maxima (minima) of intensity for attractive (repulsive) dipolar potentials (corresponding to a polarisability $\alpha>0$ (<0) are evenly spaced by the distance $\lambda/2$ along the propagation axis, corresponding to one well every 532 nm at $\lambda=$ 1064 nm. The reflection coefficient $0<R<1$ accounts for the intensity losses induced by the glass cell and retroreflection mirrors on the retro-reflected beam. In our case all mirrors have $R\simeq 1$ for $\lambda=1064$ nm and R is limited by the losses on our uncoated glass cell leading to $R\simeq 0.85$ ($R\simeq 0.96$ for a 1064 nm beam on a glass/air or air/glass interface with angle of incidence $\theta\simeq 45°$, and each beam passes through such an interface four times in our experiment, with its linear polarization oriented to maximises transmission). The global optical phase ϕ doesn't contribute to the spatial structure of the potential. However the phase difference $\delta\phi=k\times n\times\delta y$, with n the optical index of the propagation medium (vacuum and air in our case, so $n\simeq 1$) and δy twice the distance between the retroreflection mirror and the interfering point, defines the position of the wells. We do not control this phase difference actively in our experiments. Consequently, the lattice might "shake" if the optical elements such as the retro-reflection mirror(s) or the glass cell walls are moving. It is therefore advised to minimize the optical path difference between the two beams and, most importantly, to ensure mechanical stability of the optical elements on the table.

The *lattice depth* s defines the band structure of the system[7]. It is is given by the prefactor $4R\times I(x,y,z)$ of the lattice term in Equation A.10. The lattice depth is typically expressed in units of recoil energy, which is the kinetic energy $E_R=\frac{\hbar^2k^2}{2m}$ transferred to an atom of mass m upon absorption of one lattice photon — in these units, the lattice physics is independent of the mass of the considered atom and of the laser wavelength. The recoil energies of interest for the (current) RbSr experiment are

[7]The band structure associated with the band index n_{band} refers to center-of-mass degrees of freedom. In the following we discuss the (angular) oscillation frequencies ω for a single atom of mass m. For an atom pair the band structure refers to the center-of-mass of the atom pair and the harmonic oscillation frequencies ω are the ω_C frequencies of the center-of-mass harmonic motion on a lattice site, Equation 5.16.

$$\begin{aligned} E_{R,^{84}\mathrm{Sr}} &= h \times 2.10\ \mathrm{kHz} \quad \text{at} \quad \lambda = 1064\ \mathrm{nm} \\ E_{R,^{87}\mathrm{Rb}} &= h \times 2.03\ \mathrm{kHz} \quad \text{at} \quad \lambda = 1064\ \mathrm{nm} \\ E_{R,^{84}\mathrm{Sr}} &= h \times 8.40\ \mathrm{kHz} \quad \text{at} \quad \lambda = 532\ \mathrm{nm} \\ E_{R,^{87}\mathrm{Rb}} &= h \times 8.11\ \mathrm{kHz} \quad \text{at} \quad \lambda = 532\ \mathrm{nm}\ . \end{aligned} \tag{A.11}$$

Accordingly, the lattice depth is[8]

$$s(x,y,z) = U_{\mathrm{lattice}}(x,y,z)/E_R = -\frac{1}{2\epsilon_0\, c}\alpha(\lambda) \times 4R \times I(x,y,z)/E_R\ . \tag{A.12}$$

To compute the oscillation frequencies and tunneling rates of Rb or Sr on a lattice site, we use a Mathematica code produced by Bruno Laburthe-Tolra of the Laboratoire de Physique des Lasers (Université Paris 13, France). The oscillation frequencies define the center-of-mass and relative motion (angular) oscillation frequencies ω_C and ω_{rel} for an atom pair on the lattice site — see Subsection 5.1.2. Note that these on-site frequencies are *not* the trap frequencies as defined by the external confinement potential of Equation A.6. They correspond to the potential that confines particles to a single site, not to the overall potential that pushes the particles towards the waist position(s) of the beam where the intensity is maximal (for $\alpha > 0$). For a lack of better notation we use the symbol ω for both. Above $s = 20$ the oscillation frequencies follow approximately the behavior[9]

$$\omega(q=0) \propto \sqrt{s(x,y,z)} \propto \sqrt{I(xy,z)}\ , \tag{A.13}$$

where $\hbar\omega$ is estimated to be the energy $\hbar\omega(q=0)$ between the ground-state and the first excited band at the quasi-momentum $q = 0$. In the very deep lattice regime, the energy and thus ω are almost independent of q in the ground-state band because the motion is almost perfectly harmonic, as explained in Subsection 5.1.2. Experimentally, we have two ways of evaluating $\omega(q=0)$. The first is to modulate the intensity of one of the lattice beams. If the modulation frequency equals $2 \times \omega(q=0)$, atoms are parametrically excited[10]. On resonance the kinetic energy of the atoms increases exponentially with time and atoms are

[8] Note that lattice depth and external confinement are the same in the ideal case $R = 1$.

[9] The trend $s \propto \sqrt{I}$ is beautifully demonstrated in the Sr_2 STIRAP paper [48] of our group, where light shifts and lattice ground-state energy dependences on I are investigated experimentally.

[10] Also at sub-harmonic frequencies $2 \times \omega(q=0)/N$, where N is integer, parametric resonances can be excited.

heated out of the lattice, which results in observable losses [174][11,12]. The second method is to perform a Kapitza-Dirac pulse on a BEC with one lattice beam [175]. The evolution of the atomic populations in the 0 $\hbar k$, $\pm 2\ \hbar k$, $\pm 4\ \hbar k$, ... momentum states as a function of the pulse time gives the depth s of the lattice at the position of the BEC, and thus ω, obtained by comparison with the temporal evolution at a given depth s predicted by the Mathematica code. This method is extremely sensitive and is also our method of choice for lattice beam alignment: at a given lattice optical power, we minimize the pulse time for which we observe the first minimum in the 0 $\hbar k$ population (clearly seen from fitting the diffraction patterns obtained in absorption pictures) by adapting the pointing of the beam onto the BEC.

The intensity landscape $(1 + R^2 + 2R) \times I(x, y, z) = (1 + R)^2 \times I(x, y, z)$ created by the lattice beams at the positions of the lattice wells, for which $\cos(2ky - i\delta\phi) = 1$ (in the case of an attractive lattice $\alpha > 0$), defines the *external confinement* imposed by the lattice potential onto the atoms. This external confinement defines the dipolar potential experienced by an atom present on a given lattice site centered on (x, y, z). It is essentially a dipole trap roughly four times as deep as its non-counterpropagating counterpart, and the associated potential is

$$U_{\text{external confinement}}(x, y, z) = -\frac{1}{2\epsilon_0\, c}\alpha(\lambda) \times (1 + R)^2 \times I(x, y, z)\,. \tag{A.14}$$

The external confinement potential defines the local 3D chemical potential $\mu(x, y, z)$ in the local density approximation (LDA), given by

$$\mu(x, y, z) - \mu(0, 0, 0) = -U_{\text{external confinement}}(x, y, z)\,, \tag{A.15}$$

where $\mu(0, 0, 0)$ depends upon the number of atoms of the systems and on their interactions. The local chemical potential and the on-site interaction energies (i.e. the interaction energy due to the s-wave interaction of all atoms present on the lattice site) define how many lattice sites will be filled with one, two, three, ... atoms in a deep 3D optical lattice. In other words, they define the nature of the double Mott insulator and the amount of Rb-Sr pairs that we can obtain at a given geometry $U_{\text{external confinement}}(x, y, z)$, given atom numbers N_{Rb}, N_{Sr}

[11] In other words, the atoms are excited to the band $n = 2$, then $n = 4$, then $n = 6$, ... until they are not trapped by the lattice anymore.

[12] A sinusoidal intensity drive can only couple bands of same parity n_{band}, therefore the ground-state band $n_{\text{band}} = 0$ is not coupled to the $n_{\text{band}} = 1, 3, ...$ excited bands. If non-linearities are present in the drive (i.e., if it's not perfectly sinusoidal), losses or heating induced by the transition $n = 0 \rightarrow 1$ can be observed though.

and given (known) s-wave scattering lengths $a_{\mathrm{Rb,Rb}}$ (for the given $|f, mF\rangle$-state in which we produce the Rb BEC), $a_{\mathrm{Rb,Sr}}$ and $a_{\mathrm{Sr,Sr}}$.

We do not discuss here the physics of the superfluid to Mott insulator transition, which is characterized by a sharp decline in the fluctuations of the number of atoms on each lattice site — the atoms and atom pairs, initially prepared in a superfluid ensemble, get "frozen" on the trapping sites when the lattice depth reaches a threshold value. This transition happens around $s(x, y, z) = 12\ E_R$ in a 3D lattice with filling fraction $\overline{n} = 1$ atom per site. The reader is referred to Refs. [52, 150] for discussions of the nature of this transition, its relation with lattice dimensionality and for analytic formulas that can be compared to the lattice code we are using.

Appendix B

One-colour spectroscopy data tables

The reader will find in Tables B.1 and B.2 of this appendix all the resonance positions that we measured in the context of one-colour spectroscopy of Rb-Sr near the near the $^1S_0 - {}^3P_1$ electronic transition of Sr. The magnetic moments and, when extracted, the g-factor of the detected molecular states are reported in Table B.3. These data are subject to an ongoing theoretical analysis.

TABLE B.1: One-colour photoassociation spectrum and linewidths for the fermionic ^{87}Rb^{87}Sr isotopologue. Δ_{PA} is the resonance position at zero magnetic field, FWHM is the fitted Lorentzian full width at half maximum and $\gamma/2\pi$ is the fitted spontaneous decay rate of the detected molecular state. All quantities are in units of MHz. Data taken by V. Barbé and A. Ciamei, table created by A. Ciamei.

Δ_{PA}	Error	FWHM	Error	$\gamma/2\pi$	Error
4.20	0.50	–	–	1.80	0.5
15.84	0.32	4.50	1.00	3.30	0.70
65.22	3.50	–	–	–	–
249.30	0.40	2.56	0.41	1.80	0.20
260.40	3.47	–	–	–	–
275.00	3.63	–	–	–	–
288.40	2.82	–	–	–	–
458.00	3.01	–	–	–	–
483.00	3.48	–	–	–	–
509.90	0.50	9.10	1.30	8.00	1.00
573.90	2.87	–	–	–	–
611.00	3.53	–	–	–	–
622.00	3.59	–	–	–	–
686.79	0.23	1.24	0.13	0.90	0.10
799.22	2.97	–	–	–	–
829.22	3.64	–	–	–	–

1100.40	2.18	–	–	–	–
1160.90	3.07	–	–	–	–
1220.56	0.16	3.24	0.44	2.40	0.50
1492.90	3.00	–	–	–	–
1534.22	3.69	–	–	–	–
1569.00	3.41	–	–	–	–
1581.50	2.30	8.00	1.00	6.30	0.70
1799.00	2.99	–	–	–	–
1829.22	3.59	–	–	–	–
1863.00	3.37	–	–	–	–
1874.50	3.70	–	–	–	–
1913.40	0.60	9.80	1.30	7.80	1.10
2219.90	2.84	–	–	–	–
2270.90	3.53	–	–	–	–
2282.00	3.03	–	–	–	–
2335.40	0.60	10.80	1.40	8.0	00.80
3003.00	3.46	–	–	–	–
3013.90	3.26	–	–	–	–
3019.00	3.40	–	–	–	–
3670.00	3.18	–	–	–	–
3705.00	3.43	–	–	–	–
3730.00	3.18	–	–	–	–
3768.00	3.38	–	–	–	–
3892.49	3.10	–	–	–	–
3931.49	3.29	–	–	–	–
4199.20	0.30	3.00	1.00	2.50	0.80
4241.49	3.57	–	–	–	–
4385.49	3.49	–	–	–	–
4484.00	3.13	–	–	–	–
4625.49	3.06	–	–	–	–
4776.49	3.43	–	–	–	–
4850.49	3.05	–	–	–	–
4914.20	0.30	3.00	1.00	2.50	0.80
5021.49	3.06	–	–	–	–
5030.49	3.00	–	–	–	–
5076.49	3.51	–	–	–	–
5096.49	3.59	–	–	–	–
5114.49	2.73	–	–	–	–
5209.49	3.71	–	–	–	–
5281.49	3.11	–	–	–	–
5427.49	3.68	–	–	–	–
5500.00	3.13	–	–	–	–
5512.00	3.38	–	–	–	–
5546.20	0.40	5.50	1.00	4.50	0.60
5564.00	3.45	–	–	–	–
5653.22	3.48	–	–	–	–

5718.69	2.99	–	–	–	–

TABLE B.2: One-colour photoassociation spectrum and linewidths for the bosonic $^{87}Rb^{88}Sr$, $^{87}Rb^{86}Sr$ and $^{87}Rb^{84}Sr$ isotopologues. Δ_{PA} is the resonance position at zero magnetic field, FWHM is the fitted Lorentzian full width at half maximum and $\gamma/2\pi$ is the fitted spontaneous decay rate of the detected molecular state. All quantities are in units of MHz. Data taken by V. Barbé and A. Ciamei, figure created by A. Ciamei.

		$^{87}Rb^{88}Sr$			
Δ_{PA}	Error	FWHM	Error	$\gamma/2\pi$	Error
20.70	1.80	–	–	–	–
32.23	0.60	–	–	–	–
36.26	0.50	–	–	–	–
41.39	0.60	–	–	–	–
52.54	0.30	–	–	–	–
53.50	0.40	–	–	–	–
260.54	0.05	1.33	0.17	0.77	0.10
265.58	0.05	1.57	0.61	–	–
272.91	0.07	0.86	0.52	–	–
326.93	0.04	1.80	0.20	1.10	0.12
329.34	0.03	1.37	0.19	–	–
334.99	0.10	1.27	0.12	0.67	0.07
364.81	0.05	1.50	1.00	0.80	0.53
712.18	0.11	1.40	0.20	1.00	0.14
738.85	0.05	1.20	0.20	0.80	0.13
743.53	0.05	1.50	0.20	0.83	0.11
804.26	0.02	4.13	0.51	2.50	0.31
1461.09	0.13	16.50	3.50	12.00	2.55
1646.00	0.20	9.37	1.95	7.90	1.65
1680.23	0.20	6.55	1.35	5.00	1.03
1733.59	0.20	8.70	2.78	6.50	2.08
1810.81	0.20	14.10	2.00	7.80	1.11
1828.91	0.20	13.52	1.72	9.00	1.15
1855.00	0.20	4.70	0.70	3.20	0.48
1910.07	0.03	9.91	2.09	–	–
1983.41	0.21	13.84	3.21	–	–
2029.72	0.12	6.66	1.15	–	–
2043.13	1.34	14.16	3.39	–	–
2060.59	0.12	3.91	0.64	–	–
2140.29	1.82	9.80	2.67	8.30	2.26
2198.35	0.20	14.81	3.82	9.30	2.40
2227.09	0.40	14.49	6.45	11.40	5.08
2265.70	1.00	7.50	2.00	6.60	1.76
2297.60	1.00	15.02	3.53	12.70	2.99
3454.60	1.00	>20.0	–	–	–
3566.50	1.00	>10.00	–	–	–
3691.40	1.00	>15.00	–	–	–
6137.02	0.29	5.10	1.00	3.70	0.73

6154.32	0.09	6.60	1.00	4.10	0.62
6174.03	0.08	6.15	0.96	3.90	0.61
6297.79	0.28	8.50	2.00	6.10	1.44
6309.98	0.33	10.99	2.88	–	–
6323.50	0.13	12.52	2.29	–	–
6394.35	0.10	6.31	0.93	–	–
7304.84	0.20	6.41	1.36	5.10	1.08
7352.34	0.24	7.32	0.98	5.50	0.73
8101.17	0.70	9.20	1.60	6.80	1.18
8229.85	0.39	6.09	1.62	4.70	1.25
8398.85	0.24	3.40	0.81	2.00	0.47
8411.47	0.18	4.45	1.16	3.20	0.83
8463.49	0.15	13.08	2.31	–	–
8475.82	0.52	13.41	2.59	–	–
8621.03	0.79	13.50	2.50	9.80	1.81
8774.85	0.54	11.74	2.01	8.80	1.51
8984.86	0.50	16.74	3.14	11.10	2.08

		$^{87}Rb^{86}Sr$			
Δ_{PA}	Error	FWHM	Error	$\gamma/2\pi$	Error
18.44	00.08	0.79	0.07	0.40	0.03
87.80	1.00	0.79	0.19	0.64	0.15
100.20	1.00	1.10	0.17	0.89	0.14
124.70	1.00	1.10	0.12	0.70	0.07
137.13	0.08	1.72	0.35	1.40	0.29
746.96	0.13	3.49	0.46	2.10	0.27
1133.57	0.42	2.90	1.00	2.70	0.93
1195.08	0.87	>10	–	–	–
1272.73	0.32	5.70	1.40	4.10	1.01
1401.66	0.32	10.40	1.22	6.80	0.79
3277.09	0.33	4.67	1.18	4.20	1.07
3849.53	0.07	2.86	0.30	1.80	0.19
3922.59	0.07	2.98	0.25	1.80	0.15
3956.95	0.05	1.95	0.16	1.30	0.10
5273.00	10.00	>4	–	–	–

		$^{87}Rb^{84}Sr$			
Δ_{PA}	Error	FWHM	Error	$\gamma/2\pi$	Error
11.74	0.60	–	–	0.80	0.40
173.50	0.20	–	–	0.35	0.10
387.40	0.50	–	–	4.00	1.00
427.80	0.20	4.80	0.60	2.70	0.30

1429.01	0.10	0.80	0.20	0.67	0.17

TABLE B.3: Magnetic properties of the investigated one-colour photoassociation resonances of the ^{87}Rb^{87}Sr, ^{87}Rb^{88}Sr and ^{87}Rb^{84}Sr isotopologues. Δ_{PA} is the resonance position, as reported in Tables B.1 and B.2, # substates is the number of observed Zeeman substates of the excited molecular state, μ_{exc} its magnetic moment and $g\ \mu_B$ the derived g-factor times the Bohr magneton. Data taken by A. Bayerle, B. Pasquiou, C.C. Chen, S. Tzanova, V. Barbé and A. Ciamei, table created by A. Ciamei.

		^{87}Rb^{87}Sr	
Δ_{PA} (MHz)	# substates	μ_{exc}/h (MHz/G)	$g\ \mu_B$ (MHz/G)
4.20	>1	−1.40(5)	–
15.84	>1	−1.44(5)	–
249.30	>1	−0.85(6)	–
509.90	>1	−0.95(2)	–
686.79	>1	−1.61(1)	–
1220.56	>1	−1.91(4)	–
1581.50	>1	−0.48(6)	–
1913.40	>1	−0.72(2)	–
2335.40	>1	−0.96(4)	–
4199.20	>1	−0.54(2)	–
4914.20	>1	−1.15(2)	–
5546.20	>1	−1.80(5)	–

		^{87}Rb^{88}Sr	
Δ_{PA} (MHz)	# substates	μ_{exc}/h (MHz/G)	$g\ \mu_B/h$ (MHz/G)
20.70	>2	−0.99(15), 0, 0.99(15)	–
32.23	1	0.42(5)	–
36.26	5	−1.34(20), −0.67(10), 0, 0.67(10), 1.34(20)	0.67(10)
41.39	3	−0.7, 0.2, −1.10	0.90(20)
52.54	>4	−0.35, 0, 0.35, 0.6, 1.00	–
53.50	>3	−0.70, −0.45, 0, 0.45, 0.70	–
260.54	1	0.01(5)	–
265.58	5	−0.48, −0.24, 0, 0.24, 0.48	0.24(7)
272.91	7	−0.84, −0.56, −0.28, 0, 0.28, 0.56, 0.84	0.28(8)
329.34	>1	0.52(4), −0.03(4)	–
334.99	>2	0.70(1), 0.29(3), −0.04(4)	–
364.81	>2	0.70(1), −0.12(5), −0.90(6)	–
804.26	>2	−0.84(6), −0.37(8), 0.14(12)	–
1733.59	>2	−0.61(13), 0.00(1), 0.61(20)	–

^{87}Rb^{84}Sr

Δ_{PA} (MHz)	# substates	μ_{exc}/h (MHz/G)	$g\,\mu_B$ (MHz/G)
173.50	1	$-0.05(4)$	–
387.40	3	–	0.47(17)
427.80	5	–	0.50(10)

Bibliography

[1] S. Stellmer, B. Pasquiou, R. Grimm, and F. Schreck, *"Laser Cooling to Quantum Degeneracy"*, Phys. Rev. Lett. **110**, 263003 (2013), DOI: 10.1103/PhysRevLett.110.263003.

[2] B. L. Augenbraun, J. M. Doyle, T. Zelevinsky, and I. Kozyryev, *"Molecular Asymmetry and Optical Cycling: Laser Cooling Asymmetric Top Molecules"*, Phys. Rev. X **10**, 031022 (2020), DOI: 10.1103/PhysRevX.10.031022.

[3] J. J. Gilijamse, S. Hoekstra, S. Y. T. van de Meerakker, G. C. Groenenboom, and G. Meijer, *"Near-Threshold Inelastic Collisions Using Molecular Beams with a Tunable Velocity"*, Science **313**, 1617 (2006), DOI: 10.1126/science.1131867.

[4] T. Cremers, N. Janssen, E. Sweers, and S. Y. T. van de Meerakker, *"Design and construction of a multistage Zeeman decelerator for crossed molecular beams scattering experiments"*, Rev. Sci. Instrum. **90**, 013104 (2019), DOI: 10.1063/1.5066062.

[5] S. Ding, Y. Wu, I. A. Finneran, J. J. Burau, and J. Ye, *"Sub-Doppler Cooling and Compressed Trapping of* YO *Molecules at μK Temperatures"*, Phys. Rev. X **10**, 021049 (2020), DOI: 10.1103/PhysRevX.10.021049.

[6] L. W. Cheuk, L. Anderegg, B. L. Augenbraun, Y. Bao, S. Burchesky, W. Ketterle, and J. M. Doyle, *"Λ-Enhanced Imaging of Molecules in an Optical Trap"*, Phys. Rev. Lett. **121**, 083201 (2018), DOI: 10.1103/PhysRevLett.121.083201.

[7] S. Jochim, M. Bartenstein, A. Altmeyer, G. Hendl, S. Riedl, C. Chin, J. Hecker Denschlag, and R. Grimm, *"Bose-Einstein Condensation of Molecules"*, Science **302**, 2101 (2003), DOI: 10.1126/science.1093280.

[8] L. De Marco, G. Valtolina, K. Matsuda, W. G. Tobias, J. P. Covey, and J. Ye, *"A degenerate Fermi gas of polar molecules"*, Science **363**, 853 (2019), DOI: 10.1126/science.aau7230.

[9] K.-K. Ni, S. Ospelkaus, M. H. G. de Miranda, A. Pe'er, B. Neyenhuis, J. J. Zirbel, S. Kotochigova, P. S. Julienne, D. S. Jin, and J. Ye, *"A High Phase-Space-Density Gas of Polar Molecules"*, Science **322**, 231 (2008), DOI: 10.1126/science.1163861.

[10] J. G. Danzl, E. Haller, M. Gustavsson, M. J. Mark, R. Hart, N. Bouloufa, O. Dulieu, H. Ritsch, and H.-C. Nägerl, *"Quantum Gas of Deeply Bound Ground State Molecules"*, Science **321**, 1062 (2008), DOI: 10.1126/science.1159909.

[11] T. Takekoshi, L. Reichsöllner, A. Schindewolf, J. M. Hutson, C. R. Le Sueur, O. Dulieu, F. Ferlaino, R. Grimm, and H.-C. Nägerl, *"Ultracold Dense Samples of Dipolar* RbCs *Molecules in the Rovibrational and Hyperfine Ground State"*, Phys. Rev. Lett. **113**, 205301 (2014), DOI: 10.1103/PhysRevLett.113.205301.

[12] P. K. Molony, P. D. Gregory, Z. Ji, B. Lu, M. P. Köppinger, C. R. Le Sueur, C. L. Blackley, J. M. Hutson, and S. L. Cornish, *"Creation of Ultracold* ^{87}Rb^{133}Cs *Molecules in the Rovibrational Ground State"*, Phys. Rev. Lett. **113**, 255301 (2014), DOI: 10.1103/PhysRevLett.113.255301.

[13] J. W. Park, S. A. Will, and M. W. Zwierlein, *"Ultracold Dipolar Gas of Fermionic* ^{23}Na^{40}K *Molecules in Their Absolute Ground State"*, Phys. Rev. Lett. **114**, 205302 (2015), DOI: 10.1103/PhysRevLett.114.205302.

[14] M. Guo, B. Zhu, B. Lu, X. Ye, F. Wang, R. Vexiau, N. Bouloufa-Maafa, G. Quéméner, O. Dulieu, and D. Wang, *"Creation of an Ultracold Gas of Ground-State Dipolar* ^{23}Na^{87}Rb *Molecules"*, Phys. Rev. Lett. **116**, 205303 (2016), DOI: 10.1103/PhysRevLett.116.205303.

[15] T. Rvachov, H. Son, A. Sommer, S. Ebadi, J. Park, M. Zwierlein, W. Ketterle, and A. Jamison, *"Long-Lived Ultracold Molecules with Electric and Magnetic Dipole Moments"*, Phys. Rev. Lett. **119**, 143001 (2017), DOI: 10.1103/PhysRevLett.119.143001.

[16] K. K. Voges, P. Gersema, M. Meyer zum Alten Borgloh, T. A. Schulze, T. Hartmann, A. Zenesini, and S. Ospelkaus, *"Ultracold Gas of Bosonic* ^{23}Na^{39}K *Ground-State Molecules"*, Phys. Rev. Lett. **125**, 083401 (2020), DOI: 10.1103/PhysRevLett.125.083401.

[17] A. Gerdes, O. Dulieu, H. Knöckel, and E. Tiemann, *"Stark effect measurements on the* NaK *molecule"*, Eur. Phys. J. D **65**, 105 (2011), DOI: 10.1140/epjd/e2011-20048-9.

[18] R. Guérout, M. Aymar, and O. Dulieu, *"Ground state of the polar alkali-metal-atom–strontium molecules: Potential energy curve and permanent dipole moment"*, Phys. Rev. A **82**, 042508 (2010), DOI: 10.1103/PhysRevA.82.042508.

[19] J. A. Blackmore, R. Sawant, P. D. Gregory, S. L. Bromley, J. Aldegunde, J. M. Hutson, and S. L. Cornish, *"Controlling the ac Stark effect of* RbCs *with dc electric and magnetic fields"*, Phys. Rev. A **102**, 053316 (2020), DOI: 10.1103/PhysRevA.102.053316.

[20] G. Quéméner and J. L. Bohn, *"Shielding* $^2\Sigma$ *ultracold dipolar molecular collisions with electric fields"*, Phys. Rev. A **93**, 012704 (2016), DOI: 10.1103/PhysRevA.93.012704.

[21] A. Devolder, L. Eliane, O. Atabek, M. Desouter-Lecomte, and O. Dulieu, *"Laser-assisted self-induced Feshbach resonance for controlling heteronuclear quantum gas mixtures"*, Phys. Rev. A **100**, 052703 (2019), DOI: 10.1103/PhysRevA.100.052703.

[22] A. Micheli, G. Pupillo, H. Büchler, and P. Zoller, *"Cold polar molecules in 2D traps: Tailoring interactions with external fields for novel quantum phases"*, Phys. Rev. A **76**, 043604 (2007), DOI: 10.1103/PhysRevA.76.043604.

[23] B. Yan, S. Moses, B. Gadway, J. Covey, K. Hazzard, A. Rey, D. Jin, and J. Ye, *"Observation of dipolar spin-exchange interactions with lattice-confined polar molecules"*, Nature **501**, 521 (2013), DOI: 10.1038/nature12483.

[24] J. Aldegunde and J. M. Hutson, *"Hyperfine structure of* $^2\Sigma$ *molecules containing alkaline-earth-metal atoms"*, Phys. Rev. A **97**, 042505 (2018), DOI: 10.1103/PhysRevA.97.042505.

[25] P. Żuchowski, J. Aldegunde, and J. Hutson, *"Ultracold* RbSr *Molecules Can Be Formed by Magnetoassociation"*, Phys. Rev. Lett. **105**, 153201 (2010), DOI: 10.1103/PhysRevLett.105.153201.

[26] D. A. Brue and J. M. Hutson, *"Prospects of forming ultracold molecules in* $^2\Sigma$ *states by magnetoassociation of alkali-metal atoms with* Yb*"*, Phys. Rev. A **87**, 052709 (2013), DOI: 10.1103/PhysRevA.87.052709.

[27] A. Green, H. Li, J. H. See Toh, X. Tang, K. C. McCormick, M. Li, E. Tiesinga, S. Kotochigova, and S. Gupta, *"Feshbach Resonances in p-Wave Three-Body Recombination within Fermi-Fermi Mixtures of Open-Shell* ^{6}Li *and Closed-Shell* ^{173}Yb *Atoms"*, Phys. Rev. X **10**, 031037 (2020), DOI: 10.1103/PhysRevX.10.031037.

[28] S. Stellmer, R. Grimm, and F. Schreck, *"Production of quantum-degenerate strontium gases"*, Phys. Rev. A **87**, 013611 (2013), DOI: 10.1103/PhysRevA.87.013611.

[29] S. Stellmer, F. Schreck, and T. C. Killian, *"Degenerate quantum gases of* Sr*"*, Annual Review of Cold Atoms and Molecules, Chapter 1 (2014), DOI: 10.1142/9789814590174_0001.

[30] A. L. Marchant, S. Händel, S. A. Hopkins, T. P. Wiles, and S. L. Cornish, *"Bose-Einstein condensation of* ^{85}Rb *by direct evaporation in an optical dipole trap"*, Phys. Rev. A **85**, 053647 (2012), DOI: 10.1103/PhysRevA.85.053647.

[31] J. L. Bohn, A. M. Rey, and J. Ye, *"Cold molecules: Progress in quantum engineering of chemistry and quantum matter"*, Science **357**, 1002 (2017), DOI: 10.1126/science.aam6299.

[32] A. Micheli, G. K. Brennen, and P. Zoller, *"A toolbox for lattice-spin models with polar molecules"*, Nat. Phys. **2**, 341 (2006), DOI: 10.1038/nphys287.

[33] R. Sawant, J. Blackmore, P. Gregory, J. Mur-Petit, D. Jaksch, J. Aldegunde, J. Hutson, M. Tarbutt, and S. Cornish, *"Ultracold polar molecules as qudits"*, New J. Phys. **22**, 013027 (2020), DOI: 10.1088/1367-2630/ab60f4.

[34] W. Milner, J. Robinson, C. Kennedy, T. Bothwell, D. Kedar, D. Matei, T. Legero, U. Sterr, F. Riehle, H. Leopardi, T. Fortier, J. Sherman, J. Levine, J. Yao, J. Ye, and E. Oelker, *"Demonstration of a Timescale Based on a Stable Optical Carrier"*, Phys. Rev. Lett. **123**, 173201 (2019), DOI: 10.1103/PhysRevLett.123.173201.

[35] S. Dimopoulos, P. W. Graham, J. M. Hogan, M. A. Kasevich, and S. Rajendran, *"Gravitational wave detection with atom interferometry"*, Phys. Lett. B **678**, 37 (2009), DOI: 10.1016/j.physletb.2009.06.011.

[36] P. W. Graham, J. M. Hogan, M. A. Kasevich, S. Rajendran, and R. W. Romani, *"Mid-band gravitational wave detection with precision atomic sensors"*, arXiv (2017), arXiv: 1711.02225.

[37] M. Borkowski, *"Optical Lattice Clocks with Weakly Bound Molecules"*, Phys. Rev. Lett. **120**, 083202 (2018), DOI: 10.1103/PhysRevLett.120.083202.

[38] V. Andreev, D. Ang, D. DeMille, J. Doyle, G. Gabrielse, J. Haefner, N. Hutzler, Z. Lasner, C. Meisenhelder, B. O'Leary, C. Panda, A. West, E. West, and X. Wu, *"Improved limit on the electric dipole moment of the electron"*, Nature **562**, 355 (2018), DOI: 10.1038/s41586-018-0599-8.

[39] D. DeMille, Virtual AMO seminar, Standford University (2020).

[40] O. Dulieu and A. Osterwalder, *"Cold Chemistry: Molecular Scattering and Reactivity Near Absolute Zero"* (2018).

[41] V. Plomp, Z. Gao, T. Cremers, M. Besemer, and S. Y. T. van de Meerakker, *"High-resolution imaging of molecular collisions using a Zeeman decelerator"*, J. Chem. Phys. **152**, 091103 (2020), DOI: 10.1063/1.5142817.

[42] M.-G. Hu, Y. Liu, D. D. Grimes, Y.-W. Lin, A. H. Gheorghe, R. Vexiau, N. Bouloufa-Maafa, O. Dulieu, T. Rosenband, and K.-K. Ni, *"Direct observation of bimolecular reactions of ultracold* KRb *molecules"*, Science **366**, 1111 (2019), DOI: 10.1126/science.aay9531.

[43] G. Valtolina, K. Matsuda, W. G. Tobias, J.-R. Li, L. D. Marco, and J. Ye, *"Dipolar evaporation of reactive molecules to below the Fermi temperature"*, Nature **588**, 239 (2020), DOI: 10.1038/s41586-020-2980-7.

[44] K. Matsuda, L. De Marco, J.-R. Li, W. G. Tobias, G. Valtolina, G. Quéméner, and J. Ye, *"Resonant collisional shielding of reactive molecules using electric fields"*, Science **370**, 1324 (2020), DOI: 10.1126/science.abe7370.

[45] N. Vitanov, A. Rangelov, B. Shore, and K. Bergmann, *"Stimulated Raman adiabatic passage in physics, chemistry and beyond"*, Rev. Mod. Phys. **89**, 015006 (2016), DOI: 10.1103/RevModPhys.89.015006.

[46] K. Bergmann1, H.-C. Nägerl, C. Panda, G. Gabrielse, E. Miloglyadov, M. Quack, G. Seyfang, G. Wichmann, S. Ospelkaus, and A. Kuhn, *"Roadmap on STIRAP applications"*, J. Phys. B **52**, 202001 (2019), DOI: 10.1088/1361-6455/ab3995.

[47] S. Stellmer, B. Pasquiou, R. Grimm, and F. Schreck, *"Creation of Ultracold* Sr_2 *Molecules in the Electronic Ground State"*, Phys. Rev. Lett. **109**, 115302 (2012), DOI: 10.1103/PhysRevLett.109.115302.

[48] A. Ciamei, A. Bayerle, C.-C. Chen, B. Pasquiou, and F. Schreck, *"Efficient production of long-lived ultracold* Sr_2 *molecules"*, Phys. Rev. A **96**, 013406 (2017), DOI: 10.1103/PhysRevA.96.013406.

[49] A. Ciamei, A. Bayerle, B. Pasquiou, and F. Schreck, *"Observation of Bose-enhanced photoassociation products"*, EPL **119**, 46001 (2017), DOI: 10.1209/0295-5075/119/46001.

[50] D. A. Steck, *"Rubidium 87 D Line Data"*, available online at http://steck.us/alkalidata (Version 2.2.1, last revised 21 November 2019).

[51] A. Ciamei, *"Taming ultracold* RbSr *and* Sr_2*"*, PhD Thesis, Institute of Physics, University of Amsterdam, The Netherlands (2018).

[52] A. Bayerle, *"Ultracold strontium and rubidium: mixtures, quantum gases and molecules"*, PhD thesis, Institute of Physics, University of Amsterdam, The Netherlands (2017).

[53] A. Devolder, E. Luc-Koenig, O. Atabek, M. Desouter-Lecomte, and O. Dulieu, *"Proposal for the formation of ultracold deeply bound* RbSr *dipolar molecules by all-optical methods"*, Phys. Rev. A **98**, 053411 (2018), DOI: 10.1103/PhysRevA.98.053411.

[54] G. Reinaudi, C. B. Osborn, M. McDonald, S. Kotochigova, and T. Zelevinsky, *"Optical Production of Stable Ultracold* $^{88}Sr_2$ *Molecules"*, Phys. Rev. Lett. **109**, 115303 (2012), DOI: 10.1103/PhysRevLett.109.115303.

[55] R. Vexiau, *"Dynamique et contrôle optique des molécules froides"*, PhD thesis, Université Paris Sud - Paris XI (2012).

[56] A. Devolder, *"Contrôle par laser de la formation de molécules polaires paramagnétiques ultra-froides"*, PhD thesis, Université Paris-Saclay (2019).

[57] J. M. Brown and A. Carrington, *"Rotational Spectroscopy of Diatomic Molecules"*, Cambridge Molecular Science, Cambridge University Press, 2003, DOI: 10.1017/CBO9780511814808.

[58] G. Herzberg, *"Molecular spectra and molecular structure. Vol.1: Spectra of diatomic molecules"* (1950).

[59] B. Judd, *"Angular Momentum Theory for Diatomic Molecules"* (1975).

[60] J. V. Pototschnig, G. Krois, F. Lackner, and W. E. Ernst, *"Ab initio study of the* RbSr *electronic structure: Potential energy curves, transition dipole moments, and permanent electric dipole moments"*, J. Chem. Phys. **141**, 234309 (2014), DOI: 10.1063/1.4903791.

[61] R. J. Le Roy, *"Long-Range Potential Coefficients From RKR Turning Points:* C_6 *and* C_8 *for* $B(^3\Pi^+_{Ou})$*-state* Cl_2, Br_2, *and* I_2*"*, Canadian Journal of Physics **52**, 246 (1974), DOI: 10.1139/p74-035.

[62] J. C. Slater, *"Atomic Radii in Crystals"*, J. Chem. Phys. **41**, 3199 (1964), DOI: 10.1063/1.1725697.

[63] K. M. Jones, E. Tiesinga, P. D. Lett, and P. S. Julienne, *"Ultracold photoassociation spectroscopy: Long-range molecules and atomic scattering"*, Rev. Mod. Phys. **78**, 483 (2006), DOI: 10.1103/RevModPhys.78.483.

[64] D. A. Steck, *"Quantum and Atom Optics"*, available online at http://steck.us/teaching (revision 0.13.4, 24 September 2020).

[65] G. Shlyapnikov, *"Ultracold quantum Gases Part 1: Bose-condensed gases"*, Undergraduate Physics course, University of Amsterdam, Netherlands (2015 version).

[66] V. Barbé, A. Ciamei, B. Pasquiou, L. Reichsöllner, F. Schreck, P. S. Żuchowski, and J. Hutson, *"Observation of Feshbach resonances between alkali and closed-shell atoms"*, Nat. Phys. **14**, 881 (2018), DOI: https://doi.org/10.1038/s41567-018-0169-x, eprint: https://rdcu.be/b7NuQ.

[67] S. Stellmer, M. K. Tey, B. Huang, R. Grimm, and F. Schreck, *"Bose-Einstein Condensation of Strontium"*, Phys. Rev. Lett. **103**, 200401 (2009), DOI: 10.1103/PhysRevLett.103.200401.

[68] S. Taie, R. Yamazaki, S. Sugawa, and Y. Takahashi, *"An SU(6) Mott insulator of an atomic Fermi gas realized by large-spin Pomeranchuk cooling"*, Nat. Phys. **8**, 825 (2012), DOI: 10.1038/nphys2430.

[69] S. Kraft, F. Vogt, O. Appel, F. Riehle, and U. Sterr, *"Bose-Einstein Condensation of Alkaline Earth Atoms: ^{40}Ca"*, Phys. Rev. Lett. **103**, 130401 (2009), DOI: 10.1103/PhysRevLett.103.130401.

[70] J. Pérez-Ríos, F. Herrera, and R. V. Krems, *"External field control of collective spin excitations in an optical lattice of $^2\Sigma$ molecules"*, New J. Phys. **12**, 103007 (2010), DOI: 10.1088/1367-2630/12/10/103007.

[71] M. A. Baranov, M. Dalmonte, G. Pupillo, and P. Zoller, *"Condensed Matter Theory of Dipolar Quantum Gases"*, Chem. Rev. **112**, 5012 (2012), DOI: 10.1021/cr2003568.

[72] J. L. Bohn, A. M. Rey, and J. Ye, *"Cold molecules: Progress in quantum engineering of chemistry and quantum matter"*, Science **357**, 1002 (2017), DOI: 10.1126/science.aam6299.

[73] R. Krems, B. Friedrich, and W. C. Stwalley, *"Cold Molecules: Theory, Experiment, Applications"* (2009).

[74] S. V. Alyabyshev, M. Lemeshko, and R. V. Krems, *"Sensitive imaging of electromagnetic fields with paramagnetic polar molecules"*, Phys. Rev. A **86**, 013409 (2012), DOI: 10.1103/physreva.86.013409.

[75] F. Herrera, Y. Cao, S. Kais, and K. B. Whaley, *"Infrared-dressed entanglement of cold open-shell polar molecules for universal matchgate quantum computing"*, New J. Phys. **16**, 075001 (2014), DOI: 10.1088/1367-2630/16/7/075001.

[76] S. B. Cahn, J. Ammon, E. Kirilov, Y. V. Gurevich, D. Murphree, R. Paolino, D. A. Rahmlow, M. G. Kozlov, and D. DeMille, *"Zeeman-Tuned Rotational Level-Crossing Spectroscopy in a Diatomic Free Radical"*, Phys. Rev. Lett. **112**, 163002 (2014), DOI: 10.1103/PhysRevLett.112.163002.

[77] M. Kajita, *"Prospects of detecting $m_e m_p$ variance using vibrational transition frequencies of $^2\Sigma$-state molecules"*, Phys. Rev. A **77**, 012511 (2008), DOI: 10.1103/PhysRevA.77.012511.

[78] M. Safronova, D. Budker, D. DeMille, D. Kimball, A. Derevianko, and C. Clark, *"Search for New Physics with Atoms and Molecules"*, Rev. Mod. Phys. **90**, 025008 (2017), DOI: 10.1103/RevModPhys.90.025008.

[79] J. Wolf, M. Deiß, A. Krükow, E. Tiemann, B. P. Ruzic, Y. Wang, J. P. D'Incao, P. S. Julienne, and J. H. Denschlag, *"State-to-state chemistry at ultra-low temperature"*, Science **358**, 921 (2017), DOI: 10.1126/science.aan8721.

[80] S. Ospelkaus, K.-K. Ni, D. Wang, M. H. G. de Miranda, B. Neyenhuis, G. Quemener, P. S. Julienne, J. L. Bohn, D. S. Jin, and J. Ye, *"Quantum-State Controlled Chemical Reactions of Ultracold Potassium-Rubidium Molecules"*, Science **327**, 853 (2010), DOI: 10.1126/science.1184121.

[81] T. Sikorsky, Z. Meir, R. Ben-shlomi, N. Akerman, and R. Ozeri, *"Spin-controlled atom-ion chemistry"*, Nat. Commun. **9**, 920 (2018), DOI: 10.1038/s41467-018-03373-y.

[82] R. V. Krems, *"Cold controlled chemistry"*, Phys. Chem. Chem. Phys. **10**, 4079 (2008), DOI: 10.1039/b802322k.

[83] J. Szczepkowski, A. Grochola, P. Kowalczyk, O. Dulieu, R. Guérout, P. S. Żuchowski, and W. Jastrzebski, *"Experimental and theoretical study of the B(2) $\rightarrow$ X(1) system in the* KCr *molecule"*, J. Quant. Spectrosc. Radiat. Transfer **210**, 217 (2018), DOI: 10.1016/j.jqsrt.2018.02.020.

[84] J. V. Pototschnig, G. Krois, F. Lackner, and W. E. Ernst, *"Investigation of the* RbCa *molecule: Experiment and theory"*, J. Mol. Spectrosc. **310**, 126 (2015), DOI: 10.1016/j.jms.2015.01.006.

[85] M. Ivanova, A. Stein, A. Pashov, A. V. Stolyarov, H. Knöckel, and E. Tiemann, *"The $X\ ^2\Sigma^+$ state of* LiCa *studied by Fourier-transform spectroscopy"*, J. Chem. Phys. **135**, 174303 (2011), DOI: 10.1063/1.3652755.

[86] E. Schwanke, H. Knöckel, A. Stein, A. Pashov, S. Ospelkaus, and E. Tiemann, *"Laser and Fourier transform spectroscopy of ^{7}Li^{88}Sr"*, J. Phys. B **50**, 235103 (2017), DOI: 10.1088/1361-6455/aa8ca0.

[87] M. Borkowski, P. S. Żuchowski, R. Ciuryło, P. S. Julienne, D. Kędziera, Ł. Mentel, P. Tecmer, F. Münchow, C. Bruni, and A. Görlitz, *"Scattering lengths in isotopologues of the* RbYb *system"*, Phys. Rev. A **88**, 052708 (2013), DOI: 10.1103/PhysRevA.88.052708.

[88] G. Krois, J. V. Pototschnig, F. Lackner, and W. E. Ernst, *"Spectroscopy of Cold* LiCa *Molecules Formed on Helium Nanodroplets"*, J. Phys. Chem. A **117**, 13719 (2013), DOI: 10.1021/jp407818k.

[89] G. Pichler, A. Lyyra, P. Kleiber, W. Stwalley, R. Hammer, K. Sando, and H. Michels, *"Laser-induced chemiluminescence of the* LiMg *excimer"*, Chem. Phys. Lett. **156**, 467 (1989), DOI: 10.1016/S0009-2614(89)87313-0.

[90] M. Borkowski, A. A. Buchachenko, R. Ciuryło, P. S. Julienne, H. Yamada, Y. Kikuchi, Y. Takasu, and Y. Takahashi, *"Weakly bound molecules as sensors of new gravitylike forces"*, Sci. Rep. **9** (2019), DOI: https://doi.org/10.1038/s41598-019-51346-y.

[91] M Borkowski, A. A. Buchachenko, R Ciuryło, P. S. Julienne, H Yamada, K Yuu, K Takahashi, Y Takasu, and Y Takahashi, *"Probing Non-Newtonian gravity by photoassociation spectroscopy"*, J. Phys. Conf. Ser. **810**, 012014 (2017), DOI: 10.1088/1742-6596/810/1/012014.

[92] F. Münchow, C. Bruni, M. Madalinski, and A. Görlitz, *"Two-photon photoassociation spectroscopy of heteronuclear* YbRb*"*, Phys. Chem. Chem. Phys. **13**, 18734 (2011), DOI: 10.1039/c1cp21219b.

[93] M. Borkowski, P. Morzyński, R. Ciuryło, P. S. Julienne, M. Yan, B. J. DeSalvo, and T. C. Killian, *"Mass scaling and nonadiabatic effects in photoassociation spectroscopy of ultracold strontium atoms"*, Phys. Rev. A **90**, 032713 (2014), DOI: 10.1103/physreva.90.032713.

[94] J. Gerschmann, E. Schwanke, A. Pashov, H. Knöckel, S. Ospelkaus, and E. Tiemann, *"Laser and Fourier-transform spectroscopy of* KCa*"*, Phys. Rev. A **96**, 032505 (2017), DOI: 10.1103/PhysRevA.96.032505.

[95] P. S. Żuchowski, R. Guérout, and O. Dulieu, *"Ground- and excited-state properties of the polar and paramagnetic* RbSr *molecule: A comparative study"*, Phys. Rev. A **90**, 012507 (2014), DOI: 10.1103/physreva.90.012507.

[96] J. V. Pototschnig, R. Meyer, A. W. Hauser, and W. E. Ernst, *"Vibronic transitions in the alkali-metal (*Li, Na, K, Rb*) - alkaline-earth-metal (*Ca, Sr*) series: A systematic analysis of de-excitation mechanisms based on the graphical mapping of Frank-Condon integrals"*, Phys. Rev. A **95**, 022501 (2017), DOI: 10.1103/PhysRevA.95.022501.

[97] M. Debatin, T. Takekoshi, R. Rameshan, L. Reichsöllner, F. Ferlaino, R. Grimm, R. Vexiau, N. Bouloufa, O. Dulieu, and H.-C. Nägerl, *"Molecular spectroscopy for ground-state transfer of ultracold* RbCs *molecules"*, Phys. Chem. Chem. Phys. **13**, 18926 (2011), DOI: 10.1039/C1CP21769K.

[98] T. Chen, S. Zhu, X. Li, J. Qian, and Y. Wang, *"Prospects for transferring* ^{87}Rb^{84}Sr *dimers to the rovibrational ground state based on calculated molecular structures"*, Phys. Rev. A **89**, 063402 (2014), DOI: 10.1103/PhysRevA.89.063402.

[99] M. Guo, R. Vexiau, B. Zhu, B. Lu, N. Bouloufa-Maafa, O. Dulieu, and D. Wang, *"High-resolution molecular spectroscopy for producing ultracold absolute-ground-state* ^{23}Na^{87}Rb *molecules"*, Phys. Rev. A **96**, 052505 (2017), DOI: 10.1103/PhysRevA.96.052505.

[100] G. Gopakumar, M. Abe, M. Hada, and M. Kajita, *"Dipole polarizability of alkali-metal (*Na, K, Rb*)–alkaline-earth-metal (*Ca, Sr*) polar molecules: Prospects for alignment"*, J. Chem. Phys. **140**, 224303 (2014), DOI: 10.1063/1.4881396.

[101] F. Lackner, G. Krois, T. Buchsteiner, J. V. Pototschnig, and W. E. Ernst, *"Helium-Droplet-Assisted Preparation of Cold* RbSr *Molecules"*, Phys. Rev. Lett. **113**, 153001 (2014), DOI: 10.1103/PhysRevLett.113.153001.

[102] G. Krois, F. Lackner, J. V. Pototschnig, T. Buchsteiner, and W. E. Ernst, *"Characterization of* RbSr *molecules: spectral analysis on helium droplets"*, Phys. Chem. Chem. Phys. **16**, 22373 (2014), DOI: 10.1039/c4cp03135k.

[103] B. Pasquiou, A. Bayerle, S. M. Tzanova, S. Stellmer, J. Szczepkowski, M. Parigger, R. Grimm, and F. Schreck, *"Quantum degenerate mixtures of strontium and rubidium atoms"*, Phys. Rev. A **88**, 023601 (2013), DOI: 10.1103/PhysRevA.88.023601.

[104] V. V. Flambaum, G. F. Gribakin, and C. Harabati, *"Analytical calculation of cold-atom scattering"*, Phys. Rev. A **59**, 1998 (1999), DOI: 10.1103/PhysRevA.59.1998.

[105] J. Szczepkowski, A. Ciamei, and F. Schreck (in preparation).

[106] J. Jiang, Y. Cheng, and J. Mitroy, *"Long range interactions between alkali and alkaline-earth atoms"*, J. Phys. B **46**, 125004 (2013), DOI: 10.1088/0953-4075/46/12/125004.

[107] A. Derevianko, S. G. Porsev, and J. F. Babb, *"Electric dipole polarizabilities at imaginary frequencies for hydrogen, the alkali-metal, alkaline-earth, and noble gas atoms"*, At. Data Nucl. Data Tables **96**, 323 (2010), DOI: 10.1016/j.adt.2009.12.002.

[108] J. M. Standard and P. R. Certain, *"Bounds to two- and three-body long-range interaction coefficients for S-state atoms"*, J. Chem. Phys. **83**, 3002 (1985), DOI: 10.1063/1.449203.

[109] G. F. Gribakin and V. V. Flambaum, *"Calculation of the scattering length in atomic collisions using the semiclassical approximation"*, Phys. Rev. A **48**, 546 (1993), DOI: 10.1103/PhysRevA.48.546.

[110] A. Ciamei, J. Szczepkowski, A. Bayerle, V. Barbé, L. Reichsöllner, S. M. Tzanova, C. C. Chen, B. Pasquiou, A. Grochola, P. Kowalczyk, W. Jastrzebski, and F. Schreck, *"The* RbSr $^2\Sigma^+$ *ground state investigated via spectroscopy of hot and ultracold molecules"*, Phys. Chem. Chem. Phys. **20**, 26221 (2018), DOI: 10.1039/C8CP03919D.

[111] D. A. Brue and J. M. Hutson, *"Magnetically Tunable Feshbach Resonances in Ultracold* Li-Yb *Mixtures"*, Phys. Rev. Lett. **108**, 043201 (2012), DOI: 10.1103/physrevlett.108.043201.

[112] A. Mosk, S. Kraft, M. Mudrich, K. Singer, W. Wohlleben, R. Grimm, and M. Weidemüller, *"Mixture of ultracold lithium and cesium atoms in an optical dipole trap"*, Appl. Phys. B **73**, 791 (2001), DOI: 10.1007/s003400100743.

[113] M. Inguscio, S. Stringari, and C. Wieman, *"Bose-Einstein Condensation in Atomic Gases"*, Proceedings of the International School of Physics "Enrico Fermi" **140**, 321 (1999).

[114] N. S. Dattani and R. J. Le Roy, *"A DPF data analysis yields accurate analytic potentials for and that incorporate 3-state mixing near the state asymptote"*, J. Mol. Spectrosc. **268**, 199 (2011), DOI: 10.1016/j.jms.2011.03.030.

[115] M. Semczuk, X. Li, W. Gunton, M. Haw, N. S. Dattani, J. Witz, A. K. Mills, D. J. Jones, and K. W. Madison, *"High-resolution photoassociation spectroscopy of the* $^6Li_2$ $1^3\Sigma_g^+$ *state"*, Phys. Rev. A **87**, 052505 (2013), DOI: 10.1103/PhysRevA.87.052505.

[116] J. J. Lutz and J. M. Hutson, *"Deviations from Born-Oppenheimer mass scaling in spectroscopy and ultracold molecular physics"*, J. Mol. Spectrosc. **330**, 43 (2016), DOI: 10.1016/j.jms.2016.08.007.

[117] J. Y. Seto, R. J. Le Roy, J. Vergès, and C. Amiot, *"Direct potential fit analysis of the* $X\ ^1\Sigma_g^+$ *state of* Rb_2*: Nothing else will do!"*, J. Chem. Phys. **113**, 3067 (2000), DOI: 10.1063/1.1286979.

[118] E. G. van Kempen, S. J. Kokkelmans, D. J. Heinzen, and B. J. Verhaar, *"Interisotope Determination of Ultracold Rubidium Interactions from Three High-Precision Experiments"*, Phys. Rev. Lett. **88**, 093201 (2002), DOI: 10.1103/PhysRevLett.88.093201.

[119] R. J. Le Roy, C. C. Haugen, J. Tao, and H. Li, *"Long-range damping functions improve the short-range behaviour of 'MLR' potential energy functions"*, Mol. Phys. **109**, 435 (2011), DOI: 10.1080/00268976.2010.527304.

[120] C. Douketis, G. Scoles, S. Marchetti, M. Zen, and A. J. Thakkar, *"Intermolecular forces via hybrid Hartree–Fock–SCF plus damped dispersion (HFD) energy calculations. An improved spherical model"*, J. Chem. Phys. **76**, 3057 (1982), DOI: 10.1063/1.443345.

[121] NIST Database.

[122] A. Pashov, W. Jastrzebski, and P. Kowalczyk, *"Construction of potential curves for diatomic molecular states by the IPA method"*, Comput. Phys. Commun. **128**, 622 (2000), DOI: 10.1016/S0010-4655(00)00010-2.

[123] T. Nicholson, S. Blatt, B. Bloom, J. Williams, J. Thomsen, J. Ye, and P. Julienne, *"Optical Feshbach resonances: Field-dressed theory and comparison with experiments"*, Phys. Rev. A **92**, 022709 (2015), DOI: 10.1103/PhysRevA.92.022709.

[124] S. Stellmer, *"Degenerate quantum gases of strontium"*, PhD thesis, Faculty of Mathematics, Computer Science and Physics, University of Innsbruck, Austria (2013).

[125] S. Stellmer, R. Grimm, and F. Schreck, *"Detection and manipulation of nuclear spin states in fermionic strontium"*, Phys. Rev. A **84**, 043611 (2011), DOI: 10.1103/PhysRevA.84.043611.

[126] U. Schünemann, H. Engler, R. Grimm, M. Weidemüller, and M. Zielonkowski, *"Simple scheme for tunable frequency offset locking of two lasers"*, Rev. Sci. Instrum. **70**, 242 (1999), DOI: 10.1063/1.1149573.

[127] R. Grimm, M. Weidemüller, and Y. Ovchinnikov, *"Optical Dipole Traps for Neutral Atoms"*, Advances in Atomic, Molecular, and Optical Physics **42**, 95 (2000), DOI: 10.1016/S1049-250X(08)60186-X.

[128] T. Zelevinsky, M Boyd, A Ludlow, T Ido, J. Ye, R Ciuryło, P Naidon, and P. Julienne, *"Narrow Line Photoassociation in an Optical Lattice"*, Phys. Rev. Lett. **96**, 203201 (2006), DOI: 10.1103/PhysRevLett.96.203201.

[129] L. K. Reichsöllner, *"A general quantum-engineering technique for efficient production of ultracold dipolar molecules"*, PhD thesis, Department for Mathematics, Computer sciences and Physics, Leopold-Franzens-Universität, Innsbruck, Austria (2017).

[130] P. Altin, G. Dennis, G. McDonald, D. Döring, J. Debs, J. Close, C. Savage, and N. Robins, *"Collapse and three-body loss in a* ^{85}Rb *Bose-Einstein condensate"*, Phys. Rev. A **84**, 033632 (2011), DOI: 10.1103/PhysRevA.84.033632.

[131] C. Chin, R. Grimm, P. Julienne, and E. Tiesinga, *"Feshbach resonances in ultracold gases"*, Rev. Mod. Phys. **82**, 1225 (2010), DOI: 10.1103/RevModPhys.82.1225.

[132] B. C. Yang, M. D. Frye, A. Guttridge, J. Aldegunde, P. S. Żuchowski, S. L. Cornish, and J. M. Hutson, *"Magnetic Feshbach resonances in ultracold collisions between* Cs *and* Yb *atoms"*, Phys. Rev. A **100**, 022704 (2019), DOI: 10.1103/PhysRevA.100.022704.

[133] U. Fano, *"Effects of Configuration Interaction on Intensities and Phase Shifts"*, Physical Review **124**, 1866 (1961), DOI: 10.1103/PhysRev.124.1866.

[134] F. H. Mies, E. Tiesinga, and P. S. Julienne, *"Manipulation of Feshbach resonances in ultracold atomic collisions using time-dependent magnetic fields"*, Phys. Rev. A **61**, 022721 (2000), DOI: 10.1103/PhysRevA.61.022721.

[135] A Marte, T. Volz, J Schuster, S Dürr, G Rempe, E Kempen, and B. J. Verhaar, *"Feshbach Resonances in Rubidium 87: Precision Measurement and Analysis"*, Phys. Rev. Lett. **89**, 283202 (2003), DOI: 10.1103/PhysRevLett.89.283202.

[136] P. Julienne, E. Tiesinga, and T. Köhler, *"Making Cold Molecules by Time-dependent Feshbach Resonances"*, J. Mod. Opt. **51**, 1787 (2004), DOI: 10.1080/09500340410001695382.

[137] F. Deuretzbacher, K. Plassmeier, D. Pfannkuche, F. Werner, C. Ospelkaus, S. Ospelkaus, K. Sengstock, and K. Bongs, *"Heteronuclear molecules in an optical lattice: Theory and experiment"*, Phys. Rev. A **77**, 032726 (2008), DOI: 10.1103/PhysRevA.77.032726.

[138] S. A. Moses, J. P. Covey, M. T. Miecnikowski, B. Yan, B. Gadway, J. Ye, and D. S. Jin, *"Creation of a low-entropy quantum gas of polar molecules in an optical lattice"*, Science **350**, 659 (2015), DOI: 10.1126/science.aac6400.

[139] F. Mies, C. Williams, P. Julienne, and M. Krauss, *"Estimating Bounds on Collisional Relaxation Rates of Spin-Polarized* ^{87}Rb *Atoms at Ultracold Temperatures"*, J. Res. Natl. Inst. Stand. Technol. **101**, 521 (1996), DOI: 10.6028/jres.101.052.

[140] J. Walraven, *"Quantum gases"*, Undergraduate Physics course, University of Amsterdam, Netherlands, available at https://staff.fnwi.uva.nl/j.t.m.walraven/walraven/Lectures.htm (2015 version).

[141] J. P. Burke Jr., *"Theoretical Investigation of Cold Alkali Atom Collisions"*, PhD thesis, JILA, University of Colorado, USA (1999).

[142] T. Takekoshi, M. Debatin, R. Rameshan, F. Ferlaino, R. Grimm, H.-C. Nägerl, R. Le Sueur, J. Hutson, P. Julienne, S. Kotochigova, and E. Tiemann, *"Towards the production of ultracold ground-state* RbCs *molecules: Feshbach resonances, weakly bound states, and the coupled-channel model"*, Phys. Rev. A **85**, 032506 (2012), DOI: 10.1103/PhysRevA.85.032506.

[143] K. M. O'Hara, M. E. Gehm, S. R. Granade, S. Bali, and J. E. Thomas, *"Stable, Strongly Attractive, Two-State Mixture of Lithium Fermions in an Optical Trap"*, Phys. Rev. Lett. **85**, 2092 (2000), DOI: 10.1103/PhysRevLett.85.2092.

[144] S. Jochim, *"Bose-Einstein Condensation of Molecules"*, PhD thesis, Institut für Experimentalphysikunter der Leitung, Leopold-Franzens-Universität, Innsbruck, Austria (2004).

[145] C. Cohen-Tannoudji, B. Diu, and F. Laloe, *"Quantum Mechanics, Volume 2"* (1986).

[146] J. Walraven, *"Atomic Physics"*, Undergraduate Physics course, University of Amsterdam, Netherlands, available at https://staff.fnwi.uva.nl/j.t.m.walraven/walraven/Lectures.htm (2018 version).

[147] J. Werner, A. Griesmaier, S. Hensler, J. Stuhler, T. Pfau, A. Simoni, and E. Tiesinga, *"Observation of Feshbach Resonances in an Ultracold Gas of* ^{52}Cr*"*, Phys. Rev. Lett. **94**, 183201 (2005), DOI: 10.1103/PhysRevLett.94.183201.

[148] D. A. Steck, *"Rubidium* 85 *D Line Data"*, available online at http://steck.us/alkalidata (Version 2.2.1, last revised 21 November 2019).

[149] C. H. Greene, P. Giannakeas, and J. Pérez-Ríos, *"Universal few-body physics and cluster formation"*, Rev. Mod. Phys. **89**, 035006 (2017), DOI: 10.1103/RevModPhys.89.035006.

[150] I. Bloch, J. Dalibard, and W. Zwerger, *"Many-body physics with ultracold gases"*, Rev. Mod. Phys. **80**, 885 (2008), DOI: 10.1103/RevModPhys.80.885.

[151] J. M. Hutson and P. Soldán, *"Molecule formation in ultracold atomic gases"*, Int. Rev. Phys. Chem. **25**, 497 (2006), DOI: 10.1080/01442350600921772.

[152] T. Köhler, K. Góral, and P. S. Julienne, *"Production of cold molecules via magnetically tunable Feshbach resonances"*, Rev. Mod. Phys. **78**, 1311 (2006), DOI: 10.1103/RevModPhys.78.1311.

[153] S. A. Moses, J. P. Covey, M. T. Miecnikowski, D. S. Jin, and J. Ye, *"New frontiers for quantum gases of polar molecules"*, Nat. Phys. **13**, 13 (2017), DOI: 10.1038/nphys3985.

[154] E. R. Meyer and J. L. Bohn, *"Electron electric-dipole-moment searches based on alkali-metal- or alkaline-earth-metal-bearing molecules"*, Phys. Rev. A **80**, 042508 (2009), DOI: 10.1103/PhysRevA.80.042508.

[155] C. A. Regal, C. Ticknor, J. L. Bohn, and D. S. Jin, *"Creation of ultracold molecules from a Fermi gas of atoms"*, Nature **424**, 47 (2003), DOI: 10.1038/nature01738.

[156] J. Herbig, T. Kraemer, M. Mark, T. Weber, C. Chin, H.-C. Nägerl, and R. Grimm, *"Preparation of a pure molecular quantum gas"*, Science **301**, 1510 (2003), DOI: 10.1126/science.1088876.

[157] J. G. Danzl, M. J. Mark, E. Haller, M. Gustavsson, R. Hart, J. Aldegunde, J. M. Hutson, and H.-C. Nägerl, *"An ultracold, high-density sample of rovibronic ground-state molecules in an optical lattice"*, Nat. Phys. **6**, 265 (2010), DOI: 10.1038/nphys1533.

[158] H. Hara, Y. Takasu, Y. Yamaoka, J. M. Doyle, and Y. Takahashi, *"Quantum Degenerate Mixtures of Alkali and Alkaline-Earth-Like Atoms"*, Phys. Rev. Lett. **106**, 205304 (2011), DOI: 10.1103/PhysRevLett.106.205304.

[159] A. H. Hansen, A. Khramov, W. H. Dowd, A. O. Jamison, V. V. Ivanov, and S. Gupta, *"Quantum degenerate mixture of ytterbium and lithium atoms"*, Phys. Rev. A **84**, 011606 (2011), DOI: 10.1103/PhysRevA.84.011606.

[160] V. D. Vaidya, J. Tiamsuphat, S. L. Rolston, and J. V. Porto, *"Degenerate Bose-Fermi mixtures of rubidium and ytterbium"*, Phys. Rev. A **92**, 043604 (2015), DOI: 10.1103/PhysRevA.92.043604.

[161] A. Guttridge, S. A. Hopkins, S. L. Kemp, M. D. Frye, J. M. Hutson, and S. L. Cornish, *"Interspecies thermalization in an ultracold mixture of* Cs *and* Yb *in an optical trap"*, Phys. Rev. A **96**, 012704 (2017), DOI: 10.1103/PhysRevA.96.012704.

[162] W. Dowd, R. J. Roy, R. K. Shrestha, A. Petrov, C. Makrides, S. Kotochigova, and S. Gupta, *"Magnetic field dependent interactions in an ultracold* Li-Yb($^3P_2$) *mixture"*, New J. Phys. **17**, 055007 (2015), DOI: 10.1088/1367-2630/17/5/055007.

[163] S. Kato, S. Sugawa, K. Shibata, R. Yamamoto, and Y. Takahashi, *"Control of Resonant Interaction between Electronic Ground and Excited States"*, Phys. Rev. Lett. **110**, 173201 (2013), DOI: 10.1103/PhysRevLett.110.173201.

[164] G. Pagano, M. Mancini, G. Cappellini, L. Livi, C. Sias, J. Catani, M. Inguscio, and L. Fallani, *"Strongly Interacting Gas of Two-Electron Fermions at an Orbital Feshbach Resonance"*, Phys. Rev. Lett. **115**, 265301 (2015), DOI: 10.1103/PhysRevLett.115.265301.

[165] M. Höfer, L. Riegger, F. Scazza, C. Hofrichter, D. R. Fernandes, M. M. Parish, J. Levinsen, I. Bloch, and S. Fölling, *"Observation of an Orbital Interaction-Induced Feshbach Resonance in* ^{173}Yb*"*, Phys. Rev. Lett. **115**, 265302 (2015), DOI: 10.1103/PhysRevLett.115.265302.

[166] K. Aikawa, A. Frisch, M. Mark, S. Baier, A. Rietzler, R. Grimm, and F. Ferlaino, *"Bose-Einstein Condensation of Erbium"*, Phys. Rev. Lett. **108**, 210401 (2012), DOI: 10.1103/PhysRevLett.108.210401.

[167] K. Baumann, N. Q. Burdick, M. Lu, and B. L. Lev, *"Observation of low-field Fano-Feshbach resonances in ultracold gases of dysprosium"*, Phys. Rev. A **89**, 020701 (2014), DOI: 10.1103/PhysRevA.89.020701.

[168] J. Aldegunde and J. M. Hutson, *"Hyperfine structure of* $^2\Sigma$ *molecules containing alkaline-earth-metal atoms"*, Phys. Rev. A **97**, 042505 (2018), DOI: 10.1103/PhysRevA.97.042505.

[169] M. Mark, T. Kraemer, J. Herbig, C. Chin, H.-C. Nägerl, and R. Grimm, *"Efficient creation of molecules from a cesium Bose-Einstein condensate"*, EPL **69**, 706 (2005), DOI: 10.1209/epl/i2004-10427-7.

[170] N. Syassen, D. M. Bauer, M. Lettner, D. Dietze, T. Volz, S. Dürr, and G. Rempe, *"Atom-Molecule Rabi Oscillations in a Mott Insulator"*, Phys. Rev. Lett. **99**, 033201 (2007), DOI: 10.1103/PhysRevLett.99.033201.

[171] S. L. Kemp, K. L. Butler, R. Freytag, S. A. Hopkins, E. A. Hinds, M. R. Tarbutt, and S. L. Cornish, *"Production and characterization of a dual species magneto-optical trap of cesium and ytterbium"*, Rev. Sci. Instrum. **87**, 023105 (2016), DOI: 10.1063/1.4941719.

[172] G. Bismut, B. Pasquiou, E. Maréchal, P. Pedri, L. Vernac, O. Gorceix, and B. Laburthe-Tolra, *"Collective Excitations of a Dipolar Bose-Einstein Condensate"*, Phys. Rev. Lett. **105**, 040404 (2010), DOI: 10.1103/PhysRevLett.105.040404.

[173] S. Bennetts, *"1000 times closer to a continuous atom laser: Steady-state strontium withunity phase-space density"*, PhD thesis, Institute of Physics, University of Amsterdam, The Netherlands (2019).

[174] S. Friebel, C. D'andrea, J. Walz, M. Weitz, and T. W. Hänsch, *"CO_2-laser optical lattice with cold rubidium atoms"*, Phys. Rev. A **57**, R20 (1998), DOI: 10.1103/PhysRevA.57.R20.

[175] Y. B. Ovchinnikov, J. H. Müller, M. R. Doery, E. J. D. Vredenbregt, K. Helmerson, S. L. Rolston, and W. D. Phillips, *"Diffraction of a Released Bose-Einstein Condensate by a Pulsed Standing Light Wave"*, Phys. Rev. Lett. **83**, 284 (1999), DOI: 10.1103/PhysRevLett.83.284.

List of publications

B.1 Publications presented in this thesis

Observation of Feshbach resonances between alkali and closed-shell atoms
Nat. Phys. **14**, 881 (2018)
Vincent Barbé, Alessio Ciamei, Benjamin Pasquiou, Lukas Reichsöllner, Florian Schreck, , Piotr. S. Żuchowski and Jeremy M. Hutson.

Chapter 6 of this thesis: I collected most of the data presented in this publication and analysed them. I was heavily involved in writing the paper.

The RbSr $^2\Sigma^+$ ground state investigated via spectroscopy of hot and ultracold molecules
Phys. Chem. Chem. Phys. **20**, 26221 (2018)
Alessio Ciamei, Jacek Szczepkowski, Alex Bayerle, Vincent Barbé, Lukas Reichsöllner,
Slava M. Tzanova, Chun-Chia Chen, Benjamin Pasquiou, Anna Grochola, Pawel Kowalczyk, Wlodzimierz Jastrzebski and Florian Schreck.

Chapter 3 of this thesis: I performed most of the magnetic Feshbach resonance experiments and many of the two-colour spectroscopy experiments reported in this publication. I analysed the data and discussed their interpretation with Alessio Ciamei, who was in charge of the fit of the long-range part of the PEC.

B.2 Publications in preparation that were presented in this thesis

One-colour photoassociation spectroscopy of Rb-Sr mixtures (working title)

Chapter 4 and Appendix B of this thesis: I performed many of the one-colour spectroscopy experiments reported in this thesis and analysed the results. These data are subject to an ongoing theoretical analysis led by Mateusz Borkowski.

Novel power supply and stabilization scheme for sub-Tesla magnetic field production with low-noise performance (working title)

Section 7.2 of this thesis: together with Lukas Reichsöllner, I implemented a new power supply for the production of large magnetic fields (up to 1500 G, i.e. 0.15 T) with low-noise performance. The

power supply was designed by Lukas Reichsöllner, Tijs van Roon and the electronics workshop of the University of Amsterdam (of which Tijs van Roon is a member). I developped RF spectroscopy methods to probe the stability and the noise of the magnetic field using ultracold Rb atoms.

Acknowledgements

My passion for physics traces back to 2009, when I started my studies in the French preparatory classes, in Angers. These were greatly challenging times, times during which I discovered the beauty of mathematics, physics, chemistry, and their astounding capacity to describe and to act upon natural phenomena. Among the excellent professors I met during these years, I want to thank in particular Mady Reynaud, my chemistry teacher, and Franck Poquin, my second-year physics teacher. They supported me when I made unorthodox choices, i.e. when I decided to enter a third-year cursus in genetics at university with no prior background in biology, and later on when I prepared the *concours d'entrée* to the French engineering schools at home. They offered to give oral exams to help me prepare when they had no obligation to do so, and based on their teaching I successfully passed the national exams and entered the optics engineering school I had chosen to prepare for. I learned from them that in science nothing is ever achieved but through hard work and discipline, a lesson that echoes in my life to this very day.

Throughout my PhD years I have had the chance to work with many skilled scientists, and I want to thank them in the following lines. Florian was definitely an excellent PhD supervisor: he is probably one the best experimentalists in the field, extremely driven, extremely knowledgeable, yet he is a very good human being — a rare animal in this respect. He managed to find the money required to keep the RbSr experiment thriving, giving my coworkers and I the peace of mind to pursue experiments while dismissing any funding-related duties. I had four fantastic years working as a PhD in Amsterdam, so, Florian: thanks for that. I also want to thank Alex Bayerle and Alessio Ciamei, the two PhD employees I worked with first when I arrived in Amsterdam. The understanding of the PEC of ground-state RbSr and the discovery of the first Feshbach resonances were quite spectacular achievements, earned through many years of collaborative work, and gave a lot of meaning to working as a team. I also want to thank Benjamin Pasquiou for teaching me how to handle the experiment when I first arrived, and for delivering countless comments and advices throughout the years. He has been the heart and soul of the Sr group for many years now, and it is fair to say that most things wouldn't have happened without him.

In the most recent years I worked very closely with Lukas Reichsöllner, Séverin Charpignon and Premjith Thekkeppat. Lukas was an extremely skilled post-doc, incredibly knowledgeable in electronics, optics and quantum physics. He would manage to find the time to be at home with his wife and recently-born son at lunch time and in the evening, after 6 pm, and would work insanely hard in the lab the rest of the time. I cannot say how much I admire Lukas for having so brilliantly reconciled his work and his family life. Séverin is an excellent craftsman, he built from scratch the new one-colour

spectroscopy laser system that will be used very soon in the lab, and above all he was my most dedicated snooker partner. As for Prem, I think it is no secret that I couldn't have thought of a better PhD employee to take over my work on the RbSr experiment. The rapidity at which Prem got to know and handle the experiment is impressive; he even got used to my swearing, which in itself is a remarkable achievement. I am sure his hard work will pay off in the very near future.

I also want to thank all my colleagues from the nearby quantum gas laboratories. First and foremost, Shayne Bennetts and Chun-Chia Chen. They have been my late-night partners for many years, sitting next door, improving their machine while I was running spectroscopy scans till two or sometimes four in the morning. We had countless physics discussions at these late hours, and I must confess I might not have always chosen to stay that long in an empty building if I couldn't have pushed their door and get some first-hand update on the atom laser experiment. Additionally, Shayne greatly helped me out with the baking/pumping when the RbSr vacuum system was at risk — many thanks again, that was really appreciated. I also want to thank those I first met when I arrived, and who made me feel welcome: Arthur La Rooij, Maarten Soudijn, Julius de Hond, Nataly Cisternas San Martin, Graham Lochead, David Davtyan, Carla Sanna, Robert Spreeuw, Ben van Linden van den Heuvell and Klaasjan van Druten, who now contributes to the RbSr experiment. Thanks also to everyone in the Sr group, Rodrigo González Escudero of course, and Francesca Famà, Sheng Zhou, Jiri Minar, Denis Kurlov, Namrata Dutta-Mazumdar, Georgios Siviloglou, Sergueï Pyatchenkov, Alex Urech, Jens Samland, Ivo Knottnerus, Tim van Leent, Zhou Muyan Geng, Thies Plassmann... and in the hybrid atom-ion quantum systems group: Rene Gerritsma, Thomas Feldker, Thomas Secker, Jannis Joger, Henning Fürst, Norman V. Ewald, Henrik Hirzler, Matteo Mazzanti, Eleanor Trimby, Juan Arias Espinoza, Rianne Lous... I have learned a lot from the many scientific discussions I had with them all these years. Thanks also to Jook Walraven, who gave me the opportunity to assist the teaching of his atomic physics course. I learned a lot from this experience, both from the physics and from the teaching points of view.

I have met many more people than I could remember at the University of Amsterdam, but among them I want to salute the condensed matter theoreticians — also referred to as "hardcore theory freaks" — I now consider to be my friends: Enej Ilievski, Neil Robinson, Oleksandr Gamayun and Yuan Miao. Enej and Oleksandr are some of the most intense physicists I have met, and we ended up developing strong ties throughout the years. Neil Robinson became my regular snooker and jazz concert partner; I shared with him some of the best moments I had in Amsterdam. As for Yuan, he is definitely the most prominent of my fellow drinkers, accompanying me in bars over night to tell drunk people about Möbius strips and permutation symmetries.

A complex experiment such as RbSr requires the assistance of skilled technicians and engineers, well-trained in mechanics, electronics and IT. In this respect, I could always rely on the high-profile expertise of the UvA Technology Center, led by Alix Wattjes. I want to thank in particular Willem van Aartsen, who was always enthusiastic about manufacturing an urgently-needed mechanical piece, Gerrit Hardeman for his help on software-related issues, Tijs van Roon, Tjeerd Weijers and Johan Mozes for their electronics expertise, and Sven Koot, Tristan van Klingeren, Daan Giesen and Jan Kalwij for their excellent craftsmanship.

Research is in essence a collaborative process, and for this reason I want to thank all the physicists abroad that contributed to the RbSr experiment during my PhD time, in particular Olivier Dulieu and Adrien Devolder in Orsay, Jeremy Hutson and Matthew Frye in Durham, Jacek Szczepkowski, Anna Grochola, Wlodzimierz Jastrzebski and Pawel Kowalczyk in Warszawa, Piotr Żuchowski in Toruń and most recently Mateusz Borkowski who joined the RbSr laboratory. Without your support the RbSr experiment wouldn't be what it is today.

From the first day I arrived in Amsterdam, I have been immensely helped by the secretariat of the Institute of Physics at UvA: they helped me to find housing, took care fluently of all the administration surrounding my PhD contract, and were always very kind and patient when addressing my queries. For that I want to thank Natalie Wells, Anne-Marieke Crommentuijn, Joost van Mameren, Jirina Salkova, Astrid Harryson and Klaartje Wartenbergh. In this respect, I also want to thank Trúc Ngô and Laila Scharf from the HR department and Cecilia Sigvardsdotter, Ines Jonkhoff, Irene Verkist Pérez and Anna la Verge from the housing department. You all made it very easy for me to forget about administrative duties and focus on my research.

Thanks to all my friends in France, in Amsterdam and abroad. They are too numerous to mention, and there would be too much to say, but they have been with me all along. Thanks to my sister Laëtitia, my brother Jérôme and my sister-in-law Laurence, who all supported me from the very beginning of my career and were always enthusiastic about my research. And, of course: thank you, Zohra.

Je dédie cette thèse à mes parents, qui ont tout rendu possible.